DISCRETE WAVELET TRANSFORMS - THEORY AND APPLICATIONS

Edited by **Juuso Olkkonen**

INTECHWEB.ORG

Discrete Wavelet Transforms - Theory and Applications
Edited by Juuso Olkkonen

Published by InTech
Janeza Trdine 9, 51000 Rijeka, Croatia

Publishing Process Manager Ivana Lorkovic
Technical Editor Teodora Smiljanic
Cover Designer Martina Sirotic
Image Copyright Arvind Balaraman, 2010. Used under license from Shutterstock.com

First published March, 2011
Printed in India

A free online edition of this book is available at www.intechopen.com
Additional hard copies can be obtained from orders@intechweb.org

Discrete Wavelet Transforms - Theory and Applications, Edited by Juuso Olkkonen
p. cm.
ISBN 978-953-307-185-5

Contents

Preface

Discrete wavelet transform (DWT) algorithms have become standards tools for processing of signals and images in several areas in research and industry. The first DWT structures were based on the compactly supported conjugate quadrature filters (CQFs). However, a drawback in CQFs is related to the nonlinear phase effects such as image blurring and spatial dislocations in multi-scale analyses. On the contrary, in biorthogonal discrete wavelet transform (BDWT) the scaling and wavelet filters are symmetric and linear phase. The BDWT algorithms are commonly constructed by a ladder-type network called lifting scheme. The procedure consists of sequential down and uplifting steps and the reconstruction of the signal is made by running the lifting network in reverse order. Efficient lifting BDWT structures have been developed for VLSI and microprocessor applications. The analysis and synthesis filters can be implemented by integer arithmetics using only register shifts and summations. Many BDWT-based data and image processing tools have outperformed the conventional discrete cosine transform (DCT) -based approaches. For example, in JPEG2000 Standard the DCT has been replaced by the lifting BDWT.

As DWT provides both octave-scale frequency and spatial timing of the analyzed signal, it is constantly used to solve and treat more and more advanced problems. One of the main difficulties in multi-scale analysis is the dependency of the total energy of the wavelet coefficients in different scales on the fractional shifts of the analysed signal. If we have a discrete signal $x[n]$ and the corresponding time shifted signal $x[n\text{-}\tau]$, where $\tau \in [0,1]$, there may exist a significant difference in the energy of the wavelet coefficients as a function of the time shift. In shift invariant methods the real and imaginary parts of the complex wavelet coefficients are approximately a Hilbert transform pair. The energy of the wavelet coefficients equals the envelope, which provides smoothness and approximate shift-invariance. Using two parallel DWT banks, which are constructed so that the impulse responses of the scaling filters have half-sample delayed versions of each other, the corresponding wavelets are a Hilbert transform pair. The dual-tree CQF wavelet filters do not have coefficient symmetry and the nonlinearity interferes with the spatial timing in different scales and prevents accurate statistical correlations. Therefore the current developments in theory and applications of wavelets are concentrated on the dual-tree BDWT structures.

This book reviews the recent progress in theory and applications of wavelet transform algorithms. The book is intended to cover a wide range of methods (e.g. lifting DWT, shift invariance, 2D image enhancement) for constructing DWTs and to illustrate the utilization of DWTs in several non-stationary problems and in biomedical as well as industrial applications. It is organized into four major parts. Part I focuses on non-

stationary signals. Application examples include non-stationary fractal and chaotic time series, non-stationary vibration and sound signals in the vehicle engineering and motor fault detection. Part II addresses image processing and analysis applications such as image denoising and contrast enhancement, and face recognition. Part III is devoted to biomedical applications, including ECG signal compression, multi-scale analysis of EEG signals and classification of medical images in computer aided diagnosis. Finally, Part IV describes how DWT can be utilized in wireless digital communication systems and synchronization of power converters.

It should be pointed that the book comprises of both tutorial and advanced material. Therefore, it is intended to be a reference text for graduate students and researchers to obtain in-depth knowledge on specific applications. The editor is indebted to all co-authors for giving their valuable time and expertise in constructing this book. The technical editors are also acknowledged for their tedious support and help.

Juuso T. Olkkonen, Ph.D.
VTT Technical Research Centre of Finland
Espoo, Finland

Part 1

Non-stationary Signals

1

Discrete Wavelet Analyses for Time Series

José S. Murguía and Haret C. Rosu
UASLP, IPICYT
México

1. Introduction

One frequent way of collecting experimental data by scientists and engineers is as sequences of values at regularly spaced intervals in time. These sequences are called time-series. The fundamental problem with the data in the form of time-series is how to process them in order to extract meaningful and correct information, i.e., the possible signals embedded in them. If a time-series is stationary one can think that it can have harmonic components that can be detected by means of Fourier analysis, i.e., Fourier transforms (FT). However, in recent times, it became evident that many time-series are not stationary in the sense that their mean properties change in time. The waves of infinite support that form the harmonic components are not adequate in the latter case in which one needs waves localized not only in frequency but in time as well. They have been called wavelets and allow a time-scale decomposition of a signal. Significant progress in understanding the wavelet processing of non-stationary signals has been achieved over the last two decades. However, to get the dynamics that produces a non-stationary signal it is crucial that in the corresponding time-series a correct separation of the fluctuations from the average behavior, or trend, is performed. Therefore, people had to invent novel statistical methods of detrending the data that should be combined with the wavelet analysis. A bunch of such techniques have been developed lately for the important class of non-stationary time series that display multi-scaling behavior of the multi-fractal type. Our goal in this chapter is to present our experience with the wavelet processing, based mainly on the discrete wavelet transform (DWT), of non-stationary fractal time-series of elementary cellular automata and the non-stationary chaotic time-series produced by a three-state non-linear electronic circuit.

2. The wavelet transform

Let $L^2(\mathbb{R})$ denote the space of all square integrable functions on $\mathbb{R}$. In signal processing parlance, it is the space of functions with finite energy. Let $\psi(t) \in L^2(\mathbb{R})$ be a fixed function. The function $\psi(t)$ is said to be a *wavelet* if and only if its FT $\hat{\psi}(\omega)$ satisfies

$$C_\psi = \int_0^\infty \frac{|\hat{\psi}(\omega)|^2}{|\omega|} d\omega < \infty. \tag{1}$$

The relation (1) is called the *admissibility condition* (Daubechies, 1992; Mallat, 1999; Strang, 1996; Qian, 2002), which implies that the wavelet must have a zero average

$$\int_{-\infty}^{\infty} \psi(t) dt = \hat{\psi}(0) = 0, \tag{2}$$

and therefore it must be oscillatory. In other words, ψ must be a sort of *wave* (Daubechies, 1992; Mallat, 1999).
Let us now define the dilated–translated wavelets $\psi_{a,b}$ as the following functions

$$\psi_{a,b}(t) = \frac{1}{\sqrt{a}}\psi\left(\frac{t-b}{a}\right), \tag{3}$$

where $b \in \mathbb{R}$ is a translation parameter, whereas $a \in \mathbb{R}^+$ $(a \neq 0)$ is a dilation or scale parameter. The factor $a^{-1/2}$ is a normalization constant such that the energy, i.e., the value provided through the square integrability of $\psi_{a,b}$, is the same for all scales a. One notices that the scale parameter a in (3) rules the dilations of the independent variable $(t-b)$. In the same way, the factor $a^{-1/2}$ rules the dilation in the values taken by ψ, see the y-axis in Fig. 1. With (3), one is able to decompose a square integrable function $x(t)$ in terms of these dilated–translated wavelets.

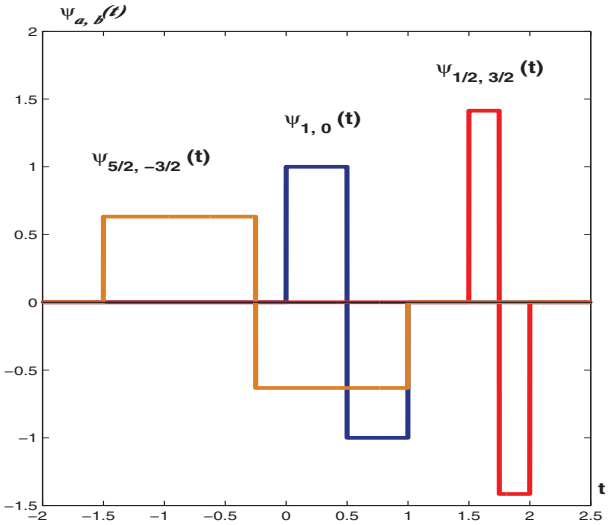

Fig. 1. The Haar wavelet function for several values of the scale parameter a and translation parameter b. If $a < 1$, the wavelet function is contracted, and if $a > 1$, the wavelet is expanded.

The *continuous wavelet transform* (CWT) of $x(t) \in L^2(\mathbb{R})$ is defined as

$$\begin{aligned} W_x(a,b) &= \langle x, \psi_{a,b}\rangle = \int_{-\infty}^{\infty} x(t)\bar{\psi}_{a,b}(t)dt \\ &= \frac{1}{\sqrt{a}}\int_{-\infty}^{\infty} x(t)\bar{\psi}\left(\frac{t-b}{a}\right)dt, \end{aligned} \tag{4}$$

where $\langle\ ,\ \rangle$ is the scalar product in $L^2(\mathbb{R})$ defined as $\langle f, g\rangle := \int f(t)\bar{g}(t)dt$, and the symbol "$\bar{}$" denotes complex conjugation. The CWT (4) measures the variation of x in a neighborhood of the point b, whose size is proportional to a.

If we are interested to reconstruct x from its wavelet transform (4), we make use of the the reconstruction formula, also called *resolution of the identity* (Daubechies, 1992; Mallat, 1999)

$$x(t) = \frac{1}{C_\psi} \int_0^\infty \int_{-\infty}^\infty W_x(a,b)\psi_{a,b}(t)\frac{dadb}{a^2}, \tag{5}$$

where it is now clear why we imposed (1).
However, a huge amount of data are represented by a finite number of values, so it is important to consider a discrete version of the CWT (4). Generally, the orthogonal(discrete) wavelets are employed because this method associates the wavelets to orthonormal bases of $L^2(\mathbb{R})$. In this case, the wavelet transform is performed only on a discrete grid of the parameters of dilation and translation, i.e., a and b take only integral values. Within this framework, an arbitrary signal $x(t)$ of finite energy can be written using an orthonormal wavelet basis:

$$x(t) = \sum_m \sum_n d_n^m \psi_n^m(t), \tag{6}$$

where the coefficients of the expansion are given by

$$d_n^m = \int_{-\infty}^\infty x(t)\psi_n^m(t)dt\ . \tag{7}$$

The orthonormal basis functions are all *dilations* and *translations* of a function referred as the analyzing wavelet $\psi(t)$, and they can be expressed in the form

$$\psi_n^m(t) = 2^{m/2}\psi(2^m t - n), \tag{8}$$

with m and n denoting the dilation and translation indices, respectively. The contribution of the signal at a particular wavelet level m is given by

$$d_m(t) = \sum_n d_n^m \psi_n^m(t), \tag{9}$$

which provides information on the time behavior of the signal within different scale bands. Additionally, it provides knowledge of their contribution to the total signal energy.
In this context, Mallat (1999) developed a computationally efficient method to calculate (6) and (7). This method is known as multiresolution analysis (MRA). The MRA approach provides a general method for constructing orthogonal wavelet basis and leads to the implementation of the fast wavelet transform (FWT). This algorithm connects, in an elegant way, wavelets and filter banks. A multiresolution signal decomposition of a signal X is based on successive decomposition into a series of approximations and details, which become increasingly coarse. Associated with the wavelet function $\psi(t)$ is a corresponding scaling function, $\varphi(t)$, and scaling coefficients, a_n^m (Mallat, 1999). The scaling and wavelet coefficients at scale m can be computed from the scaling coefficients at the next finer scale $m+1$ using

$$a_n^m = \sum_l h[l-2n]a_l^{m+1}, \tag{10}$$

$$d_n^m = \sum_l g[l-2n]a_l^{m+1}, \tag{11}$$

where $h[n]$ and $g[n]$ are typically called lowpass and highpass filters in the associated filter bank. Equations (10) and (11) represent the fast wavelet transform (FWT) for computing (7). In

fact, the signals a_n^m and d_n^m are the convolutions of a_n^{m+1} with the filters $h[n]$ and $g[n]$ followed by a downsampling of factor 2 (Mallat, 1999).
Conversely, a reconstruction of the original scaling coefficients a_n^{m+1} can be made from

$$a_n^{m+1} = \sum_l \left(h[2l-n]a_l^m + g[2l-n]d_l^m\right), \tag{12}$$

a combination of the scaling and wavelet coefficients at a coarse scale. Equation (12) represents the inverse of FWT for computing (6), and it corresponds to the synthesis filter bank. This part can be viewed as the discrete convolutions between the upsampled signal a_l^m and the filters $h[n]$ and $g[n]$, that is, following an "upsampling" of factor 2 one calculates the convolutions between the upsampled signal and the filters $h[n]$ and $g[n]$. The number of levels in the multiresolution algorithm depends on the length of the signal. A signal with 2^k values can be decomposed into $k+1$ levels. To initialize the FWT, one considers a discrete time signal $X = \{x[1], x[2], \ldots, x[N]\}$ of length $N = 2^M$. The first application of (10) and (11), beginning with $a_n^{m+1} = x[n]$, defines the first level of the FWT of X. The process goes on, always adopting the "$m+1$" scaling coefficients to calculate the "m" scaling and wavelet coefficients. Iterating (10) and (11) M times, the transformed signal consists of M sets of wavelet coefficients at scales $m = 1, \ldots, M$, and a signal set of scaling coefficients at scale M. There are exactly $2^{(k-m)}$ wavelet coefficients d_n^m at each scale m, and $2^{(k-M)}$ scaling coefficients a_n^M. The maximum number of iterations $M_{\max}$ is k. This property of the MRA is generally the key factor to identify crucial information in the respective frequency bands. A three-level decomposition process of the FWT is shown in Fig. 2.

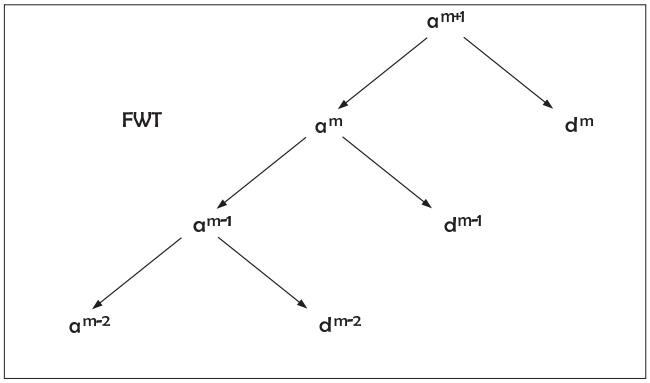

Fig. 2. The structure of a three-level fast wavelet transform.

In a broad sense, with this approach, the low-pass coefficients capture the trend and the high-pass coefficients keep track of the fluctuations in the data. The scaling and wavelet functions are naturally endowed with an appropriate window size, which manifests in the scale index or level, and hence they can capture the local averages and differences, in a window of one's choice.
When someone is interested to measure the local or global regularity of a signal, some degree of regularity is useful in the wavelet basis for the representation to be well behaved (Daubechies, 1992; Mallat, 1999). To achieve this, a wavelet function should have n vanishing moments. A wavelet is said to have n vanishing moments if and only if it satisfies $\int_{-\infty}^{\infty} t^k \psi(t)dt = 0$ for $k = 0, 1, \ldots, n-1$ and $\int_{-\infty}^{\infty} t^k \psi(t)dt \neq 0$ for $k = n$. This means that

a wavelet with n vanishing moments is orthogonal to all polynomials up to order $n-1$. Thus, the DWT of $x(t)$ performed with a wavelet $\psi(t)$ with n vanishing moments is nothing else but a "smoothed version" of the $n-$th derivative of $x(t)$ on various scales. This important property helps detrending the data.
In addition, another important property is that the total energy of the signal may be expressed as follows

$$\sum_{n=1}^{N} |x[n]|^2 = \sum_{n=1}^{N} |a_n^M|^2 + \sum_{m=1}^{M} \sum_{n=1}^{N} |d_n^m|^2. \tag{13}$$

This can be identified as Parseval's relation in terms of wavelets, where the signal energy can be calculated in terms of the different resolution levels of the corresponding wavelet-transformed signal. A more detailed treatment of this subject can be found in (Mallat, 1999).

3. Multifractal analysis of cellular automata time series

3.1 Cellular automata

An elementary cellular automaton(ECA) can be considered as a discrete dynamical that evolve at discrete time steps. An ECA is a cellular automata consisting of a chain of N lattice sites with each site is denoted by an index i. Associated with each site i is a dynamical variable x_i which can take only k discrete values. Most of the studies have been done with $k = 2$, where $x_i = 0$ or 1. Therefore there are 2^N different states for these automata. One can see that the time, space, and states of this system take only discrete values. The ECA considered evolves according to the local rule

$$x_n^{t+1} = [x_{n-1}^t + x_{n+1}^t] \bmod 2\,, \tag{14}$$

which corresponds to the rule 90. Table 1 is the lookup table of this ECA rule, where it is specified the evolution from the neighborhood configuration (first row) to the next state (second row), that is, the next state of $i-$th cell depends on the present states of its left and right neighbors.

Neighborhood	111	110	101	100	011	010	001	000
Rule result	0	1	0	1	1	0	1	0

Table 1. Elementary rule 90. The second row shows the future state of the cell if it and its neighbors are in the arrangement shown above in the first row.

In fact, a rule is numbered by the unsigned decimal equivalent of the binary expression in the second row. When the same rule is applied to update cells of ECA, such ECA are called uniform ECA; otherwise the ECA are called non-uniform or hybrids. It is important to observe that the evolution rules of ECA are determined by two main factors, the rule and the initial conditions.

3.2 WMF-DFA algorithm

To reveal the MF properties (Halsey et al., 1986) of ECA, we follow a variant of the MF-DFA with the discrete wavelet method proposed in (Manimaran et al., 2005). This algorithm will separate the trends from fluctuations, in the ECA time series, using the fact that the low-pass version resembles the original data in an "averaged" manner in different resolutions. Instead

of a polynomial fit, we consider the different versions of the low-pass coefficients to calculate the "local" trend. This method involves the following steps.
Let $x(t_k)$ be a time series type of data, where $t_k = k\Delta t$ and $k = 1, 2, \ldots, N$.

1. Determine the profile $Y(k) = \sum_{i=1}^{k}(x(t_i) - \langle x \rangle)$ of the time series, which is the cumulative sum of the series from which the series mean value is subtracted.
2. Compute the fast wavelet transform (FWT), i.e., the multilevel wavelet decomposition of the profile. For each level m, we get the fluctuations of the $Y(k)$ by subtracting the "local" trend of the Y data, i.e., $\Delta Y(k;m) = Y(k) - \tilde{Y}(k;m)$, where $\tilde{Y}(k;m)$ is the reconstructed profile after removal of successive details coefficients at each level m. These fluctuations at level m are subdivided into windows, i.e., into $M_s = \text{int}(N/s)$ non-overlapping segments of length s. This division is performed starting from both the beginning and the end of the fluctuations series (i.e., one has $2M_s$ segments). Next, one calculates the local variances associated to each window ν

$$F^2(\nu, s; m) = \text{var}\left[\Delta Y((\nu-1)s + j; m)\right] \ , j = 1, ..., s \ , \ \nu = 1, ..., 2M_s \ , \ M_s = \text{int}(N/s) \ . \quad (15)$$

3. Calculate a $q-$th order fluctuation function defined as

$$F_q(s;m) = \left\{ \frac{1}{2M_s} \sum_{\nu=1}^{2M_s} |F^2(\nu, s; m)|^{q/2} \right\}^{1/q} \quad (16)$$

where $q \in \mathbb{Z}$ with $q \neq 0$. Because of the diverging exponent when $q \to 0$ we employed in this limit a logarithmic averaging $F_0(s;m) = \exp\left\{ \frac{1}{2M_s} \sum_{\nu=1}^{2M_s} \ln |F^2(\nu, s; m)| \right\}$ as in (Kantelhardt et al., 2002; Telesca et al., 2004).

To determine if the analyzed time series have a fractal scaling behavior, the fluctuation function $F_q(s;m)$ should reveal a power law scaling

$$F_q(s;m) \sim s^{h(q)}, \quad (17)$$

where $h(q)$ is called the generalized Hurst exponent (Telesca et al., 2004) since it can depend on q, while the original Hurst exponent is $h(2)$. If h is constant for all q then the time series is monofractal, otherwise it has a MF behavior. In the latter case, one can calculate various other MF scaling exponents, such as $\tau(q) = qh(q) - 1$ and $f(\alpha)$ (Halsey et al., 1986). A linear behavior of $\tau(q)$ indicates monofractality whereas the non-linear behavior indicates a multifractal signal. A fundamental result in the multifractal formalism states that the singularity spectrum $f(\alpha)$ is the Legendre transform of $\tau(q)$, i.e.,

$$\alpha = \tau'(q), \qquad \text{and} \qquad f(\alpha) = q\alpha - \tau(q).$$

The singularity spectrum $f(\alpha)$ is a non-negative convex function that is supported on the closed interval $[\alpha_{\min}, \alpha_{\max}]$. In fact, the strength of the multifractality is roughly measured with the width $\Delta\alpha = \alpha_{\max} - \alpha_{\min}$ of the parabolic singularity spectrum $f(\alpha)$ on the α axis, where the boundary values of the support, $\alpha_{\min}$ for $q > 0$ and $\alpha_{\max}$ for $q < 0$, correspond to the strongest and weakest singularity, respectively.

3.3 Application of WMF-DFA

To illustrate the efficiency of the wavelet multifractal procedure, we first carry out the analysis of the binomial multifractal model (Feder, 1998; Kantelhardt et al., 2002).
For the multifractal time series generated through the binomial multifractal model , a series of $N = 2^{n_{\max}}$ numbers x_k, with $k = 1, \ldots, N$, is defined by

$$x_k = a^{n(k-1)}(1-a)^{n_{\max}-n(k-1)}. \tag{18}$$

where $0.5 < a < 1$ is a parameter and $n(k)$ is the number of digits equal to 1 in the binary representation of the index k. The scaling exponent $h(q)$ and $\tau(q)$ can be calculated exactly in this model. These exponents have the closed form

$$h(q) = \frac{1}{q} - \frac{\ln[a^q + (1-a)^q]}{q \ln 2}, \qquad \tau(q) = -\frac{\ln[a^q + (1-a)^q]}{\ln 2}. \tag{19}$$

In Table 2 and Fig. 3, we present the comparison of the multifractal quantity h for $a = 2/3$ between the values for the theoretical case ($h_T(q)$), with the numerical results obtained through wavelet analysis ($h_W(q)$). Notice that the numerical values have a slight downward translation. Adding a vertical offset ($\Delta = h_T(1) - h_W(1)$) to $h_W(q)$, we can notice that both values theoretically and numerically are very close.

q	$h_T(q)$	$h_W(q)$	$h_W(q) + \Delta$
-10	1.4851	1.4601	1.4851
-9	1.4742	1.4498	1.4749
-8	1.4607	1.4373	1.4623
-7	1.4437	1.4217	1.4467
-6	1.4220	1.4018	1.4269
-5	1.3938	1.3761	1.4012
-4	1.3568	1.3422	1.3673
-3	1.3083	1.2971	1.3221
-2	1.2459	1.2376	1.2627
-1	1.1699	1.1626	1.1876
0	0.0000	1.0742	1.0992
1	1.0000	0.9809	1.0059
2	0.9240	0.8961	0.9212
3	0.8617	0.8286	0.8537
4	0.8131	0.7780	0.8031
5	0.7761	0.7401	0.7652
6	0.7479	0.7112	0.7362
7	0.7262	0.6887	0.7137
8	0.7093	0.6711	0.6961
9	0.6958	0.6570	0.6821
10	0.6848	0.6457	0.6707

Table 2. The values of the generalized Hurst exponent h for the binomial multifractal model with $a = 2/3$, which were computed analytically and with the wavelet approach.

In a similar way, we analyze the time series of the so-called row sum ECA signals, i.e., the sum of ones in sequences of rows, employing the db-4 wavelet function, another wavelet function that belongs to the Daubechies family (Daubechies, 1992; Mallat, 1999). We have found that

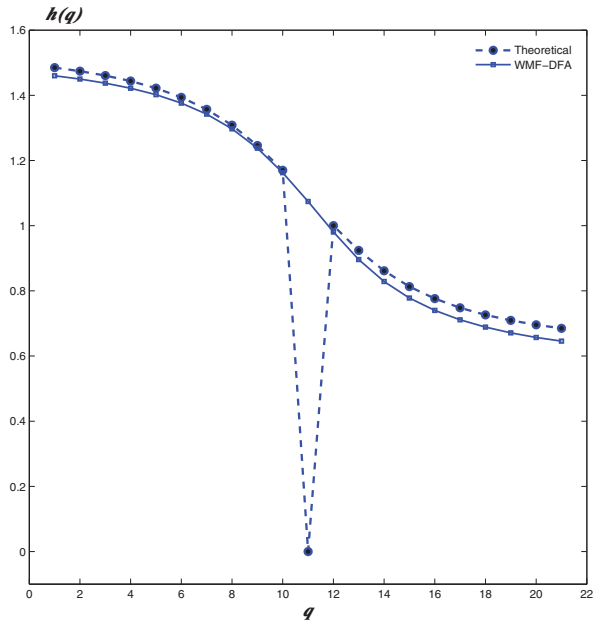

Fig. 3. The generalized Hurst exponent h for the binomial multifractal model with $a = 2/3$. The theoretical values of $h(q)$ with the WMF-DFA calculations are shown for comparison.

a better matching of the results given by the WMF-DFA method with those of other methods is provided with this wavelet function. Figure 4 illustrates the results for the rule 90, when the first row is all 0s with a 1 in the center, i.e., the impulsive initial condition. The fact that the generalized Hurst exponent is not a constant horizontal line is indicative of a multifractal behavior in this ECA time series. In addition, if the τ index is not of a single slope, it can be considered as another clear feature of multifractality.

For the impulsive initial condition in ECA rule 90 the most "frequent" singularity for the analyzed time series occurs at $\alpha = 0.568$, and $\Delta\alpha = 1.0132(0.9998)$ when the WMF-DFA (MF-DFA) are employed. Reference (Murguía et al., 2009) presents the results for different initial center pulses for rules 90, 105, and 150, where the width $\Delta\alpha$ of rule 90 is shifted to the right with respect to those of 105 and 150. In addition, the strongest singularity, $\alpha_{\min}$, of all these time series corresponds to the rule 90 and the weakest singularity, $\alpha_{\max}$, to the rule 150.

With the aim of computing the pseudo-random sequences of N bits, in Reference (Mejía & Urías, 2001) an algorithm based on the backward evolution of the CA rule 90 has been proposed. A modification of the generator producing pseudo-random sequences has been recently considered in (Murguía et al., 2010). The latter proposal is implemented and studied in terms of the sequence matrix $\mathbf{H}_N$, which was used to generate recursively the pseudo-random sequences.

This matrix has dimensions $(2N+1) \times (2N+1)$. Since the evolution of the sequence matrix $\mathbf{H}_N$ is based on the evolution of the ECA rule 90, the structure of the patterns of bits of the latter must be directly reflected in the structure of the entries of $\mathbf{H}_N$.

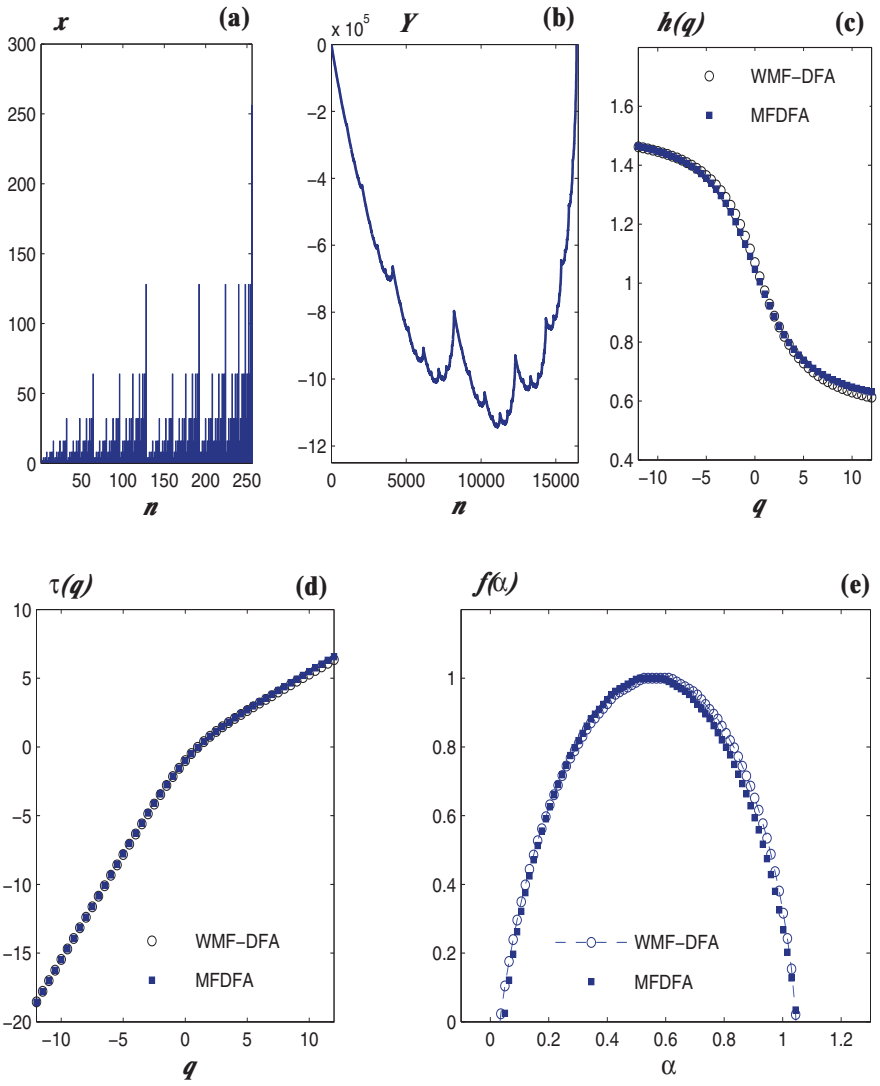

Fig. 4. (a) Time series of the row signal of the cellular automata rule 90. Only the first 2^8 points are shown of the whole set of 2^{14} data points. Profile Y of the row signal. (d) Generalized Hurst exponent $h(q)$. (e) The τ exponent, $\tau(q) = qh(q) - 1$. (f) The singularity spectrum $f(\alpha) = q\frac{d\tau(q)}{dq} - \tau(q)$. The calculations of the multifractal quantities h, τ, and $f(\alpha)$ are performed both with the MF-DFA and the wavelet-based WMF-DFA.

Here, in the same spirit as in Ref. (Murguía et al., 2009), we also analyze the sum of ones in the sequences of the rows of the matrix $\mathbf{H}_N$ with the db-4 wavelet function. The results for the row sums of $\mathbf{H}_{2047}$ are illustrated in Fig. 5, through which we confirm the multifractality of this time series. The width $\Delta\alpha_{H_{2047}} = 1.12 - 0.145 = 0.975$, and the most "frequent" singularity occurs at $\alpha_{\mathrm{mf}_{\mathrm{H}_{2047}}} = 0.638$. Although the profile is different, the results are similar with those obtained for the rule 90 with a slight shifting, see Fig. 4. A more complete analysis of this matrix is carried out in (Murguía et al., 2010).

4. Chaotic time series

In this section, we study the dynamics of experimental time series generated by an electronic chaotic circuit. The wavelet analysis of these experimental chaotic time series gives us useful information of such system through the energy concentration at specific wavelet levels.
It is known that the wavelet variance provides a very efficient measure of the structure contained within a time series because of the ability of wavelet transforms to allot small wavelet coefficients to the smoother parts of a signal in contrast with the sharp, non-stationary behavior which gives rise to local maxima (see, for example, Chapter 8 in the book of Percival and Walden (Percival & Walden, 2000)).

4.1 Chaotic electronic circuit

The electronic circuit of Fig. 6 (a) has been employed to study chaos synchronization (Rulkov, 1996; Rulkov & Sushchik, 1997). This circuit, despite its simplicity, exhibits complex chaotic dynamics and it has received wide coverage in different areas of mathematics, physics, engineering and others (Campos-Cantón et al., 2008; Rulkov, 1996; Rulkov & Sushchik, 1997). It consists of a linear feedback and a nonlinear converter, which is the block labeled N. The linear feedback is composed of a low-pass filter RC' and a resonator circuit rLC.
The dynamics of this chaotic circuit is very well modeled by the following set of differential equations:

$$\begin{aligned} \dot{x} &= y, \\ \dot{y} &= z - x - \delta y, \\ \dot{z} &= \gamma\left[kf(x) - z\right] - \sigma y, \end{aligned} \tag{20}$$

where $x(t)$ and $z(t)$ are the voltages across the capacitors, C and C', respectively, and $y(t) = J(t)(L/C)^{1/2}$ is the current through the inductor L. The unit of time is given by $\tau = 1/\sqrt{LC}$. The parameters γ, δ, and σ have the following dependence on the physical values of the circuit elements: $\gamma = \sqrt{LC}/RC'$, $\delta = r\sqrt{C/L}$ and $\sigma = C/C'$. The main characteristic of the nonlinear converter N in Fig. 6 is to transform the input voltage $x(t)$ into an output voltage with nonlinear dependence $F(x) = kf(x)$ on the input. The parameter k corresponds to the gain of the converter at $x = 0$. The detailed circuit structure of N is shown in Fig. 6 (b).
It is worth mentioning that depending on the component values of the linear feedback and the parameter k, the behavior of the chaotic circuit can be in regimes of either *periodic* or *chaotic* oscillations. Due to the characteristics of the inductor in the linear feedback, it turns out to be hard to scale to arbitrary frequencies and analyze it because of its frequency-dependent resistive losses. Therefore, the parameter k has been considered to analyze this chaotic circuit, since it appeared to be a very useful bifurcation parameter in both the numerical and experimental cases (Campos-Cantón et al., 2008). Two different attractors, projected on the plane (x, y), generated by this electronic circuit, are shown in Fig. 7. These attractors have

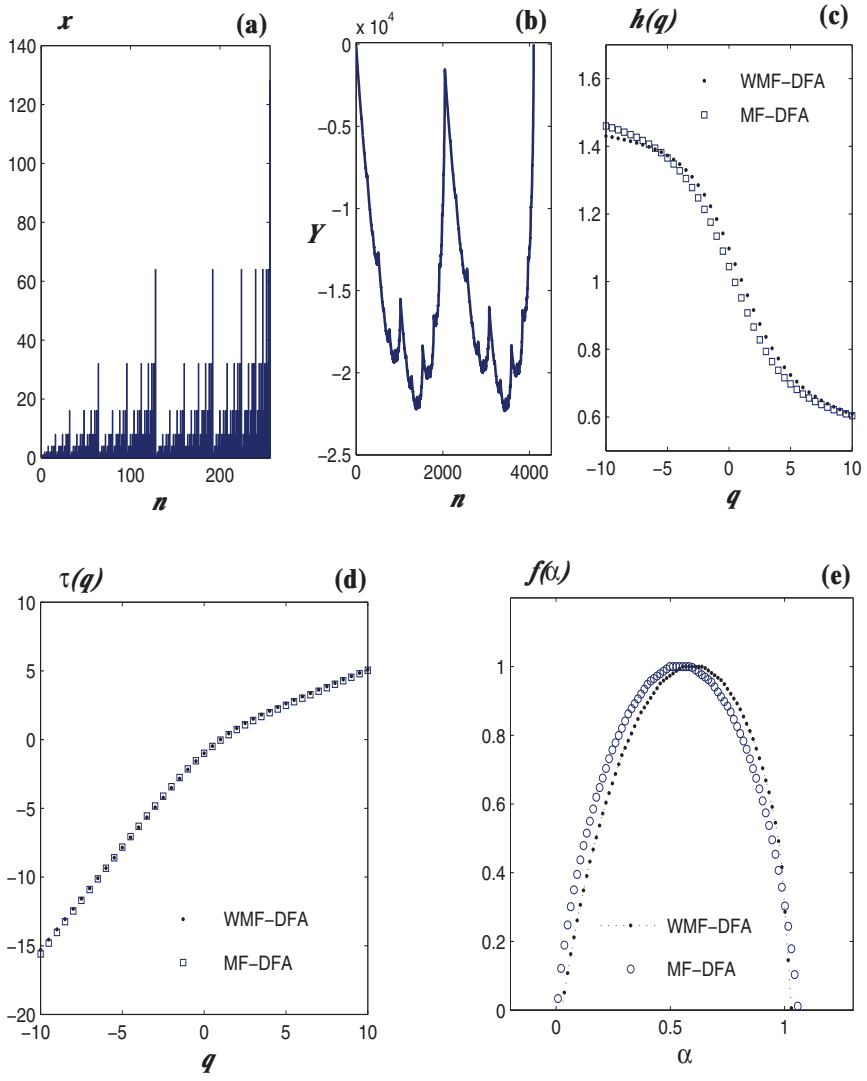

Fig. 5. (a) Time series of the row signal of $\mathbf{H}_{2047}$. Only the first 256 points are shown of the whole set of $2^{11} - 1$ data points. (b) Profile of the row signal of $\mathbf{H}_{2047}$. (c) Generalized Hurst exponent $h(q)$, (d) the $\tau(q)$ exponent, and (e) the singularity spectrum $f(\alpha)$.

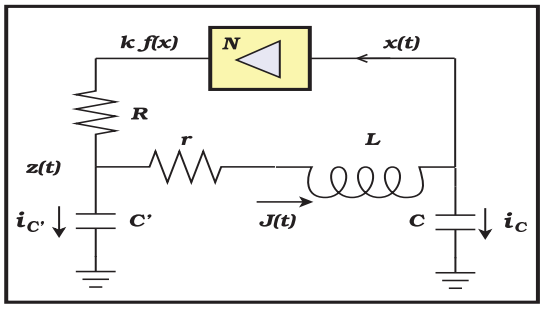

(a)

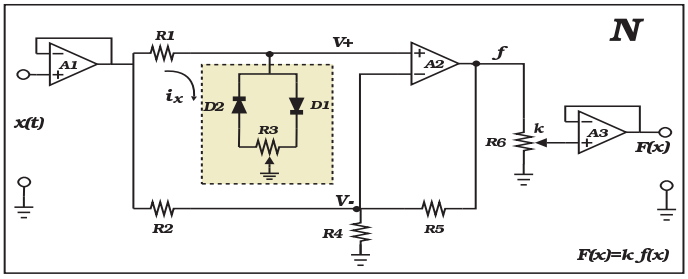

(b)

Fig. 6. (a) The circuit diagram of a nonlinear chaotic oscillator. The component values employed are $C' = 100.2$ nF, $C = 200.1$ nF, $L = 63.8$ mH, $r = 138.9\ \Omega$, and $R = 1018\ \Omega$. (b) Schematic diagram of the nonlinear converter N. The electronic component values are $R1 = 2.7$ kΩ, $R2 = R4 = 7.5$ kΩ, $R3 = 50\ \Omega$, $R5 = 177$ kΩ, $R6 = 20$ kΩ. The diodes D1 and D2 are 1N4148, the operational amplifiers A1 and A2 are both TL082, and the operational amplifier A3 is LF356N.

a shape similar to a Rössler oscillator (Fig. 7(a)), and to a double scroll oscillator (Fig. 7(b)). They can be easily obtained by just fixing the bifurcation parameter k to be equal to 0.4010, and 0.3964, respectively.

4.2 Wavelet variance

In the wavelet approach the fractal character of a certain signal can be inferred from the behavior of its power spectrum $P(\omega)$, which is the Fourier transform of the autocorrelation function and in differential form $P(\omega)d\omega$ represents the contribution to the variance of the part of the signal contained between frequencies ω and $\omega + d\omega$. Indeed, it is known that for self-similar random processes the spectral behavior of the power spectrum is given by

$$P(\omega) \sim \mid \omega \mid^{-\beta}, \tag{21}$$

where β is the spectral parameter of the signal. In addition, the variance of the wavelet coefficients var $\{d_n^m\}$ is related to the level m through a power law of the type (Wornell & Oppenheim, 1992)

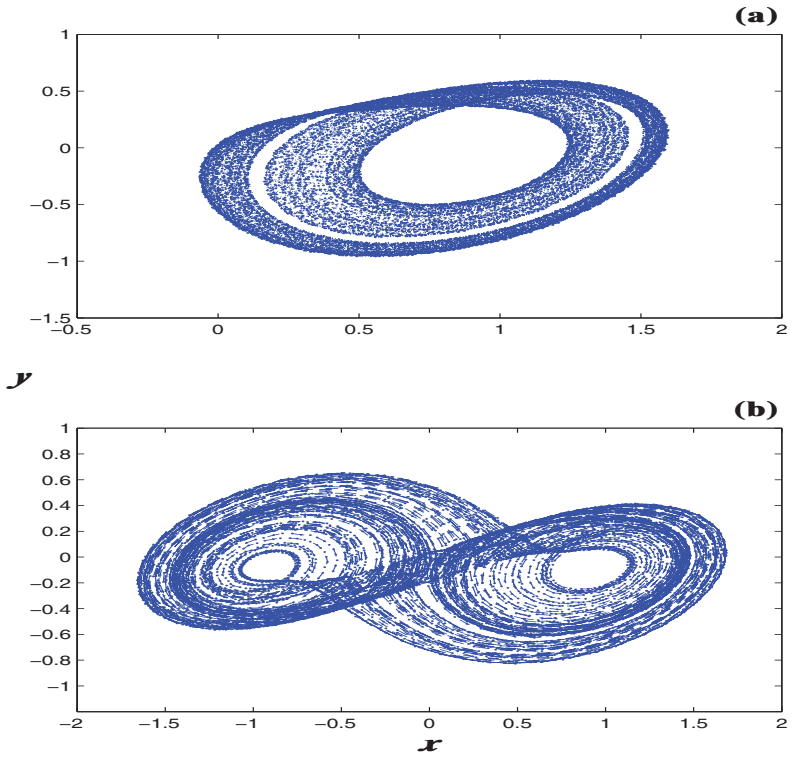

Fig. 7. Attractors of the electronic chaotic circuit projected on the plane $x - y$ obtained experimentally for two different values of the bifurcation parameter k: (a) 0.4010, and (b) 0.3964.

$$\text{var}\,\{d_n^m\} \approx (2^m)^{-\beta}. \tag{22}$$

This wavelet variance has been used to find dominant levels associated with the signal, for example, in the study of numerical and experimental chaotic time series (Campos-Cantón et al., 2008; Murguía & Campos-Cantón, 2006; Staszewski & Worden, 1999). In order to estimate β we used a least squares fit of the linear model

$$\log_2(\text{var}\{d_n^m\}) = \beta_m + (K + v_m), \tag{23}$$

where K and v_m are constants related to the linear fitting procedure. Equation (22) is certainly suitable for studying discrete chaotic time series, because their variance plot has a well-defined form as pointed out in (Murguía & Campos-Cantón, 2006; Staszewski & Worden, 1999). If the variance plot shows a maximum at a particular scale, or a bump over a group of scales, which means a high energy concentration, it will often correspond to a coherent

structure. In general, the gradient of a noisy time series turns out to be zero in the variance plot, therefore it does not show any energy concentration at specific wavelet level. In certain cases the gradient of some chaotic time series has a similar appearance with Gaussian noise at lower scales, which implies that these chaotic time series do not present a fundamental "carrier" frequency at any scale.
For our illustrative analysis and comparison with the experiments, we study the time series of the x states of the attractors displayed in Fig. 7(a)-(b), because they are of very different type and we want to emphasize the versatility of the wavelet approach. The acquisition of the experimental data was carried out with a DAQ with a sampling frequency of 180 kHz, i.e. we collected the experimental data for a total time of 182 ms for both signals. In the analysis of these time series we employed the db-8 wavelet, a wavelet function that belongs to the Daubechies family (Daubechies, 1992; Mallat, 1999).

- Case $k = 0.4010$.

  The first time series to consider corresponds to the x state of the experimental attractor of Fig. 7 (a). The first 12 ms of this time series are shown in Fig. 8 (a), whereas Fig. 8 (b) shows a semi-logarithmic plot of the wavelet coefficient variance as a function of level m, which is denominated as variance plot of the wavelet coefficients. One can notice that the whole series is dominated by the 12th wavelet level, i.e., this wavelet level has the major energy concentration, and it is plotted in isolation in Fig. 8 (c). The energy rate between the reconstructed signal with respect to the original signal was $(E_{x_{12}}/E_x) = 0.9565$, which means an energy close to 96% of the total one in this case. Since it does not properly show the structure of the chaotic time series, we considered and added together the three neighbor wavelet levels, $m = 11 - 13$, achieving an energy concentration of 99% of the total one. In this case, the reconstruction of the signal at these wavelet levels is shown in Fig. 8(d), where the structure of the original signal can be noticed. Both reconstructed time series present a slight downward translation, because of the DC component of this chaotic time series.

- Case $k = 0.3964$.

  For this value of k, the behaviour of the chaotic electronic circuit is similar to that of a double scroll oscillator with the shape of the attractor displayed in Fig. 7. The experimental time series corresponding to the x state of this attractor is shown in Fig. 9 (a), while the variance plot is given in Fig. 9 (b) where the gradient is close to zero, which means that no significant energy concentration can be seen. We have found that when summing over the wavelet levels $m = 6 - 12$ the energy concentration is close to 99% of the total one but without any pronounced peak. Thus, this case does not present a fundamental "carrier" frequency and therefore this attractor has a Gaussian noisy behavior. The reconstructed time series with the mentioned wavelet levels is displayed in Fig. 9 (c).

5. Conclusion

The DWT is currently a standard tool to study time-series produced by all sorts of non-stationary dynamical systems. In this chapter, we first reviewed the main properties of DWT and the basic concepts related to the corresponding mathematical formalism. Next, we presented the way the DWT characterizes the type of dynamics embedded in the time-series. In general, the DWT reveals with high accuracy the dynamical features obeying power-like scaling properties of the processed signals and has been already successfully incorporated in the multifractal formalism. The interesting case of the time-series of the elementary cellular

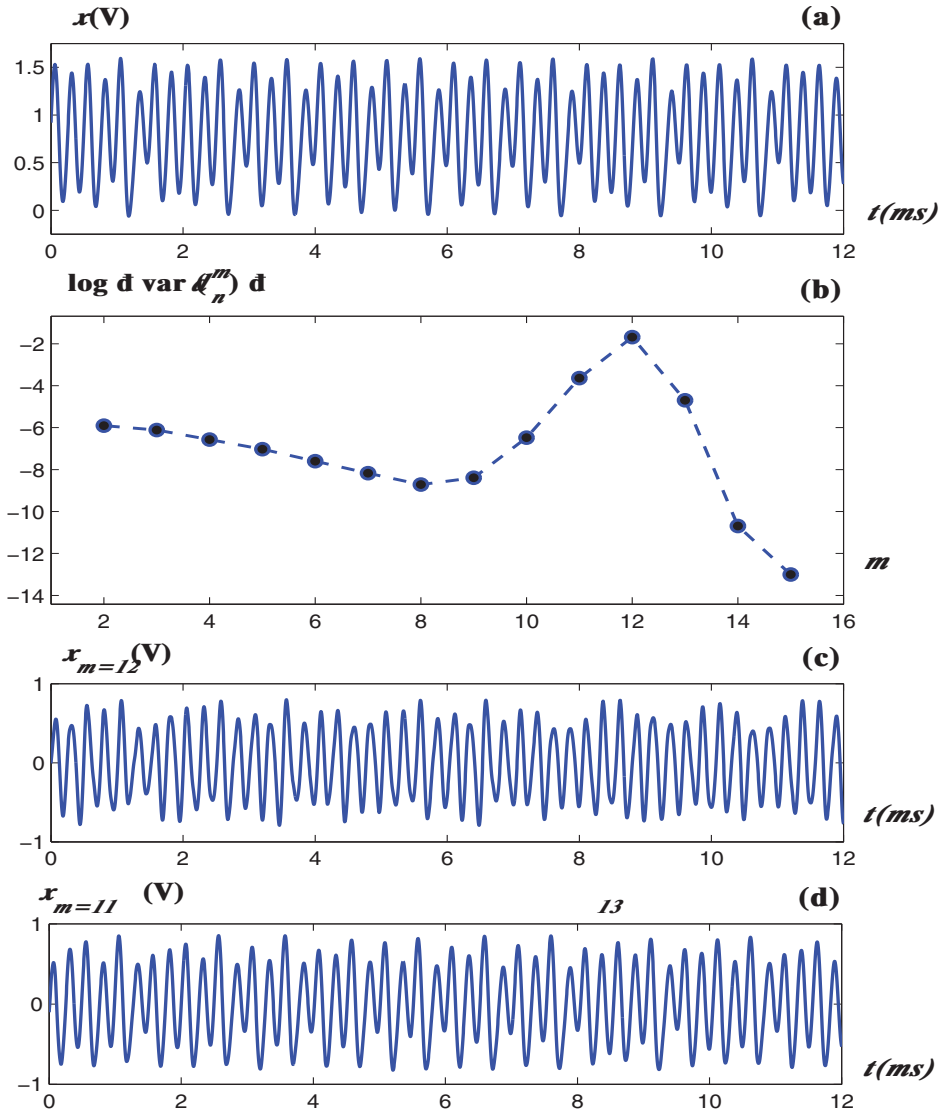

Fig. 8. The case $k = 0.4010$: (a) experimental time series of the x state, (b) wavelet coefficient variance, (c) time series of the 12th wavelet level, and (d) the time series of the sum from 11th to the 13th wavelet levels.

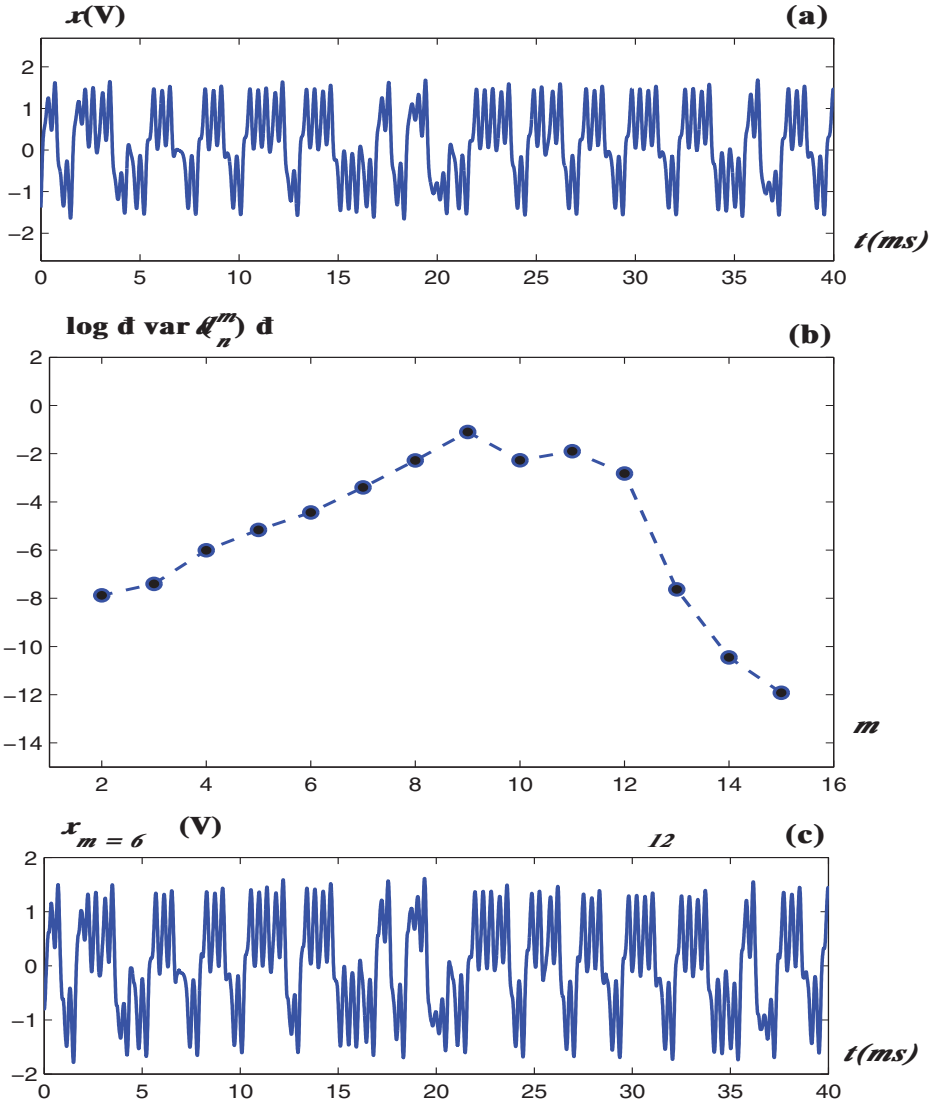

Fig. 9. The case $k = 0.3964$: (a) experimental time series of the x state, (b) wavelet coefficient variance, (c) time series of the sum from 6th to the 12th wavelet levels.

automata has been presented in the case of rule 90 and the concentration of energy by means of the concept of wavelet variance for the chaotic time-series of a three-state non-linear electronic circuit was also briefly discussed.

6. References

Campos-Cantón, E.; Murguía, J. S. & Rosu, H. C. (2008). Chaotic dynamics of a nonlinear electronic converter, *International Journal of Bifurcation and Chaos*, 18(10), October 2008 (2981-3000), ISSN 0218-1274.

Daubechies, I. (1992). *Ten lectures on Wavelets*, SIAM, ISBN 10: 0-89871-274-2, Philadelphia, PA.

Feder, J. (1998). *Fractals*, Plenum Press, ISBN 3-0642-851-2, New York, 1998 (Appendix B).

Halsey T.C.; Jensen M. H.; Kadanoff L. P.; Procaccia I. & Shraiman B. I. (1986). Fractal measures and their singularities: The characterization of strange sets, *Physical Review A*, 33(2), February 1986 (1141-1151), ISSN 1050-2947.

Kantelhardt, J.,W.; Zschinegner, S.,A.; Koscielny-Bunde, E.; Havlin, S.; Bunde, A. & Stanley. H. E. (2002). Multifractal detrended fluctuation analysis of nonstationary time series, *Physica A*, 316(1-4), December 2002 (87-114), ISSN 0378-4371.

Mallat, S. (1999).*A Wavelet Tour of Signal Processing*, 2nd. Edition, Academic Press, ISBN-13:978-0-12-466606-1, San Diego, California, USA.

Manimaran P.; Panigrahi P. K. & Parikh J. C. (2005). Wavelet analysis and scaling properties of time series, *Physical Review E*, 72(4) October 2005 (046120, 5 pages), ISSN 1539-3755.

Mejía M. & Urías J. (2001). An asymptotically perfect pseudorandom generator, *Discrete and Continuos Dynamical Systems*, 7(1), January 2001 (115-126), ISSN 1078-0947.

Murguía, J. S. & Campos-Cantón, E. (2006). Wavelet analysis of chaotic time series, *Revista Mexicana de Física*, 52(2), April 2006 (155-162), ISSN 0035-001X.

Murguía, J. S.; Pérez-Terrazas, J. E. & Rosu, H. C. (2009). Multifractal properties of elementary cellular automata in a discrete wavelet approach of MF-DFA, *Europhysics Letters*, 87(2), July 2009 (28003, 5 pages), ISSN 0295-5075.

Murguía, J. S.; Mejía-Carlos, M; Rosu, H. C. & Flores-Eraña, G. (2010). Improvement and analysis of a pseudo random bit generator by means of CA, *International Journal of Modern Physics C*, 21(6), June 2010 (741-756), ISSN 0129-1831.

Nagler J. & Claussen J. C. (2005). $1/f^{\alpha}$ spectra in elementary cellular automata and fractal signals, *Physical Review E*, 71(6) June 2005 (067103, 4 pages), ISSN 1539-3755.

Percival, D. B. & Walden, A. T. (2000) *Wavelet Methods for Time Series Analysis*, Cambridge University Press, ISBN 0-52164-068-7, Cambridge.

Rulkov, N. F. (1996). Images of synchronized chaos: Experiments with circuits, *CHAOS*, 6(3), September 1996 (262-279), ISSN 1054-1500.

Rulkov, N. F. & Sushchik, M. M.(1997). Robustness of Synchronized Chaotic Oscillations, *International Journal of Bifurcation and Chaos* 7(3), March 1997(625-643), ISSN 0218-1274.

Rulkov, N. F., Afraimovich, V. S., Lewis, C. T., Chazottes, J. R., & Cordonet, J. R. (2001). Multivalued mappings in generalized chaos synchronization. *Physical Review E* 64(1), July 2001(016217 1-11), ISSN 1539-3755.

Sanchez J. R. (2003). Multifractal characteristics of linear one-dimensional cellular automata, *International Journal of Modern Physics C*, 14(4), May 2003 (491-499), ISSN 0129-1831.

Staszewski, W. J. & Worden, K. (1999). Wavelet analysis of time series: Coherent structures, chaos and noise, *International Journal of Bifurcation and Chaos*, 9(3), September 1999 (455-471), ISSN 0218-1274.

Strang, G. & Nyugen, T. (1996). *Wavelets and Filter Banks*, Wellesley Cambridge Press, ISBN 0-96140-887-1, Wellesley, MA, USA.

Telesca L., Colangelo G., Lapenna V. & Macchiato M. (2004). Fluctuation dynamics in geoelectrical data: an investigation by using multifractal detrended fluctuation analysis, *Physics Letters A*, 332(5-6), November 2004 (398-404), ISSN 0375-9601.

Qian, S. (2002). *Introduction to Time-Frequency and Wavelet Transforms*, Prentice Hall PTR, ISBN 0-13030-360-7.

Wornell, G. W. & Oppenheim, A. V. (1992). Wavelet-based representations for a class of self-similar signals with application to fractal modulation, *IEEE Transactions on Information and Theory*, 38(2), 1992(785-800), ISSN 0018-9448.

2

Discrete Wavelet Transfom for Nonstationary Signal Processing

Yansong Wang, Weiwei Wu, Qiang Zhu and Gongqi Shen
Shanghai University of Engineering Science,
P. R. China

1. Introduction

In engineering, digital signal processing techniques need to be carefully selected according to the characteristics of the signals of interest. The frequency-based and time-frequency techniques have been frequently mentioned in some literature (Cohen, 1995). The frequency-based techniques (FBTs) have been widely used for stationary signal analysis. For nonstationary signals, the time-frequency techniques (TFTs) in common use, such as short-time Fourier transform (STFT), wavelet transform (WT), ambiguity function (AF) and wigner-ville distribution (WVD), etc., are usually performed for extracting transient features of the signals. These techniques use different algorithms to produce a time-frequency representation for a signal.

The STFT uses a standard Fourier transform over several types of windows. Wavelet-based techniques apply a mother wavelet with either discrete or continuous scales to a waveform to resolve the fixed time-frequency resolution issues inherent in STFT. In applications, the fast version of wavelet transform, that is attributed to a pair of mirror filters with variable sampling rates, is usually used for reducing the number of calculations to be done, thereby saving computer running time. AF and WVD are quadratic time-frequency representations, that use advanced techniques to combat these resolution difficulties. They have better resolution than STFT but suffer from cross-term interference and produce results with coarser granularity than wavelet techniques do. Of the wavelet-based techniques, discrete wavelet transform (DWT), especially its fast version, is usually used for encoding and decoding signals, while wavelet packet analysis (WPA) are successful in signal recognition and characteristic extraction. AF and WVD with excessive transformation durations are obviously unacceptable in the development of real-time monitoring systems.

In applications, the FBTs were typically used in noise and vibration engineering (Brigham, 1988). They provide the time-averaged energy information from a signal segment in frequency domain, but remain nothing in time domain. For nonstationary signals such as vehicle noises, some implementation examples are the STFT (Hodges & Power, 1985), WVD, smoothed pseudo-WVD (Baydar & Ball, 2001) and WT (Chen, 1998). In particular, the WT as "mathematical microscope" in engineering allows the changing spectral composition of a nonstationary signal to be measured and presented in the form of a time-frequency map and thus, was suggested as an effective tool for nonstationary signal analysis.

This chapter includes three sections. We firstly briefly introduce the theory background of the Wavelet-based techniques, such as the CWT, DWT, WPA, as well as the Mallat filtering scheme and algorithm for the DWT-based calculation. Secondly, we discuss the advantages and drawbacks of the DWT-based methods in nonstationary signal processing by comparing the DWT with other TFTs. Some successful examples of the DWT used for nonstationary vibration and sound signals in the vehicle engineering will be given in the third section.

2. Theory background

2.1 Continuous wavelet transform

For a function or signal $x(t)$ $L^2(R)$, if a prototype or mother wavelet is given as $\psi(t)$, then the wavelet transform can be expressed as:

$$\mathrm{CWT_x(a,b)} = \frac{1}{\sqrt{a}}\int \mathrm{x(t)}\overline{\psi(\frac{t-b}{a})}\mathrm{dt} = \left\langle \mathrm{x(t)}, \psi_{ab}(t) \right\rangle \tag{1}$$

Here a and b change continuously, so comes the name continuous wavelet transform (CWT). A family of wavelets $\psi_{ab}(t)$, each of which can be seen as a filter, is defined in (1) by dilating and translating of $\psi(t)$. Obviously, b changes along the time axle, its role is simple and clear. Varible a acts as a scale function, its change alters not only the spectrum of the wavelet function, but also the size of its time-frequency window. The local information in time and frequency domain, which reflects different characteristics of the signal, is extracted by CWT.

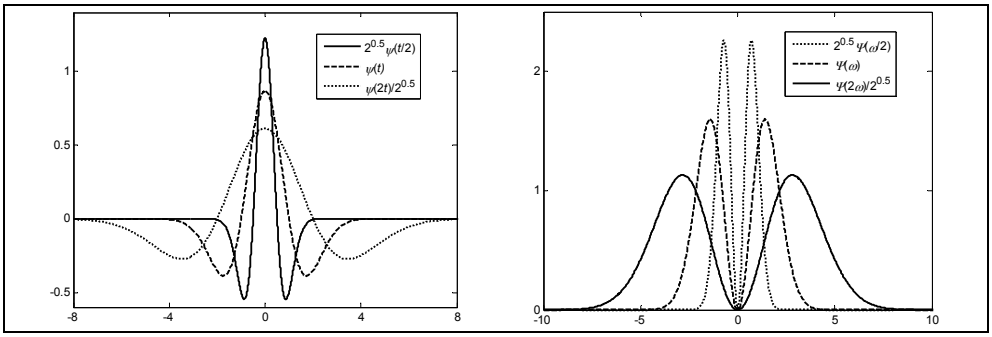

Fig. 1. "mexico hat" wavelets with different a and their spectra

If $\mathrm{c_\psi} = \int \frac{|\Psi(\omega)|^2}{\omega}\mathrm{d}\omega < \infty$ is satisfied, where $\Psi(\omega)$ is the Fourier transform of $\psi(t)$, then $\psi(t)$ is an admissible wavelet. In this condition, original signal $x(t)$ can be recovered from its CWT by:

$$\mathrm{x(t)} = \frac{1}{\mathrm{c_\psi}}\iint \mathrm{CWT_x(a,b)}\psi_{ab}(\mathrm{t})\frac{\mathrm{dadb}}{\mathrm{a^2}} \tag{2}$$

In the case where ψ is also $L^1(R)$, the admissibility condition implies that $\Psi(0)=0$; ψ has mean value 0, is oscillating, and decays to zero at infinity; these properties explain the qualification as "wavelet" of this function $\psi(t)$. From the view of signal processing, $\psi(t)$ acts as a band pass filter.

2.2 Discrete wavelet transform

The time-frequency windows of $\psi_{ab}(t)$ are overlapped each other, which means there is information redundancy in CWT. This is a disadvantage of CWT when it is used for signal compression or feature extraction. Thus the wavelet transform can be computed discretely on the time-frequency plane, to reduce the redundancy. The crucial point is how to sample a and b to guarantee the precise reconstruction of original signal $x(t)$ from its wavelet transform. There are several forms of wavelet transform according to the different level of discretization.

Simply let $a = a_0^j$, where $a_0 > 0$ and $j \in Z$, we can discretize a. Generally we have $a_0 = 2$, thus the scale is sampled along a dyadic sequence, so the function $\psi_{jb}(t) = \frac{1}{\sqrt{2^j}}\psi(\frac{t-b}{2^j})$ is a dyadic wavelet, and the corresponding transform $WT_x(j,b) = \frac{1}{\sqrt{2^j}}\int x(t)\overline{\psi(\frac{t-b}{2^j})}dt = \langle x(t), \psi_{jb}(t)\rangle$ is called dyadic wavelet transform.

To recover $x(t)$ from its dyadic wavelet transform, the dual wavelet $\hat{\psi}(t)$ of $\psi(t)$ must be introduced. Dual wavelet has the same scale and time shift as original wavelet, that is $\hat{\psi}_{jb}(t) = \frac{1}{\sqrt{2^j}}\hat{\psi}(\frac{t-b}{2^j})$. The relationship between $\hat{\psi}(t)$ and $\psi(t)$ is: $\hat{\Psi}(\omega) = \frac{\Psi(\omega)}{\sum_{j=-\infty}^{\infty}\left|\Psi(2^j\omega)\right|^2}$, where $\hat{\Psi}(\omega)$ is the Fourier transform of $\hat{\psi}(t)$. We can prove $x(t)$ is reconstructed by:

$$x(t) = \sum_{j=-\infty}^{\infty} 2^{-3j/2}\int WT_x(j,b)\hat{\psi}(\frac{t-b}{2^j})db \tag{3}$$

To ensure the recovery, there should be $A \le \sum_{j=-\infty}^{\infty}\left|\Psi(2^j\omega)\right|^2 \le B$, where A and B are constants, this is the stability condition. Obviously, dual wavelet of a stable function is also stable.

To step further, we sample time domain by taking $b=kb_0$, where b_0 should be chosen to ensure the recovery of $x(t)$. When a is changed from a_0^{j-1} to a_0^j, the central frequency and the band width of the wavelet are all decreased by a_0 times, so the sample interval can increase to a_0 times. In this case, the discretized wavelet function is $\psi_{jk}(t) = \frac{1}{\sqrt{a_0^j}}\psi(\frac{t-ka_0^jb_0}{a_0^j})$, and its wavelet transform is: $WT_x(j,k) = \frac{1}{\sqrt{a_0^j}}\int x(t)\overline{\psi(\frac{t-ka_0^jb_0}{a_0^j})}dt = \langle x(t), \psi_{jk}(t)\rangle$. This decomposition is called discrete wavelet transform (DWT). From this formula, while time t is still continuous, we only compute the wavelet transform on a grid in the time-frequency plane, as depicted in Fig. 2.

Given $d_j(k)=WT_x(j,k)$, we hope to recover $x(t)$ from formula like

$$x(t) = \sum_{j=0}^{\infty}\sum_{k=-\infty}^{\infty} d_j(k)\hat{\psi}_{jk}(t) \tag{4}$$

This formula is called wavelet series, in which $d_j(k)$ is wavelet coefficients and $\hat{\psi}_{jk}(t)$ is dual wavelet. To recover $x(t)$ using (4), many questions should be answered, such as: are $\psi_{jk}(t)$ complete to describe arbitrary signal $x(t)$ $L^2(R)$; is there information redundancy in the decomposition; how to determine the sample interval of a and b. Daubechies studied them thoroughly, and her wavelet frame theory answered these questions [1].

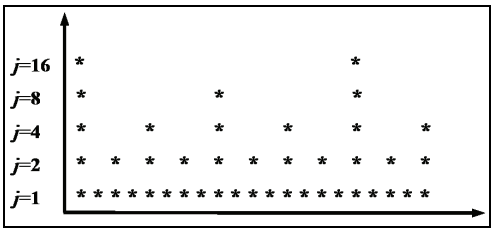

Fig. 2. The computing grid of DWT

We call a function family $\{\psi_n\}$ a frame if there exist two constants $A>0$ and $B>0$ such that for an arbitrary $x(t)$ $L^2(R)$, $A\|x\|^2 \le \sum_n |\langle x, \psi_n \rangle|^2 \le B\|x\|^2$ is satisfied. When $A=B$ the frame is said to be tight. A frame defines a complete and stable signal representation, which may also be redundant. When the frame vectors are normalized $\|\psi_n\|^2 = 1$, the redundancy is measured by the frame bounds A and B. The frame is an orthogonal basis if and only if $A=B=1$. If $A>1$ then the frame is redundant and A can be interpreted as a minimum redundancy factor.

If a frame operator S is defined as $Sx = \sum_n \langle x, \psi_n \rangle \psi_n$, then $x = \sum_n \langle x, S^{-1}\psi_n \rangle \psi_n = \sum_n \langle x, \psi_n \rangle S^{-1}\psi_n$, so we can define $\hat{\psi}_n = S^{-1}\psi_n$ as the dual frame of ψ_n, with bounds A^{-1} and B^{-1}. If $A=B$, we have $\hat{\psi}_n = \frac{1}{A}\psi_n$. So the recovery process in (4) is well founded. In many cases where precise reconstruction is not a pursuit, we can take $\hat{\psi}_{jk}(t) \approx \frac{2}{A+B}\psi_{jk}(t)$, $x(t) = \frac{2}{A+B}\sum_{j,k} \langle x(t), \psi_{jk}(t) \rangle \psi_{jk}(t) + e(t)$, here $e(t)$ is the error and $\|e(t)\| \le \frac{B-A}{B+A}\|f\|$.

The only remain problem is how to construct a wavelet frame. Obviously, the smaller b_0 and a_0 are, the greater the information redundancy is, and the reconstruction is easier. On the contrary, ψ_n will be incomplete when b_0 and a_0 are big enough, which make precise recovery of $x(t)$ impossible. For this problem, there are two theorems: (1) If $\psi_{jk}(t) = a_0^{\frac{-j}{2}}\psi(a_0^{-j}t - kb_0)$ is a frame of $L^2(R)$ then the frame bounds satisfy $A \le \frac{2\pi\int_0^\infty \frac{|\Psi(\omega)|^2}{\omega}d\omega}{b_0 \ln a_0} \le B$; (2) Define $\beta(\xi) = \sup_{0\le|\omega|\le a_0} \sum_{j=-\infty}^{\infty} |\Psi(a_0^j\omega)||\Psi(a_0^j\omega + \xi)|$ and $\Delta = \sum_{\substack{k=-\infty \\ k\ne 0}}^{\infty} [\beta(\frac{2\pi k}{b_0})\beta(\frac{-2\pi k}{b_0})]^{\frac{1}{2}}$, if b_0 and a_0 are such that

$A_0 = \frac{1}{b_0}(\inf_{0\le|\omega|\le a_0}\sum_{j=-\infty}^{\infty}\left|\Psi(a_0^j\omega)\right|^2 - \Delta) > 0$ and $B_0 = \frac{1}{b_0}(\inf_{0\le|\omega|\le a_0}\sum_{j=-\infty}^{\infty}\left|\Psi(a_0^j\omega)\right|^2 + \Delta) < \infty$, then $\{\psi_{jk}(t)\}$ is a frame of $L^2(R)$. These two theorems are the sufficient and necessary conditions to construct wavelet frame.

In some cases, wavelet frame $\{\psi_{jk}(t)\}$ is orthogonal or independent, the more correlated the functions are , the smaller the subspace spanned by the frame is. This is useful in noise reduction. When b_0 and a_0 is close to 0 and 1, the functions of the frame are strongly related and behave like continuous wavelet. In other cases, redundancy or dependency is avoided as possible, so ψ, b_0 and a_0 are chosen to compose an orthogonal basis.

2.3 Multiresolution analysis and mallat algorithm

Multiresolution analyze (MRA) provides an elegant way to construct wavelet with different properties. A sequence $\{V_j\}_{j\ Z}$ of closed subspaces of $L^2(R)$ is a MRA if the following 6 properties are satisfied:

1. $\forall(j,k)\in Z, f(t)\in V_j \Leftrightarrow f(t-2^j k)\in V_j$,
2. $\forall j\in Z, V_{j+1}\subset V_j$,
3. $\forall j\in Z, f(t)\in V_j \Leftrightarrow f(\frac{t}{2})\in V_{j+1}$,
4. $\lim_{j\to\infty} V_j = \bigcap_{j=-\infty}^{\infty} V_j = \{0\}$,
5. $\lim_{j\to-\infty} V_j = \text{Closure}(\bigcup_{j=-\infty}^{\infty} V_j) = L^2(R)$,
6. There exists θ such that $\{\theta(t-n)\}_{n\ z}$ is a Riesz basis of V_0.

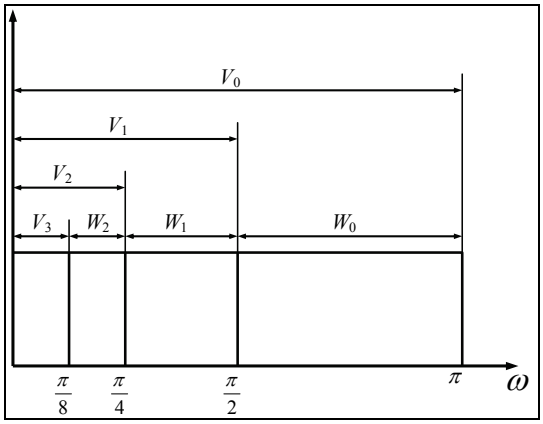

Fig. 3. Partition of function space by multiresolution analyze

The main idea of MRA is described in Fig. 3, the space $L^2(R)$ is orderly partitioned. The relationship between adjacent spaces V_j and V_{j+1} is reflected from condition 2) and 3), so the

basis of V_j and V_{j+1} differs only on the scale by 2. We only discuss how to construct an orthogonal wavelet basis here, so a space series W_j which satisfy $V_j \oplus W_j \subset V_{j-1}$ are introduced. By this idea, the function space can be decomposed like $V_0 = W_1 \oplus W_2 \oplus \cdots \oplus W_j \oplus V_j$ and so $L^2(R) = \bigoplus_{m=-\infty}^{\infty} W_m$, which can be seen in Fig. 3. By this kind of decomposition, components in each space W_j contain different details of the function, or from the view of signal processing, the original signal is decomposed by a group of orthogonal filters.

To construct an orthogonal wavelet basis, we first need to find an orthogonal basis of V_0. From the following theorem: a family $\{\varphi(t-n)\}_{n\,z}$ is a standard orthogonal basis $\leftrightarrow$ $\sum_{k\in Z} |\Phi(\omega + 2k\pi)|^2 = 1$, where $\Phi(\omega)$ is the Fourier transform of $\varphi(t)$. If $\{\theta(t-n)\}_{n\,z}$, with Fourier transform $\Theta(\omega)$, is not an orthogonal basis of V_0, from the above theorem, we can compute $\Phi(\omega) = \dfrac{\Theta(\omega)}{\sum_{k\in Z} |\Theta(\omega + 2k\pi)|^2}$, and $\{\varphi(t-n)\}_{n\,z}$ must be orthogonal. We call $\varphi(t)$ the scale function, and we will take $\{\varphi(t-n)\}_{n\,z}$ as the orthogonal basis of V_0 in this chapter.

From above discussion, $\{\varphi(t-n)\}_{n\,z}$ is an orthogonal basis of V_0, and $\varphi(\frac{t}{2}) \in V_1 \subset V_0$, we have $\varphi(\frac{t}{2}) = \sqrt{2} \sum_{k=-\infty}^{\infty} h(k)\varphi(t-k)$. In the frequency, $\sqrt{2}\Phi(2\omega) = H(\omega)\Phi(\omega)$, where $H(\omega) = \sum_{k=-\infty}^{\infty} h(k)e^{-ik\omega}$. If we take $\{\psi(\frac{t}{2} - n)\}_{n\in Z}$ as an orthogonal basis of W_1, since we have $V_0 = V_1 \oplus W_1$ from above discussion of MRA, then $\psi(\frac{t}{2}) = \sqrt{2} \sum_{k=-\infty}^{\infty} g(k)\varphi(t-k)$ and $\sqrt{2}\Psi(2\omega) = G(\omega)\Phi(\omega)$ are hold. Combine all these expressions with $\int \psi(t)dt = 0$ and $\int \varphi(t)dt = 1$, we have following conclusions: 1) $\sum_k h(k) = \sqrt{2}$ and $\sum_k g(k) = 0$; 2) $H(0) = \sqrt{2}$ and $G(0)=0$. From this, H is a low pass filter and G band pass filter.

From formula $\sum_{k\in Z} |\Phi(\omega + 2k\pi)|^2 = 1$, which means $\{\varphi(t-n)\}_{n\,z}$ is an orthogonal basis, we have

$$|H(\omega)|^2 + |H(\omega + \pi)|^2 = 2 \tag{5}$$

hold for arbitrary ω. The same conclusion is hold for G, that is

$$|G(\omega)|^2 + |G(\omega + \pi)|^2 = 2 \tag{6}$$

Since the orthogonality between $\{\varphi(t-n)\}_{n\,z}$ and $\{\psi(t-n)\}_{n\,z}$,

$$H(\omega)\overline{G(\omega)} + H(\omega + \pi)\overline{G(\omega + \pi)} = 0 \tag{7}$$

must be satisfied. One solution of (7) is $G(\omega) = -e^{-i\omega}\overline{H(\omega+\pi)}$, or equivalently $g(k) = (-1)^k h(1-k)$. Till here, the constructive method of an orthogonal wavelet basis is completed.

From MRA, Mallat developed a fast algorithm to compute DWT of a given signal. Suppose $x_{j-1}(k)$, $x_j(k)$ and $d_j(k)$ are coefficients of $x(t)$ projected on V_{j-1}, V_j and W_j, $d_j(k)$ here has the same meaning with that in (4), which is $WT_x(j,k)$. The Mallat algorithm includes the following Eqs:

$$x_j(k) = \sum_{n=-\infty}^{\infty} x_{j-1}(n)h(n-2k) = x_{j-1}(k) * h(2k) \tag{8}$$

$$d_j(k) = \sum_{n=-\infty}^{\infty} x_{j-1}(n)g(n-2k) = x_{j-1}(k) * g(2k) \tag{9}$$

$$x_{j-1}(k) = \sum_{n=-\infty}^{\infty} x_j(n)h(k-2n) + \sum_{n=-\infty}^{\infty} d_j(n)g(k-2n) \tag{10}$$

In them, (8) and (9) are for decomposition and (10) is for reconstruction. By decomposing it recursively, as in Fig. 4(a), the approximate signal $x_j(k)$ and detail signal $d_j(k)$ are computed out successively.

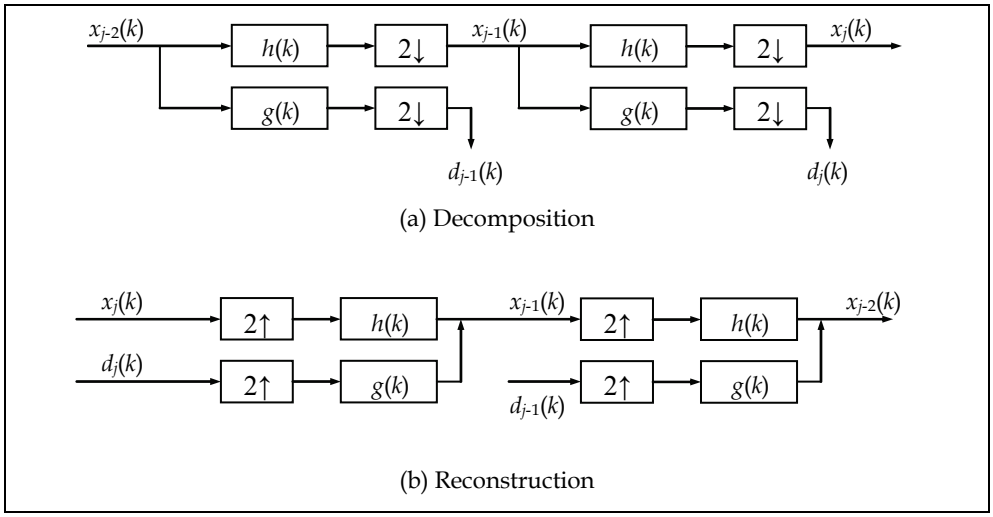

Fig. 4. The Mallat algorithm

3. Time-frequency representation comparisons

The task of signal processing is to find the traits of the signals of interest. As known that most of the signals in engineering are obtained in time domain. However, features of the signals can usually be interpreted in frequency domain, so the frequency domain analysis is

important in signal analysis. The Fourier transform and its inversion connect the frequency domain features with the time domain features. Their definitions are as below:

$$X(f) = \int x(t)e^{-j2\pi ft}dt \tag{11}$$

$$x(t) = \int X(f)e^{j2\pi ft}df \tag{12}$$

In the stationary signal analysis, one may use the Fourier transform and its inversion to establish the mapping relation between the time and frequency domains. However, in the practical applications, the Fourier transform is not the best tool for signal analysis due to the nonstationary and time varying feature in the most engineering signals, such as engine vibration and noise signals. For these signals, although their frequency elements can be observed from their frequency spectrum, the time of frequency occurrence and frequency change relationship over time can not be acquired. For further research on these signals, the time-frequency descriptions are introduced. Fig. 5 shows three time-frequency descriptions of the linear frequency modulation signal generated from the Matlab Toolbox: (a) is the frequency domain description which loses the time information; (c) is the time domain description which loses the frequency information; (b) is the time-frequency description which shows the change rule of frequency over time clearly.

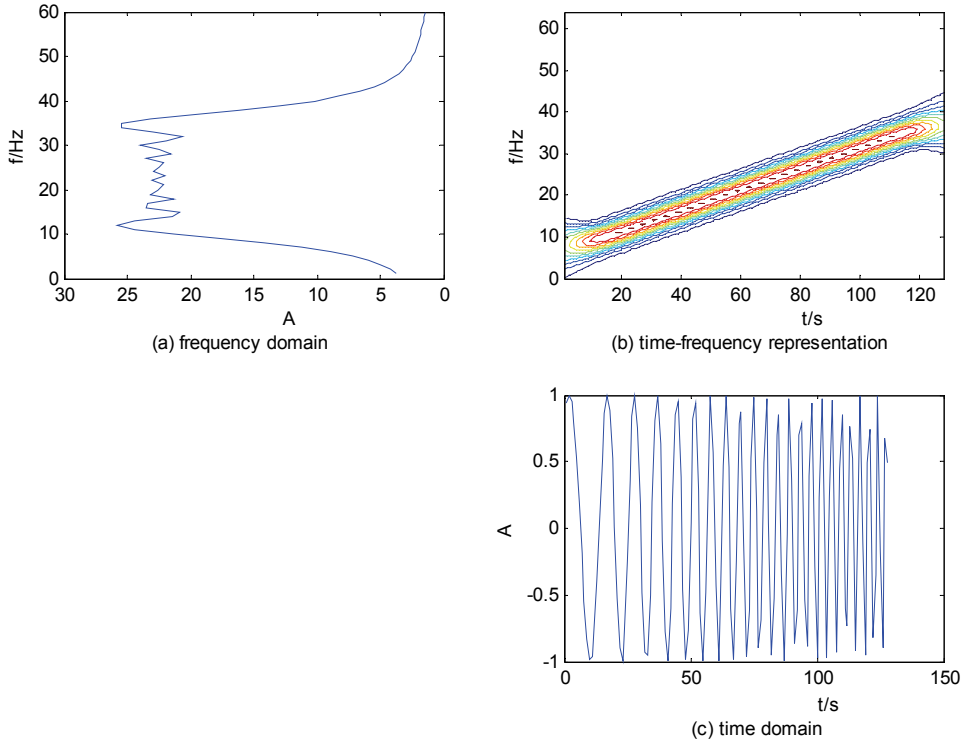

Fig. 5. Three description methods of linear frequency modulation signal

The basic idea of time-frequency analysis is to develop a joint function to combine the time and frequency factors. The time-frequency analysis, which can describe the signal traits on a time-frequency plane, has become an important research field. Many time-frequency methods have been presented, which can be divided into three types: linear, quadratic and nonlinear. The STFT and WT belong to the linear type, and the Wigner-Ville distribution (WVD) and pseudo Wigner-Ville distribution (PWVD) belong to the quadratic type. This section compares the STFT, WVD, PWVD and WT for showing the advantage of WT.

The basic idea of STFT, which is presented by Gabor in 1946, is to cut out the signal by a window function, in which the signal can be regard as stationary, and analyze the signal to make sure the frequency elements in the window by the Fourier Transform, then move the window function along the time axle to obtain the change relationship of frequency over time. This is time-frequency analysis process of STFT and the STFT of the signal x(t) can be described as:

$$\mathrm{STFT}_x(t,f) = \int x(t')g^*(t'-t)e^{-j2\pi ft'}dt' \tag{13}$$

The WVD, which was presented by Wigner in the research of quantum mechanics in 1932 and applied to signal, processing by Ville later, satisfies many mathematical properties expected by time-frequency analysis. The WVD of the signal x(t) can be described as:

$$\mathrm{WD}_x(t,f) = \int x(t+\tau/2)x^*(t-\tau/2)e^{-j2\pi f\tau}d\tau \tag{14}$$

To suppress the disturbing of cross term in the WVD, the PWVD, which can be equivalent to smooth the WVD, is introduced. The PWVD of the signal x(t) can be described as:

$$\mathrm{PWVD}_x(t,f) = \int h(\tau)x(t+\tau/2)x^*(t+\tau/2)e^{-j2\pi f\tau}d\tau \tag{15}$$

A nonstationary signal is analyzed in four time-frequency methods, i.e., STFT, WVD, PWVD and WT. Fig. 6 shows the oscillogram of a signal contain four Gauss components. The four time-frequency analysis results are showed in Fig. 7, in which (a), (b), (c) and (d) denote the results of STFT, WVD, PWVD and WT respectively. As shown in Fig. 7 (a), the resolution of STFT is lower and fixed. Although the WVD and PWVD have higher resolution and time-frequency concentration, they are disturbed strictly by cross terms as shown in Figs. 7 (b) and (c). In contrast, the resolution of WT is higher than STFT and can change with frequency. There have a good frequency resolution in the low frequency range, and a good time resolution in the high frequency range. And the cross terms in WVD and PWVD disappeare. Though the STFT covers the shortage of the FT to some extent in local analysis, its defects can not be overcome. That is, when the window function is determined, the size of windows is fixed and the time resolution and frequency resolution is fixed. As the resolution of window function is restricted by Heisenberg uncertainty principle, the frequency resolution is higher and the time resolution is lower when a long window is used, the situation is reversed when a short window is used. Therefore, the key of application is how to choose reasonable window length. When the signal which contains a variety of difference of scales is analyzed, the method of STFT becomes useless.

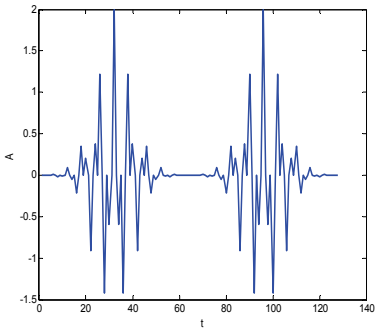

Fig. 6. The oscillogram of a signal contain four Gauss components

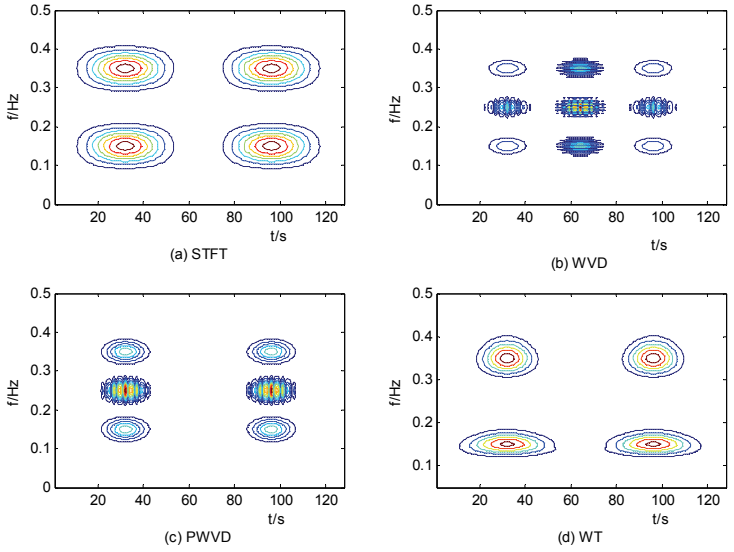

Fig. 7. Four time-frequency representations

The WVD has higher time-frequency resolution and many mathematical properties such as time-frequency concentration, symmetry, reversibility and normalizing. But the shortage is that it can not ensure non-negative and produce strictly cross terms especially for nonlinear signals, thus many researchers presented a variety of new patterns such as PWVD. These methods can suppress the disturbing signal of cross term to a certain extent, but they can not eliminate completely and damage many mathematical properties in WVD.

Although the WT is also restricted by Heisenberg uncertainty principle, the window in WT can be adjusted. In the WT, the mother wavelet can be stretched according to frequency to provide reasonable window, a long time window is used in low frequency and a short time window is used in high frequency. This time-frequency analysis which fully reflects the thought of multiresolution analysis is in accordance with the features of time varying nonstationary signal. Though the resolution of WT is lower than WVD and PWVD, the cross terms don't appear as the WT is linear time-frequency analysis.

4. Applications of the WT on nonstationary signals

This section gives some examples of the DWT successfully applied to nonstationary vehicle vibration and sound signals (Wang, et al, 2004, 2007, 2009, 2010).

4.1 Wavelet transform for nonstationary vehicle vibration

Most of the research on vehicle vibration systems assumed that the vehicles were running at certain constant speeds, therefore, were regarded as a stationary random process. In more usual cases such as starting, accelerating and braking, vehicles work under variable speed conditions, and its vibration should be considered as a nonstationary process accordingly. For nonstationary signals, both the frequencies and their magnitudes vary with time, thus the conventional Fast Fourier Transform is incapable for dealing with them. The CWT and DWT were used to study the nonstationary inputs and responses of the vehicle vibration system (Wang and Lee, 2004).

A dynamic model of a full vehicle with eight degrees of freedom, was built shown in Fig. 8. And the corresponding differential equations were derived from the Lagrange equation as,

$$[M]\{\ddot{Z}\}+[C]\{\dot{Z}\}+[K]\{Z\}=[P]\{I(t)\} \tag{16}$$

Where $[M],[C],[K]$ are matrixes of mass, damping and stiffness respectively, $\{I(t)\}$ is the road roughness vector; $[P]$ is the transfer matrix from the road roughness vector to the force excitation. $\{z\}$ is the system response vector.

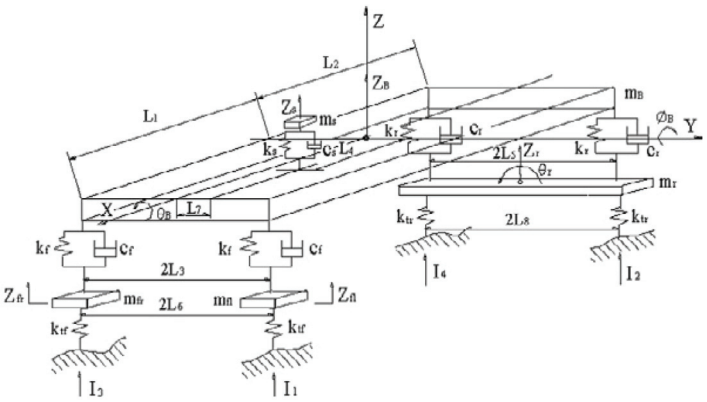

Fig. 8. Dynamic model of a vehicle with 8 DOFs

Assuming that the vehicle starting at a speed $v_0=0$, first accelerating with an acceleration a_1 up to v_m, and then braking with a deceleration a_2 down to v_f, the instantaneous vehicle speed at any time *t* were shown as,

$$V(t)=\begin{cases} v_0+a_1 t & 0<t<v_m/a_1 \\ v_m+a_2(t-v_m/a_1) & v_m/a_1<t<(v_m/a_1-v_m/a_2) \end{cases} \tag{17}$$

The above process was called "AAB" process. Using the Runge-Kutta Method, the time series of road roughness and vehicle response were calculated by Eqs. (16) and (17).

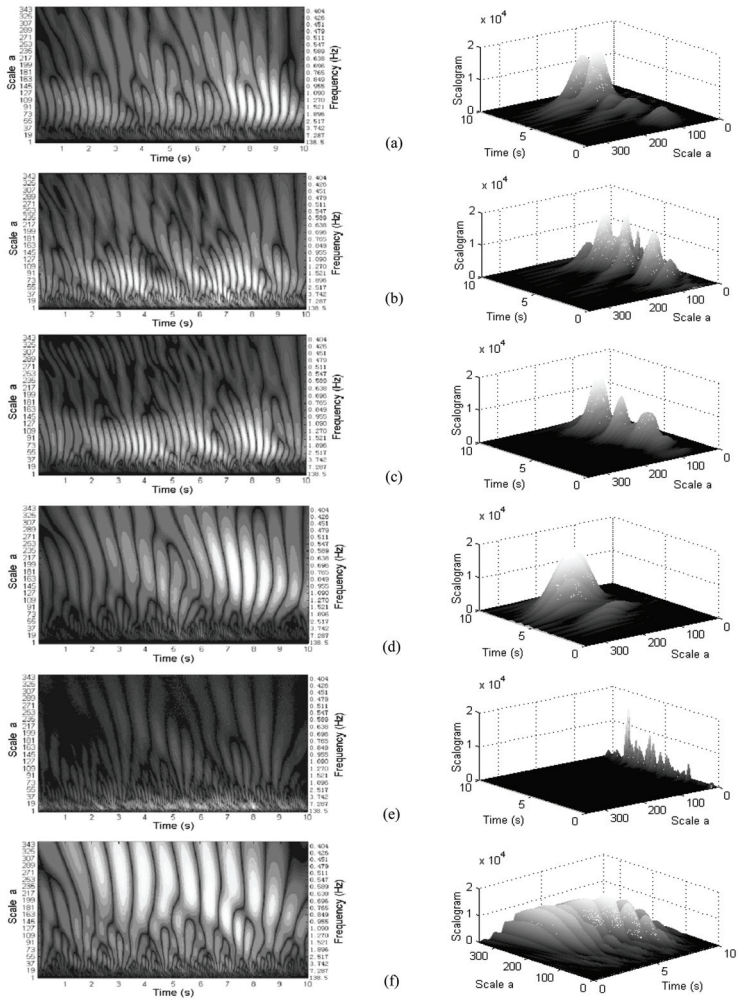

Fig. 9. 2D and 3D scalograms result from CWT during the "AAB" process: (a) the vertical vibration of the driver seat; (b), (c) and (d) the vertical, pitch and roll vibrations of the vehicle body; (e) the vertical vibration of the front axle; (f) the road roughness of the right-rear wheel.

The CWT and DWT are performed by using the Mallat algorithm in the Matlab toolbox. The selected parameters for calculation are: the Daubechies wavelet with a filter length of seven, the scaling factor a=1-350, i.e., the frequency range: 0.404-138.5 Hz. Fig. 9 (a)-(f) shows the acceleration scalograms, which were obtained from the CWT, of the seat, vehicle body, axle and road roughness during the "AAB" process, respectively. As seen from Fig. 9, the worst ride performance of the vehicle happened at 8s during the "AAB", and there was a little time delay in the vibrations transfer from road to the vehicle system. In the accelerating process, the vibration energies of the vehicle are getting bigger, moving, as well, to the

higher-frequency area; their frequency bands are getting broader, and vice versa in the braking process. As a rule, these phenomena of energy flow are transmitted to the other levels through the suspension system.
In view of the vehicle design, the ride comfort of the passenger seat is the most important. Comparing Fig. 9 (a)-(f), the energy of road excitation has been greatly restrained by the suspension system of the vehicle. However, the similar time frequency traits can be seen in (a), (b) and (c), and the ride comfort of the seat deteriorates suddenly at a certain running speed. That means that the vertical and the pitching movement of the vehicle body have more effect on the vibration of seats than the rolling movement, and that the vibration energy of the vehicle body flowed into the resonance frequency region of the seat vibration system during the "AAB" process.
From the above findings, the WT can provide the time-frequency map of transient "energy flow" of the examined points of interest in the vehicle vibration system. Thus, the WT may be used in vehicle vibration system design, especially for the transient working cases.

4.2 DWT-based denoising for nonstationary sound signals

In sound quality evaluation (SQE) engineering, distortion of the measured sounds by certain additive noises occurred inevitably, which came from both ambient background noise and the hardware of the measurement system; therefore, the signal needed to be denoised. In the former researches, we found that the unwanted noises are mainly write random noises which distributed in a wide frequency band but with small amplitudes. Some techniques for white noise suppression in common use, such as the least square, spectral subtraction, matching pursuit methods, and the wavelet threshold method have been used successfully in various applications. The wavelet threshold method in particular has proved very powerful in the denoising of a nonstationary signal. Here a DWT-based shrinkage denoising technique was applied for SQE of vehicle interior noise.
Sample vehicle interior noises were prepared using the binaural recording technique. The following data acquisition parameters were used: signal length, 10 s, sampling rate, 22 050 Hz. The measured sounds have been distorted by the random write random noises, and then wavelet threshold method is applied. This technique may be performed in three steps: (a) decomposition of the signal, (b) determination of threshold and nonlinear shrinking of the coefficients, and (c) reconstruction of the signal. Mathematically, the soft threshold signal is sign(x) (|x|-t) if |x|>t, and otherwise is 0, where t denotes the threshold. The selected parameters were: Daubechies wavelet "db3", 7 levels, soft universal threshold equal to the root square of 2 log (length(f)). As an example, a denoised interior signal and corresponding specrum are shown in Fig. 10. It can be seen that the harmony and white noise components of the sample interior noise are well-controlled. The wavelet shrinkage denoising technique is effective and sufficient for denoising vehicle noises.
Based on the denoised signals, the SQE for vehicle interior noise was performed by the wavelet-based neural-network (WT-NN) model which will be mentioned in detail in the next section, the overall schematic presentation of the WT-NN model is shown in Fig. 11. After the model was well trained, the signals were fed to the trained WT-NN model and the Zwicker loudness model which is as reference. It can be seen that the predicted specific loudness and sharpness in Fig.12 are consistent with those from the Zwicker models. The wavelet threshold method can effectively suppress the write noises in the nonstationary sound signal.

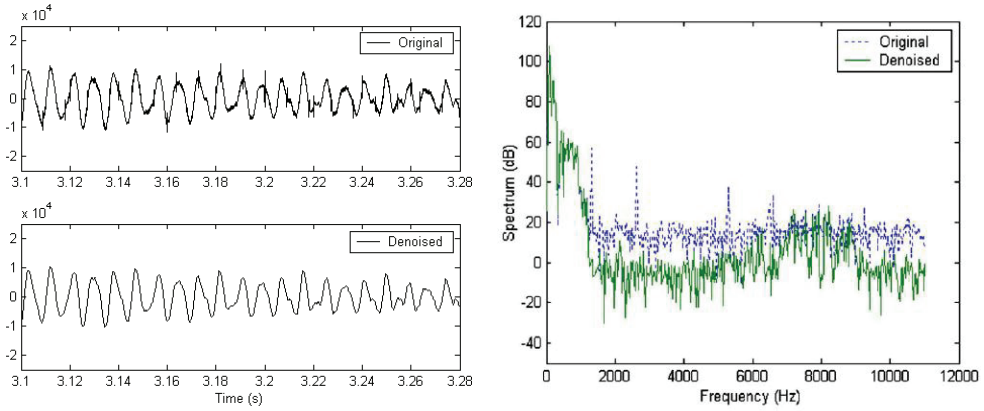

Fig. 10. Comparison of the interior noises (left panel) and their spectra (right panel) before and after the wavelet denoising model.

4.3 DWT for nonstationary sound feature extraction

In the above section, we mentioned a new model called WT-NN used for SQE for vehicle interior noise shown in Fig. 11. A wavelet-based, 21-point model was used as the pre-processor of the new WT-NN SQE model for extracting the feature of the nonstationary vehicle interior noise. For interpreting this new proposed model in detail, here we extend this model to another kind of noise-passing vehicle noise.

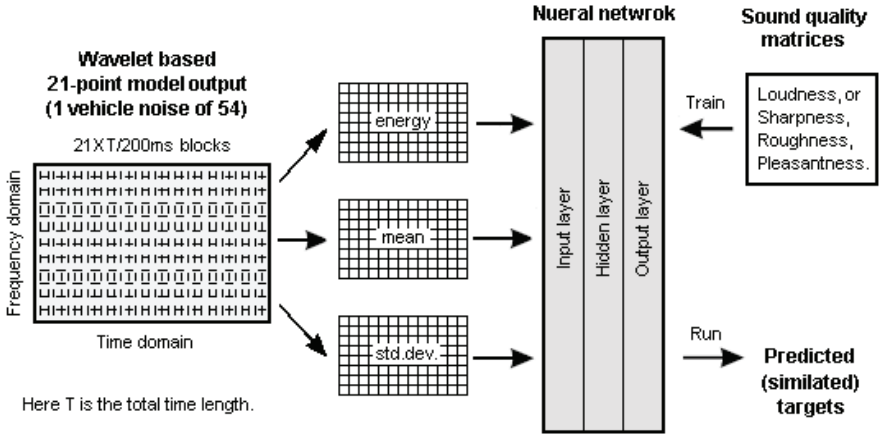

Fig. 11. Schematic presentation of the data inputs and outputs to the neural network

Sample passing vehicle noises were prepared identically as the above vehicle interior noises. The measured signals were denoised by using the wavelet threshold method mentioned before. Based on the pass-by vehicle noises, the 21-point feature extraction model for pass-by noises was designed by combining the a five-level DWT and a four-level WPA shown in Fig.13. It was used to extract features of the pass-by noises. The results are shown in Fig. 14.

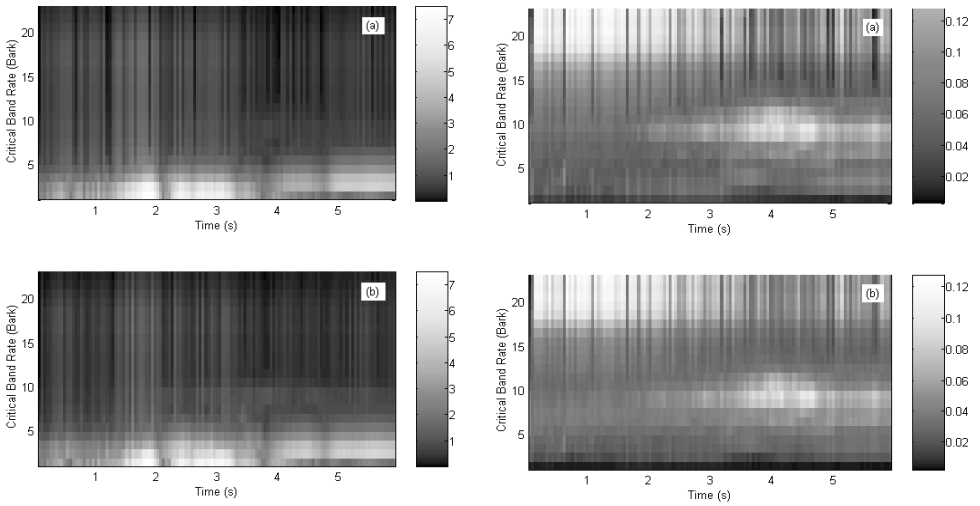

Fig. 12. Comparisons of specific loudness (left panel) and sharpness (right panel) between (a) the Zwicker model (upper), and (b) the WT-NN model (down)

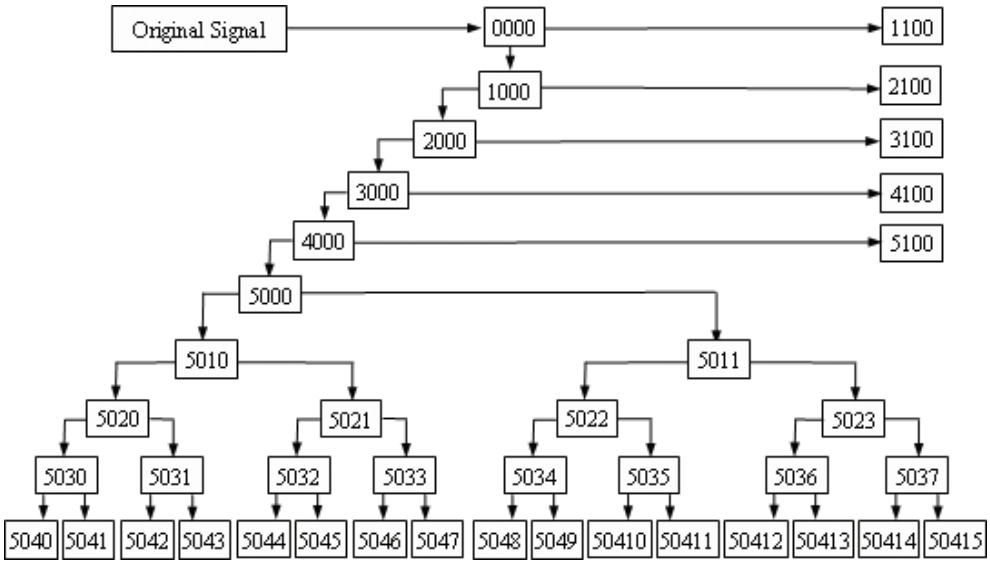

Fig. 13. Twenty-one-point wavelet-based feature extraction model for pass-by noise analysis

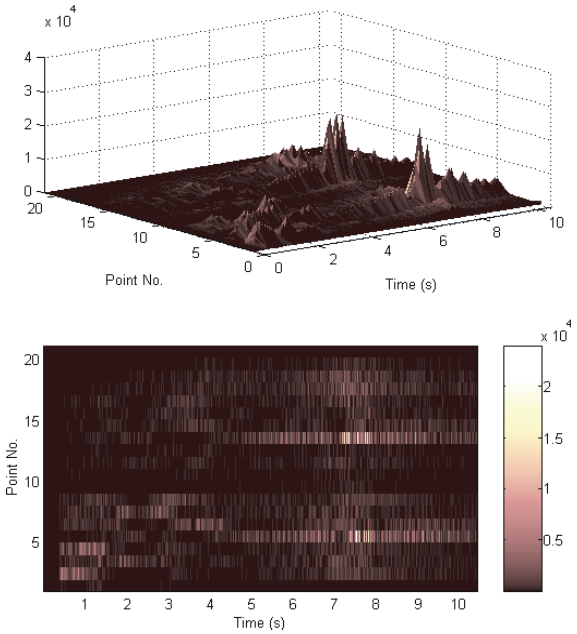

Fig. 14. Feature of the pass-by noise in time-frequency map extracted by the 21-point model

As the inputs of the WT-NN models, the above wavelet analysis results provide the time-frequency features of the signals. The SQM (sound equality matrices) of the pass-by noise as the outputs is taken from the psychoacoustical model. The loudness was adopted, which is related to the SQE of the vehicle pass-by noises. The output SQM is expressed as,

$$\mathrm{SQM} = [\mathrm{TL} \quad \mathrm{SL}]^{\mathrm{T}}$$

where the vectors TL and SL denote the total and specific values of loudness, respectively. After training the WT-NN model, the signals were fed into the Zwicker loudness model and the trained WT-NN model. It can be seen that the predicted specific loudness in Fig. 15 coincide well with those from the Zwicker models, thus as the pre-processor of the WT-NN model, the newly proposed wavelet-based, 21-point model can extract the feature of nonstationary signal precisely.

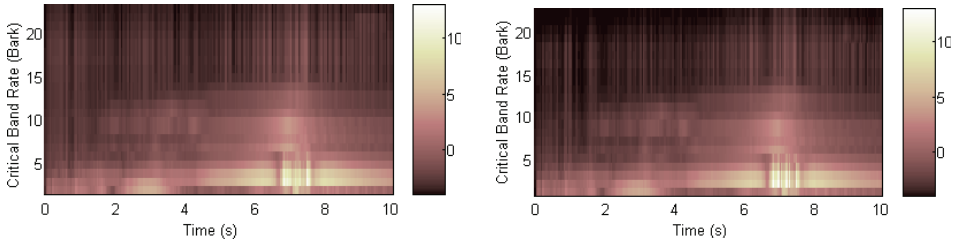

Fig. 15. Specific loudness comparison between (left panel) the Zwicker model, and (right panel) the WT-NN model.

4.4 DWT for nonstationary sound quality evaluation

In this section a DWT-based filter bank is performed for sound octave band analysis (OBA). Verification results show that the DWT-based method (DWT-OBA) is accurate and effective for SQE of nonstationary vehicle noises.

In the measurements, a sample vehicle is accelerated up to a running speed 50 km/h. The following parameters for data acquisition are used: signal length, five seconds, sampling rate, 50 kHz. The measured sound signals need to be denoised for avoiding signal distortion by using the wavelet threshold method. Based on the measured interior vehicle noise, a DWT-OBA procedure is performed here. The determined wavelet function is the Daubechies wavelet with filter length of 70, i.e., 'db35'. The sound DWT-OBA of the interior noise can be performed in three steps: (a) signal resampling, (b) DWT filtering, and (c) band SPL calculation. The calculation procedure for the DWT-OBA of a sound signal is shown in Fig. 16. Then, the octave-band SPL values can be calculated from the sub-band filtered signals using the definition of sound pressure level in time domain,

$$L_i = 10\log\left(\frac{1}{m_i}\sum_{j=1}^{m_i} p^2_{ij} / p_{ref}\right) \tag{18}$$

where L_i is the ith band SPL, m_i is the total points of the ith band signal, P_{ij} is the ith band sound pressure on the j_{th} point, and P_{ref} is the reference sound pressure, P_{ij} =20e-6. Comparing with the measured results, the errors of the band SPLs in Fig. 21 are within [-0.3, +0.2] dB, which are much less than the band error scope of ±1 dB defined in the IEC 651 standard. The total SPL are also computed by Eq. (19),.

$$L_T = 10\log\left(\sum_i 10^{L_i}\right) \tag{19}$$

It is exact same as the measured value 83.7 dB. In view of the A-weighted total SPL, the measured value is 66.1 dB (A), and the calculated value is 66.2 dB(A). To prove transient characteristic of the DWT-OBA algorithm, furthermore, the time-varying A-weighted total SPLs of the interior vehicle noise are carried out by using the DWT-OBA and MF-OBA algorithms, respectively. MF-OBA is a self-designed multi-filter octave band analysis method also used for SQE and here is adopted as reference. The selected calculation parameters are: time frame length, 200 ms, frame amount, 25, and A-weightings, [-56.7 -39.4 -26.2 -16.1 -8.6 -3.2 0 1.2 1.0 -1.1] dB, for octave band number from one to 10. The results shown in Fig. 17 imply a very good transient characteristic of the DWT-OBA.

In order to examine the effectiveness of the presented DWT-OBA algorithm for more practical uses, we applied it and the self-designed filtering algorithm to the measured exterior vehicle noise, respectively. The exterior noise signal has been pre-processed following the DWT denoising procedure. The A-weighted band SPLs of the exterior vehicle noise calculated from the filtering and DWT algorithms, as well as the measurement results, are shown in Figs. 18 and 19. And the calculated results are summarized in Table 1.

Fig. 16. The calculation flowchart for DWT octave-band analysis of a sound signal

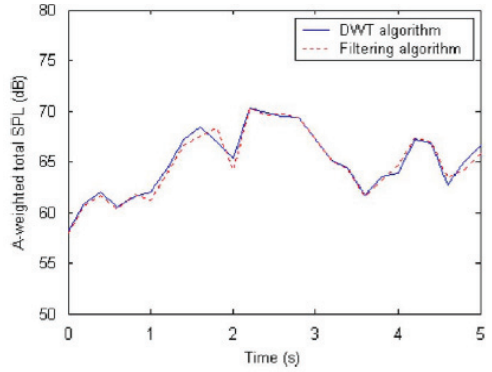

Fig. 17. Calculated time-varying A-weighted total SPLs of the interior vehicle noise by using the newly proposed DWT and filtering algorithms.

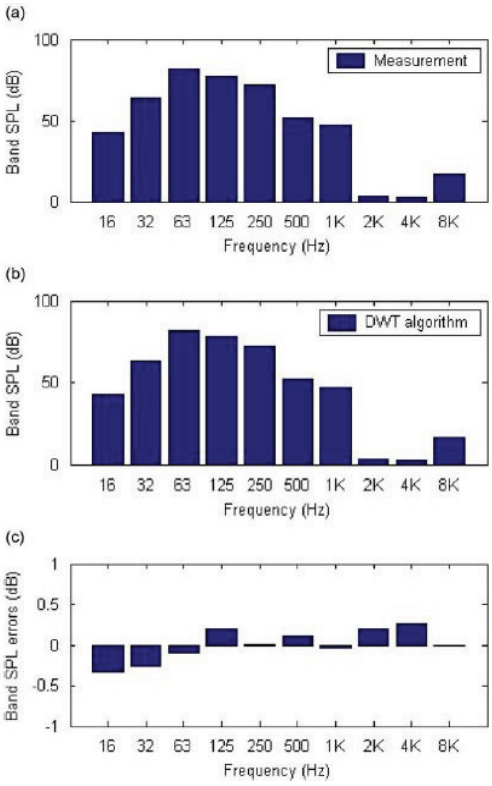

Fig. 18. Linear SPL comparison of the octave-band analysis of the interior vehicle noise: (a) the measured result, (b) SPL values calculated by the db35 filter bank, and (c) the band SPL errors

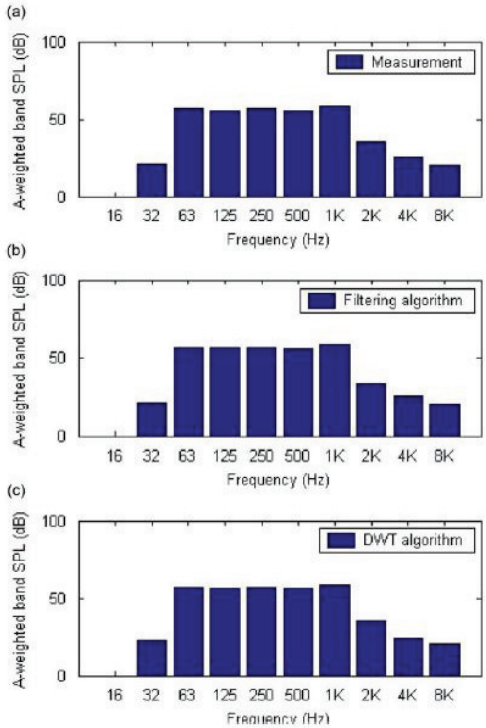

Fig. 19. A-weighted octave-band SPLs of the exterior vehicle noise from (a) the measurement, (b) self-designed filtering algorithm, and (c) the DWT algorithm.

Octave band number	1	2	3	4	5	6	7	8	9	10
Measured band SPLs(dB)	-13.2	21.0	56.8	55.9	56.7	55.9	58.8	35.4	25.5	20.2
Filtering band SPL error(dB)	-0.09	0.48	0.05	0.37	0.19	0.12	0	-0.07	0.27	0.17
DWT band SPL errors(dB)	-0.008	0.25	-0.08	0.24	0.09	0.18	0.04	0.02	0.03	-0.01
A-weighted total SPLs(dB)	64.0 (measured)				64.1476 (filtering)			64.0953 (DWT)		
Error percentage of total SPLs	0.2306% (filtering)				0.1489% (DWT)					

Table 1. Summary of the calculated A-weighted SPLs of the exterior vehicle noise from different methods

It can be seen that, for the exterior vehicle noise, the A-weighted SPLs from different methods have almost same octave patterns in frequency domain. From Table 1, the maximum errors of the filtering and DWT band SPLs are 0.48 and 0.25 dB, respectively,

which are all occurred in the octave band with a center frequency of 32 Hz. These errors can make very small contributions to the total SPL values, due to the special frequency characteristics of the vehicle noises. The octave band SPLs from the presented methods are satisfied the error limitation of ± 1 dB published in the IEC 651 standard. The error percentage of the A-weighted total SPLs are 0.2306% and 0.1489% for the filtering and DWT algorithms, respectively. The above comparisons indicate that the presented DWT-OBA algorithm is effective and feasible for sound quality estimation of vehicle noises.

4.5 DWT pattern identification for engine fault diagnosis

In Section 4.2, 4.3 we proposed a new model called WT-NN in which the wavelet-based, 21-point feature extraction model was designed as the pre-processor. Here we performed this model for engine fault diagnosis (EFD), so called EFD WT-NN model.

To establish the EFD WT-NN model, firstly, a database including the engine fault phenomena and their corresponding sound intensity signals needs to be built. Based on the 2VQS type of EFI engine mounted on the GW-II engine test bed, the sound intensities in different failure conditions were measured using the two-microphone recording technique recommended by the standard ISO 9614. The experimental equipments are arranged as that in Fig. 20. The measured signals were denoised by using the wavelet threshold method.

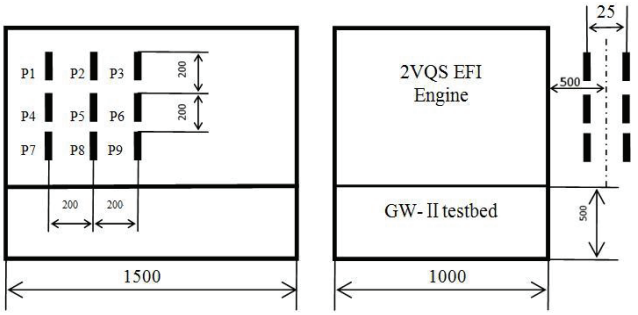

Fig. 20. Experimental setup for sound intensity measurements

To determine the structure of the time-frequency feature extraction model, the FFT-based spectral analysis is imposed on the above saved engine noise signals. The results suggest that the sound energies of the engine noises mainly distribute in a low-frequency range up to 3000 Hz (focus on the frequency interval [0-350Hz]), and decrease with increasing frequency. According to the above discussions, the wavelet-based, 21-point model for feature extraction of engine noises was applied. Using the 21-point model, the feature of the engine noises is extracted, and an example is shown in three dimensions in Fig. 21. Then the WT-NN model is built and performed for EFD. The noise signals in different engine state have been dealt with by applying the 21- point feature extraction model; the outputs of the pre-processor are defined in matrices and fed to a NN as the its inputs. Then, the failure phenomena corresponding to the engine state noise signals, which have been defined and quantified in matrices as shown in Table 2, are taken as the outputs of the NN.

After training, we respectively fed all the signals of different engine states to the trained WT-NN model. Typically, we listed the outputs of WT-NN model and the simulated diagnosis results (patterns) at the measuring point "P1" in Table 3, where the S0, S1, S2, …, and S8, denoting the engine fault patterns have the same meanings as those in Table 2, and U is an uncertain result.

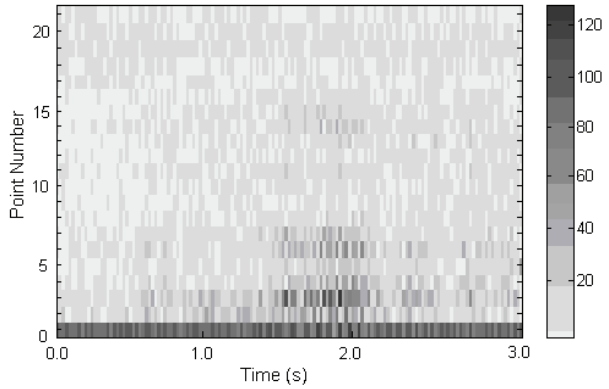

Fig. 21. The 21-point time-frequency feature of the engine fault state that the ECU does not receive the knock signals (meshing point no.2)

Engine working state	Target output
Normal idling state of the engine (S0)	[0 0 0 0 0 0 0 0 0 0]
The nozzle in the first cylinder doesn't work (S1)	[0 1 0 0 0 0 0 0 0 0]
The second and third cylinders do not work (S2)	[0 0 1 0 0 0 0 0 0 0]
The electric motor doesn't work (S3)	[0 0 0 1 0 0 0 0 0 0]
ECU does not receive the hall senor signals (S4)	[0 0 0 0 1 0 0 0 0 0]
The throttle orientation potentionmeter is broken (S5)	[0 0 0 0 0 1 0 0 0 0]
ECU does not receive the knock signals (S6)	[0 0 0 0 0 0 1 0 0 0]
The 5-voltage power of the hall sensor is broken (S7)	[0 0 0 0 0 0 0 1 0 0]
ECU does not receive the oxygen sensor signal (S8)	[0 0 0 0 0 0 0 0 1 0]

Table 2. The target output definition of the engine working states

Since the NN outputs are continuous values, the thresholds need to be defined to identify the calculated diagnosis results of the WT-NN model. Mathematically, the threshold rule is described as,

$$S_{fs} = \begin{cases} 0 & 0 \le S_v \le 0.45 \\ \text{uncertain} & 0.45 \le S_v \le 0.55 \\ 1 & 0.55 \le S_v \le 1.0 \end{cases}$$

where, S_{fs} denotes the fault state of the engine, S_v denotes the calculated output values of the WT-NN model. It can be seen that the diagnosis results in Table 4 is exactly same as that expected.

We obtained similar comparison results from the simulations using engine noise signals at other measuring points. We found that, for the sample signals used in the NN learning, the outputs of the BP network are in general conformity with the desired results; when the input data deviate from the samples within a certain range, the NN output has a tendency to approach the sample failure characteristics. For a real failure diagnosis, one may select in measurement points under the guidance of the NN designer of the diagnosis system. According to the above findings, the wavelet-based model may be used to diagnose engine failures in vehicle EFD engineering.

State	S0	S1	S2	S3	S4	S5	S6	S7	S8
Model output	0	0.164	0	0	0.027	0	0	0	0
	0	0.610	0	0	0.023	0	0	0	0
	0	0.022	0.989	0	0	0	0.009	0	0
	0.001	0	0	0.987	0.001	0	0.002	0.002	0
	0	0.016	0	0.034	0.970	0.002	0	0	0.085
	0.009	0	0	0.013	0	0.995	0.002	0.011	0
	0	0	0	0	0	0.001	0.979	0	0.088
	0	0	0	0.008	0	0	0	0.885	0
	0	0	0	0	0.023	0.004	0.030	0	0.976
Result	S0	S1	S2	S3	S4	S5	S6	S7	S8

Table 4. The outputs of the WT-NN model and diagnosis results at point "P1"

5. Acknowledgments

This work was supported by the NSFC (grant no. 51045007), and partly supported by the Program for Professor of Special Appointment (Eastern Scholar) at Shanghai Institutions of Higher Learning, China.

6. References

Cohen, L. *Time-Frequency Analysis*. Prentice-Hall, New Jersey, USA, 1995.

Brigham E. O., *The fast fourier transform and its applications*. Prentice-Hall, Englewood Cliffs, New Jersey, 1988

Hodges C. H., Power J., Woodhouse J., The use of the sonogram in structure acoustics and an application to the vibrations of cylindrical shells, *Journal of Sound and Vibration*. 101, 203-218, 1985

Baydar N., Ball A., A comparative study of acoustic and vibration signals in detection of gear failures using wigner-ville distribution. *Mechanical Systems and Signal Proceeding*, 15(6), 1091-1107, 2001

Chen F. S., Wavelet transform in signal processing theory and applications. National Defense Publication of China, 1998

Daubachies I., *Ten Lectures on Wavelets*, Philadelphia, PA: SIAM, 1992

Wang Y. S., Lee C.-M., Zhang L. J., Wavelet Analysis of Vehicle Nonstationary Vibration Under Correlated Four-wheel Random Excitation, *International Journal of Automotive Technology*, Vol.5 No.4, 2004.

Wang Y. S., Lee C.-M., Kim D.-G, Xu Y., Sound quality prediction for nonstationary vehicle interior noise based on wavelet pre-processing neural network model, *Journal of Sound and Vibration*, Vol 299, 933-947, 2007.

Wang Y. S., Lee C.-M., Evaluation of nonstationary vehicle passing loudness based on an antinoise wavelet pre-processing neural network model, *Int. J. Wavelets, Multiresolution and Information Processing*, Vol 7, No.4, 459-480, 2009.

Wang Y. S., Sound Quality Estimation for Nonstationary Vehicle Noises Based on Discrete Wavelet Transform, Journal of Sound and Vibration, Vol 324, 1124-1140, 2009.

Wang Yansong, Xing Yanfeng, He Hui, An Intelligent Approach for Engine Fault Diagnosis Based on Wavelet Pre-processing Neural Network Model, *Proceedings of the 2010 IEEE International Conference on Information and Automation*, June 20-23, Harbin, China.

3

Transient Analysis and Motor Fault Detection using the Wavelet Transform

Jordi Cusidó i Roura and Jose Luis Romeral Martínez
MCIA Group, Technical University of Catalonia, Spain

1. Introduction

Induction motors are the most common means of converting electrical power to mechanical power in the industry. Induction machines were typically considered robust machines; however, this perception began to change toward the end of the last decade as low-cost motors became available on the market. Nowadays the most widely used induction motor in the industry is a machine which works at the limits of its mechanical and physical properties. A good diagnosis system is mandatory in order to ensure proper behavior in operation.
The history of fault diagnosis and protection is as outdated as the machines themselves. Initially, manufacturers and users of electrical machines used to rely on simple protection against, for instance, overcurrent, overvoltage and earth faults to ensure safe and reliable operation of the motor. However as the tasks performed by these machines became more complex, improvements were also sought in the field of fault diagnosis. It has now become essential to diagnose faults at their very inception, as unscheduled machine downtime can upset deadlines and cause significant financial losses.
The major faults of electrical machines can be broadly classified as follows:
Electrical faults (Singh et al., 2003):
1. Stator faults resulting in the opening or shorting of one or more stator windings;
2. Abnormal connection of the stator windings;

Mechanical faults:
3. Broken rotor bars or rotor end-rings;
4. Static and/or dynamic air-gap irregularities;
5. Bent shaft (similar to dynamic eccentricity) which can result in frictions between the rotor and the stator, causing serious damage to the stator core and the windings;
6. Bearing and gearbox failures.

However, as is introduced in the basic bibliography by Devaney (Devaney et al., 2004), the effect of bearing faults is, in most cases, similar to eccentricities and has the same effects on the motor.
The operation during faults generates at least one of the following symptoms:
1. Unbalanced air-gap voltages and line currents
2. Increased torque pulsations
3. Decreased average torque
4. Increase in losses and decrease in efficiency
5. Excessive heating
6. Appearance of vibrations

Many diagnostic methods have been developed so far for the purpose of detecting such fault-related signals. These methods come from different types and areas of science and technology, and can be summarized as follows (Jardine et al., 2006) (Meador, 2003):

1. Electromagnetic field monitoring by means of search coils, and coils placed around motor shafts (axial flux-related detection). This is associated with the capacity for capturing the presence of magnetic fields around an IM. Field evaluation must provide information about motor-operation states.
2. Temperature measurements: Temperature is a typical second-order effect of operation conditions. Induction motors typically have an operational temperature range, defined in the motor nameplate, which is associated with the tests performed. Any fault-operation condition shows a temperature increment. By performing a temperature analysis the first approach to fault conditions can be made.
3. Infrared recognition: This is used to evaluate the state of the material, especially for bearings. This cannot be performed in an online system.
4. Radio frequency (RF) emissions monitoring: Radio frequency is a second-order effect of fault conditions which is currently used for gearbox diagnosis.
5. Vibration monitoring: This is the typical method for fault diagnosis in industrial applications; it achieves good results for bearing analysis although it presents some deficiencies with electrical faults and rotor faults.
6. Chemical analysis: This is used to analyze bearing grease; it is only used with big motors and not with the typical small ones.
7. Acoustic noise measurement: This is a new trend in the field of gearbox failure (Tahori et al., 2007).
8. Motor current signature analysis (MCSA), which is explained further below.
9. Model-based artificial intelligence and neural-network-based techniques: These are new approaches which combine multi-modal data acquisition with advanced signal-processing techniques.

Motor current signature analysis (MCSA) is one of the most widely used techniques for fault detection analysis in induction machines. It is based on the Fast Fourier transform (FFT), which is currently considered the standard.

Finally, other pieces of work introduce all the motor faults (Benbouzid et al., 2000) (Thomson et al., 2003) at the same time, typifying the different harmonic effects of every fault.

The classic MCSA method works well under constant load torque and with high-power motors, but difficulties emerge when it is applied to pulsating load torques, in applications such as mills, freight elevators and reciprocating compressors. On the other hand, the results of the common signal processing method (typically FFT, Fast Fourier transform) should vary according to the application, especially during transient states. In the cases described above, the FFT algorithm is likely to cause errors due to the averaging of spectral amplitudes during sampling time.

The need to find other signal processing techniques for non-stationary signals becomes, therefore essential. Time-frequency transforms such as the short time Fourier transform or the wavelet analysis (Ukil et al., 2006) (Valsan et al., 2008) have been successfully used with electrical systems in order to evaluate faults during transient states. The detection of induction motor faults using the wavelet transform has also been introduced (Kar et al., 2006), especially in the case of noise or vibration signals. Interesting approaches have been presented recently (Calis et al., 2007) (Bacha et al., 2008) which introduce the analysis and

monitoring of fluctuations of motor current zero-crossing instants and the use of artificial intelligence solutions such as neural networks. A recent publication (Niu et al., 2008) presents an interesting approach of DWT applied to the evaluation of different statistic feature extraction techniques. In this paper different statistic methodologies are applied over wavelet decomposition details showing interesting results for specific details. However the feature extraction has been done without taking the motor fault behavior into consideration. This chapter proposes a different approach that begins with a detailed analysis of motor current decomposition for the further application of DWT at specific faulty bands. An energy estimation of the analyzed bands is proposed to define fault factors.

PSD (power spectral density) (Ayhan et al., 2003) describes the distribution of power along frequencies. A similar concept applied to the wavelet transform could be useful for diagnosing a motor under variable load torque. The energy estimation of specific details improves the diagnosis, as it introduces a specific fault factor.

This chapter starts with a description of the theoretical approach of MCSA bases and signal processing techniques proposed, followed by a presentation of experimental results. The use of the wavelet transform improves fault detection, and the energy estimation provides the fault factor needed to implement an online monitoring system. Conclusions are presented in the last section.

2. Basic theory

2.1 Motor current signature analysis (MCSA)

This method focuses its efforts on the spectral analysis of the stator current and has been successfully introduced for the detection of broken rotor bars (Deleroi, 1984), bearing damage and dynamic eccentricities (Devaney et al., 2004) caused by a variable air gap due to a bent shaft or a thermal bow. The procedure consists in evaluating the relative amplitudes of the different current harmonics which appear as a result of the fault.

The frequencies related to the different faults in the induction machine, such as air-gap eccentricity, broken rotor bars (Figure 1), and the effect of bearing damage, are expressed by equations (1), (2) and (3), respectively (Tahori et al., 2007)

$$f_{ecc} = f_1\left[1 \pm m\left(\frac{1-s}{p}\right)\right] \tag{1}$$

$$f_{brb} = f_1\left[m\left(\frac{1-s}{\frac{p}{2}}\right) \pm s\right] \tag{2}$$

$$f_{i,o} = \frac{n}{2} f_r\left[1 \pm \frac{bd}{pd}\cos\beta\right] \tag{3}$$

where fi is the rotational speed frequency of the rotor, $f1$ is the frequency supply, m is the harmonic order, s is the slip and p is the number of poles. In the bearing fault equation, bd, pd and $\cos\beta$ correspond to the constructive bearing parameters (Figure 2).

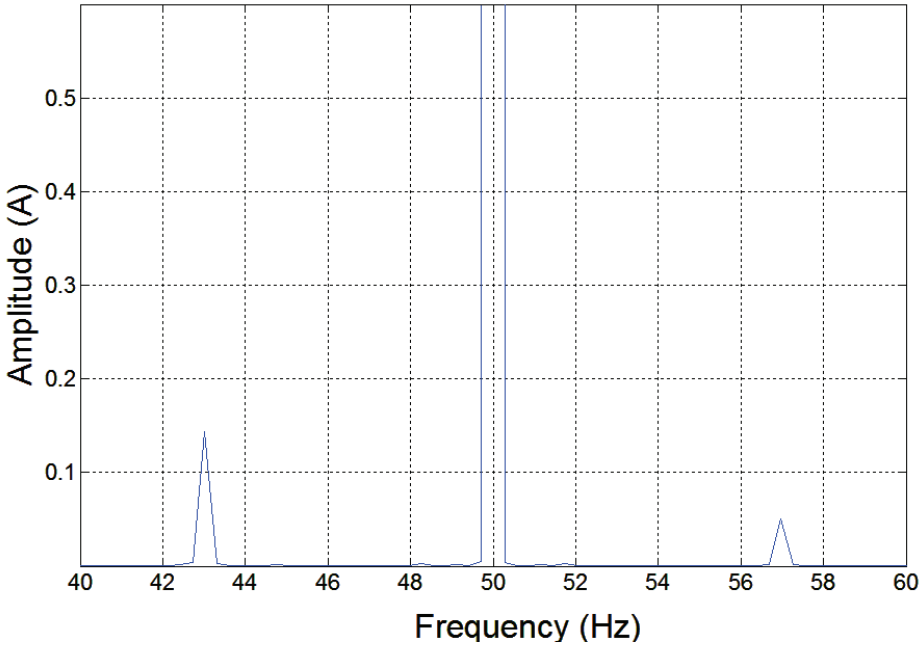

Fig. 1. Stator current spectrum for an induction motor with broken bars. Base frequency of 50 Hz

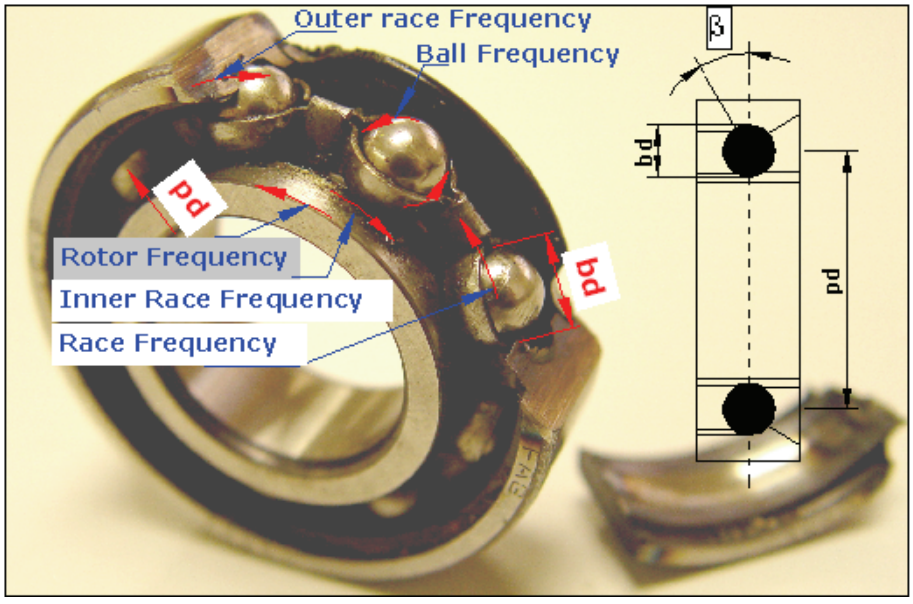

Fig. 2. Bearing parameters

2.2 Stator current composition

Fault detection in induction machines cannot be considered individually. In order to obtain a successful fault detection system harmonic distribution, it must be considered in a holistic way. The holistic analysis of all the current spectra makes it possible to develop a successful system. By looking at different components of MCSA, the approach to current spectra can be defined as follows:

Considering eccentricities first sideband components are about $f_1 = \frac{f_s}{2}$ and $f_2 = f_s + \frac{f_s}{2}$ and the upper-sideband components about $f_3 = 2 \cdot f_s + \frac{f_s}{2}$ and $f_4 = 3 \cdot f_s + \frac{f_s}{2}$ (Singh et al., 2003).

Considering broken rotor bars, first sideband components are about $f_1 = f_s\left(1-2s\right)$ and $f_2 = f_s\left(1+2s\right)$ and fifth sideband components are about $f_3 = f_s\left(4-5s\right)$ and $f_4 = f_s\left(5-6s\right)$ (Tahori et al., 2007). fs is the main frequency supply.

Three-phase currents under a fault condition can generally be expressed as follows:

$$i_R(t) = \sqrt{2}\, I_R \cos 2\pi f_s t + \sqrt{2} \sum_{n=0}^{N} I_{Rn} \cos\left(2\pi f_n t - \phi_{Rn}\right) \tag{4}$$

$$i_S(t) = \sqrt{2}\, I_S \cos\left(2\pi f_s t - 2\pi/3\right) + \sqrt{2} \sum_{n=0}^{N} I_{Sn} \cos\left(2\pi f_n t - \phi_{Sn} - 2\pi/3\right) \tag{5}$$

$$i_T(t) = \sqrt{2}\, I_T \cos\left(2\pi f_s t - 4\pi/3\right) + \sqrt{2} \sum_{n=0}^{N} I_{Tn} \cos\left(2\pi f_n t - \phi_{Tn} - 4\pi/3\right) \tag{6}$$

where $I_R = I_S = I_T = I$ are the RMS values of the fundamental component of the line current, I_{Rn}, I_{Sn}, $I_{Tn}$are the RMS values of the fault components and φ_{Rn}, φ_{Sn}, φ_{Tn} are the angular displacements of the fault components.

The space vector $\vec{i}_s$ referred to the stator reference frame is obtained by applying the transformation of the symmetrical components:

$$\vec{i}_R = \sqrt{\frac{2}{3}}\left[i_R + i_S\, e^{j2\pi/3} + i_T\, e^{-j2\pi/3} \right] = \sqrt{3}\left[I\, e^{j2\pi f_s t} + I_1\, e^{j[2\pi f_1 t - \phi_1]} + I_2\, e^{j[2\pi f_2 t - \phi_2]} \ldots + I_n\, e^{j[2\pi f_n t - \phi_n]} \right] \tag{7}$$

A way of understanding the Fourier analysis is to consider it a mathematical transform to convert our view of the signal from time-based to frequency-based. This involves splitting the signal into its constituent harmonics, providing a fault detection system.

Yet, the Fourier analysis implies a serious drawback for our purposes: in the process of transformation to the frequency domain, the time information is lost. When examining the Fourier transform of a signal, it is impossible to know the precise instant when a particular event took place.

If signal properties do not change over time —that is, if we are examining a stationary signal— this is not a problem. However, most interesting signals contain a great deal of non-stationary or transitory characteristics: drift, trends, abrupt changes, and first and last occurrences of events. In this case, such characteristics are often the most important part of the signal, and the Fourier analysis is not suitable for their detection. Therefore, we need to

apply another signal processing technique, such as the Wavelet transform, that can reveal aspects that a simple Fourier analysis misses.

2.3 Continuous wavelet transform (CWT)

The Fourier analysis consists in breaking up a signal into sine waves with different frequencies. Similarly, a wavelet analysis is the breaking-up of a signal into shifted and scaled versions of the function called the 'mother wavelet'.

The continuous wavelet transform is the sum over time of the signal multiplied by scaled and shifted versions of the wavelet. This process produces wavelet coefficients that are a function of scale and position.

The integral wavelet transform of a function $f(t) \in L^2$ with respect to an analyzing wavelet ϕ is defined as

$$W_\phi f(b,a) = \int_{-\infty}^{\infty} f(t)\phi_{b,a}(t)\,dt \tag{8}$$

where

$$\phi_{b,a}(t) = \frac{1}{\sqrt{a}}\,\phi\,\frac{t-b}{a} \qquad a>0 \tag{9}$$

Parameters b and a are called translation and dilation parameters respectively. The normalization factor $\sqrt{a}$ is included so that $\|\phi_{b,a}\| = \|\phi\|$

The expression for the inverse wavelet transform is

$$f(t) = \frac{1}{C_\phi}\int_{-\infty}^{\infty} db \int_{-\infty}^{\infty} \frac{1}{a^2}\left[W_\phi f(b,a)\right]\phi_{b,a}(t)\,da \tag{10}$$

Where C_ϕ is a constant that depends on the choice of wavelet and is given by

$$C_\phi = \int \frac{\left|\hat{\phi}(\omega)\right|^2}{|\omega|}\,d\omega < \infty \tag{11}$$

The coefficients constitute the results of a regression of the original signal performed on the wavelets. A plot can be generated with the x-axis representing position along the signal (time), the y-axis representing scale, and the color at the x-y point representing the magnitude of wavelet coefficient C. These coefficient plots are generated with graphical tools.

2.4 Discrete wavelet transform (DWT)

The discrete version of the wavelet transform, DWT, consists in sampling the scaling and shifted parameters, but neither the signal nor the transform. This leads to high-frequency resolution at low frequencies and high-time resolution for higher frequencies, with the same time and frequency resolution for all frequencies.

A discrete signal x[n] can be decomposed as (Mallat, 1998):

$$x[n] = \sum_{k} a_{j_0,k}\phi_{j_0,k}[n] + \sum_{j=j_o}^{J-1}\sum_{k} d_{j,k}\varphi_{j,k}[n] \tag{12}$$

where

$\phi[n]$ is the scaling function,

$\phi_{j_0,k}[n] = 2^{j_0/2}\phi(2^{j_0}n-k)$, is the scaling function at a scale of $s = 2^{j_o}$ shifted by k,

$\varphi[n]$, is the mother wavelet,

$\varphi_{j,k}[n] = 2^{j/2}\varphi\left(2^{j}n-k\right)$, is the mother wavelet at a scale of $s = 2^{j}$ shifted by k,

$a_{j_0,k}$, is the approximation coefficients at a scale of $s = 2^{j_o}$

$d_{j,k}$, is the detail coefficients at a scale of $s = 2^{j_o}$

and $N = 2^{J}$, where N is the number of x[n] samples.

The scaling function can be defined as an aggregation of wavelets at scales larger than 1. A discrete signal can be constructed by using a sum of J-j0 details and an approximation to 1 of a signal at a scale of $s = 2^{j_o}$.

A quick way to obtain the forward DWT coefficients is to use the filter bank structure shown in Figure 3. The approximation coefficients at a lower level are transferred through a high-pass (h[n]) and a low-pass filter (g[n]), followed by a downsampling by two to compute both the detail (from the high-pass filter) and the approximation (from the low-pass filter) coefficients at a higher level. The two filters are linked to each other and they are known as quadrature mirror filters. High-pass and low-pass filters are derived from the mother wavelet and the scaling function, considered respectively in (Mallat, 1998) and (Mallat, 1989).

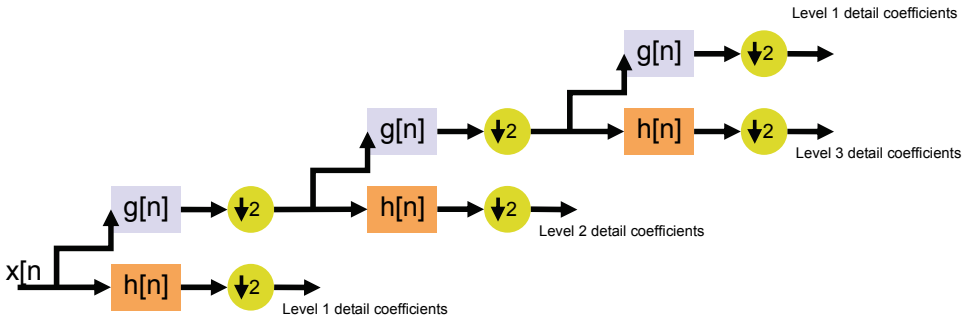

Fig. 3. Wavelet tree decomposition for three levels of detail

The various frequency range coverings for the details and the final approximation for a three-level decomposition are shown in Figure 4. These are directly related to the bands where the analysis will be performed.

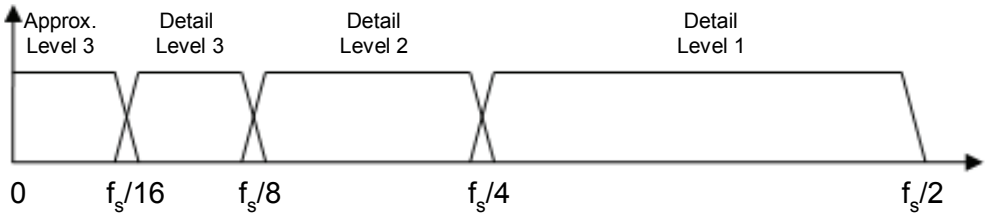

Fig. 4. Frequency ranges for details and final approximation

Figure 5 represents in a graphical manner the time-frequency window, which has better resolution on the time domain for high frequencies, and better frequency resolution for low frequencies, which means fewer resources for processing.

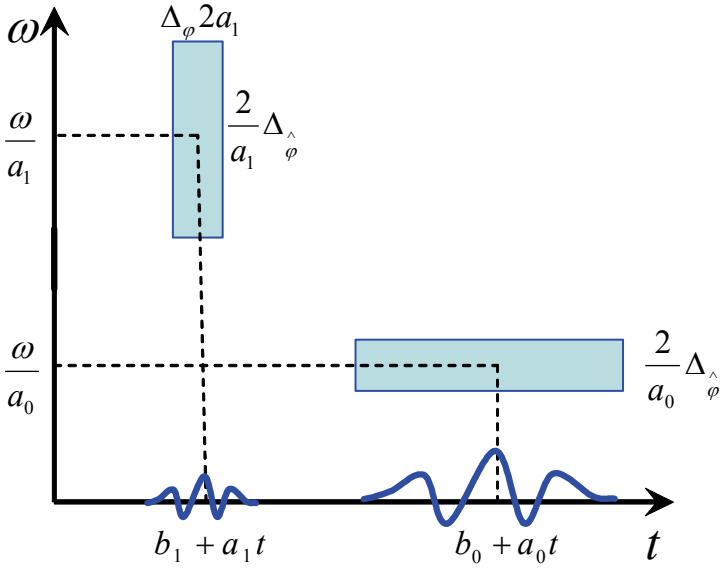

Fig. 5. Time-Frequency window for the wavelet transform

The shape of the frequency response for these filters depends on the type and the order of the mother wavelet used in the analysis. In order to avoid overlapping between two adjacent frequency bands, a high-order mother wavelet has to be used that results in a high-order frequency filter.

In order to separate the different frequency bands there is an obvious trade-off between the order of the mother wavelet and the computational cost. Thus, intensive study is needed in order to adapt the order of the mother wavelet to the requirements.

Taking a common wavelet family such as the Daubechies mother wavelet, the mother wavelet time shape shows an evolution if we just change the Daubechies order as is shown in Figure 6. Yet, this does not provide clear information for our purpose.

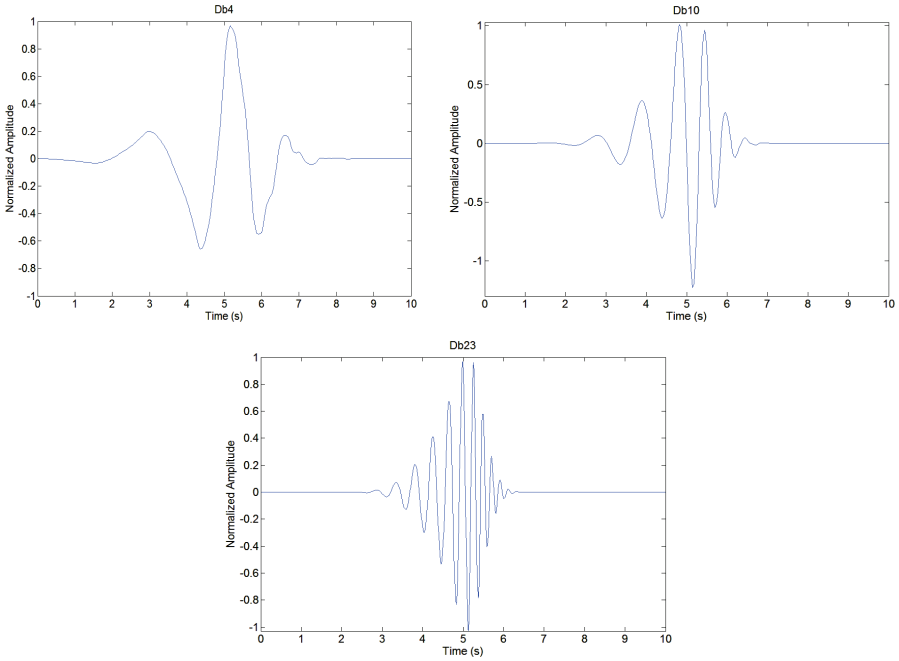

Fig. 6. Daubechies mother wavelet time evolution for order increase

Figure 7 shows the frequency response for low-pass and high-pass filters, which determines the detail and approximation decomposition for different orders. For low orders the power of one harmonic near the cut frequency could be split into two different details. This could give a false impression of the the time evolution of the analyzed signal's frequency component. By increasing the Daubechies order it is possible to idealize the filters and, hence, to obtain better frequency decomposition.

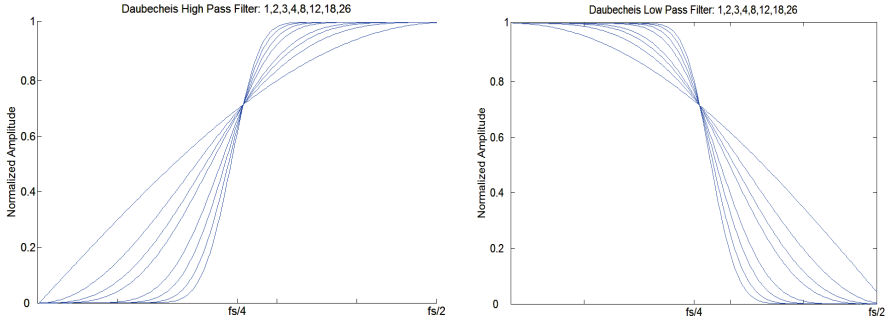

Fig. 7. Low- and high-pass filter frequency response corresponding to details

Figure 8 shows an example of this drawback. A test signal has been built with two harmonic components, one at 100 Hz and the other one at 45 Hz, and the signal has been sampled at 1000 Hz. The wavelet analysis is performed with a Daubechies db3 mother wavelet.

Harmonic content due to the 100 Hz superimposed frequency appears on details 2 and 3; when it should only appear on detail 3, corresponding to the analysis band between 125 and 62.5 Hz. A high-order Daubechies mother wavelet is needed to prevent this drawback, which is due to the db3 associated filter not being ideal enough to filter the 100 Hz harmonic content on detail 2.

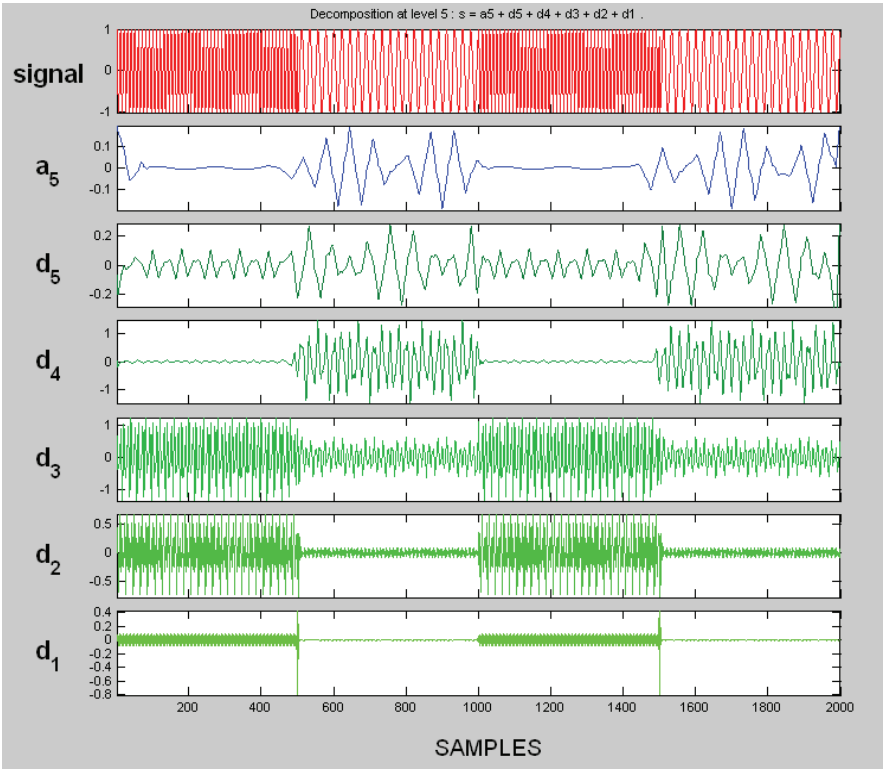

Fig. 8. Test decomposition signal with an overlapping effect

2.5 Power detail density (PDD)

In a classical Fourier analysis, the power of a signal can be obtained by integrating the power spectral density (PSD), which is the square of the Fourier transform's absolute value. The power carried by a defined spectral band can be obtained by integrating the PSD along this band.

A similar derivation can be obtained for a wavelet transform. The power detail density (PDD) can be described as the squares of the coefficients for one particular detail. The power energy carried by this detail can be obtained by integrating its PDD.

Discrete wavelet transforms show variations in the harmonic amplitude and location, and are the most suitable transform to be applied to non-stationary signals. The power detail density function resulting from a wavelet transform has proven to be one of the best suited methods for motor fault analysis under variable load, which presents the stator current as a non-stationary signal.

The average power for a signal $x(t)$ is:

$$P = \lim_{\tau\to\infty}\left[\frac{1}{2\tau}\int_{-\tau}^{\tau}|x(t)|^2\,dt\right] = \lim_{\tau\to\infty}\left[\frac{1}{2\tau}\int_{-\infty}^{\infty}|x_\tau(t)|^2\,dt\right] \tag{13}$$

Applying Parseval's theorem, this could be expressed as:

$$P = \frac{1}{2\pi}\lim_{\tau\to\infty}\left[\frac{1}{2\tau}\int_{-\tau}^{\tau}|x_\tau(\omega)|^2\,d\omega\right] = \frac{1}{2\pi}\int_{-\infty}^{\infty}\lim_{\tau\to\infty}\left[\frac{|x_\tau(\omega)|^2}{2\tau}\right]d\omega = \frac{1}{2\pi}\int_{-\infty}^{\infty}S(\omega)\,d\omega \tag{14}$$

Where:

$$S(\omega) = \lim_{\tau\to\infty}\left[\frac{|x_\tau(\omega)|^2}{2\tau}\right] \tag{15}$$

$S(\omega)$ is the spectral density of the signal $x(t)$, and represents the distribution or the density of power as a function of ω.
The energy of a discrete signal can be calculated by averaging the square of all the signal components inside the unity window, following equation 12:

$$Power = \frac{1}{T}\int_{0}^{T}\left(i_R(t) * \phi(t)\right)^2 dt \tag{16}$$

3. Experimental results

3.1 Experimental setup

A three-phase, 1.1 kW, 380 V and 2.6 A, 50 Hz, 1410 rpm, four-pole induction motor was used in this study. Firstly, its healthy performance was analyzed and, afterwards, a sixth of the rotor bars was damaged as is shown in Figure 8.
The motor nameplate is shown as follows:

Induction motor	Value
Rated power	1.1kW. :Y 400/ D 230V 2.6/4.5A
Number of poles	4
Nominal speed	1410 rev/min
Cos φ	0.81

Table I. Specifications for an induction motor

The current has been measured by an A622 Tektronix 100 Ampere AC/DC current probe. The current ranges are 0/100 mV/A, and the typical DC accuracy is ±3% ± 50 mA at 100 mV/A (50 mA to a 10 A peak). The frequency range extends from DC to 100 kHz (-3 dB).
The test rig and the data processing are displayed in Figure 9.

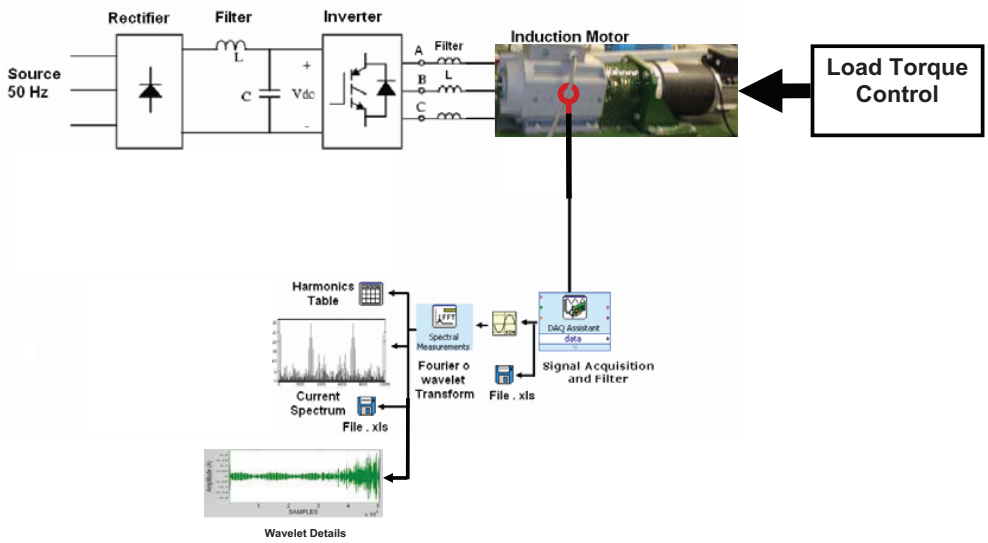

Fig. 9. Experimental setup

Load control has been implemented by using a PMSM and an inverter where variable load torque was introduced. The variable load torque follows an implemented increasing ramp as a torque control reference. Figure 10 depicts the evolution of the acquired currents.

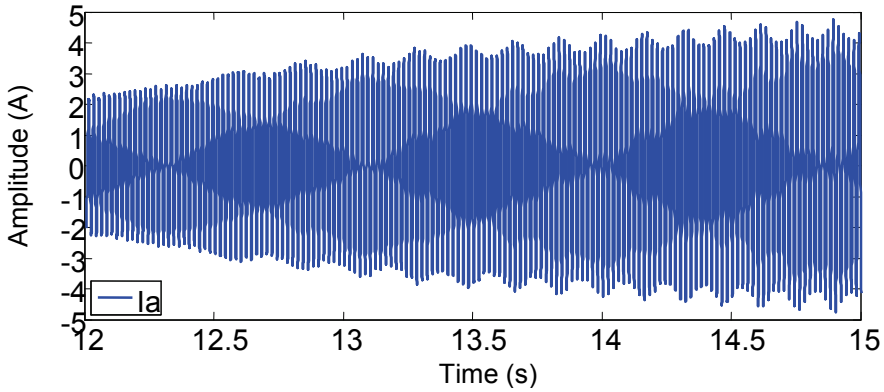

Fig. 10. Current supply to the motor

3.2 Signal acquisition requirements

When carrying out experimental analyses one of the key elements to obtain good results is to choose appropriate acquisition parameters: sampling frequency and number of samples. There are three different constraints: analysis signal bandwidth, frequency resolution for the FFT analysis and wavelet decomposition spectral bands.

For an IM, the most significant information about the stator current signal is focused around the 0-400 Hz band (Devaney et al., 2004), (Benbouzid et al., 2000) & (Thomson et al., 2003). The application of Nyquist's theorem results in a minimum sampling frequency (fs) of 800 Hz.

Furthermore, in case of an FFT analysis, it is necessary to get the right resolution. As for the inverter supply, several harmonics could be mixed up in case low resolution of the band side was chosen. The minimum resolution needed in order to obtain good results is 0.5 Hz. Equation (17) defines the number of samples to achieve the correct resolution required.

$$N_s = \frac{f_s}{R} \tag{17}$$

N_s is the number of samples needed and R is the resolution.
On the other hand, wavelet analysis will show different frequency bands, centered at different frequencies. Frequency bands will depend on the sampling frequency, and will decrease as shown in Figure 4. The band covered by the wavelet decomposition will start with $\left[f/4 , f_s/2 \right]$ and will then decrease as of $1/2$. The band suitable for analysis is about 40 Hz (Tahori et al., 2007), needs to be covered by one detail, and depends on the sampling frequency.
Finally, a sample frequency fs = 6 kHz was chosen and 50,000 samples were obtained. The full analysis band ranges from 0 to 3 kHz with a resolution of 0.12 Hz for the FFT analysis. The frequency bands of the wavelet decomposition are shown in Table II.

Decomposition details	Frequency bands (Hz)
Detail at level 1	3000-1500
Detail at level 2	1500-750
Detail at level 3	750-375
Detail at level 4	375-187.5
Detail at level 5	187.5-92.75
Detail at level 6	92.75-46.37
Detail at level 7	46.37-23.18

Table II. Wavelet decomposition frequency bands for our test

3.3 Experimental results

This section presents the experimental results. To clearly demonstrate the effectiveness of the method, different test have been performed. Firstly, tests were done in order to verify the state of the faulty motor at nominal torque on stationary state. These allow us to check MCSA harmonics resulting from the fault condition and their amplitude. The results show us that the performance of the DWT is far superior to the FFT. Finally, PSD calculations over the wavelet details are used to define a fault factor.
After an FFT analysis, the current spectra for a faulty motor operating under constant and nominal load torque and a frequency supply of 50 Hz show a mark with an amplitude of 0.15 A (Figure 1) caused by a fault in the motor's rotor bars.
Equation (2) determines the frequency where the fault harmonics are located. The frequency of the fault harmonic depends on the slip, and the slip, in turn, depends on the load torque. This means that a variable load torque condition results in a time-dependent slip value, which causes variations in the spectrum. The measured speed values have a slip between 5 and 10%. Frequency locations for the fault harmonic are depicted in equations (18) and (19).

$$f_{fault} = f_s(1-2_s) = 50(1-2\cdot 0.05) = 45Hz \tag{18}$$

$$f_{fault} = f_s(1-2_s) = 50(1-2\cdot 0.1) = 40Hz \tag{19}$$

Figure 11 corresponds to experimental harmonic distribution for a faulty motor working under variable load torque. An FFT analysis shows the spread of the power of a fault harmonic along the spectrum and the decrease of its amplitude. The wavelet analysis shows the temporary changes in the fault frequency band, and achieves great results under these particular conditions.

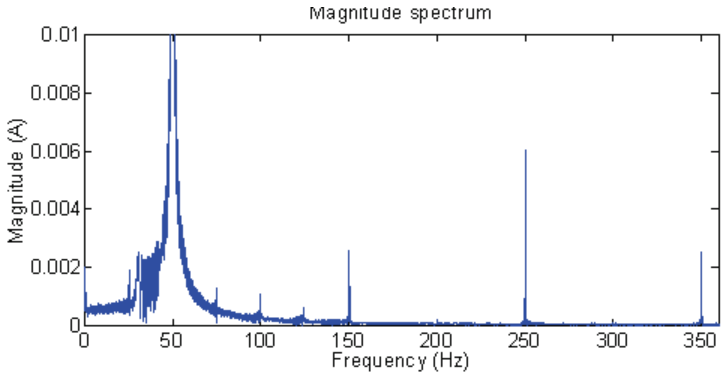

Fig. 11. Spectrum under variable load conditions

The harmonic amplitude found due to the fault (2.5 mA) is too low to use standard FFT. The wavelet transform will be used in order to find the correct amplitude.
The CWT scalogram is shown in Figure 12. It clearly shows the fault evolution on the increased value from 30 to 50 coefficients

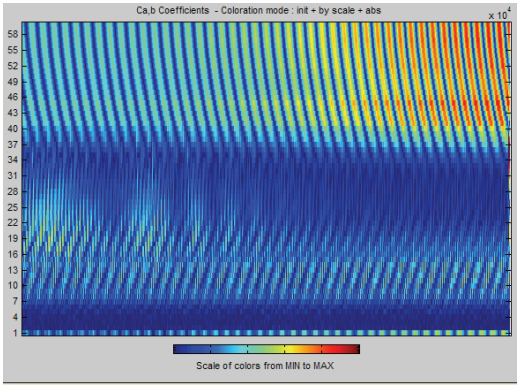

Fig. 12. Coefficient scalogram for the continuous wavelet transform

Figures 13 and 14 show the details of the wavelet decomposition for healthy and faulty motors when computing the transform with a Daubechies 23 mother wavelet. Daubechies 23 ensures correct signal decomposition, isolating the fault harmonic content, which gives proper results for our diagnostic purposes.

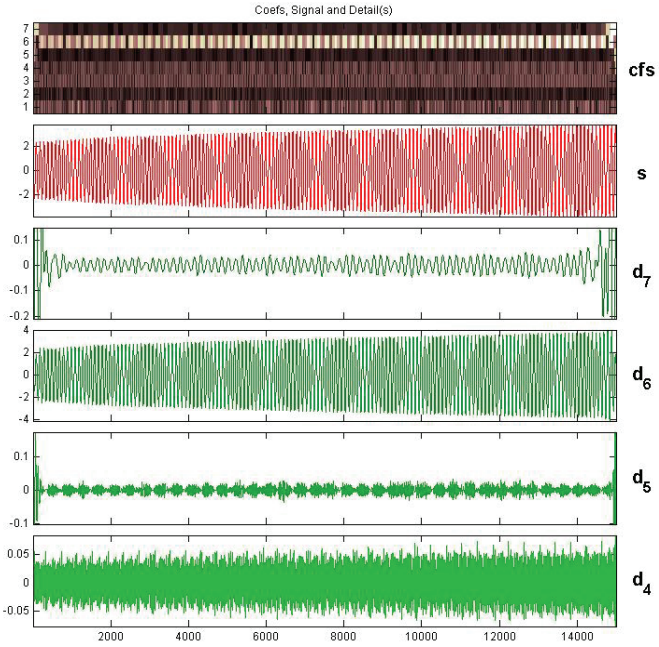

Fig. 13. DWT decomposition of a healthy motor

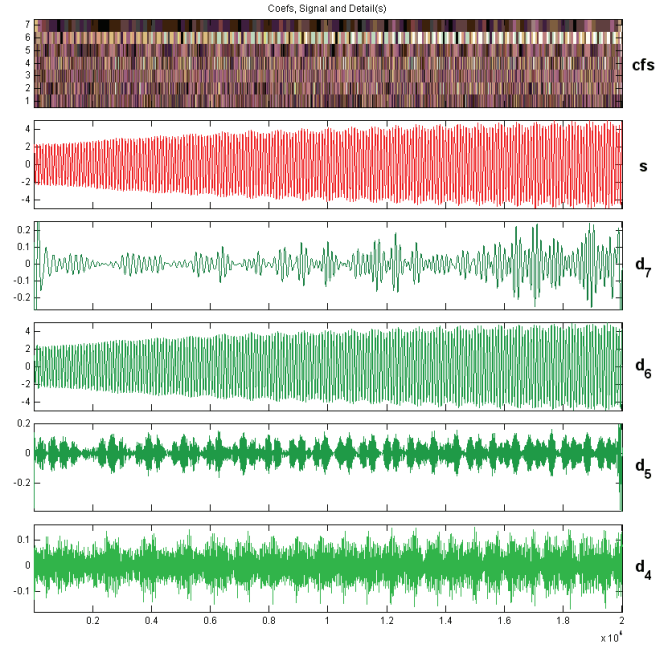

Fig. 14. DWT decomposition of a faulty motor

Detail levels of high frequency bands provide virtually no information about the original signal. Detail 6 corresponds to the frequency band of the main harmonic and detail 7 corresponds to the frequency band where the fault harmonic is located in the test.
Comparing Figure 13 to Figure 14, we can clearly see the increase of the coefficient values as a result of the fault condition on the depicted scalograms (cfs). Also, the increase of the signal content is clearly appreciated on details 4, 5 and 7.
Promising results are also obtained using wavelet transforms and evaluating the proper signal evolution during acquisition time. Figure 14 shows the advantage of the use of wavelets under variable load torque. Comparing the FFT decomposition and the DWT proves how using the Fourier decomposition (Figure 11) will reveal low amplitude for the spectrum in the 40 Hz band, lower than 3 mA. However, analyzing the wavelet time-amplitude decomposition (Figure 14) will show that the amplitude value follows the change of the amplitude in the fault harmonic over time, eventually achieving a value higher than 0.15 A when maximum torque is applied. The maximum torque value is the same that was applied to the constant torque test. The result of the analysis using the wavelet decomposition under a variable load torque matches the results obtained using an FFT analysis in the constant load torque test (Figure 1.)
To perform the diagnosis, we also need to determine the fault factor, which is defined as the estimation of the energy content of any decomposed detail. Energy is estimated applying equation (16).
Table III illustrates the energy increment for a fault condition of the approximation and detail decompositions at level 7. This energy has been calculated according to equation (12).

Power [W]						
	D1	D2	D3	D5	D6	D7
Healthy motor						
Phase A	0.00	0.00	0.11	9.9	929.2	35.75
Motor with broken rotor bars						
Phase A	0.00	0.00	1.1	13	887.7	88.11

Table III. Power spectral density (power detail density)

Table III clearly illustrates the energy increment of the decompositions chosen. Both wavelet decompositions shown in Table III can be used to detect rotor faults in the motor at any point of operation. The fault condition can be clearly identified by analyzing the energy content of faulty harmonics (PSD). A clear efficiency decrease of about 6% is appreciated on the main supply harmonic and a clear increase due to the fault condition is appreciated on the fault frequency bands. In D7, which is placed over the main fault harmonic, there is an increase of 2.5 times the energy content.
This technique combines the time and frequency analysis of wavelet decompositions, allowing for better fault factor estimation. Combining DWT and PSD allows for further development of expert algorithms to implement an autonomous fault diagnosis system for induction machines.

4. Conclusions

This chapter has introduced the problems of fault detection under a variable load torque. The classical computation of MCSA using the FFT introduces average errors in the

amplitude harmonic evaluation, hampering fault detection. To ensure proper results a time-frequency analysis is required.

As with time-frequency analysis, the proposed alternative is the discrete wavelet transform (DWT). DWT has different resolutions on time and frequency depending on the different frequency bands defined. The use of DWT ensures good time-frequency analysis. DWT has been used to analyze motors with eccentricity and broken rotor bars under fault conditions, achieving good results.

Moving toward an autonomous diagnosis sensor, a fault condition parameter has been studied and the power spectral density has been used as a power detail density with wavelets, ensuring proper results.

To sum up, we can say that:

- Wavelet decomposition is the proper technique for isolating time components of non-stationary signals, with low computational costs.
- Analyzing the energy of some wavelet decompositions is the right way to detect rotor faults in industrial motor applications with non-constant load torque.
- The evolution of wavelet coefficients gives good results in terms of fault detection.
- Orthogonal properties of wavelet functions ensure the detection of major variations on small amplitude signals, which is the case of reduced fault condition operation.

5. References

B. Ayhan, M.Y.Chow, H.J. Trussell, M.H. Song, E.S. Kang, H.J.Woe: "Statistical Analysis on a Case Study of Load Effect on PSD Technique for Induction Motor Broken Rotor Bar Fault Detection", *Symposium on Diagnostics for Electric Machines, Power Electronics and Drives*, SDEMPED 2003, Atlanta GA, USA 24-26 August 2003.

Khmais Bacha, Humberto Henao, Moncef Gossa, Gérard-André Capolino; "Induction machine fault detection using stray flux EMF measurement and neural network-based decision"; *Electric Power Systems Research*, Volume 78, Issue 7, July 2008, Pages 1247-1255.

Mohamed El Hachemi Benbouzid: "A Review of Induction Motor Signature Analysis as a Medium for Faults Detection", *IEEE Transactions on Industrial Electronics*, Vol. 47, nº 5, Oct 2000, pp. 984-993.

Hakan Çalış and Abdülkadir Çakır, Rotor bar fault diagnosis in three phase induction motors by monitoring fluctuations of motor current zero crossing instants; *Electric Power Systems Research*, Volume 77, Issues 5-6, April 2007, Pages 385-392.

J. R. Cameron, W. T. Thomson, and A.. B. Dow: "Vibration and current monitoring for detecting airgap eccentricity in large induction motors", *IEE Proceedings*, pp. 155-163, Vol.133, Pt. B, No.3, May 1986.

W. Deleroi, "Broken bars in squirrel cage rotor of an induction motor- Part 1: Description by superimposed fault currents" (in German) *Arch. Elektrotech*, vol. 67, pp. 91-99, 1984.

Michael J. Devaney, Levent Eren; "Detecting Motor Bearing Faults" *IEEE Transactions on Instrumentation and Measurement Magazine*, pp 30-50, December 2004.

Andrew K.S. Jardine, Daming Lin, Dragan Banjevic, A review on machinery diagnostics and prognostics implementing condition-based maintenance, *Mechanical Systems and Signal Processing* 20 (2006), 1483-1510

Chinmaya Kar, A.R. Mohanty, Monitoring gear vibrations through motor current signature analysis and wavelet transform, *Mechanical Systems and Signal Processing* 20 (2006) 158-187.

S. G. Mallat "A Theory for multiresolution Signal Decomposition: The Wavelet Representation" *IEEE Transactions on Pattern Analysis and Machine intelligence* Vol II No 7, July 1989.

S. G. Mallat, "A Wavelet tour of signal Processing" *Academic Press* 1998 Second Edition

Dick Meador; "Tools for O&M, from Building Controls to Thermal Imaging" *O&M Workshop for Government Facility Managers*, June 19, 2003, US Department of Energy.

Gang Niu, Achmad Widodo, Jong-Duk Son, Bo-Suk Yang, Don-Ha Hwang, Dong-Sik Kang; "Decision-level fusion based on wavelet decomposition for induction motor fault diagnosis using transient current signal"; *Expert Systems with Applications*, Volume 35, Issue 3, October 2008, Pages 918-928.

G. K. Singh, Saad Ahmed Saleh Al Kazzaz; "Induction machine drive condition monitoring and diagnostic research—a survey", *Electric Power Systems Research*, Volume 64, Issue 2, February 2003, Pages 145-158.

Easa Tahori Oskouel, Alan James Roddis: "A condition Monitoring Device using Acoustic Emission Sensors and data Storage Devices", *UK Patent Application* GB 2340034 A, data of publication 03/14/2007.

W. T. Thomson, and M. Fenger: "Case histories of current signature analysis to detect faults in induction motor drives", *IEEE International Conference on Electric Machines and Drives*, IEMDC'03, Vol. 3, pp. 1459-1465, June 2003.

Abhisek Ukil and Rastko Živanović, "Abrupt change detection in power system fault analysis using adaptive whitening filter and wavelet transform"; *Electric Power Systems Research*, Volume 76, Issues 9-10, June 2006, Pages 815-823

Simi P. Valsan, K.S. Swarup; "Wavelet based transformer protection using high frequency power directional signals"; *Electric Power Systems Research*, Volume 78, Issue 4, April 2008, Pages 547-558.

Part 2

Image Processing and Analysis

4

A MAP-MRF Approach for Wavelet-Based Image Denoising

Alexandre L. M. Levada[1], Nelson D. A. Mascarenhas[2] and Alberto Tannús[3]
[1,2]*Federal University of São Carlos (UFSCar)*
[3]*University of São Paulo (USP)*
Brazil

1. Introduction

Image denoising is a required pre-processing step in several applications in image processing and pattern recognition, from simple image segmentation tasks to higher-level computer vision ones, as tracking and object detection for example. Therefore, estimating a signal that is degraded by noise has been of interest to a wide community of researchers. Basically, the goal of image denoising is to remove the noise as much as possible, while retaining important features, such as edges and fine details. Traditional denoising methods have been based on linear filtering, where the most usual choices were Wiener, convolutional finite impulse response (FIR) or infinitie impulse response (IIR) filters. Lately, a vast literature on non-linear filtering has emerged Barash (2002); Dong & Acton (2007); Elad (2002); Tomasi & Manduchi (1998); Zhang & Allebach (2008); Zhang & Gunturk (2008), especially those based on wavelets Chang et al. (2000); H. et al. (2009); Ji & Fermüller (2009); Nasri & Nezamabadi-pour (2009); Yoon & Vaidyanathan (2004) inspired by the remarkable works of Mallat (1989) and after Donoho (1995).

The basic wavelet denoising problem consists in, given an input noisy image, dividing all its wavelet coefficients into relevant (if greater than a critical value) or irrelevant (if less than a critical value) and then process the coefficients from each one of these groups by certain specific rules. Usually, in most denoising applications *soft* and *hard* thresholding are considered, in a way that filtering is performed by comparing each wavelet coefficient to a given threshold and supressing it if its magnitude is less than the threshold; otherwise, it is kept untouched (hard) or shrinked (soft). *Soft-thresholding* rule is generally preferred over *hard-thresholding* for several reasons. First, it has been shown that *soft-thresholding* has several interesting and desirable mathematical properties Donoho (1995), Donoho & Johnstone (1994). Second, in practice, the *soft-thresholding* method yields more visually pleasant images over *hard-thresholding* because the latter is discontinuous and generates abrupt artifacts in the recovered images, especially when the noise energy is significant. Last but not least, some results found in the literature Chang et al. (2000) conclude that the optimal *soft-thresholding* estimator yields a smaller estimation error than the optimal *hard-thresholding* estimator.

However, for some classes of signals and images, *hard-thresholding* results in superior estimates to that of *soft-thresholding*, despite some of its disadvantages Yoon & Vaidyanathan (2004). To tackle this problem, several hybrid thresholding functions have been proposed in the literature.

To test and evaluate our method, we built a series of experiments using both real Nuclear Magnetic Resonance (NMR) images and simulated data, considering several wavelet basis. The obtained results show the effectiveness of *GSAShrink*, indicating a clear improvement on the wavelet denoising performance in comparison to the traditional approaches. As in this chapter we are using a sub-optimal combinatorial optimization algorithm to approximate the optimal MAP solution, *GSAShrink* converges to a local maximum, making our method sensitive to different initializations. What at first could look like a disadvantage, actually revealed to be an interesting and promissing feature, mostly because we can incorporate other non-linear filtering techniques in a really straighforward way, by simply using them to generate better initial conditions for the algorithm. Results obtained by combining Bilateral Filtering and *GSAShrink* show that the MAP-MRF method under investigation is capable of suppressing the noise while preserving most relevant image details, avoiding the appearance of visible artifacts.
The remaining of the chapter is organized as follows. Section 2 describes the Discrete Wavelet Transform (DWT) in the context of digital signal processing, showing that, in practice, this transform can be implemented by a *Perfect Reconstruction Filter Bank* (PRFB), being completely characterized by a pair of *Quadrature Mirror Filters* (QMF), $h_0[]$, a low-pass filter and $g_1[]$, a high-pass filter. Section 3 briefly introduces the wavelet-based denoising problem, describing the proposed MAP-MRF solution, as well as the statistical modeling and threshold estimation, a crucial step in this kind of application. In Section 4 we briefly discuss the MRF Maximum Pseudo-Likelihood parameter estimation. The experimental setup and the obtained results are described in Section 5. Finally, Section 6 brings the our conclusions and final remarks.

2. The Wavelet transform

The basic tool for our MAP-MRF approach is the wavelet transform. Roughly speaking, in mathematical terms, the wavelet transform is an expansion that decomposes a given signal in a basis of orthogonal functions. In this sense, we can set a complete analogy with the Fourier Transform. While the Fourier Transform uses periodic, smooth and unlimited basis functions (i.e., sines and cosines), the wavelet transform uses non-periodic, non-smooth and finite support basis functions (i.e., Haar, Daubechies,...), allowing a much more meaningful representation through multi-resolution analysis, since it can capture a wide . In practice, the Discrete Wavelet Transform (DWT) can be implemented by a Perfect Reconstruction Filter Bank (PRFB), being completely characterized by a pair of Quadrature Mirror Filters (QMF) $h_0[]$, a low-pass filter, and $g_1[]$, the corresponding high-pass filter, known as analysis filters.

2.1 Perfect reconstruction filter banks (PRFB)

This section describes the Discrete Wavelet Transform from a digital signal processing perspective, by characterizing its underlying mathematical model by means of the Z-Transform. For an excellent review on wavelet theory and mathematical aspects of filter banks the reader is refered to Jensen & Cour-Harbo (2001); Strang & Nguyen (1997), from where most results described in this section were taken. A two-channel *perfect reconstruction □lter bank* (PRFB) consists of two parts: an analysis filter bank, responsible for the decomposition of the signal in wavelet sub-bands (DWT) and a synthesis filter bank, that reconstructs the signal by synthesizing these wavelet sub-bands Ji & Fermüller (2009). Figure 1 shows the block diagram of a two-channel PRFB, where $H_0(z)$ and $G_1(z)$ are the Z-transforms of the pair of analysis filters, $r_0[n]$ and $r_1[n]$ are the resulting signals after low-pass and high-pass filtering, respectively, $y_0[n]$ and $y_1[n]$ are the downsampled signals, $t_0[n]$ and $t_1[n]$

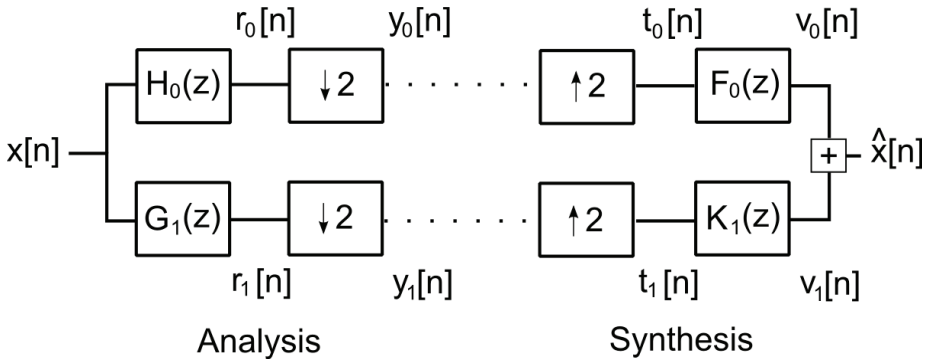

Fig. 1. Block diagram of a two-channel *Perfect Reconstruction Filter Bank*

are the upsampled signals obtained by placing zeros between each pair of samples, $F_0(z)$ and $K_1(z)$ are the Z-transforms of the pair of synthesis filters, and finally, $v_0[n]$ and $v_1[n]$ are interpolated signals that are combined to produce the reconstructed output $\hat{x}[n]$.
The basic assumption for perfect reconstruction is that the output $\hat{x}[n]$ has to be a delayed version of the input signal $x[n]$. Suppose that in the filter bank depicted in Figure 1, we have ℓ levels, each one causing a delay. Then, in mathematical terms, the condition for perfect reconstruction is:

$$\hat{x}[n] = x[n - \ell] \tag{1}$$

which means that the entire system can be replaced by a single transfer function. Equivalently, in the Z-domain we have:

$$\hat{X}(z) = z^{-\ell} X(z) \tag{2}$$

As the filter bank defines a linear time invariant (LTI) system and using the convolution theorem, we have:

$$R_0(z) = H_0(z)X(z) \tag{3}$$
$$R_1(z) = G_1(z)X(z) \tag{4}$$

and using the Z-transform property of decimation operators:

$$Y_0(z) = \frac{1}{2}\left\{R_0\left(z^{1/2}\right) + R_0\left(-z^{1/2}\right)\right\} \tag{5}$$
$$Y_1(z) = \frac{1}{2}\left\{R_1\left(z^{1/2}\right) + R_1\left(-z^{1/2}\right)\right\} \tag{6}$$

leading to the following relationship:

$$Y_0(z) = \frac{1}{2}\left\{H_0(z^{1/2})X(z^{1/2}) + H_0(-z^{1/2})X(-z^{1/2})\right\} \tag{7}$$

$$Y_1(z) = \frac{1}{2}\left\{G_1(z^{1/2})X(z^{1/2}) + G_1(-z^{1/2})X(-z^{1/2})\right\} \tag{8}$$

Since $H_0(z)$ and $G_1(z)$ are not ideal half-band filters, downsampling can introduce aliasing since we cannot reduce the interval between samples by half because we would be sampling below the Nyquist rate. To overcome this problem, conditions for alias cancellation must be enforced. According to the perfect reconstruction condition:

$$V_0(z) + V_1(z) = z^{-\ell}X(z) \tag{9}$$

Using the upsampling property of the Z-transform, we have the following expressions for $V_0(z)$ and $V_1(z)$:

$$V_0(z) = F_0(z)T_0(z) = F_0(z)Y_0(z^2) \tag{10}$$

$$V_1(z) = K_1(z)T_1(z) = K_1(z)Y_1(z^2) \tag{11}$$

which leads to:

$$V_0(z) = \frac{1}{2}F_0(z)\left\{H_0(z)X(z) + H_0(-z)X(-z)\right\} \tag{12}$$

$$V_1(z) = \frac{1}{2}K_1(z)\left\{G_1(z)X(z) + G_1(-z)X(-z)\right\} \tag{13}$$

Thus, grouping similar terms and enforcing the perfect reconstruction condition, we have the following equation that relates the input, analysis filters, synthesis filters and the output of the LTI system:

$$\begin{aligned}&\frac{1}{2}\left\{F_0(z)H_0(z) + K_1(z)G_1(z)\right\}X(z) + \\ &\frac{1}{2}\left\{F_0(z)H_0(-z) + K_1(z)G_1(-z)\right\}X(-z) = z^{-\ell}X(z)\end{aligned} \tag{14}$$

Therefore, a *perfect reconstruction filter bank* must satisfy the following conditions:

1. *Alias cancellation*

$$F_0(z)H_0(-z) + K_1(z)G_1(-z) = 0 \tag{15}$$

2. *Perfect Reconstruction (No distortion)*

$$F_0(z)H_0(z) + K_1(z)G_1(z) = 2z^{-\ell} \tag{16}$$

The first condition is trivially satisfied by defining the synthesis filters as:

$$F_0(z) = G_1(-z) \tag{17}$$
$$K_1(z) = -H_0(-z) \tag{18}$$

This condition implies that:

$$\begin{aligned} F_0(z) &= G_1(-z) \\ &= \sum_{-\infty}^{\infty} g_1[n](-z)^{-n} \\ &= \sum_{-\infty}^{\infty} (-1)^n g_1[n] z^{-n} \end{aligned} \tag{19}$$

and

$$\begin{aligned} K_1(z) &= -H_0(-z) \\ &= -\sum_{-\infty}^{\infty} h_0[n](-z)^{-n} \\ &= \sum_{-\infty}^{\infty} (-1)^{n+1} h_0[n] z^{-n} \end{aligned} \tag{20}$$

so that the synthesis filters coefficients are obtained directly from the analysis filters by a simple alternating signs rule:

$$\begin{aligned} f_0[n] &= (-1)^n g_1[n] \\ k_1[n] &= (-1)^{n+1} h_0[n] \end{aligned} \tag{21}$$

Defining $P_0(z) = F_0(z)H_0(z)$ and using equation (19) on (16) leads to:

$$P_0(z) - P_0(-z) = 2z^{-\ell} \tag{22}$$

where ℓ must be odd since the left hand side of (22) is an odd function, since all even terms cancel each other. Let $P(z) = z^{\ell} P_0(z)$. Then, $P(-z) = -z^{\ell} P_0(-z)$, since ℓ is odd. Rewriting equation (22) we finally have:

$$P(z) + P(-z) = 2 \tag{23}$$

showing that for perfect reconstruction the low-pass filter $P(z)$ requires all even powers to be zero, except the constant term. The design process starts with the specification of $P(z)$ and

then the factorization of $P_0(z)$ into $F_0(z)H_0(z)$. Finally, the alias cancellation condition is used to define $G_1(z)$ and $K_1(z)$. It has been shown that flattest $P(z)$ leads to the widely recognized Daubechies wavelet filter Daubechies (1988).
In this chapter, we consider the traditional 2-D separable DWT, also known as Square Wavelet Transform, that is based on consecutive one dimensional operations on columns and rows of the pixel matrix. The method first performs one step of the 1-D DWT on all rows, yielding a matrix where the left side contains down-sampled low-pass (h filter) coefficients of each row, and the right contains the high-pass (g filter) coefficients. Next, we apply one step to all columns, resulting in four wavelet sub-bands: LL (which is known as approximation signal), LH, HL and HH. A multilevel decomposition scheme can be generated in a straghtforward way, always expanding the approximation signal.
The analysis of a signal or image wavelet coefficients suggests that small coefficients are dominated by noise, while coefficients with a large absolute value carry more signal information. Thus, supressing or smoothing the smallest, noisy coefficients and applying the Inverse Wavelet Transform (IDWT) lead to a reconstruction with the essential signal or image characteristics, removing the noise. More precisely, this idea is motivated by three assumptions Jansen (2001):

- The decorrelating property of a DWT creates a sparse signal, where most coefficients are zero or close to zero.
- Noise is spread out equally over all coefficients and the important signal singularities are still distinguishable from the noise coefficients.
- The noise level is not too high, so that we can recognize the signal wavelet coefficients.

2.2 Wavelet-based denoising

Basically, the problem of wavelet denoising by thresholding can be stated as follows. Let $\mathbf{g} = \left\{ g_{i,j}; i,j = 1,2,\ldots,M \right\}$ denotes the $M \times M$ observed image corrupted by additive Gaussian noise:

$$g_{i,j} = f_{i,j} + n_{i,j} \tag{24}$$

where $f_{i,j}$ is the noise-free pixel, $n_{i,j}$ has a $N(0,\sigma^2)$ distribution and σ^2 is the noise variance. Then, considering the linearity of the DWT:

$$y_{j,k} = x_{j,k} + z_{j,k} \tag{25}$$

with $y_{j,k}$, $x_{j,k}$ and $z_{j,k}$ denoting the k-th wavelet coefficient from the j-th decomposition level of the observed image, original image and noise image, respectively. The goal is to recover the unknown wavelet coefficients $x_{j,k}$ from the observed noisy coefficients $y_{j,k}$. One way to estimate $x_{j,k}$ is through Bayesian inference, by adopting a MAP approach. In this chapter, we introduce a MAP-MRF iterative method based on the combinatorial optimization algorithm *Game Strategy Approach* (GSA) Yu & Berthod (1995a), an alternative to the deterministic and widely known Besag's *Iterated Conditional Modes* (ICM) Besag (1986a). By iterative method we mean that an initial solution $\mathbf{x}^{(0)}$ is given and the algorithm successively improves it, by using the output from one iteration as the input to the next. Thus, the algorithm updates the current wavelet coefficients given a previous estimative according to the following MAP criterion:

$$\hat{x}_{j,k}^{(p+1)} = \boldsymbol{arg\,max}_{x_{j,k}} \left\{ p\left(x_{j,k} | x_{j,k}^{(p)}, y_{j,k}, \vec{\Psi} \right) \right\} \tag{26}$$

where $p\left(x_{j,k}|x_{j,k}^{(p)}, y_{j,k}, \vec{\Psi}\right)$ represents the *a posteriori* probability obtained by adopting a Generalized Gaussian distribution as likelihood (model for observations) and a Generalized Isotropic Multi-Level Logistic (GIMLL) MRF model as *a priori* knowledge (for contextual modeling), $x_{j,k}^{(p)}$ denotes the wavelet coefficient at p-th iteration and $\vec{\Psi}$ is the model parameter vector. This vector contains the parameters that control the behavior of the probability laws. More details on the statistical modeling and how these parameters are estimated are shown in Sections 3 and 4. In the following, we will derive an algorithm for approximating the MAP estimator by iteratively updating the wavelet coefficients.

3. The MAP-MRF framework for bayesian inference

The main problem with MAP-MRF approaches is that there is no analytical solution for MAP estimation. Hence, algorithms for numerically approximating the MAP estimator are required. It has been shown, in combinatorial optimization theory, that convergence to the global maximum of the posterior distribution can be achieved by the *Simulated Annealing* (SA) algorithm Geman & Geman (1984). However, as SA is extremely time consuming and demands a high computational burden, sub-optimal combinatorial optimization algorithms, which yield computationally feasible solutions to MAP estimation, are often used in real problems. Some of the most popular iterative algorithms found in image processing literature are: the widely used Besag's *Iterated Conditional Modes* (ICM) Besag (1986a), *Maximizer of the Posterior Marginals* (MPM) Marroquin et al. (1987a), *Graduated Non-Convexity* (GNC) Blake & Zisserman (1987), *Highest Con□dence First* (HCF) Chou & M. (1990) and *Deterministic Pseudo Annealing* Berthod et al. (1995). In this chapter, we introduce *GSAShrink*, a modified version of an alternative algorithm known as *Game Strategy Approach* (GSA) Yu & Berthod (1995a), based on non-cooperative game theory concepts and originally proposed for solving MRF image labeling problems.

3.1 Statistical modeling

3.1.1 Generalized gaussian distribution

It has been shown that the distribution of the wavelet coefficients within a sub-band can be modeled by a Generalized Gaussian (GG) with zero mean Mallat (1989), Westerink et al. (1991). The zero mean GG distribution has the probability density function:

$$p\left(w|\nu,\beta\right) = \frac{\nu}{2\beta\Gamma\left(1/\nu\right)} exp\left\{-\left(\frac{|w|}{\beta}\right)^{\nu}\right\} \tag{27}$$

where $\nu > 0$ controls the shape of the distribution and β the spread. Two special cases of the GG distribution are the Gaussian and the Laplace distributions. When $\nu = 2$ and $\beta = \sqrt{2}\sigma$, it becomes a standard Gaussian distribution. The Laplace distribution is obtained by setting $\nu = 1$ and $\beta = 1/\lambda$. According to Sharifi & Leon-Garcia (1995), the parameters ν and β can be empirically determined by directing computing the sample moments $\chi = E\left[|w|\right]$ and $\psi = E\left[w^2\right]$ (method of moments), because of this useful relationship:

$$\frac{\psi}{\chi^2} = \frac{\Gamma\left(\frac{1}{\tilde{\nu}}\right)\Gamma\left(\frac{3}{\tilde{\nu}}\right)}{\Gamma^2\left(\frac{2}{\tilde{\nu}}\right)} \tag{28}$$

and we can use a look-up table with different values of ν and determine is value from the ratio ψ/χ^2. After, it is possible to obtain $\hat{\beta}$ by:

$$\hat{\beta} = \frac{\psi\Gamma\left(\frac{1}{\tilde{\nu}}\right)}{\Gamma\left(\frac{3}{\tilde{\nu}}\right)} \tag{29}$$

3.1.2 Generalized isotropic multi-level logistic

Basically, MRF models represent how individual elements are influenced by the behavior of other individuals in their vicinity (neighborhood system). MRF models have proved to be powerful mathematical tools for contextual modeling in several image processing applications. In this chapter, we adopt a model originally proposed in Li (2009) that generalizes both Potts and standard isotropic Multi-Level Logistic (MLL) MRF models for continuous random variables. According to the Hammersley-Clifford theorem any MRF can be equivalently defined by a joint Gibbs distribution (global model) or by a set of local conditional density functions (LCDF's). From now on, we will refer to this model as Generalized Isotropic MLL MRF model (GIMLL). Due to our purposes and also for mathematical tractability, we define the following LCDF to characterize this model, assuming the wavelet coefficients are quantized into $\tilde{M}$ levels:

$$p\left(x_s|\eta_s,\theta\right) = \frac{\exp\left\{-\theta D_s\left(x_s\right)\right\}}{\sum_{y\in G}\exp\left\{-\theta D_s\left(y\right)\right\}} \tag{30}$$

where $D_s(y) = \sum_{k\in\eta_s}\left[1 - 2exp\left(-\left(y - x_k\right)^2\right)\right]$, x_s is the s-th element of the field, η_s is the neighborhood of x_s, x_k is an element belonging to the neighborhood of x_s, θ is a parameter that controls the spatial dependency between neighboring elements, and G is the set of all possible values of x_s, given by $G = \{g \in \Re / m \leq g \leq M\}$, where m and M are respectively, the minimum and maximum sub-band coefficients, with $|G| = \tilde{M}$ (cardinality of the set). This model provides a probability for a given coefficient depending on the similarity between its value and the neighboring coefficient values. Acording to Li (2009), the motivation for this model is that it is more meaningful in texture representation and easier to process than the isotropic MLL model, since it incorporates similarity in a softer way.

For GIMLL MRF model parameter estimation we adopt a Maximum Pseudo-Likelihood (MPL) framework that uses the observed Fisher information to approximate the asymptotic variance of this estimator, which provides a mathematically meaningful way to set this regularization parameter based on the observations. Besides, the MPL framework is useful in assessing the accuracy of MRF model parameter estimation.

3.2 Game strategy approach

In a n-person game, $I = \{1, 2, \ldots, n\}$ denotes the set of all players. Each player i has a set of pure strategies S_i. The game process consists in, at a given instant, each player choosing a strategy $s_i \in S_i$. Hence, a situation (or play) $\mathbf{s} = (s_1, s_2, \ldots, s_n)$ is yielded, and a payoff $H_i(\mathbf{s})$ is assigned to each player. In the approach proposed by Yu & Berthod (1995a), the payoff $H_i(\mathbf{s})$ of a player is defined in such a way that it depends only on its own strategy and on the set of strategies of neighboring players.

In non-cooperative game theory each player tries to maximize his payoff by choosing his own strategy independently. In other words, it is the problem of maximizing the global payoff through local and independent decisions, similar to what happens in MAP-MRF applications with the conditional independence assumption.

A mixed strategy for a player is a probability distribution defined over the set of pure strategies. In GSA, it is supposed that each player knows all possible strategies, as well as the payoff given by each one of them. Additionally, the solutions for a non-cooperative n-person game are given by the set of points satisfying the Nash Equilibrium condition (or *Nash points*). It has been shown that Nash Equilibrium points always exist in non-cooperative n-person games Nash (1950). A play $\mathbf{t}^* = \left(t_1^*, t_2^*, \ldots, t_n^*\right)$ satisfies the Nash Equilibrium condition if none of the players can improve you payoff by changing his strategy unilaterally, or in mathematical terms:

$$\forall i : H_i\left(\mathbf{t}^*\right) = max_{s_i \in S_i} H_i\left(\mathbf{t}^* || \mathbf{t}\right) \tag{31}$$

where $\mathbf{t}^* || \mathbf{t}$ is the play obtained by replacing $\mathbf{t}^*$ by $\mathbf{t}$.
The connection between game theory and combinatorial optimization algorithms is demonstrated in Yu & Berthod (1995a). It has been proved that the GSA algorithm fundamentals are based on two major results that states the equivalence between MAP-MRF estimation and non-cooperative games Yu & Berthod (1995a):

Theorem 3.1. (MAP-MRF Nash Points Equivalence Theorem) *The set of local maximum points of the a posteriori probability in MAP-MRF image labeling problems is identical to the set of Nash equilibrium points of the corresponding non-cooperative game.*

Theorem 3.2. (GSA Convergence Theorem) *The GSA algorithm converges to a Nash point in a finite number of iterations, given an arbitrary initial condition.*

Actually, a complete analogy between game theory and the wavelet denoising problem can be made, since the wavelet denoising process can be thought as being a generalization of image labeling, where instead of discrete labels, the unknown coefficients are continuous random variables. In Table 1 we show how concepts of non-cooperative game theory and our algorithm are in fact closely related.

Wavelet Denoising	Game Theory
sub-band lattice	n-person game structure
sub-band elements	players
wavelet coefficients	pure strategies
an entire sub-band at p-th iteration	a play or situation
posterior distribution	payoff
local conditional densities	mixed strategies
local maximum points (MAP)	Nash equilibrium points

Table 1. Correspondence between concepts of game theory and the MAP-MRF wavelet denoising approach.

3.3 GSAShrink for wavelet denoising

Given the observed data $\mathbf{y}$ (noisy image wavelet coefficients), and the estimated parameters for all the sub-bands $\vec{\Psi}_r = \left\{\hat{v}_r, \hat{\beta}_r, \hat{\theta}_r\right\}, r = 1, \ldots, S$, where S is the total number of sub-bands in the decomposition, our purpose is to recover the optimal wavelet coefficient field $\mathbf{x}^*$ using a Bayesian approach. As the number of possible candidates for $\mathbf{x}^*$ is huge, to make the problem computationally feasible, we adopt an iterative approach, where the wavelet coefficient field

at a previous iteration, let's say $\mathbf{x}^{(p)}$, is assumed to be known. Hence, the new wavelet coefficient $x_{j,k}^{(p+1)}$ can be obtained by:

$$x_{j,k}^{(p+1)} = \boldsymbol{argmax}_{x_{j,k}} \left\{ log\ p\left(x_{j,k} | \mathbf{x}^{(p)}, y_{j,k}, \vec{\Psi}_j\right)\right\} \tag{32}$$

Basically, *GSAShrink* consists in, given an initial solution, improve it iteratively by scanning all wavelet coefficients sequentially until the convergence of the algorithm or until a maximum number of iterations is reached. In this manuscript, we are setting the initial conditions as the own noisy image wavelet sub-band, that is, $\mathbf{x}^{(0)} = \mathbf{y}$, although some kind of previous preprocessing may provide better initializations. Considering the statistical modeling previously described, we can define the following approximation:

$$log\ p\left(x_{j,k} | \mathbf{x}^{(p)}, y_{j,k}, \vec{\Psi}_j\right) \propto log\left(\frac{\hat{v}_j}{2\hat{\beta}_j \Gamma\left(\frac{1}{\hat{v}_j}\right)}\right) - \tag{33}$$

$$\left[\frac{\left|y_{j,k}\right|}{\hat{\beta}_j}\right]^{\hat{v}_j} - \hat{\theta}_j \sum_{(\ell \in \eta_{j,k})} \left[1 - 2exp\left(-\left(x_{j,k}^{(p)} - x_{j,\ell}^{(p)}\right)^2\right)\right]$$

Therefore, we can define the following rule for updating the wavelet coefficient $x_{j,k}^{(p)}$, based on minimizing the negative of each player payoff, denoted by $H_{j,k}\left(\mathbf{x}, \mathbf{y}, \vec{\Psi}_j\right)$, considering $\mathbf{x}^{(0)} = \mathbf{y}$:

$$x_{j,k}^{(p+1)} = \boldsymbol{argmin}_{x_{j,k}} \left\{ H_{j,k}\left(\mathbf{x}, \mathbf{y}, \vec{\Psi}_j\right)\right\} \tag{34}$$

where

$$H_{j,k}\left(\mathbf{x}, \mathbf{y}, \vec{\Psi}_j\right) = \tag{35}$$

$$\left[\frac{\left|x_{j,k}\right|}{\hat{\beta}_j}\right]^{\hat{v}_j} + \hat{\theta}_j \sum_{(\ell \in \eta_{j,k})} \left[1 - 2exp\left(-\left(x_{j,k}^{(p)} - x_{j,\ell}^{(p)}\right)^2\right)\right]$$

The analysis of the above functional (the payoff of each player), reveals that while the first term favors low valued strategies (coefficients near zero), since the mean value of wavelet coefficients in a sub-band is zero, the MRF term favors strategies that are similar to those belonging to the neighborhood (coefficients close to the neighboring ones), defining a tradeoff between supression and smoothing, or hard and soft thresholding. In this scenario, the MRF model parameter plays the role of a regularization parameter, since it controls the compromisse between these two extreme behavior. Thus, our method can be considered a hybrid adaptive approach since identical wavelet coeficients belonging to different regions of a given sub-band are modified by completely different rules. In other words, coefficients belonging to smooth regions tend to be more attenuated than those belonging to coarser regions. In the following, we present the *GSAShrink* algorithm for wavelet-based image denoising.

ALGORITHM: GSAShrink for wavelet denoising

Require: The S sub-bands of the wavelet decomposition (LH_1, HL_1, HH_1, ...), a payoff function ($H_{j,k}$), the probability of acceptance of new strategies (α), the attenuation parameter for noisy coefficients (β), the gain parameter for relevant image coefficients (γ), the threshold (T) and the number of iterations (MAX).

Ensure: Shrinked wavelet sub-bands

while $p \leq MAX$ **do**
  for $j = 1$ to S **do**
    for $k = 1$ to $L(j)$ **do** {$L(j)$: size of current sub-band}
      $x^*_{j,k} = argmin_{x_{j,k}} \left\{ H_{j,k} \left(\mathbf{x}, \mathbf{y}, \vec{\Psi}_j \right) \right\}$
      if $\left(H\left(x^*_{j,k}\right) \leq H\left(x^{(p)}_{j,k}\right) \right)$ **then**
        if $\left(\left| x^{(p)}_{j,k} \right| \geq T \right)$ or $\left(max \left\{ \left| \eta_{j,k} \right| \right\} \geq T \right)$ **then**
          $x^{(p+1)}_{j,k} = x^{(p)}_{j,k} \times (1+\gamma)$
        else
          $x^{(p+1)}_{j,k} = x^*_{j,k}$ w. p. α;
          Otherwise,
            $x^{(p+1)}_{j,k} = x^{(p)}_{j,k} \times (1-\beta)$ w. p. $(1-\alpha)$;
        end if
      end if
    end for
  end for
end while

It is interesting to note that an observation can be set forward to explain why there are a large number of "small" coefficients but relatively few "large" coefficients as the GGD suggests: the small ones correspond to smooth regions in a image and the large ones to edges, details or textures Chang et al. (2000). Therefore, the application of the derived MAP-MRF rule in all sub-bands of the wavelet decomposition removes noise in an adaptive manner by smoothing the wavelet coeficients in a selective way.

Basically, the *GSAShrink* algorithm works as follows: for each wavelet coefficient, the value that maximizes the payoff is chosen and the new payoff is calculated. If this new payoff is less than the original one, then nothing is done (since in the Nash equilibrium none of the playes can improve its payoff by uniterally changing its strategy). Otherwise, if the absolute value of the current wavelet coefficient $x_{j,k}$ or any of its neighbors is above the threshold T, which means that we are probably dealing with relevant image information such as edges or fine details, then $x_{j,k}$ is amplified by a factor of $(1+\gamma)$. The goal of this procedure is to perform some image enhancement during noise removal. However, if its magnitude is less a threshold, then the new coefficient $x^*_{j,k}$ is accepted with probability α, which is a way to smooth the wavelet coefficients since we are employing the MAP-MRF functional given by equation (35). The level of suppression/shrinkage depends basically on two main issues: the contextual information and the MRF model parameter, that controls the tradeoff between suppression and smoothing. On the other hand, with probability $(1-\alpha)$ the coefficient is attenuated by a constant factor of $(1-\beta)$, since we are probably facing a noise coefficient. It is worthwhile to note that the only parameter originally existing in the traditional GSA algorithm for image labeling problems is α, that controls the probability of acceptance of new strategies. Both β

and γ parameters have been included to better represent the nature of our problem. Also, in all experiments thoughout this chapter, we have adopted the following parameter values: $\alpha = 0.9$, $\beta = 0.1$, $\gamma = 0.05$ and $MAX = 5$.

3.4 Wavelet thresholds

As we have seen, a critical issue in the method is the choice of the thresholding value. Several works in the wavelet literature discuss threshold estimation Chang et al. (2000); Jansen & Bultheel (1999). In the experiments throughout this chapter we adopted four different wavelet thresholdings: universal Donoho (1995); Donoho et al. (1995), SURE Jansen (2001), Bayes and Oracle thresholds Chang et al. (2000).

3.4.1 Universal threshold

Despite its simplicity, it has been shown that the Universal Threshold has some optimal asymptotic properties Donoho (1995); Donoho & Johnstone (1994). The Universal Threshold is obtained by the following expression:

$$\lambda_{UNIV} = \sqrt{2logN\sigma^2} \tag{36}$$

where N is the number of data points and σ^2 denotes the noise variance. Thus, the Universal Threshold does not depend directly on the observed input signal, but only on simple statistics derived from it.

3.4.2 SURE threshold

The SURE (*Steins's Unbiased Risk Estimator*) threshold is obtained by minimizing a risk function $R(.)$, assuming the coefficients are normally distributed Hudson (1978); Stein (1981). In this chapter, we use the approximation for $R(.)$ derived in Jansen (2001) and given by:

$$R(\lambda) = \left[\frac{1}{N}\left\|\omega_\lambda - \omega\right\|^2 - \sigma^2\right] + \left[2\sigma^2\frac{(N - N_0)}{N}\right] \tag{37}$$

where N is the number of wavelet coefficients, σ^2 is the noise variance, ω_λ and ω denote the wavelet coefficients before and after thresholding, respectively, and N_0 is number of null wavelet coefficients after thresholding. The SURE threshold λ_{SURE}, is defined as the one that minimizes $R(\lambda)$, that is:

$$\lambda_{SURE} = \boldsymbol{argmin}_\lambda \left\{R(\lambda)\right\} \tag{38}$$

Analyzing the expression we can see that this method for threshold estimation seeks a tradeoff between data fidelity and noise removal.

3.4.3 Bayes threshold

The Bayes Threshold is a data-driven threshold derived in Bayesian framework by using a generalized Gaussian distribution as prior for the wavelet coefficients. It is a simple and closed-form threshold that is obtained in a sub-band adaptive way by Chang et al. (2000):

$$\lambda_{BAYES} = \frac{\hat{\sigma}^2}{\hat{\sigma}_x} \tag{39}$$

where

$$\hat{\sigma}_x = \sqrt{max\left(\hat{\sigma}_y^2 - \hat{\sigma}^2, 0\right)} \tag{40}$$

$$\hat{\sigma}_y^2 = \frac{1}{N^2}\sum_{1}^{N} y_i^2 \tag{41}$$

$$\hat{\sigma} = \frac{Median\left(|y_i|\right)}{0.6745} \tag{42}$$

It is worth mentioning that in case of $\hat{\sigma}^2 > \hat{\sigma}_y^2$, $\hat{\sigma}_x$ is taken to be zero, implying that $\lambda_{BAYES} = \infty$, which means, in practice, that all coefficients within the sub-band are suppressed.

3.4.4 Oracle thresholds

The Oracle Thresholds are the theoretic optimal sub-band adaptive thresholds in a MSE sense, assuming the original image is known, a condition that obviously is possible only in simulations. The *OracleShrink* threshold is defined as:

$$\lambda_S^* = \boldsymbol{argmin}_\lambda \left\{ \sum_{k=1}^{N} \left(\eta_\lambda\left(y_k\right) - x_k\right)^2 \right\} \tag{43}$$

where N is the number of wavelet coefficients in the sub-band, η_λ denotes the soft thresholding operator and x_k is the *k-th* coefficient of the original image. Similarly, the *OracleThresh* threshold is given by:

$$\lambda_H^* = \boldsymbol{argmin}_\lambda \left\{ \sum_{k=1}^{N} \left(\psi_\lambda\left(y_k\right) - x_k\right)^2 \right\} \tag{44}$$

where ψ_λ denotes the hard threshold operator.

4. Statistical inference on MRF models

With advances on probability and statistics, such as the remarkable Hammersley-Clifford Theorem Hammersley & Clifford (1971), which states the Gibbs-Markov equivalence, Bayesian inference and the development of Markov Chain Monte Carlo simulation methods (MCMC) Metropolis et al. (1953), Geman & Geman (1984), Swendsen & Wang (1987), Wolff (1989) together with combinatorial optimization algorithms to solve numerical maximization of complex high dimensional functions Besag (1986b), Marroquin et al. (1987b), Yu & Berthod (1995b), Markov Random Fields became a central topic in a variety of research fields including pattern recognition, game theory, computer vision and image processing. Those important contributions have led to a huge number of novel methodologies and techniques in statistical applications, especially those regarding contextual modeling and spatial data analysis.
However, in most applications the MRF model parameters are still chosen by trial-and-error through simple manual adjustments Solberg (2004), Wu & Chung (2007). Therefore, statistical inference on several MRF models remains an open problem. The main reason is that the most general estimation method, maximum likelihood (ML), is computationally intractable. An alternative solution proposed by Besag (1974) is to use the local conditional density functions (LCDF) to perform Maximum Pseudo-Likelihood (MPL) estimation.

4.1 Maximum pseudo-likelihood estimation

This section briefly describes the MLP estimation of the Generalized isotropic MLL parameter model θ, given by equation (30). Basically, our motivations for this approach are:

- MPL estimation is a computationally feasible method.
- From a statistical perspective, MPL estimators have a series of desirable properties, such as consistency and asymptotic normality Jensen & Künsh (1994), Winkler (2006).

In recent works found in MRF literature, analytical pseudo-likelihood equations for Potts MRF model on higher-order neighborhood systems have been derived Levada et al. (2008c), showing the importance of MRF parameter estimation assessment. In the experiments along this chapter, the proposed methodology is based on the approximation for the asymptotic variance of the Potts MRF model reported in Levada et al. (2008b) and Levada et al. (2008a).

4.1.1 Pseudo-likelihood equation

The main advantage of maximum pseudo-likelihood estimation is its mathematical tractability and computational simplicity. The pseudo-likelihood function for the Generalized Potts MRF model is defined as:

$$PL(X;\theta) = \prod_{s=1}^{N} \frac{\exp\{-\theta D_s(x_s)\}}{\sum_{y\in G}\exp\{-\theta D_s(y)\}} \tag{45}$$

where N denotes the number of elements on the field.
Taking the logarithms, differentiating on the parameter and setting the result to zero, lead to the following expression (pseudo-likelihood equation):

$$\sum_{s=1}^{N}\left[\frac{\sum_{y\in G} D_s(y)\, exp\{-\theta D_s(y)\}}{\sum_{y\in G} exp\{-\theta D_s(y)\}}\right] = \sum_{s=1}^{N} D_s(x_s) \tag{46}$$

In the experiments, the solution is obtained by finding the zero of the resultant equation. We chose the Brent's method Brent (1973), a numerical algorithm that does not require the computation (or even the existence) of derivatives. The advantages of this method are: it uses a combination of bisection, secant, and inverse quadratic interpolation methods, leading to a very robust approach. Besides, it has superlinear convergence rate.

4.2 Bilateral filtering

Bilateral Filtering (BF) is a noniterative and local non-linear spatial domain filtering technique that originally was proposed as an intuitive tool Tomasi & Manduchi (1998) but later has showed to be closely related to classical partial differential equation based methods, more precisely, anisotropic diffusion Barash (2002); Dong & Acton (2007); Elad (2002). The basic idea of bilateral filtering is to use a weighted average of degraded pixels to recover the original pixel by combining a low-pass function (h_D) and a edge stoping function (h_P) according to the following relationship:

$$\hat{f}[i,j] = \frac{\sum_{(k,n)\in\Omega_{i,j}} h_D[k,n]h_P[k,n]g(k,n)}{\sum_{(k,n)\in\Omega_{i,j}} h_D[k,n]h_P[k,n]} \tag{47}$$

where $\Omega_{i,j}$ is a $(2N+1)\times(2N+1)$ window centered at (i,j) and

$$h_D[k,n] = exp\left\{-\frac{(k-i)^2+(n-j)^2}{2\sigma_D^2}\right\} \tag{48}$$

$$h_P[k,n] = exp\left\{-\frac{(g[k,n]-g[i,j])^2}{2\sigma_P^2}\right\} \tag{49}$$

where the parameters σ_D and σ_P control the effect of the spatial and radiometric weight factors. The first weight, h_D, measures the geometric distance between the central pixel and each one of its neighbors, in a way that the nearest samples have more influence on the final result than the distant ones. The second weight, h_P, penalizes the neighboring pixels that vary greatly in intensity from the central pixel, in a way that the larger the difference, the smaller will be the pixel's contribution during the smoothing. In all experiments along this chapter, we set $N = 2$ (5×5 window), $\sigma_D^2 = 1$ and $\sigma_P^2 = 0.1$.

Basis	**Metrics**			
		Soft	Hard	*GSAShrink*
HAAR	ISNR	-0.8484	0.4388	0.5823
	PSNR	25.613	27.032	27.777
	SSIM	0.8012	0.8625	**0.8903**
DB4	ISNR	0.4864	1.6952	2.2662
	PSNR	27.067	28.705	29.365
	SSIM	0.8598	0.9017	**0.9108**
SYM4	ISNR	0.6580	1.8093	2.3455
	PSNR	27.257	28.662	29.266
	SSIM	0.8639	0.9001	**0.9113**
BIOR6.8	ISNR	0.8336	1.9868	2.587
	PSNR	27.549	28.856	29.829
	SSIM	0.8655	0.8981	**0.9176**

Table 2. Performance of wavelet denoising algorithms on Lena image corrupted by additive Gaussian noise (PSNR = 26.949 dB) using the Universal Threshold.

5. Experiments and results

In order to test and evaluate the *GSAShrink* algorithm for wavelet-based image denoising, we show the results of some experiments performed by using both simulated and real noisy image data:

- Lena image corrupted by gaussian noise.
- Real Nuclear Magnetic Resonance (NMR) images from primate brains (marmosets and brown capuchin monkeys).

In all experiments the wavelet thresholds were estimated in a sub-band adaptive way, which means that we used a different threshold λ_j, $j = 1, 2, \ldots, 6$, for each sub-band, except the LL_2 (approximation), since we are using a Level-2 wavelet decomposition, resulting in the six details sub-bands known as LL_2, LH_2, HL_2,HH_2, LH_1,HL_1 and HH_1. Also, in all experiments, we compared the performance of *GSAShrink* against *soft* and *hard-thresholding* techniques, by using several wavelet basis: *Haar*, *Daubechies4*, *Symlet4* and *Biorthogonal6.8*, a kind of

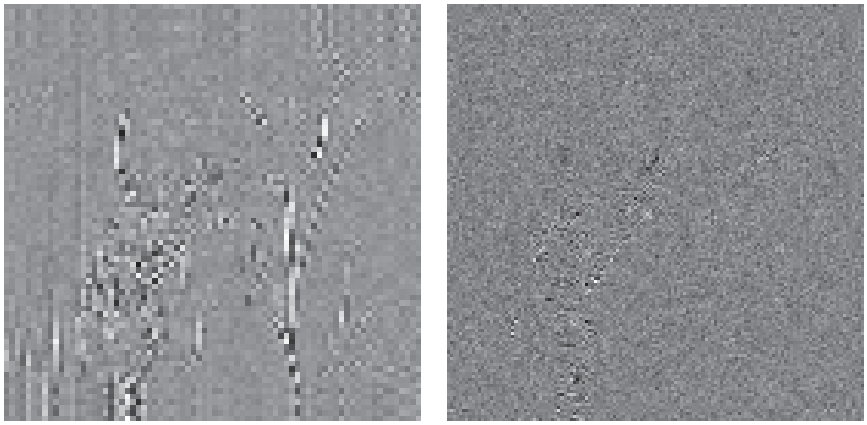

(a) LHL wavelet subband. (b) HH wavelet subband.

Fig. 2. HL_2 and HH_1 wavelet sub-bands for the Lena image: (a) a more homogeneous situation ($\theta = 1.1754$) and (b) a more heterogeneous case ($\theta = 0.9397$), defined by statistically different MRF parameter values.

wavelet transform that has filters with symmetrical impulse response, that is, linear phase filters. The motivation for including Biorthogonal wavelets is that it has been reported that in image processing applications filters with non-linear phase aften introduce visually annoying artifacts in the denoised images.

To perform quantitative analysis of the obtained results, we compared several metrics for image quality assessment. In this manuscript, we selected three different metrics that are: Improvement in Signal-To-Noise-Ratio (ISNR), Peak Signal-To-Noise Ratio (PSNR) and Structural Similarity Index (SSIM), since MSE based metrics have proved to be inconsistent with the human eye perception Wang & Bovik (2009).

Sub-band	$\hat{\theta}_{MPL}$	$\hat{\sigma}_n^2(\hat{\theta}_{MPL})$
LH_2	1.1441	3.1884×10^{-6}
HL_2	1.1754	9.1622×10^{-6}
HH_2	1.0533	1.8808×10^{-5}
LH_1	0.9822	6.2161×10^{-6}
HL_1	0.9991	7.3409×10^{-6}
HH_1	0.9397	4.5530×10^{-6}

Table 3. MPL estimators for θ and asymptotic variances for the Lena image wavelet sub-bands.

Table 2 shows the results for *GSAShrink* denoising on the Lena image, corrupted by additive Gaussian noise ($PSNR = 26.949$ dB). Table 3 shows the estimated regularization MRF parameters and their respective asymptotic variances for each one of the details sub-bands. Figure 2 shows the HL_2 and HH_1 sub-bands of wavelet decomposition. Note that the coarser a sub-band, the smaller is the regularization parameter, indicating that suppression is favored over smoothing, forcing a more intense noise removal.

Analyzing the results, we see that *GSAShrink* had superior performance in all cases. Furthermore, the best result was obtained by using *GSAShrink* with Biorthogonal 6.8 wavelets. To illustrate these numerical results, Figure 3 shows some visual results for the best performances.

(a) Noisy Lena. (b) Soft-Threshold.

(c) Hard Threshold. (d) GSAShrink.

Fig. 3. Visual results for wavelet denoising using Biorthogonal6.8 wavelets with sub-band adaptive Universal threshold (Table 2): (a) Noisy Lena; (b) Soft-Threshold; (c) Hard-Threshold; (d) GSAShrink.

The same experiment was repeated by considering other threshold estimation methods. The use of SURE and Bayes thresholds improved the denoising performance, as indicate Table 4. As the use of Biothogonal6.8 wavelets resulted in uniformly superior performances, from now on we are omitting the other wavelet filters. Figure 4 shows the visual results for the best results (SURE).

As *GSAShrink* iterativelly converges to local maxima solutions, we performed an experiment to illustrate the effect of using different initializations on the final result by combining spatial domain (*Bilateral Filtering*) and wavelet-domain (*GSAShrink*) non-linear filtering. If instead of considering the observed noisy image directly as input to our algorithm, we use the result of *Bilateral Filtering*, the performance can be further improved. Table 5 shows a comparison between simple *Bilateral Filtering* and the combined approach. Figure 5 shows that the use of

Threshold	Metrics			
		Soft	Hard	*GSAShrink*
SURE	ISNR	2.0235	2.8836	3.3458
	PSNR	28.702	29.641	30.441
	SSIM	0.8918	0.8991	0.9270
Bayes	ISNR	2.8511	1.2721	3.2280
	PSNR	29.433	28.270	29.880
	SSIM	0.8942	0.8306	0.9157
Oracle	ISNR	3.3713	2.7318	3.6411
	PSNR	30.045	29.586	30.609
	SSIM	0.9103	0.8964	0.9277

Table 4. Performance of wavelet denoising algorithms on Lena image corrupted by additive Gaussian noise (PSNR = 26.949 dB) using the SURE, Bayes and Oracle thresholds with Biorthogonal6.8 wavelets.

(a) Noisy Lena. (b) Soft-Threshold.

(c) Hard-Threshold. (d) GSAShrink.

Fig. 4. Visual results for wavelet denoising using Biorthogonal6.8 wavelets with sub-band adaptive SURE threshold (Table 4): (a) Noisy Lena; (b) Soft-Threshold; (c) Hard-Threshold; (d) GSAShrink.

Bilateral Filtering in the generation of initial conditions to the *GSAShrink* algorithm prevents the appearance of visible artifacts that are usually found in wavelet-based methods.

Metric	BF	*GSAShrink*	BF + *GSAShrink*
ISNR	4.6211	3.2280	4.6912
PSNR	31.149	29.880	31.481
SSIM	0.9142	0.9157	0.9310

Table 5. Results of using Bilateral Filtering to generate better initial conditions to our MAP-MRF approach.

Sub-band	$\hat{\theta}_{MPL}$	$\hat{\sigma}_n^2(\hat{\theta}_{MPL})$
LH_2	0.8066	2.4572×10^{-5}
HL_2	0.8898	3.7826×10^{-5}
HH_2	0.7338	1.0153×10^{-5}
LH_1	0.7245	3.9822×10^{-5}
HL_1	0.7674	5.8675×10^{-5}
HH_1	0.6195	4.4578×10^{-5}

Table 6. MPL estimators for θ and asymptotic variances for the NMR image wavelet sub-bands.

5.1 Results on real image data

Additionally to the simulations, we have performed some experiments on real NMR image data to test and evaluate *GSAShrink*. The NMR images considered here are from primate brains (both marmosets and brown capuchin monkeys) and were acquired by the CInAPCe project, an abbreviation for the Portuguese expression "Inter-Institutional Cooperation to Support Brain Research" a Brazilian research project that has as main purpose the establishment of a scientific network seeking the development of neuroscience research through multidisciplinary approaches. In this sense, image processing can contribute to the development of new methods and tools for analyzing magnetic resonance imaging and its integration with other methodologies in the investigation of brain diseases.

Figure 6 shows some visual results for NMR image denoising. Analyzing the results, it is possible to see that *GSAShrink* acts more like *soft-thresholding* in homogeneous areas and more like *hard-thresholding* in regions with a lot of details. Table 6 shows the estimated regularization MRF parameters and their respective asymptotic variances for each one of the details sub-bands. Figure 7 shows the subbands HL_2 and HH_1.

6. Conclusion

In this chapter, we investigated a novel MAP-MRF iterative algorithm for wavelet-based image denoising (*GSAShrink*). Basically, it uses the Bayesian approach and game-theoretic concepts to build a flexible and general framework for wavelet shrinkage. Despite its simplicity, *GSAShrink* has demonstrated to be efficient in edge-preserving image filtering. The Generalized Gaussian distribution and a GIMLL MRF model were combined to derive a payoff function which provides a rule for iterativelly update the current value of a wavelet coefficient. This was, to the best of our knowledge, the first time these two models were combined for this purpose. Also, we have shown that in this scenario, the MRF model parameter plays the same role of a regularization parameter, since it controls the tradeoff between supression and atenuation, defining a hybrid approach.

Experiments with both simulated and real NMR image data provided good results that were validated by several quantitative image quality assessment metrics. The obtained results

(a) Original Lena. (b) Bilateral Filtering (BF).

(c) GSAShrink. (d) BL + GSAShrink.

Fig. 5. Results for wavelet denoising using combination of *Bilateral Filtering* and our MAP-MRF approach (Table 5): (a) Original Lena; (b) Bilateral Filtering (BF); (c) GSAShrink; (d) Bilateral Filtering + GSAShrink.

indicated a significant improvement in the denoising performance, showing the efectiveness of the proposed method.

Future works may include the use and investigation of more wavelet decomposition levels, other kinds of wavelet transforms, such as wavelet packets and undecimated or stationary transforms, as well as the filtering of other kinds of noise such as multiplicative speckle and signal-dependent Poisson noise (by using the Anscombe Transform). Finally, we intend to proposed and study the viability of other combinatorial optimization shrinkage methods as *ICMShrink* and *MPMShrink*, based on modified versions of ICM and MPM algorithms respectively. Regarding the influence of the initial conditions on the final result, we believe that the use of multiple initializations instead of a single one, together with information fusion techniques, can further improve the denoising performance, particularly in multiframe image filtering/restoration or video denoising, where several frames from the same scene are available and only the noise changes from one frame to another.

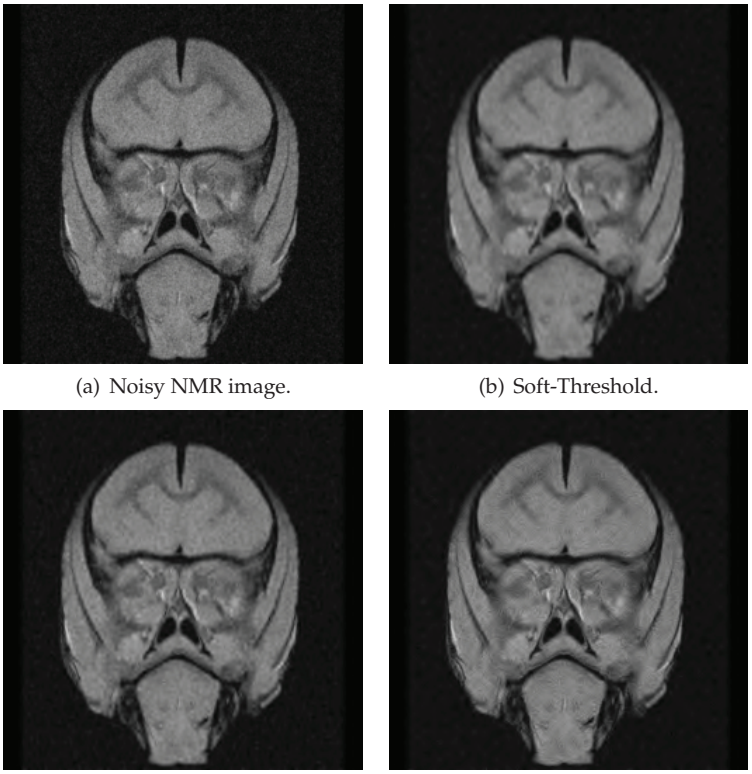

(a) Noisy NMR image. (b) Soft-Threshold.

(c) Hard-Threshold. (d) BL + GSAShrink.

Fig. 6. Results for wavelet denoising on real NMR marmoset brain image data: (a) Noisy NMR image; (b) Soft-Threshold; (c) Hard-Threshold; (d) Bilateral Filtering + GSAShrink.

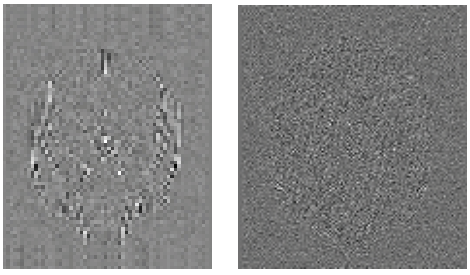

(a) LHL subband. (b) HH subband.

Fig. 7. HL_2 and HH_1 wavelet sub-bands for the NMR image: (a) a more homogeneous situation ($\theta = 0.8898$) and (b) a more heterogeneous case ($\theta = 0.6195$), defined by statistically different MRF parameter values.

7. References

Barash, D. (2002). A fundamental relationship between bilateral filtering, adaptive smoothing and the nonlinear diffusion equation, *IEEE Transactions on Pattern Analysis and Machine Intelligence* 24(6): 844–847.

Berthod, M., Kato, Z. & Zerubia, J. (1995). Dpa: Deterministic approach to the map problem, *IEEE Transactions on Image Processing* 4(9): 1312–1314.

Besag, J. (1974). Spatial interaction and the statistical analysis of lattice systems, *Journal of the Royal Statistical Society - Series B* 36: 192–236.

Besag, J. (1986a). On the statistical analysis of dirty pictures, *Journal of the Royal Statistical Society B* 48(3): 192–236.

Besag, J. (1986b). On the statistical analysis of dirty pictures, *Journal of Royal Statistical Society Series B* 48(3): 259–302.

Blake, A. & Zisserman, A. (1987). *Visual Reconstruction*, MIT Press.

Brent, R. (1973). *Algorithms for minimization without derivatives*, Prentice Hall.

Chang, S. G., Yu, B. & Vetterli, M. (2000). Adaptive wavelet thresholding for image denoising and compression, *IEEE Trans. on Image Processing* 9(9): 1532–1546.

Chou, P. B. & M., B. C. (1990). The theory and practice of bayesian image labeling, *International Journal of Computer Vision* 4: 185–210.

Daubechies, I. (1988). Orthonormal bases of compactly supported wavelets, *Communications on Pure and Applied Mathematics* 41(7): 909–996.

Dong, G. & Acton, S. T. (2007). On the convergence of bilateral filter for edge-preserving image smoothing, *IEEE Signal Processing Letters* 14(9): 617–620.

Donoho, D. L. (1995). De-noising by soft-thresholding, *IEEE Trans. on Information Theory* 41(3): 613–627.

Donoho, D. L. & Johnstone, I. M. (1994). Ideal spatial adaptation via wavelet shrinkage, *Biometrika* 81: 425–455.

Donoho, J., Johnstone, I. M., Kerkyacharian, G. & Picard, D. (1995). Wavelet shrinkage: Asymptopia ?, *Journal of the Royal Statistical Society B* 52(2): 301–369.

Elad, M. (2002). On the origin of the bilateral filtering and ways to improve it, *IEEE Transactions on Image Processing* 11(10): 1141–1151.

Geman, S. & Geman, D. (1984). Stochastic relaxation, Gibbs distributions, and the Bayesian restoration of images, *IEEE Trans. on Pattern Analysis Machine Intelligence* 6(6): 721–741.

H., Y., Zhao, L. & Wang, H. (2009). Image denoising using trivariate shrinkage filter in the wavelet domain and joint bilateral filter in the spatial domain, *IEEE Transactions on Image Processing* 18(10): 2364–2369.

Hammersley, J. & Clifford, P. (1971). Markov field on finite graphs and lattices. unpublished.

Hudson, H. M. (1978). A natural identity for exponential families with applications in multiparameter estimation, *Annals of Statistics* 6(3): 473–484.

Jansen, A. & Bultheel, A. (1999). Multiple wavelet threshold estimation by generalized crossvalidation for images with correlated noise, *IEEE Transactions on Image Processing* 8(7): 947–953.

Jansen, M. (2001). *Noise reduction by wavelet thresholding*, Springer-Verlag.

Jensen, A. & Cour-Harbo, A. (2001). *Ripples in Mathematics*, Springer-Verlag Berlin.

Jensen, J. & Künsh, H. (1994). On asymptotic normality of pseudo likelihood estimates for pairwiseinteraction processes, *Annals of the Institute of Statistical Mathematics* 46(3): 475–486.

Ji, H. & Fermüller, C. (2009). Robust wavelet-based super-resolution reconstruction: Theory and algorithm, *IEEE Transactions on Pattern Analysis and Machine Intelligence* 31(4): 649–660.

Levada, A. L. M., Mascarenhas, N. D. A. & Tannús, A. (2008a). A novel pseudo-likelihood equation for potts mrf model parameter estimation in image analysis, INTERNATIONAL CONFERENCE ON IMAGE PROCESSING, ICIP, 15., 2008, San Diego. *Proceedings...*, IEEE, San Diego/CA, pp. 1828–1831.

Levada, A. L. M., Mascarenhas, N. D. A. & Tannús, A. (2008b). On the asymptotic variances of gaussian markov random field model hyperparameters in stochastic image modeling, INTERNATIONAL CONFERENCE ON PATTERN RECOGNITION, ICPR, 19., 2008, Tampa. *Proceedings...*, IEEE, Tampa/FL, pp. 1–4.

Levada, A., Mascarenhas, N. & Tannús, A. (2008c). Pseudolikelihood equations for potts mrf model parameter estimationon higher-order neighborhood systems, *IEEE Geoscience and Remote Sensing Letters* 5(3): 522–526.

LI, S. Z. (2009). *Markov Random Field Modeling in Image Analysis*, 3 edn, Springer-Verlag London, Inc.

Mallat, S. G. (1989). A theory of multiresolution image decomposition: The wavelet representation, *IEEE Transactions on Pattern Analysis and Machine Intelligence* 11(7): 647–693.

Marroquin, J., Mitter, S. & Poggio, T. (1987a). Probabilistic solution of ill-posed problems in computer vision, *Journal of American Statistical Society* 82: 76–89.

Marroquin, J., Mitter, S. & Poggio, T. (1987b). Probabilistic solution of ill-posed problems in computer vision, *Journal of American Statistical Society* 82: 76–89.

Metropolis, N., Rosenbluth, A., Rosenbluth, M. & Teller, A.and Teller, E. (1953). Equation of state calculations by fast computer machines, *Journal of Physical Chemistry* 21: 1987–2092.

Nash, J. F. (1950). Equilibrium points in n-person games, *Proceedings of the National Academy of Sciences* 36: 48–49.

Nasri, M. & Nezamabadi-pour, H. (2009). Image denoising in the wavelet domain using a new adaptive thresholding function, *Neurocomputing* 72: 1012–1025.

Sharifi, K. & Leon-Garcia, A. (1995). Estimation of shape parameter for generalized gaussian distributions in sub-band decompositions of video, *IEEE Transactions on Circuits and Systems for Video Technology* 5(1): 52–56.

Solberg, A. H. S. (2004). Flexible nonlinear contextual classification, *Pattern Recognition Letters* 25: 1501–1508.

Stein, C. (1981). Estimation of the mean of a multivariate normal distribution, *Annals of Statistics* 9(6): 1135–1151.

Strang, G. & Nguyen, T. (1997). *Wavelets and Filter Banks*, Wellesley-Cambridge Press.

Swendsen, R. & Wang, J. (1987). Nonuniversal critical dynamics in monte carlo simulations, *Physical Review Letters* 58: 86–88.

Tomasi, C. & Manduchi, R. (1998). Bilateral filtering for gray and color images, INTERNATIONAL CONFERENCE ON COMPUTER VISION, ICCV, 6., 1998, Bombay. *Proceedings...*, IEEE, Bombay, India, pp. 839–846.

Wang, Z. & Bovik, A. C. (2009). Mean squared error: Love it or leave it ? a new look at signal fidelity measures, *IEEE Signal Processing Magazine* 26(1): 98–117.

Westerink, P. H., Biemond, J. & Boekee, D. E. (1991). *Sub-band Image Coding*, Kluwer Academic, chapter Sub-band coding of color images.

Winkler, G. (2006). *Image Analysis, Random Fields and Markov Chain Monte Carlo Methods: A Mathematical Introduction*, Springer.

Wolff, U. (1989). Collective monte carlo updating for spin systems, *Physical Review Letters* 62: 361–364.

Wu, J. & Chung, A. C. S. (2007). A segmentation model using compound markov random fields based ona boundary model, *IEEE Transactions on Image Processing* 16(1): 241–252.

Yoon, B. J. & Vaidyanathan, P. P. (2004). Wavelet-based denoising by customized thresholding, *Proceedings of International Conference on Acoustics, Speech, and Signal Processing*, Vol. 2, pp. 925–928.

Yu, S. & Berthod, M. (1995a). A game strategy approach for image labeling, *Computer Vision and Image Understanding* 61(1): 32–35.

Yu, S. & Berthod, M. (1995b). A game strategy approach for image labeling, *Computer Vision and Image Understanding* 61(1): 32–37.

Zhang, B. & Allebach, J. P. (2008). Adaptive bilateral filter for sharpness enhancement and noise removal, *IEEE Transactions on Image Processing* 17(5): 664–678.

Zhang, M. & Gunturk, B. K. (2008). Multiresolution bilateral filtering for image denoising, *IEEE Transactions on Image Processing* 17(12): 2324–2333.

5

Image Equalization Using Singular Value Decomposition and Discrete Wavelet Transform

Cagri Ozcinar[1], Hasan Demirel[2] and Gholamreza Anbarjafari[3]
[1]Department of Electronic Engineering, University of Surrey, GU2 7XH Surrey
[2]Department of Electrical and Electronic Engineering, Eastern Mediterranean University, Gazimagusa, KKTC, via Mersin 10
[3]Department of Information Systems Engineering, Cyprus international University, Lefkosa, KKTC, via Mersin 10
[1]England
[2,3]Turkey

1. Introduction

Contrast enhancement is frequently referred as one of the most important issues in image processing. Contrast is created by the difference in luminance reflected from two adjacent surfaces. In other words, contrast is the difference in visual properties that makes an object distinguishable from other objects and the background. In visual perception, contrast is determined by the difference in the color and brightness of the object with other objects. Our visual system is more sensitive to contrast than absolute luminance; therefore, we can perceive the world similarly regardless of the considerable changes in illumination conditions.

If the contrast of an image is highly concentrated on a specific range, e.g. an image is very dark; the information may be lost in those areas which are excessively and uniformly concentrated. The problem is to optimize the contrast of an image in order to represent all the information in the input image. There have been several techniques to overcome this issue (Shadeed et al., 2003; Gonzales and Woods, 2007; Kim et al., 1998; Chitwong et al., 2002). One of the most frequently used techniques is general histogram equalization (GHE). After the introduction of GHE, researchers came out with better techniques such as local histogram equalization (LHE). However, the contrast issue is yet to be improved and even these days many researchers are proposing new techniques for image equalization. In this work, we are comparing our results with two state-of-art techniques, namely, dynamic histogram equalization (DHE) (Abdullah Al Wadud et al., 2007) and our previously introduced singular value equalization (SVE) (Demirel et al. ISCIS 2008).

As motioned before, in many image-processing applications, GHE technique is one of the simplest and most effective primitives for contrast enhancement (Kim and Yang, 2006),

which attempts to produce an output histogram that is uniform (Weeks et al., 1999). One of the disadvantages of the GHE is that the information laid on the histogram or probability distribution function (PDF) of the image will be lost. Demirel and Anbarjafari showed that the PDF of face images can be used for face recognition (Demirel and Anbarjafari, IEEE Signal Processing Letter, 2008), hence preserving the shape of PDF of the image is of vital importance. Techniques such as DHE or SVE are preserving the general pattern of the PDF of an image. DHE is obtained from dynamic histogram specification (Sun et al., 2005) which generates the specified histogram dynamically from the input image. DHE algorithm works in the following way (Abdullah Al Wadud et al., 2007): Firstly, the locations of local minimums of the histogram are found and then the histogram is divided into several sub-histograms based on those local minimums. Then the mean, μ, and standard deviation, σ, for each sub-histogram is calculated. If gray levels(GLs) of having frequencies within (μ-σ) to (μ+σ) is more than an specific value, e.g. 68.3% of the total number of GLs of a sub-histogram, then that sub-histogram can be considered as a normal distribution of frequencies and there is no dominating portion. But if it is less then that threshold value, the sub histogram splits again. Then weights for GL range of i^{th} sub-histogram are calculated by the following equation (Abdullah Al Wadud et al., 2007):

$$\text{weight}_i = \text{span}_i \times (\log S_i) x \tag{1}$$

where $span_i$ is GL range of sub-histogram i , S_i is summation of all histogram values of i^{th} sub-histogram, and x is a coefficient to control the strength of image contrast. Then the range which is the expansion value to determine how many times to expand its sub-histogram is calculated by using the fallowing formula (Abdullah Al Wadud et al., 2007):

$$\text{range}_i = \frac{\text{weight}_i}{\sum_{i=1}^{n} \text{weight}_i} * (L-1) \tag{2}$$

where L is total number of available GLs. Finally, GHE is applied for each sub-histogram.
SVE (Demirel et al. ISCIS 2008; Demirel and Anbarjafari, IEEE Signal Processing Letter, 2008) technique is based on equalizing the singular value matrix obtained by singular value decomposition (SVD). SVD of an image, which can be interpreted as a matrix is written as follows:

$$A = U_A \Sigma_A V_A^T \tag{3}$$

where U_A and V_A are orthogonal square matrices known as hanger and aligner respectively, and Σ_A matrix contains the sorted singular values on its main diagonal. The idea of using SVD for image equalization comes from this fact that Σ_A contains the intensity information of the given image (Tian et al., 2003). The objective of SVE proposed by Demirel et al. (ISCIS 2008) is to equalize a low contrast image in such a way that the mean moves towards the neighborhood of 8-bit mean gray value 128 in the way that the general pattern of the PDF of the image is preserved.
In our earlier work (Demirel and Anbarjafari, IEEE Signal Processing Letter, 2008), where we introduced PDF based face recognition, singular value decomposition was used to deal with the illumination problem. The method uses the ratio of the largest singular value of the

generated normalized matrix over a normalized image which can be calculated according to equation (4).

$$\xi = \frac{\max\left(\Sigma_{N(\mu=0,\text{var}=1)}\right)}{\max\left(\Sigma_A\right)} \tag{4}$$

where $\Sigma_{N(\mu=0,\text{var}=1)}$ is the singular value matrix of the synthetic intensity matrix. This coefficient can be used to regenerate an equalized image using equation (5).

$$\Xi_{equalized_A} = U_A\left(\xi\Sigma_A\right)V_A^T \tag{5}$$

where $\Xi_{equalized_A}$ is representing the equalized image A. This task is eliminating the illumination problem.

Nowadays, wavelets have been used quite frequently in image processing. It has been used for feature extraction (Wang and Chen, 2006), denoising (Starck et al., 2002), compression (Lamard et al., 2005), image equalization enhancement (Demirel et al., IEEE Geoscience and Remote Sensing Letter, 2010), and face recognition (Liu et al., 2007). The decomposition of images into different frequency ranges permits the isolation of the frequency components introduced by "intrinsic deformations" or "extrinsic factors" into certain subbands (Dai and Yan, 2007). This process results in isolating small changes in an image mainly in high frequency subband images. Hence discrete wavelet transform (DWT) is a suitable tool to be used for designing pose invariant face recognition system. The two-dimensional wavelet decomposition of an image is performed by applying the one-dimensional DWT along the rows of the image first, and then the results are decomposed along the columns. This operation results in four decomposed subband images refer to Low-Low (LL), Low-High (LH), High-Low (HL), and High-High (HH). The frequency components of those subband images cover the frequency components of the original image.

In this work, we have proposed a new method for image equalization which is an extension of SVE and it is based on SVD of LL subband image obtained by DWT. DWT is used to separate the input image into different frequency subbands, where LL subband concentrates the illumination information. That is why, only LL subband goes through SVE process, which preserves high frequency components (i.e. edges). Hence, after IDWT, the resultant image will be sharper. In this chapter, the proposed method has been compared with conventional GHE technique as well as LHE and some state-of-art technique such as DHE an SVE. The results indicate the superiority of the proposed method over the aforementioned methods.

2. The proposed image equalization technique

There are two significant parts of the proposed method. The first one is the use of SVD. As it was mentioned, the singular value matrix obtained by SVD contains the illumination information. Therefore, changing singular values will directly affect the illumination of the image hence the other information in the image will not be changed. The second important aspect of this work is the application of DWT. As it was mentioned in the introduction, the illumination information is embedded in LL subband. The edges are concentrated in other subbands (i.e. LH, HL, and HH). Hence, separating the high frequency subbands and

applying the illumination enhancement in LL subband only, will protect the edge information from possible degradation (Demirel et al., IEEE Geoscience and Remote Sensing Letter, 2010). After reconstructing the final image by using IDWT, the resultant image will not only be enhanced with respect to illumination, but also it will be sharper.
The general procedure of the proposed technique is as follows. The input image, *A*, is first processed by using GHE to generate $\hat{A}$. Then both of these images are transformed by DWT into four subband images. The correction coefficient for singular value matrix is calculated by using the following equation:

$$\zeta = \frac{\max\left(\Sigma_{LL_{\hat{A}}}\right)}{\max\left(\Sigma_{LL_A}\right)} \tag{6}$$

where Σ_{LL_A} is the LL singular value matrix of the input image and $\Sigma_{LL_{\hat{A}}}$ is the LL singular value matrix of the output of the GHE. The new LL image is composed by:

$$\begin{aligned} \overline{\Sigma}_{LL_A} &= \zeta \Sigma_{LL_A} \\ \overline{LL_A} &= U_{LL_A} \overline{\Sigma}_{LL_A} V_{LL_A} \end{aligned} \tag{7}$$

Now the $\overline{LL_A}$ and LH_A, HL_A, and HH_A subband images of the original image are recombined by applying IDWT, to generate the resultant equalized image $\overline{A}$.

$$\overline{A} = IDWT\left(\overline{LL}_A, LH_A, HL_A, HH_A\right) \tag{8}$$

In this chapter we have used db.9/7 wavelet function as the mother function of the DWT. In the following section the experimental results and the comparison of the aforementioned conventional and state-of-art techniques are discussed. Fig. 1 illustrates all steps of the proposed image equalization technique.

3. Experimental results and discussions

Fig. 2 (a) illustrates a low contrast image which has been used in (Abdullah Al Wadud et al., 2007). This image has been equalized by using GHE (b), SVE (c), DHE (d), LHE (e), and the proposed equalization technique (f). The quality of the visual results indicates that the proposed equalization technique is sharper and brighter than the one achieved by DHE, GHE, and LHE. The resultant image generated by SVE is comparable with the image achieved by the proposed method.
In order to show the superiority of the proposed method over the SVE, GHE and LHE, Fig 3, and Fig. 4 have been generated. Both figures are showing that the proposed method have a brighter and sharper output, also there is no wash out problem as it has occurred in Fig. 3 and 4 (c) obtained by SVE and there is also no blurring effect like Fig. 3 and 4 (e) obtained by LHE.

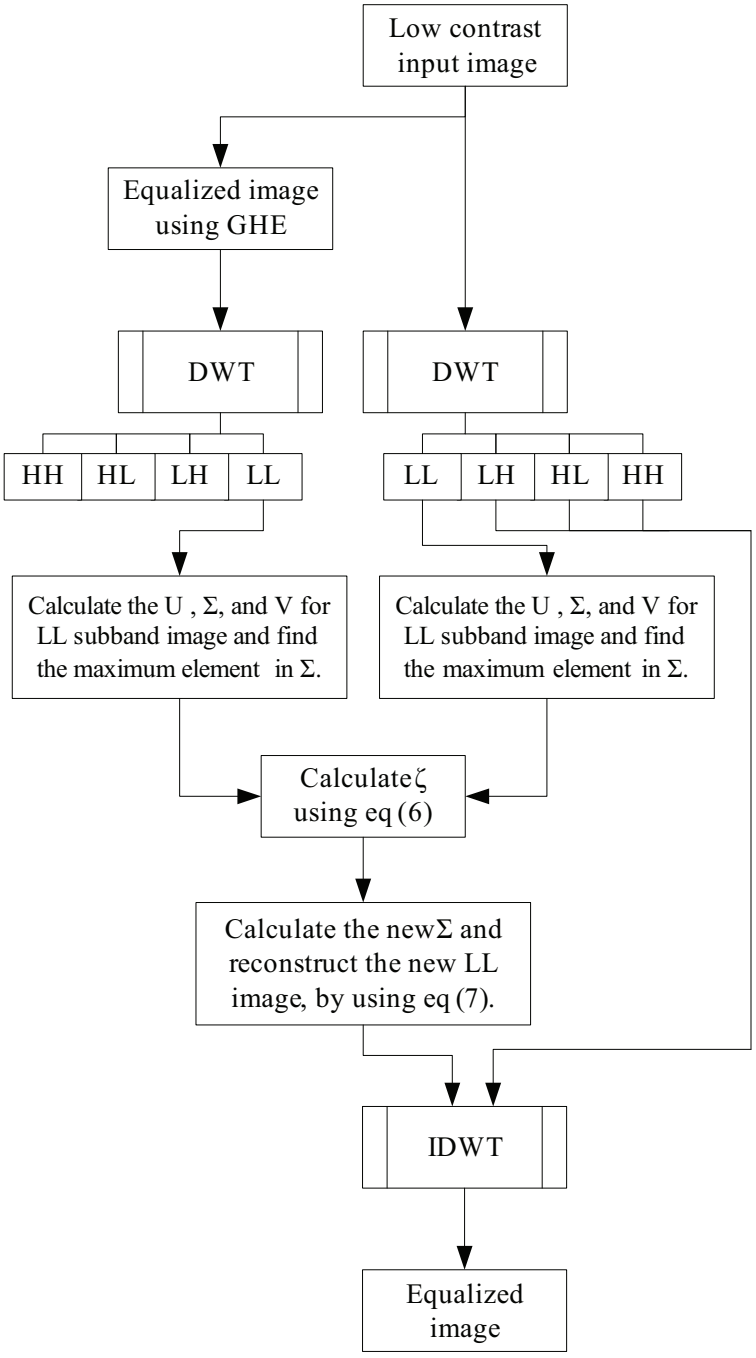

Fig. 1. The detailed steps of the proposed equalization technique.

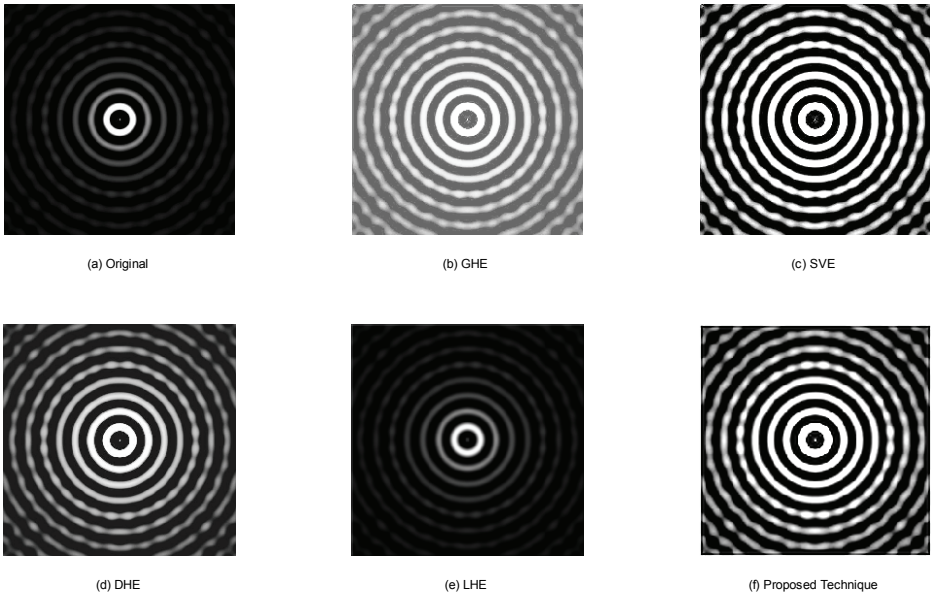

Fig. 2. (a) Low contrast image, Equalized image using: (b) GHE, (c) SVE, (d) DHE, (e) LHE, and (f) the proposed technique.

Fig. 3. (a) Low contrast image, Equalized image using: (b) GHE, (c) SVE, (d) LHE, and (e) the proposed technique.

Fig. 4. (a) Low contrast image, Equalized image using: (b) GHE, (c) SVE, (d) LHE, and (e) the proposed technique.

4. Conclusions

In this work, a new image equalization technique based on SVD and DWT was proposed. The proposed technique converted the image from spatial domain into the DWT domain and after equalizing the singular value matrix of the LL subband image, it reconstructed the image in the spatial domain by using IDWT. The technique was compared with the GHE, LHE, DHE and SVE techniques. The experimental results were showing the superiority of the proposed method over the conventional and the state-of-art techniques.

5. Acknowledgements

Authors would like to thank Haidi Ibrahim and Nicholas Sia Pik Kong from School of Electrical and Electronic Engineering, Universiti Sains Malaysia for providing the equalized output images of DHE technique.

6. References

A. R. Weeks, L. J. Sartor, and H. R. Myler, 'Histogram specification of 24-bit color images in the color difference (C-Y) color space', Proc. SPIE, 1999, 3646, pp. 319–329.

C. C. Liu, D. Q. Dai, and H. Yan, "Local discriminant wavelet packet coordinates for face recognition", Journal of Machine Learning Research, 2007, Vol. 8, pp: 1165-1195.

C. C. Sun, S. J. Ruan, M. C. Shie, and T, W. Pai, "Dynamic contrast enhancement based on histogram specification", IEEE Transactions on Consumer Electronics, Vol. 51, No. 4, 2005, pp.1300–1305.

D. Q. Dai and H. Yan, “Wavelet and face recognition”, Face recognition, Chapter 4, K. Delac and M. Grgic (Eds), ISBN: 978-3-902613-03-5, Austria, pp: 59-74, 2007.

H. Demirel, G. Anbarjafari, and M. N. S. Jahromi, "Image equalization based on singular value decomposition", 23rd IEEE International Symposium on Computer and Information Sciences, Turkey, Oct 2008, pp. 1-5.

H. Demirel and G. Anbarjafari, “Pose invariant face recognition using probability distribution function in different color channels", IEEE Signal Processing Letter, Vol. 15, 2008, pp. 537 - 540.

H. Demirel, C. Ozcinar, and G. Anbarjafari, "Satellite Image Contrast Enhancement Using Discrete Wavelet Transform and Singular Value Decomposition", IEEE Geoscience and Remote Sensing Letter, April 2010, Vol. 7, No. 2, pp. 334-338.

J. L. Starck, E. J. Candes, and D. L. Donoho, “The curvelet transform for image denoising”, IEEE Transactions on Image Processing, 2002, Vol. 11, pp: 670-684.

J. W. Wang and W. Y. Chen, “Eye detection based on head contour geometry and wavelet subband projection”, Optical Engineering, 2006, Vol. 45, No. 5.

M. Abdullah-Al-Wadud, H. Kabir, M. A. A.Dewan, C. Oksam, “A dynamic histogram equalization for image contrast enhancement”, IEEE Transaction on Consumer Electronics, Vol. 53, No 2, May 2007, pp. 593-600.

M. Lamard, W. Daccache, G. Cazuguel, C. Roux, and B. Cochener, "Use of a JPEG-2000 wavelet compression scheme for content-based ophtalmologic retinal images retrieval", 27th Annual International Conference of the Engineering in Medicine and Biology Society, IEEE-EMBS 2005, pp: 4010 – 4013.

R. C. Gonzalez, and R. E. Woods, Digital Image Processing, Prentice Hall, ISBN 013168728X, 2007.

S. Chitwong, T. Boonmee, and F. Cheevasuvit, ‘Enhancement of colour image obtained from PCA-FCM technique using local area histogram equalization’, Proc. SPIE, 2002, 4787, pp. 98–106.

T. K. Kim, J. K. Paik, and B. S. Kang, “Contrast enhancement system using spatially adaptive histogram equalization with temporal filtering,” IEEE Transactions on Consumer Electronics, Vol. 44, No. 1, 1998, pp. 82–86.

T. Kim, H.S. Yang, “A Multidimensional Histogram Equalization by Fitting an Isotropic Gaussian Mixture to a Uniform Distribution”, IEEE International Conference on Image Processing, 8-11 Oct. 2006, pp. 2865 – 2868.

W. G. Shadeed, D. I. Abu-Al-Nadi, and M. J. Mismar, “Road traffic sign detection in color images”, 10th International Conference on Environmental and Computer Science, Vol. 2, Dec 2003, pp. 890-893.

Y. Tian, T. Tan, Y. Wang, and Y. Fang, “Do singular values contain adequate information for face recognition?”, Pattern Recognition, Vol. 36, 2003, pp. 649 – 655.

6

Probability Distribution Functions Based Face Recognition System Using Discrete Wavelet Subbands

Hasan Demirel[1] and Gholamreza Anbarjafari[2]
[1]*Department of Electrical and Electronic Engineering,*
Eastern Mediterranean University,
Gazimagusa, KKTC, via Mersin 10
[2]*Department of Information Systems Engineering,*
Cyprus International University,
Lefkosa, KKTC, via Mersin 10
Turkey

1. Introduction

Face recognition has recently been the centre of attention of many researchers (Jain et al. 2004). The earliest work in digital face recognition was reported by Bledsoe in 1964. Statistical face recognition systems such as principal component analysis (PCA) based eigenfaces introduced by Turk and Pentland in 1991, attracted lots of attention. Fisherfaces method based on linear discriminant analysis was introduced later on by Belhumeur et al. (1997).

Many of these methods are based on grey scale images; however colour images are increasingly being used since they add additional biometric information for face recognition (Marcel and Bengio, 381). PDFs obtained from different colour channels of a face image can be considered as the signature of the face, which can be used to represent the face image in a low dimensional space (Demirel and Anbarjafari, VISSAP 2008). Images with small changes in translation, rotation and illumination still possess high correlation in their corresponding PDFs. PDF of an image is a normalized version of an image histogram which have been used in many image processing applications such as object detection (Laptev, 2006) and face recognition (Yoo and Oh, 1999; Rodriguez and Marcel, 2006; Demirel and Anbarjafari, IEEE Signal Processing Letter, 2008).

Nowadays, wavelets have been used quite frequently in image processing. It has been used for feature extraction (Wang and chen, 2006), denoising (Starck et al., 2002), compression (Lamard et al. 2005), and face recognition (Liu et al., 2007; Demirel et al., 2008). The decomposition of images into different frequency ranges permits the isolation of the frequency components introduced by "intrinsic deformations" or "extrinsic factors" into certain subbands (Dai and Yan, 2007). This process results in isolating small changes in an image mainly in high frequency subband images. Hence discrete wavelet transform (DWT) is a suitable tool to be used for designing pose invariant face recognition system.

Another important issue in face recognition system is face localization. There are several methods for this task such as skin tone based face localization for face segmentation. Skin is

a widely used feature in human image processing with a range of applications (Yang et al., 2002; Demirel et al., EECS 2008). Many methods have been proposed to use skin colour pixels for face localization. Chai and Ngan (1999) modelled the skin colour in *YCbCr* colour space. One of the recent methods for face localization is proposed by Nilsson (2007) which is using local Successive Mean Quantization Transform (SMQT) technique. Local SMQT has been claimed to be robust for illumination changes and the Receiver Operation Characteristics of the method is reported to be very successful for the segmentation of faces (Nilsson et al., ICASSP2007). In order to enhance the robustness of the system under changing illumination conditions, a reliable image equalization technique such as dynamic histogram equalization (Abdullah et al., 2007) or singular value decomposition based image equalization (Demirel and Anbarjafari, IEEE Signal Processing Letter, 2008; Sabet et al., ISCIS 2008) can be applied in the pre-processing stage.

In this chapter, after the face localization, 2-norm based image equalization technique has been employed to enhance the robustness of the system under changing illumination. Then the PDFs of the equalized and segmented faces in different subbands obtained from discrete wavelet transform (DWT) are calculated. These PDFs are used as statistical feature vectors for the recognition of faces by minimizing the Kullback-Leibler Divergence (KLD) between the PDF of a given face and the PDFs of faces in the database. The effect of well-known decision fusion techniques such as sum rule, median rule, max rule, product rule, majority voting (MV), and feature vector fusion (FVF), for combining feature vectors in *HSI* and *YCbCr* colour spaces of Low-Low, Low-High, High-Low, and High-High subbands, have been studied in order to achieve higher recognition performance.

The Head Pose (HP) face database (Gourier et al., 2004) and a subset from the FERET (Philips et al., 2000) database with faces containing varying poses changing from -90^o to +90^o of rotation around the vertical axis passing through the neck were used to test the proposed system. Both databases include face images with varying poses and face images have little illumination variation. The results are compared with principle component analyses (PCA), and three state-of-art face recognition systems: adaptive local binary pattern [LBP] PDFs based face recognition (Rodriguez and Marcel, 2006), nonnegative matrix factorization (NMF) introduced by Lee et al. (1999, 2001) and supervised incremental NMF (INMF) introduced and described by Wen-Sheng et al. (Wen Sheng et al., 2008).

2. Pre-processing of face images

The proposed face recognition system has been tested on the databases with no significant illumination changes, but singular value decomposition (SVD) based equalization (SVE) (Demirel and Anbarjafari, IEEE Signal Processing Letter, 2008; Sabet et al., ISCIS 2008) have been applied to the input images in both training and recognition stages. In this section SVE technique is explained.

In general, for any intensity image matrix Ξ_A, $A=\{R, G, B\}$, SVD can be written as:

$$\Xi_A = U_A \Sigma_A V_A^T \qquad A = \{R, G, B\} \tag{1}$$

where U_A and V_A are orthogonal square matrices (hanger and aligner matrices) and Σ_A matrix contains the sorted singular values on its main diagonal (stretcher matrix). As reported in (Tian et al., 2003), Σ_A represents the intensity information of a given image. If an image is a low contrast image this problem can be corrected to replace the Σ_A of the image

with another singular matrix obtained from an image with no contrast problem. A normalized intensity image matrix with no illumination problem can be considered to be the one with a PDF having a Gaussian distribution with mean of 0.5 and variance of 1. Such a synthetic intensity matrix with the same size of the original image can easily be obtained by generating random pixel values with Gaussian distribution with mean of 0.5 and variance of 1. Then the ratio of the largest singular value of the generated normalized matrix over a normalized image can be calculated according to equation (2):

$$\xi_A = \frac{\max\left(\Sigma_{g(\mu=0.5,\sigma=1)}\right)}{\max\left(\Sigma_A\right)} \quad , \quad A = \{R, G, B\} \tag{2}$$

where $\Sigma_{g(\mu=0.5,\sigma=1)}$ is the singular value matrix of the synthetic intensity matrix. This coefficient can be used to regenerate a new singular value matrix which is actually an equalized intensity matrix of the image generated by equation (3):

$$\Xi_{equalized_A} = U_A\left(\xi_A \Sigma_A\right) V_A^T \quad , \quad A = \{R, G, B\} \tag{3}$$

where $\Xi_{equalized\ A}$ is representing the equalized image in A-colour channel.
As equation (3) states the equalized image is just a multiplication of ξ_A with the original image. From the computational complexity point of view singular value decomposition of a matrix is an expensive process which takes quite significant amount of time to calculate the orthogonal matrices of U and V while they are not being used in the equalization process. Hence, finding a cheaper method to obtain or estimate ξ_A can be an improvement to the technique. Recall,

$$\|A\| = \sqrt{\lambda_{\max}} \tag{4}$$

where λ_{max} is the maximum eigenvalue of A^TA. By using SVD,

$$A = U\Sigma V^T \rightarrow A^T A = V\Sigma^2 V^T \tag{5}$$

This follows that the eigenvalues of A^TA are the square of elements of the main diagonal of Σ, and that the eigenvector of A^TA is V. Because Σ is in the form of:

$$\Sigma = \begin{bmatrix} \lambda_1 & & & \\ & \lambda_2 & & \\ & & \ddots & \\ & & & \lambda_k \cdots \end{bmatrix}_{m \times n} \qquad \lambda_1 > \lambda_2 > \cdots > \lambda_k \quad k = \min(m,n) \tag{6}$$

Thus,

$$\|A\| = \lambda_1 \tag{7}$$

The 2-norm of a matrix is equal to the largest singular value of the matrix. Therefore ξ_A can be easily obtained from:

$$\xi_A = \frac{\left\| \Xi_{g(\mu=0.5,\sigma=1)} \right\|}{\left\| \Xi_A \right\|} \quad , \quad A = \{R, G, B\} \tag{8}$$

where $\Xi_{g(\mu=0.5,\sigma=1)}$ is a random matrix with mean of *0.5* and variance of *1* and Ξ_A is the intensity image in *R*, *G*, or *B*. Hence the equalized image can be obtained by:

$$\Xi_{equalized_A} = \xi_A \, \Xi_A = \frac{\left\| \Xi_{g(\mu=0.5,\sigma=1)} \right\|}{\left\| \Xi_A \right\|} \Xi_A \quad , \quad A = \{R, G, B\} \tag{9}$$

which shows there is no need to use singular value decomposition of intensity matrices. This procedure reduces the complexity of the equalization procedure. This task, which is actually equalizing the images, will eliminate the illumination problem. The SVE technique has been tested on the Oulu face database (Marszalec et al., 2000) as well as the FERET and HP face databases. Fig. 1 shows the general required steps of the pre-processing phases of the proposed system.

After applying SVE, the equalized images can be used as an input for the face detector prepared by Mike Nilsson (MathWirks, 2008) in order to localize and then crop the face region and eliminate the undesired background. The segmented face images are used as inputs of DWT for the generation of PDFs of different subband images in *H, S, I, Y, Cb,* and *Cr* colour channels. If there is no face in the image, then there will be no output from the face detector software, so it means the probability of having a random noise which has the same colour distribution of a face but with different shape is zero, which makes the proposed method reliable.

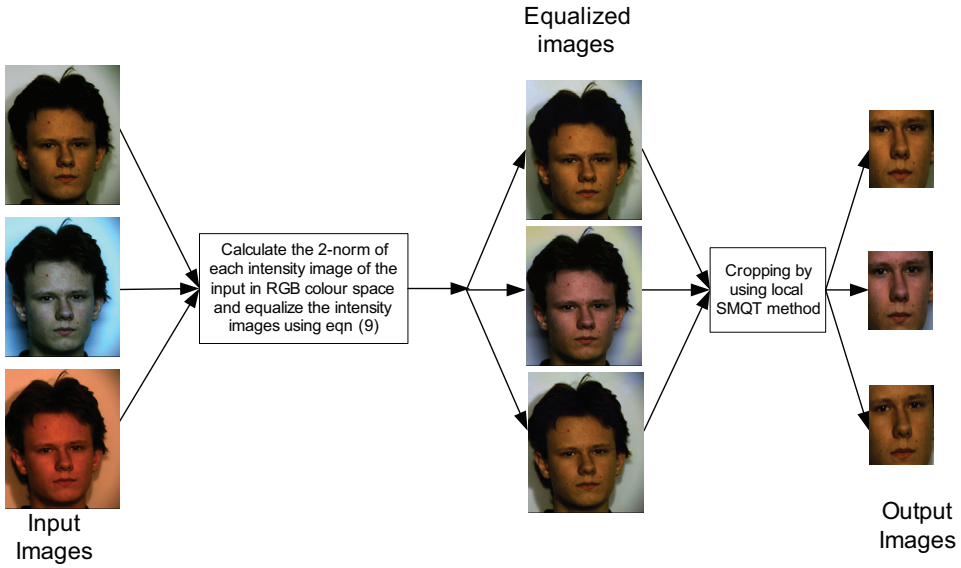

Fig. 1. The algorithm, with a sample image with different illumination from Oulu face database, of pre-processing of the face images to obtain a segmented face from the input face image.

The two-dimensional wavelet decomposition of an image is performed by applying the one-dimensional DWT along the rows of the image first, and then the results are decomposed along the columns (MATLAB 2009). This operation results in four decomposed subband images refer to Low-Low (LL), Low-High (LH), High-Low (HL), and High-High (HH). The frequency components of those subband images cover the frequency components of the original image.

3. PCA and LBP based face recognition

3.1 PCA based face recognition

Eigenfaces method is based on linear PCA where a face image is encoded to a low dimensional vector. All face images are decomposed into a small set of characteristic feature images called eigenfaces. Each face image is projected on the subspace of meaningful eigenfaces (ones with nonzero eigenvalues). Hence, the collection of weights describes each face. Recognition of a new face is performed by projecting it on the subspace of eigenfaces and then comparing its weights with corresponding weights of each face from a known database.

Assume that all face images in a database are of the same size $w \times h$. Eigenfaces are obtained as the eigenvectors of the covariance matrix of the data points. Let Γ_i be an image from the collection of M images in the database. A face image is a 2-dimensional array of size $w \times h$, where w and h are width and height of the image, respectively. Each image can be represented as a vector of dimension $w \times h$ and the average image, Ψ, is defined as:

$$\Psi = \frac{1}{M}\sum_{i=1}^{M}\Gamma_i \tag{10}$$

Each image Γ_i differ from the average image Ψ by the vector:

$$\Phi_i = \Gamma_i - \Psi \tag{11}$$

The covariance matrix of the dataset is defined as:

$$C = \frac{1}{M}\sum_{n=1}^{M}\Phi_n\Phi_n^T = \Lambda\ \Lambda^T \qquad \Lambda=[\ \Phi_1\ \Phi_2\ \ldots\ \Phi_M\ ] \tag{12}$$

Since there are M images in the database, the covariance matrix C has only $M-1$ meaningful eigenvectors. Those eigenvectors u_l, can be obtained by multiplying eigenvectors v_l, of matrix $L=\Lambda^T\Lambda$ (of size $M \times M$) with difference vectors in matrix Λ.

$$u_l = \sum_{k=1}^{M} v_{lk}\Phi_k \tag{13}$$

The eigenvectors, u_l, are called the eigenfaces. Eigenfaces with higher eigenvalues contribute more in representation of a face image. The face subspace projection vector for every image is defined by:

$$\begin{aligned}\Omega^T &= [\omega_1 \quad \omega_2\ \ldots\ \omega_M] \\ \omega_k &= u_k^T(\Gamma - \Psi) \quad k = 1,2,\ldots,M\end{aligned} \tag{14}$$

The projection vectors are indispensable in face recognition tasks, due to their uniqueness. The projection vector, which represents a given face image in the eigenspace can be used for the recognition of faces. Euclidian distance, ε, between projection vectors of two different images (Ω_1 and Ω_2) is used to determine whether a face is recognized correctly or not.

$$\varepsilon = \left\|\Omega_1 - \Omega_2\right\|^2 = \sqrt{\sum_{i=1}^{M}\left(\omega_{1i} - \omega_{2i}\right)^2} \tag{15}$$

PCA face recognition system has been applied to the different colour channels (*H, S, I, Y, Cb* and *Cr*) and as it will be shown in section *7*, the recognition rate of PCA based face recognition system is being increased by fusion of the decisions of different colour channels using MV.

3.2 Language, style spelling

The local binary pattern (LBP) is a non-parametric operator which describes the local spatial structure of an image. Ojala et al. introduced this operator and showed its high discriminative power for texture classification (Ojala et al., 1996). At a given pixel position *(x,y)*, LBP is defined as an ordered set of binary comparisons of pixel intensities between the centre pixel and its eight neighbour pixels, as shown in Fig 2.

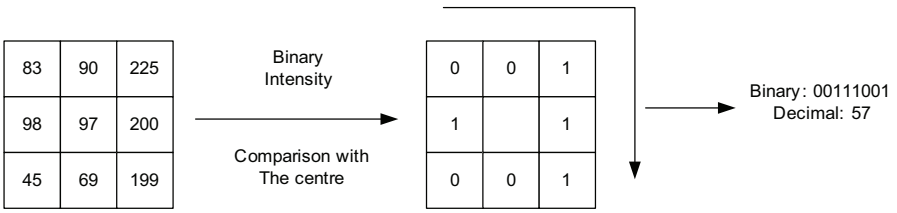

Fig. 2. The local binary pattern (LBP) operator

The decimal form of the resulting 8-bit word of LBP code can be expressed as follows:

$$\mathrm{LBP}(x,y) = \sum_{n=0}^{7} 2^n s\left(i_n - i_{(x,y)}\right) \tag{16}$$

where $i_{(x,y)}$ corresponds to the grey value of the centre pixel *(x,y)*, i_n to the grey values of the 8 neighbour pixels, and function *s(x)* is defined as:

$$s(x) = \begin{cases} 1 & \text{if } x \geq 0 \\ 0 & \text{if } x < 0 \end{cases} \tag{17}$$

By definition, the LBP operator is unaffected by any monotonic greyscale transformation which preserves the pixel intensity order in a local neighbourhood. Note that each bit of the LBP code has the same significance level and that two successive bit values may have a totally different meaning. Sometimes, the LBP code is referred as a kernel structure index.
Ojala et al extended their previous work to a circular neighbourhood of different radius size (Ojala et al., 2002). They used $LBP_{P,R}$ notation which refers to *P* equally spaced pixels on a circle of radius *R*. Two of the main motivations of using LBP are its low computational

complexity and its texture discriminative property. LBP has been used in many image processing applications such as motion detection, visual inspection, image retrieval, face detection, and face recognition.

In most aforementioned applications a face image was usually divided in small regions. For each region, a cumulative histogram of LBP code computed at each pixel location within the region was used as a feature vector.

Ahonen et al. used LBP operator for face recognition (Ahnon et al., 2004). Their face recognition system can be explained as follows: A histogram of the labelled image $f_1(x,y)$ can be defined as:

$$H_i = \sum_{x,y} I\{f_1(x,y) = i\} \qquad i = 0,\cdots,n-1 \tag{18}$$

where n is the number of different labels produced by the LBP operator and

$$I\{A\} = \begin{cases} 1 & A \text{ is true} \\ 0 & A \text{ is false} \end{cases} \tag{19}$$

This histogram contains information about the distribution of the local micropatterns, such as edges, spots, and flat areas, over the whole image. For efficient face representation, retaining the spatial information is required; hence the image is divided into regions R_0, R_1, …, R_{m-1}, as shown in Fig 3.

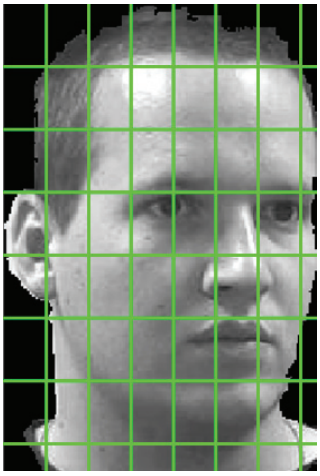

Fig. 3. An example of a facial image divided into 8x8windows.

As reported in (Ojala et al., 1996), the spatially enhanced histogram is defined as:

$$H_{i,j} = \sum_{x,y} I\{f_1(x,y) = i\} I\{(x,y) \in R_j\} \quad , \quad i = 0,\cdots,n-1 \ , \ j = 0,\cdots,m-1 \tag{20}$$

where m is the number of blocks and n is the LBP bins. In this histogram, a description of the face on three different levels of locality exists: the labels for the histogram contain information about the patterns on a pixel level, the labels are summed over a small region to

produce information on a regional level, and the regional histograms are concatenated to build a global description of the face.
Although Ahonen et al. have mentioned several dissimilarity measures such as histogram intersections and log-likelihood statistics, they used nearest neighbour classifier with Chi square dissimilarity measure in their work (Ahnon et al., 2004).
When the image has been divided into several regions, it can be expected that some of the regions contain more useful information than others in terms of distinguishing between people, such as eyes. In order to contribute such information, a weight can be set for each region based on level of information it contains.

4. PDF based face recognition system

The PDF of an image is a statistical description of the distribution of occurrence probabilities of pixel intensities. In a general mathematical sense, a PDF of an image is simply a mapping to represent the probability of the pixel intensity levels that fall into various disjoint intervals, known as bins. In this work the bin size is set as 256. Given an intensity image, PDF, p, meets the following conditions:

$$p = \left[\tau_0, \tau_1, \cdots, \tau_{255} \right], \ \tau_i = \frac{\eta_i}{N}, \ i = 0, \cdots, 255 \tag{21}$$

where N is the total number of pixels in an image and η_i is the number of pixels having i intensity.
Given two PDFs the divergence between them can be calculated by using Kullback-Leibler Divergence (KLD). The KLD value, κ, between two given PDFs, p_C and q_C, can be calculated as follows:

$$\kappa(\mathrm{q_C}, \mathrm{p_C}) = \sum_i \mathrm{q}_{i_C} \log\left(\frac{\mathrm{q}_{i_C}}{\mathrm{p}_{i_C}}\right) \qquad \mathrm{i}=0,1,2,...,\beta\text{-}1 \tag{22}$$

where β is the number of bins and C is $(H, S, I, Y, Cb, \text{or } Cr)_{LL,LH,HL,HH}$. However, KLD is not a distance measure but it represents the similarity of the two PDFs. In other words, the smaller the KLD value the more similar the PDFs.

$$\chi_{j_C} = \min\left(\kappa\left(\mathrm{q}_C, \mathrm{p}_{jC}\right)\right), \ C = \begin{cases} (H,S,I,Y,Cb,Cr)_{LL} \\ (H,S,I,Y,Cb,Cr)_{LH} \\ (H,S,I,Y,Cb,Cr)_{HL} \\ (H,S,I,Y,Cb,Cr)_{HH} \end{cases}, \ j = 1,2,\cdots,M \tag{23}$$

Here, χ_{i_C}, is the minimum KLD reflecting the similarity of the i^{th} image in the training set in C subband colour channel and the query face and M is the number of image samples. The colour PDFs used in the proposed system is generated only from the segmented face, and hence the effect of background regions is eliminated. Fig. 4 shows two subjects with two different poses and their segmented faces from the FERET face database.

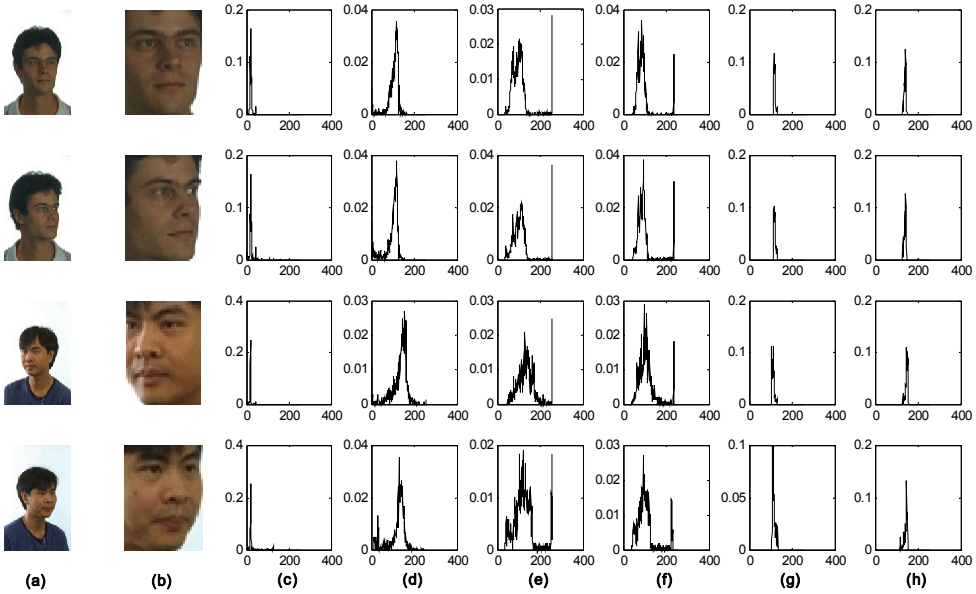

Fig. 4. Two subjects from FERET database with 2 different poses (a), their segmented faces (b) and their PDFs in *H*(c), *S*(d), *I*(e), *Y*(f), *Cb*(g), and *Cr*(h) colour channels in LL subband respectively.

5. Proposed PDF based face recognition using DWT

In this work, the local SMQT algorithm has been adopted for the localization and cropping of faces in the pre-processing stage. Then each face image has been equalized by using the proposed equalization technique in order to reduce the illumination problems. Colour PDFs of the isolated face images in different frequency subbands in *HSI* and *YCbCr* colour spaces are used as the face descriptors. Face recognition is achieved using the KLD between the PDF of the input face and the PDFs of the faces in the training set. In order to increase the recognition performance of the system, several well-known decision fusion techniques which are explained in the proceeding section have been used to improve the recognition performance. Fig. 5 illustrates the building blocks of the proposed face recognition system.

The HP face database and a subset from the FERET database were used to test the proposed system. The HP face database is consisting of 150 face samples of 15 different classes with 10 samples per class and the FERET face database is consisting of 500 face samples of 50 different classes with 10 samples per class. Both databases include face images with varying poses and face images have little illumination variation. The results are compared with conventional techniques such as PCA and LDA, and three state-of-art face recognition systems namely, adaptive LBP PDFs based face recognition, PDF based face recognition system using FVF, NMF, and INMF.

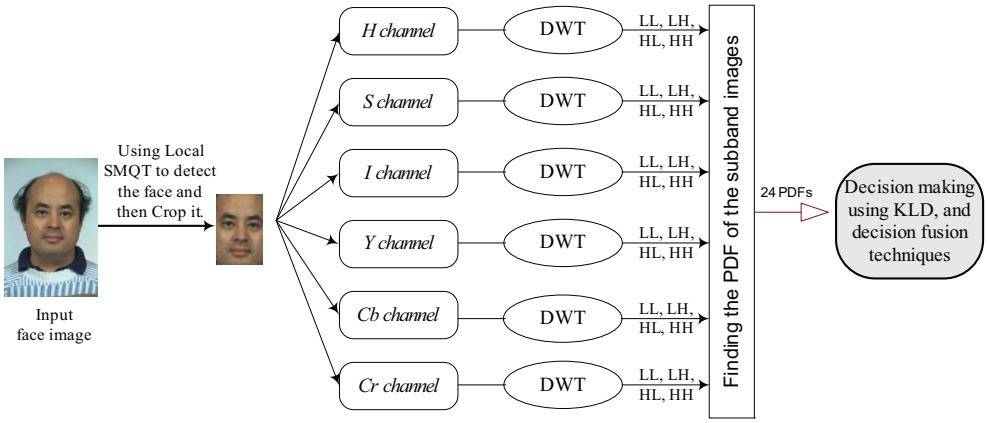

Fig. 5. Building blocks of the proposed system.

6. Decision fusion of different wavelet subbands in different colour channels

The proposed face recognition system as explained in the previous section can be applied to different colour channels (*H*, *S*, *I*, *Y*, *Cb,* and *Cr*) of different subband images obtained by DWT (*LL, LH, HL,* and *HH*). Hence, given a face image the image can be represented in these 24 channels with dedicated colour PDFs for each channel. Different channels contain different information regarding the image; therefore all of these 24 PDFs can be combined to represent a face image. There are many techniques to combine the resultant decision. In this paper, several well-known techniques such as sum rule, median rule, max rule, product rule, majority voting (MV), and feature vector fusion (FVF) have been used to do this combination. These methods have been described in much detailed in by Polikar (2006). The aim of this work is not to introduce but to implement these fusion techniques on PDF based face recognition system.

These data fusion techniques use probability of the decisions they provide through classifiers. That is why it is necessary to calculate the probability of the decision of each classifier based on the minimum KLD value. This is achieved by calculating the probability of the decision in each colour channel, γ_C, which can be formulated as follows:

$$\varsigma_C = \frac{\begin{bmatrix}\chi_1 & \chi_2 & \cdots & \chi_{nM}\end{bmatrix}_C}{\sum_{i=1}^{nM}\chi_i} \qquad C = \begin{cases}(H,S,I,Y,Cb,Cr)_{LL}\\(H,S,I,Y,Cb,Cr)_{LH}\\(H,S,I,Y,Cb,Cr)_{HL}\\(H,S,I,Y,Cb,Cr)_{HH}\end{cases} \tag{24}$$

$$\gamma_C = \max\left(1-\varsigma_C\right)$$

where ς_C is the normalized KLD value, χ_i is indicating the KLD value of the query image from the i^{th} image in the training set, n shows the number of face samples in each class and M is the number of classes. The highest similarity between two projection vectors is when the minimum KLD value is zero. This represents a perfect match, i.e. the probability of selection is 1. So zero KLD value represents probability of 1 that is why ς_C has been subtracted from 1, the maximum probability corresponds to the probability of the selected class. The sum rule is applied, by adding all the probabilities of a class in different colour

channels of different subbands, followed by declaring the class with the highest accumulated probability to be the selected class. The maximum rule, as its name implies, simply takes the maximum among the probabilities of a class in different colour channels of different subbands, followed by declaring the class with the highest probability to be the selected class. The median rule similarly takes the median among the sorted probabilities of a class in different channels. The product rule is achieved from the product of all probabilities of a class in different colour channels of different subbands. Product rule is very sensitive as a low probability (close to 0) will remove any chance of that class being selected.

MV is one of the most frequently used decision fusion technique. The main idea behind MV is to achieve increased recognition rate by combining decisions of the PDF based face recognition procedures of different colour spaces and subbands. By considering the *H, S, I, Y, Cb* and *Cr* PDFs in different wavelet subbands separately and combining their results by using MV, the performance of the classification process will be increased. The MV procedure can be explained as follows. Consider $\{p_1,p_2,\ldots,p_M\}_C$ to be a set of PDFs of training face images in wavelet subband colour channels $(C=(H, S, I, Y, Cb, or\ Cr)_{LL,LH,HL,HH})$, then a given a PDF of a query face image, q, colour PDFs of the query image q_C can be used to calculate the KLD between q_C and PDFs of the images in the training samples by equation (24). The image with the minimum distance in a channel, χ_C, is declared to be the vector representing the recognized subject. Given the decisions of each classifier in each colour space, the voted class E, can be chosen as follows.

$$\mathrm{E} = \mathrm{mode}\left(\chi_{H_{LL}},\cdots,\chi_{H_{HH}},\cdots,\chi_{Cr_{LL}},\cdots,\chi_{Cr_{HH}}\right) \tag{25}$$

where *mode* is declaring the most repeated class.

Data fusion is not the only way to improve the recognition performance. PDF vectors can also be concatenated with the FVF process which is a source fusion technique and can be explained as follows. Consider $\{p_1,p_2,\ldots,p_M\}_C$ to be a set of training face images in subband colour channels $C, (H, S, I, Y, Cb, or\ Cr)_{LL,LH,HL,HH}$, then for a given query face image, the fvf_q is defined as a vector which is the combination of all PDFs of the query image q as follow:

$$fvf_q = \left[\mathrm{q}_{\mathrm{H}_{LL}}\cdots\mathrm{q}_{\mathrm{H}_{LH}}\cdots\mathrm{q}_{\mathrm{H}_{HL}}\cdots\mathrm{q}_{\mathrm{H}_{HH}}\cdots\right]_{1\times 6144} \tag{26}$$

where only the *H* colour channel components are shown in equation (26). This new PDF can be used to calculate the KLD between fvf_q and fvf_{pi} of the images in the training samples. fvf_q is a vector of 1×6144, where 6144 is multiplication of the bin size (which is 256) by number of colour channels (which is 6) by number of subbands (which is 4).

This new PDF can be used to calculate the KLD between fvf_q and fvf_{pj} of the images in the training samples as follows:

$$\chi_i = \min\left(\kappa\left(fvf_q, fvf_{pj}\right)\right) \quad , \quad j = 1,\cdots,M \tag{27}$$

where M is the number of images in the training set and fvf_{pj} is the combined PDFs of the j^{th} image in the training set. Thus, the similarity of the i^{th} image in the training set and the query face can be reflected by χ_i, which is the minimum KLD value. The image with the lowest KLD distance, χ_i , is declared to be the vector representing the recognized subject.

6. Results and discussions

In this paper the PCA, PCA-MV, LDA, LBP, LBP-MV, PDF based face recognition by using FVF, NMF, INMF, and the proposed PDF based face recognition system have been tested on the FERET face database with faces containing varying poses changing from -90^o to +90^o of rotation of 500 face images of 50 different classes.

6.1 Simulation results

Table 1 shows the performance of PCA based face recognition system of the FERET face database in *HSI* and *YCbCr* colour spaces respectively.

	Recognition rates of the proposed PDF based system					
# of face images in the training set	**H**	**S**	**I**	**Y**	**Cb**	**Cr**
1	36.89	48.67	49.11	47.33	49.78	49.11
2	41.50	54.75	53.50	52.50	58.25	57.75
3	52.86	62.86	56.29	56.57	67.71	64.00
4	58.00	69.00	64.67	66.00	73.67	70.33
5	62.40	74.80	69.60	72.80	77.60	74.80

Table 1. Performance of the PCA based system in *H, S, I, Y, Cb* and *Cr* colour channels of the FERET face database.

Table 2 shows the performance of LBP based face recognition system of the FERET face databases in *HSI* and *YCbCr* colour spaces.

	Recognition rates of the proposed PDF based system					
# of face images in the training set	**H**	**S**	**I**	**Y**	**Cb**	**Cr**
1	59.33	50.67	48.22	48.44	61.11	62.67
2	64.50	56.75	54.50	54.75	66.50	66.50
3	74.57	66.00	64.29	64.86	76.86	76.57
4	85.67	79.00	77.00	77.67	87.67	86.67
5	87.60	80.40	78.00	78.40	89.00	89.60

Table 2. Performance of the LBP based system in *H, S, I, Y, Cb* and *Cr* colour channels of the FERET face database.

The correct recognition rates in percent of the PDF based face recognition of LL, LH, HL, and HH subband images in different colour channels of *HSI* and *YCbCr* for the FERET face database are included in Table 3. Each result is an average of 100 runs, where we have randomly shuffled the faces in each class.

Number of training images		Recognition rates of the proposed PDF based system				
		1	**2**	**3**	**4**	**5**
H	LL	67.16	80.43	86.43	89.83	92.96
	LH	62.89	74.28	76.86	82.43	84.44
	HL	68.84	79.73	84.00	85.13	88.88
	HH	68.40	78.48	83.54	86.07	89.08
S	LL	48.27	60.23	64.20	71.00	74.72
	LH	37.27	48.10	49.14	55.20	57.56
	HL	42.76	51.63	55.46	59.63	64.76
	HH	42.49	52.60	55.83	60.17	65.84
I	LL	44.02	54.93	59.74	66.30	70.16
	LH	37.31	47.88	50.43	55.83	60.44
	HL	41.96	47.90	52.34	57.27	62.36
	HH	40.20	47.78	52.37	57.87	60.68
Y	LL	53.93	64.55	70.14	76.33	81.24
	LH	36.47	48.13	50.54	57.90	60.80
	HL	40.18	47.78	52.31	59.27	63.00
	HH	41.27	49.53	54.34	60.60	63.48
Cb	LL	56.09	67.90	74.43	79.23	83.36
	LH	29.49	33.23	35.89	40.60	42.84
	HL	42.93	50.78	55.37	56.03	58.24
	HH	29.84	33.33	35.14	37.23	38.96
Cr	LL	14.65	15.89	17.31	18.33	20.24
	LH	26.24	32.95	36.94	38.60	40.24
	HL	30.84	39.35	39.94	40.63	43.68
	HH	22.04	37.35	52.60	59.47	62.20

Table 3. Performance of the proposed PDF based face recognition system of the DWT subbands of colour images in *H, S, I, Y, Cb* and *Cr* colour channels separately for the FERET face database.

The performances of the proposed system using data fusion techniques such as sum rule, median rule, max rule, product rule, MV, and FVF, between all 24 decisions (an image with its 4 subband images in 6 colour channels) for the FERET face database are shown in Table 4. The performance of the conventional PCA, PCA-MV, LDA, and the state-of-art face recognition systems: LBP, LBP-MV, PDF based face recognition by using FVF, NMF, and INMF based face recognition systems for the FERET face database are also included in the Table 4.

Number of training images		**Recognition rate**				
		1	2	3	4	5
MV		82.22	90.45	93.69	95.60	**96.88**
FVF	H (DWT subbands)	80.44	85.50	95.43	96.33	96.40
	S (DWT subbands)	60.89	68.25	81.71	88.00	90.00
	I (DWT subbands)	63.11	68.50	84.57	91.67	93.60
	Y (DWT subbands)	80.67	85.75	95.71	96.67	96.80
	Cb (DWT subbands)	66.89	70.75	84.00	86.33	89.60
	Cr (DWT subbands)	63.33	61.50	74.29	79.67	83.20
	All subbands	82.89	87.00	96.57	98.80	**99.33**
SUM RULE		94.53	97.03	98.08	98.49	98.84
MEDIAN RULE		93.82	96.23	97.80	97.98	98.39
MAX RULE		81.71	87.78	90.37	91.83	92.87
PRODUCT RULE		16.58	0.67	0.67	0.67	0.67
PCA		44.00	52.00	58.29	66.17	68.80
LDA		61.98	70.33	77.78	781.43	85.00
PCA-MV		57.11	62.50	65.71	74.00	77.60
LBP		50.89	56.25	74.57	77.67	79.60
LBP-MV		54.44	58.75	69.14	81.00	83.20
PDF based face recognition by FVF (Demirel and Anbarjafari, IEEE Signal Processing Letter, 2008)		80.44	83.75	94.00	97.67	98.00
NMF		61.33	64.67	69.89	77.35	80.37
INMF		63.65	67.87	75.83	80.07	83.20

Table 4. Performance of the proposed face recognition system using MV, FVF, PCA, LDA, LBP, PDF based face recognition, NMF, and INMF based face recognition system for the FERET database.

The performances of the proposed system using aforementioned data fusion techniques between all decisions for the HP face database are shown in Table 5.

		Recognition Rate				
Number of training images		1	2	3	4	5
MV		77.93	91.00	92.67	95.11	97.53
FVF	H (DWT subbands)	68.89	79.17	85.71	88.89	88.00
	S (DWT subbands)	64.44	77.50	87.62	92.22	93.33
	I (DWT subbands)	54.07	64.17	77.14	87.78	84.00
	Y (DWT subbands)	69.63	80.00	86.67	90.00	89.33
	Cb (DWT subbands)	59.17	60.00	67.62	75.56	77.33
	Cr (DWT subbands)	28.15	34.17	41.90	40.00	48.00
	All subbands	88.15	93.33	97.14	98.67	**98.89**
SUM RULE		83.85	96.42	96.76	96.67	97.33
MEDIAN RULE		84.74	97.00	96.19	97.00	98.53
MAX RULE		74.74	88.17	90.95	91.47	91.67
PRODUCT RULE		84.22	97.33	96.86	97.11	96.27

Table 5. Performance of the proposed face recognition system using MV, and FVF based face recognition system for the HP face databases

6.2 Discussions

The combination of feature vectors, with 5 samples per subject in the training set, achieve 99.33% and 96.88% recognition rates by using FVF and MV methods for the FERET face database respectively. The MV and FVF results are 98.89% and 97.53% for the HP face database, when 5 samples per subject is available in the training set, respectively. The results obtained by the proposed system using FVF for the FERET database shows 30.53%, 21.73%, 14.33%, 19.73%, 16.13%, 1.33%, 18.96%, and 16.13% improvement over PCA, PCA-MV, LDA, LBP, LBP-MV, PDF based face recognition system by using FVF, NMF, and INMF respectively. In all cases both FVF and MV approaches outperform the conventional methods in the literature. As it could be predicted sum rule, median rule, and max rule are improving the recognition rate but as table 4 and 5 are showing, FVF is over performing the other fusion techniques.

7. Conclusion

In this chapter, a new high performance face recognition system using the PDFs obtained from DWT subbands in different colour channels followed by data fusion has been proposed. The PDFs of the equalized and segmented face images in different subbands of different colour channels were used as feature vectors for the recognition of faces by minimizing the KLD between the PDF of a given face and the PDFs of faces in the database. Several fusion techniques including sum rule, median rule, max rule, product rule, MV, and FVF have been employed in order to improve the recognition performance. The system was tested on the FERET and the HP face databases. The results have been compared with the conventional PCA, improved PCA by applying MV, LDA and state-of-art face recognition techniques including LBP, improved LBP by using MV, previously introduced PDF based

face recognition by using FVF, NMF, and INMF. The performance of the proposed face recognition system has clearly shown the superiority of the system over the conventional and state-of-art techniques.

8. References

A. K. Jain, R. Ross, and S. Prabhakar, "An introduction to biometric recognition", IEEE Transaction on Circuits and Systems for Video Technology, 2004, Vol. 14, No. 1, pp: 84-92.

C. C. Liu, D. Q. Dai, and H. Yan, "Local discriminant wavelet packet coordinates for face recognition", Journal of Machine Learning Research, 2007, Vol. 8, pp: 1165-1195.

C. Wen-Sheng, P. Binbin, F. Bin, L. Ming, and T. Jianliang, "Incremental nonnegative matrix factorization for face recognition", Mathematical problems in Engineering, June 2008, Vol. 2008.

D. Chai and K.N. Ngan "Face segmentation using skin color map in videophone application", IEEE Transactions on Circuits and Systems for Video Technology, 1999, Vol. 9, No. 4, pp: 551-564.

D. D. Lee, and H. S. Seung, "Learning the parts of objects by nonnegative matrix factorization", Nature, 1999, Vol. 401, No. 6755, pp: 788-791.

D. D. Lee, and H. S. Seung, "Algorithm for nonnegative matrix factorization", In proc. Of the advances in natural information processing system (NIPS' 01), 2001, Vol.13, pp: 556-562.

D. Q. Dai and H. Yan, "Wavelet and face recognition", Face recognition, Chapter 4, K. Delac and M. Grgic (Eds), ISBN: 978-3-902613-03-5, Austria, pp: 59-74, 2007.

E. Marszalec, B. Martinkauppi, M. Soriano, and M. Pietikäinen, "A physics-based face database for colour research", Journal of Electronic Imaging, 2000, Vol. 9, No. 1 pp: 32-38.

Face detector software written by M. Nilsson, provided in MathWorks. Retrieved in January 2008, http://www.mathworks.com/matlabcentral/fileexchange/13701

H. Demirel, and G. Anbarjafari, "Pose invariant face recognition using image histograms", The 3rd International Conference On Computer Vision Theory and Applications (VISAPP 2008), Portugal, Vol. 2, pp: 282-285.

H. Demirel, and G. Anbarjafari, "Pose invariant face recognition using probability distribution functions in different color channels", IEEE Signal Processing Letter, 2008, Vol. 15, pp: 537-540.

H. Demirel, A. Eleyan, and H. Özkaramanli, "Complex wavelet transform based face recognition", Eurasip Journal on Advance in Signal Processing, 2008, Vol. 2008, doi: 10.1155/2008/185281

H. Demirel, G. Anbarjafari, and M. N. Sabet Jahromi, "Skin detection in HSI colour space", 5th International Conference on Electrical and Computer Systems (EECS'08), November 27-28, 2008, Lefke, North Cyprus.

I. Laptev, "Improvements of object detection using boosted histograms", British Machine Vision Conference (BMVC), 2006, pp: III-949-958.

J. L. Starck, E. J. Candes, and D. L. Donoho, "The curvelet transform for image denoising", IEEE Transactions on Image Processing, 2002, Vol. 11, pp: 670-684.

J. W. Wang and W. Y. Chen, "Eye detection based on head contour geometry and wavelet subband projection", Optical Engineering, 2006, Vol. 45, No. 5.

M. H. Yang, D. Kriegman, and N. Ahuja. "Detecting faces in images: A survey". IEEE Transaction on Pattern Analysis and Machine Intelligence, 2002, Vol. 24(1), pp: 34–58.

M. Abdullah-Al-Wadud, H. Kabir, M. A. A.Dewan, C. Oksam, "A dynamic histogram equalization for image contrast enhancement", IEEE Transaction on Consumer Electronics, 2007, Vol. 53, pp: 593-600.

M. Lamard, W. Daccache, G. Cazuguel, C. Roux, and B. Cochener, "Use of a JPEG-2000 wavelet compression scheme for content-based ophtalmologic retinal images retrieval", 27th Annual International Conference of the Engineering in Medicine and Biology Society, IEEE-EMBS 2005, pp: 4010 – 4013.

M. Nilsson, J. Nordberg, and I. Claesson, " Face detection using local SMQT features and split up SNOW classifier ", International Conference on Acoustic, Speech, and Signal Processing (ICASSP) 2007, Vol. 2, pp: II-589 – II-592.

M. N. Sabet Jahromi, H. Demirel, and G. Anbarjafari, "Image equalization based on singular value decomposition", 23rd International Symposium on Computer and Information Sciences, ISCIS 2008, Istanbul, Turkey.

M. Turk and A. Pentland, "Face recognition using eigenfaces," in Proceeding of International Conference On Pattern Recognition, 1991, pp: 586-591.

N. Gourier, D. Hall, J. L. Crowley, "Estimating face orientation from robust detection of salient facial features", Proceedings of Pointing International Workshop on Visual Observation of Deictic Gestures 2004, Cambridge, UK.

P. Belhumeur, J. Hespanha, and D. Kreigman, "Eigenfaces vs. Fisherfaces: Recognition using class specific linear projection," IEEE Transactions on Pattern Analysis and Machine Intelligence, 1997, Vol. 19, pp: 7 11-720.

P. J. Philips, H. Moon, S. A. Rizvi, and P.J. Rauss, "The FERET evaluation methodology for face recognition algorithm", IEEE Transaction on Pattern Analysis and Machine Intelligence, 2000, Vol. 22, No. 10.

R. Polikar, "Ensemble based systems in decision making", IEEE Circuits and Systems Magazine, 2006, Vol.6, No.3, pp: 21-45.

S. Marcel, and S. Bengio, "Improving face verification using skin color information," Proceeding 16th International Conference on Pattern Recognition, 11-15 Aug 2002, Vol. 2, pp: 378-381.

T. Ahnon, A. Hadid, and Pietikainen, "Face recognition with local binary patterns", European Conference on Computer Vision, 2004, pp. 469-481.

T. Ojala, M. Pietikainen, and D. Harwood, "A comparative study of texture measures with classification based on featured distributions", Pattern Recognition, 1996, Vol. 29, pp. 51-59.

T. Ojala, M. Pietikainen, and T. Maenpaa, "Multiresolution gray-scale and rotation invariant texture classification with local binary patterns", IEEE Transactions on Pattern Analysis and Machine Intelligence, 2002, Vol. 24, pp. 971–987.

Tae-Woong Yoo, Il-Seok Oh, "A fast algorithm for tracking human faces based on chromatic PDFs", Pattern Recognition Letters, 1999, Vol. 20, pp:967-978.

Wavelet MATLAB Toolbox prepared by Ivan Selesnick, Retrieved in January 2009, http://taco.poly.edu/WaveletSoftware/

W.W. Bledsoe, "The Model Method in Facial Recognition", Panoramic Research Inc., Palo Alto, Cal., and Rep. PRI: 15, CA, 1964.

Y. Rodriguez and S. Marcel, "Face authentication using adapted local binary pattern PDFs". Proceedings of the 9th European Conference on Computer Vision (ECCV), Graz, Austria, May 7-13 2006, pp: 321-332.

Y. Tian, T. Tan, Y. Wang, and Y. Fang, "Do singular values contain adequate information for face recognition?", Pattern Recognition, 2003, Vol. 36, pp: 649 – 655.

7

An Improved Low Complexity Algorithm for 2-D Integer Lifting-Based Discrete Wavelet Transform Using Symmetric Mask-Based Scheme

Chih-Hsien Hsia[1], Jing-Ming Guo[1] and Jen-Shiun Chiang[2]
[1]*Department of Electrical Engineering,*
National Taiwan University of Science and Technology
[2]*Department of Electrical Engineering, Tamkang University*
Taipei,
Taiwan

1. Introduction

Communication and multimedia have been developed rapidly in recent years. Digital media and services found in daily life include, such as digital cameras, VCD (Video Compact Disc), DVD (Digital Video Disc), HDTV (High-Definition TeleVision) and video conferences. Several well-known compression schemes, such as Differential Pulse Code Modulation (DPCM)-based method (Habibi & Hershel, 1974), DCT-based methods (Feig et al., 1995)(Kondo & Oishi, 2000), and Wavelet-based methods (Mallat, 1989) have been well-developed in recent years. The lifting-based scheme has recently provided a less-complexity solution for image/video applications, e.g., JPEG2000, Motion-JPEG2000, MPEG-4 still image coding, and MC-EZBC (Motion Compensation- Embedded Zero Block Coding). However, the real-time 2-D DWT (software-based) is still difficult to be achieved. Hence, an efficient transformation scheme for large of multimedia files is highly demanded.

Filter banks for the applications of subband image/video coding were introduced in the 1990s. Wavelet coding has been studied extensively since then. Wavelet coding has been successfully applied to many applications. The most significant applications include subband coding for audio, image, video, signal analysis and representation using wavelets. In the past few years, DWT (Mallat, 1989) has been adopted in a wide range of applications including image coding and video compression, including speech analysis, numerical analysis, signal analysis, image coding, pattern recognition, computer vision and biometrics. The DWT can be viewed as a multi-resolution decomposition of a signal, meaning which decomposes a signal into several components in different wavelet frequency bands. Moreover, 2-D DWT is a modern tool for signal processing applications, such as JPEG2000 still image compression, denoising, region of interest (ROI), and watermarking. By factoring the classical wavelet filter into lifting steps, the computational complexity of the corresponding DWT can be reduced by up to 50% (Daubechies & Sweldens, 1998). The lifting steps can be easily implemented, which is different from the direct finite impulse

response (FIR) implementations of Mallat's algorithm (Daubechies & Sweldens, 1998). Several lifting-based DWT hardware architectures have recently been proposed. The 2-D DWT architecture described by Chiang *et al.* (Chiang et al., 2005) is based on the new interlaced read scan algorithm with pipeline processing to achieve low-transpose memory size and high-speed operation. Chiang *et al.* (Chiang & Hsia, 2005) proposed a 2-D DWT folded architecture to improve the hardware utilization. Andra *et al.* (Andra et al., 2000) and (Andra et al., 2002) proposed simple processing units that compute several stages of the DWT at a time. An architecture performs the lifting-based DWT with the 5/3 filter, which is based on the interleaving technique presented in (Diou et al., 2001). Chen *et al.* (Chen & Wu, 2002) used a 1-D folded architecture to improve the hardware utilization for 2-D 5/3 and 9/7 filters. The recursive architecture is a general scheme to implement any wavelet filter that is decomposable into lifting steps (Lian et al., 2001) in small-size and low-power design. Despite these efficiency improvements of the existing architecture, further improvements in the algorithm and architecture are required. For this, Tan *et al.* (Tan & Arslan, 2003) presented a novel shift-accumulator arithmetic logic units architecture for 2-D lifting-based JPEG2000 5/3 DWT. The architecture has an efficient memory organization, which uses a smaller amount of embedded memory for processing and buffering. Lee *et al.* (Lee et al., 2003) proposed a new signal flow operation approach for the DWT implementation, and adopted only a memory size of N is employed for an $N \times N$ 2-D DWT. Varshney *et al.* (Varshney et al., 2007) presented energy efficient single-processor and fully pipelined architectures for the 2-D 5/3 lifting-based JPEG2000. The single processor performs both the row-wise and column-wise processing simultaneously, thus achieving, full 2-D transform with 100% hardware utilization. In (Chen, 2002) proposed one flexible and folded architecture for 3-level 1-D Lifting-based DWT to increase hardware utilization. Liao *et al*. (Liao et al., 2004) proposed two similar 2-D lifting-based 9/7 DWT generic architectures by employing parallel and pipeline techniques with recursive pyramid algorithms. Those architectures achieve multilevel decomposition using an interleaving scheme that reduces the size of memory and the number of memory accesses, while having a slow throughput rate and inefficient hardware utilization. Some VLSI architectures of 2-D lifting-based DWT reduce the transpose memory requirements and communication between the processors. However, these architectures need large transpose memory and long latency time.

Low-transpose memory requirement and latency reduction are the major concerns in 2-D DWT implementation. This work presents a new approach, namely 2-D Symmetric Mask-based DWT algorithm (SMDWT), to improve the 2-D lifting-based DWT (LDWT), and further applies it 2-D DWT real-time applications.

2. Lifting-based Discrete Wavelet Transform

Filtering and convolution are applied to achieve the signal decomposition in classical DWT. In 1986, Meyer and Mallat found that the orthonormal wavelet decomposition and reconstruction can be implemented in the multi-resolution signal analysis framework (Mallat, 1989). Multi-resolution analysis is now a standard method for constructing the orthonormal wavelet bases. Figure 1 shows the framework of the 2-D DWT. In the decomposition process, the low-pass filter H and high-pass filter G denote the scaling functions and the corresponding wavelets, respectively. Given a filter of length four, the corresponding transfer functions of filters H and G can be represented as,

$$H(z)=h_0+h_1z^{-1}+h_2z^{-2}+h_3z^{-3}, \tag{1}$$

$$G(z)=g_0+g_1z^{-1}+g_2z^{-2}+g_3z^{-3}. \tag{2}$$

The downsampling operation is then applied to the filtered results. A pair of filters are applied to the signal to decompose the image into the low-low (LL), low-high (LH), high-low (HL), and high-high (HH) wavelet frequency bands. Consider an image of size $N\times N$, Each band is subsampled by a factor of two, so that each wavelet frequency band contains $N/2\times N/2$ samples. The four bands can be integrated to generate an output image with the same number of samples as the original.

In most image compression applications, the above 2-D wavelet decomposition can be applied again to the *LL* sub-image, forming four new subband images, and so on to achieve a compact energy in the lower frequency bands.

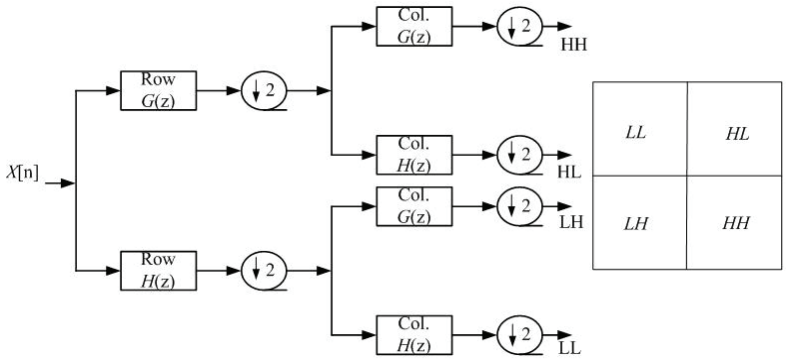

Fig. 1. The 2-D analysis DWT image decomposition process.

2.1 Lifting-based DWT algorithm

The lifting-based scheme proposed by Daubechies and Sweldens requires fewer computations than the traditional convolution-based approach (Sweldens, 1996)(Daubechies & Sweldens, 1998). The lifting-based scheme is an efficient implementation for DWT. It can easily use integer operations, and avoids the problems caused by the finite precision or rounding. The Euclidean algorithm can be used to factorize the poly-phase matrix of a DWT filter into a sequence of alternating upper and lower triangular matrices and a diagonal matrix. The variables $h(z)$ and $g(z)$ in Eq. 3 respectively denote the low-pass and high-pass analysis filters, which can be divided into even and odd parts to generate a poly-phase matrix $P(z)$ as in Eq. 4.

$$\begin{aligned} g(z)&=g_e(z^2)+z^{-1}g_o(z^2),\\ h(z)&=h_e(z^2)+z^{-1}h_o(z^2). \end{aligned} \tag{3}$$

$$P(z)=\begin{bmatrix} h_e(z) & g_e(z) \\ h_o(z) & g_o(z) \end{bmatrix}. \tag{4}$$

The Euclidean algorithm recursively finds the greatest common divisors of the even and odd parts of the original filters. Since $h(z)$ and $g(z)$ form a complementary filter pair, $P(z)$ can be factorized into Eq. 5.

$$P(z)=\prod_{i=1}^{m}\begin{pmatrix}1 & si(z)\\ 0 & 1\end{pmatrix}\begin{pmatrix}1 & 0\\ ti(z) & 1\end{pmatrix}\begin{pmatrix}k & 0\\ 0 & 1/k\end{pmatrix}. \quad (5)$$

where $si(z)$ and $ti(z)$ are Laurent polynomials corresponding to the prediction and update steps, respectively, and k is a nonzero constant. Therefore, the filter bank can be factorized into three lifting steps. As illustrated in Fig. 2, a lifting-based scheme has the following four stages:

1) Split phase: The original signal is divided into two disjoint subsets. Significantly, the variable *Xe* denotes the set of even samples and *Xo* denotes the set of odd samples. This phase is called lazy wavelet transform because it does not decorrelate the data, but only subsamples the signal into even and odd samples.

2) Predict phase: The predicting operator P is applied to the subset *Xo* to obtain the wavelet coefficients d[n] as in Eq. 6.

$$d[n]=Xo[n]+P\times(Xe[n]). \quad (6)$$

3) Update phase: Xe[n] and d[n] are combined to obtain the scaling coefficients s[n] after an update operator U as in Eq. 7.

$$s[n]=Xe[n]+U\times(d[n]). \quad (7)$$

4) Scaling: In the final step, the normalization factor is applied on s[n] and d[n] to obtain the wavelet coefficients. Equations 8 and 9 describe the implementation of the 5/3 integer lifting analysis DWT and are used to calculate the odd coefficients (high-pass coefficients) and even coefficients (low-pass coefficients), respectively.

$$d^*[n]=X(2n+1)-\lfloor X(2n)+X(2n+2)/2\rfloor \quad (8)$$

$$s^*[n]=X(2n)+\lfloor d(2n-1)+d(2n+1)+2/4\rfloor \quad (9)$$

Although the lifting-based scheme has less complexity, its long and irregular data paths constitute a major limitation for efficient hardware implementation. Additionally, the increasing number of pipelined registers increases the transpose memory size of the 2-D DWT architecture.

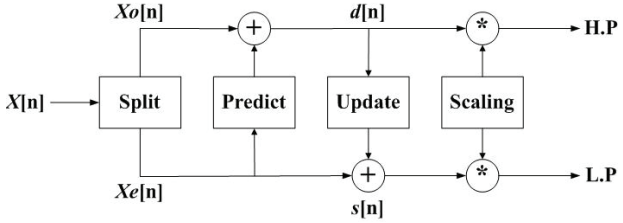

Fig. 2. Block diagram of the lifting-based DWT.

2.2 Lossless 2-D 5/3 lifting-based DWT structure

The 2-D DWT uses a vertical 1-D DWT subband decomposition and a horizontal 1-D DWT subband decomposition to obtain the 2-D DWT coefficients. Therefore, the memory

requirement dominates the hardware cost and complexity of the architectures for 2-D DWT. The 2-D transform operation is shown in Fig. 3.

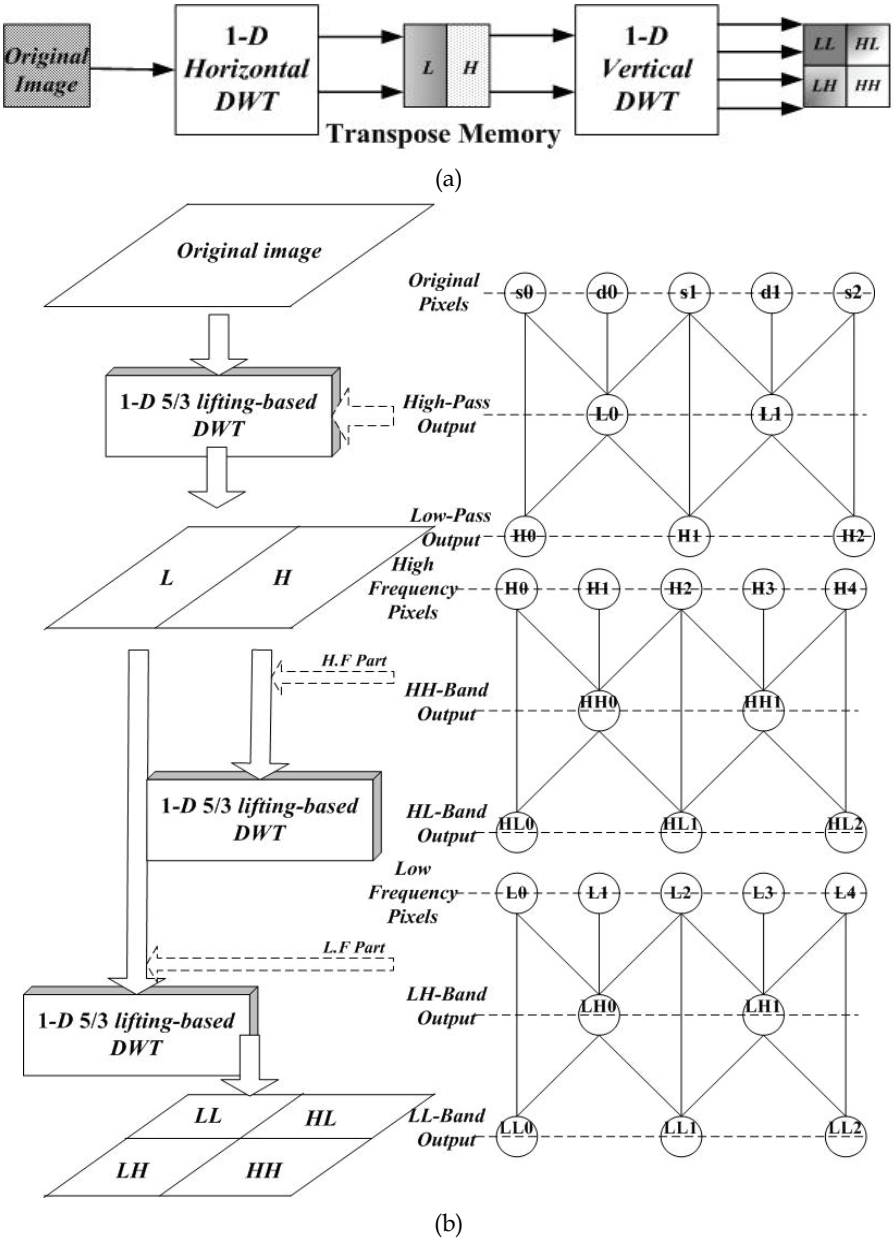

Fig. 3. 2-D LDWT operation. (a) The flow of a traditional 2-D DWT. (b) Detailed processing flow.

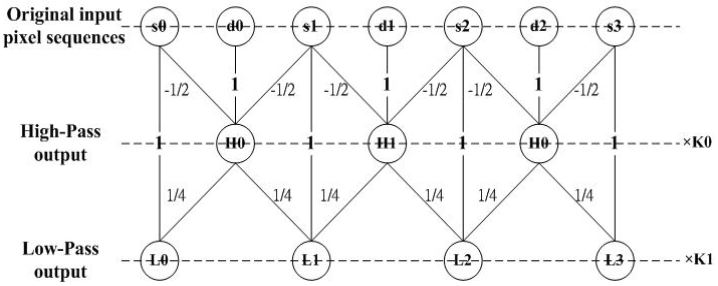

Fig. 4. Lifting-based 5/3 DWT algorithm.

Figure 4 shows the lifting step associated with the wavelet. The original signals including *s*0, *d*0, *s*1, *d*1, *s*2, *d*2, ... are the original input pixel sequences. If the original data are infinite in length, then the first-stage lifting is applied to update the odd index data *s*0, *s*1, …. In Eq. 10, the parameters -1/2 and H*i* denote the first stage lifting parameter and outcome, respectively. After all the odd index data points are calculated, the second stage lifting can be performed with Eq. 11, where those parameters denote the second stage lifting parameters and outcomes, respectively. The variables H*n* and L*n* are the high-pass and low-pass coefficients. The values of the lifting parameters -1/2, 1, and 1/4 as shown in Fig. 4 are used for the prediction module (H*i*), the update module (L*i*) and the K*n* module (scaling by K*n*=1), respectively.

$$H_i = [(s_i + s_{i+1}) \times -1/2 + d_i] \times K_0, \tag{10}$$

$$L_i = [(H_i + H_{i-1}) \times 1/4 + s_i] \times K_1, \tag{11}$$

$$K_0 = K_1 = 1. \tag{12}$$

3. The proposed 2-D symmetric mask-based Discrete Wavelet Transform

LDWT is widely employed in the visual subband coding, because it inherently has the well-known perfect reconstruction property. However, LDWT has high-transpose memory requirement and operation time in 2-D transform, as shown in Fig. 3. The memory requirement and operation speed are the two major concerns in 2-D DWT implementation. The row and column-wise signal flow operation is generally adopted for an $N \times N$ 2-D DWT. However, the memory requirement of this scheme ranges from $2.5N$ to N^2. To solve the transpose memory access problem, this work proposes a low-latency and low-memory architecture for 1-level 2-D lifting-based DWT. The previous signal flow from row- and column-wise is replaced with mask-based processing, SMDWT, to reduce the transpose memory requirement for the 2-D DWT. The SMDWT has many advanced features, such as short critical path, less latency time, regular signal coding, and independent subband processing. The following subsections introduce the 2-D SMDWT where the coefficients of mask wavelet coefficient derivation are based on the 2-D 5/3 integer lifting-based DWT.

3.1 The 2-D SMDWT structure

This sub-section, the proposed SMDWT is discussed in three aspects: lifting structure, transpose memory, as well as latency and critical path. The proposed SMDWT algorithm

has the advantages of fast computational speed, less complexity, reduced latency, and regular data flow.

For speed and simplicity, four-masks, 3×3, 5×3, 3×5, and 5×5, are generally used to perform spatial filtering tasks. Moreover, the four-subband processing can be further optimized to speed up and reduce the transpose memory of DWT coefficients. The four-matrix processors consist of four mask filters, and each filter is derived from one 2-D DWT of 5/3 integer lifting-based coefficients. In LDWT implementation, a 1-D DWT needs massive computations, so the computation unit dominants the hardware cost (Chiang & Hsia, 2005)(Andra et al., 2002). A 2-D DWT is compose of two 1-D DWTs and a block of transpose memory, which is of the same size of the processed image. The transpose memory is the main overhead of the computation unit in the 2-D DWT. Figure 3 shows the block diagram of a traditional 2-D DWT. Without loss of generality, the 5/3 lifting-based 2-D DWT is adopted for comparison. Assuming that the image is of size $N \times N$, during the transformation, a large amount of transpose memory (order of N^2) is needed to store the temporary data after the first stage 1-D DWT decomposition. The second stage 1-D DWT is then applied to the stored data to obtain the four-subband (HH, HL, LH, and LL) results of the 2-D DWT. Because the memory requirement of size N^2 is huge and the processing is too long, this work proposes a new approach, called 2-D SMDWT, to reduce the transpose computing latency and critical path. Figure 5(a) shows the concept of the proposed SMDWT architecture, which consists of input arrangement, processing element, memory unit, and control unit, as shown in Fig. 5(b). The outputs are fed to the 2-D DWT four-subband coefficients, HH, HL, LH, and LL. Significant transpose memory can be saved using the proposed approach. This architecture is described in detail in the following subsections, and is illustrated in Figs. 5, 7(c), 8(c), 11(c), and 14(c). This study focuses on the 5/3 lifting-based 2-D DWT complexity reduction.

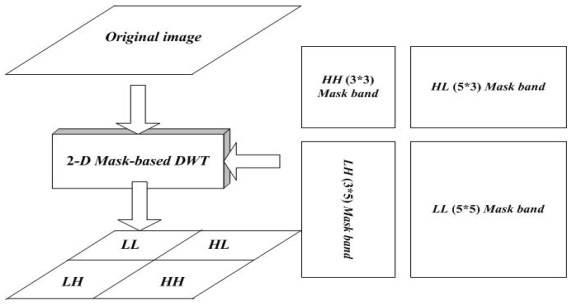

(a)

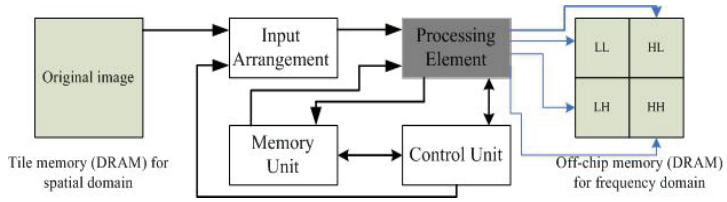

(b)

Fig. 5. The system block diagram of the proposed 2-D DWT. (a) 2-D SMDWT. (b) Block diagram of the proposed system architecture.

Without loss of generality, let us take a 6×6-pixel image is employed to demonstrate the 5/3 LDWT operations as shown in Fig. 6. In Fig. 6, the variable $x(i,j)$ denotes the original image. The upper part of Fig. 6 shows the first stage 1-D LDWT operations, and the lower part of Fig. 6 shows the second stage 1-D LDWT operations for evaluating the four-subband coefficients, HH, HL, LH, and LL. In the first stage of the 1-D LDWT, three pixels are used to evaluate a 1-D high-frequency coefficient. For example, $x(0,0)$, $x(0,1)$, and $x(0,2)$ are used to calculate the high-frequency wavelet coefficient $b(0,0)$, where

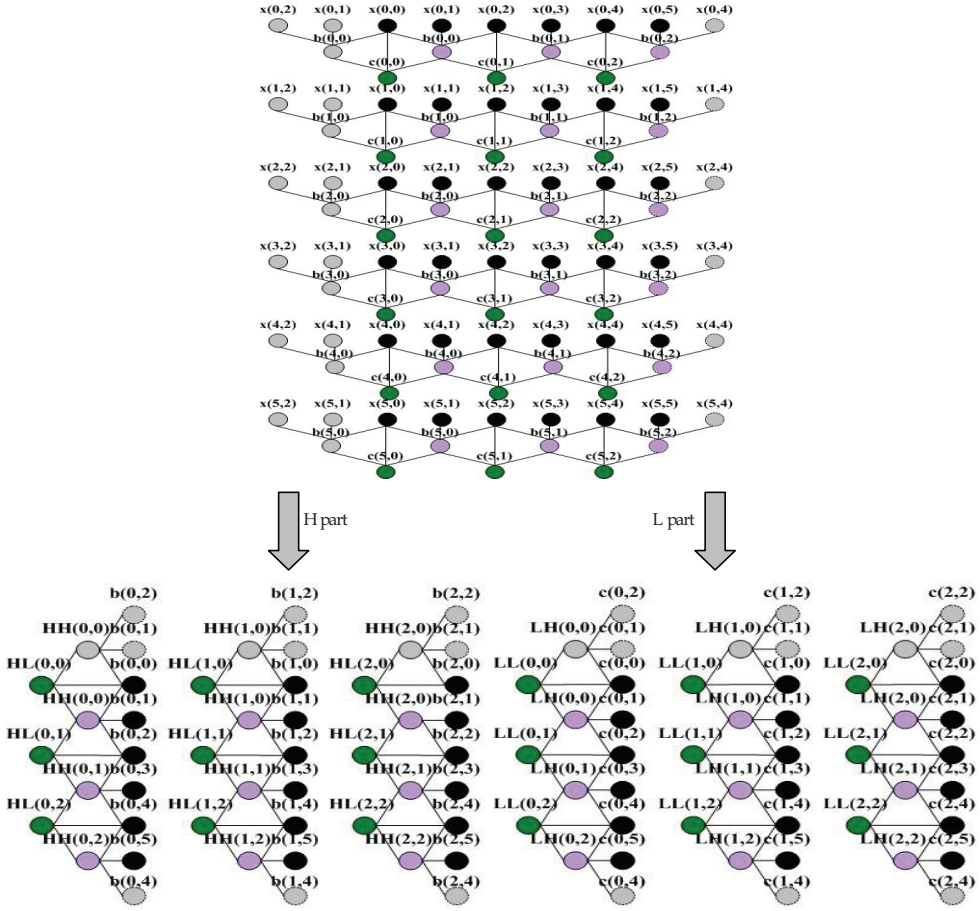

$x(i,j)$: original image, i = 0~5 and j = 0~5
$b(i,j)$: high frequency wavelet coefficient of 1-D LDWT
$c(i,j)$: low frequency wavelet coefficient of 1-D LDWT
HH: high-high frequency wavelet coefficient of 2-D LDWT
HL: high-low frequency wavelet coefficient of 2-D LDWT
LH: low-high frequency wavelet coefficient of 2-D LDWT
LL: low-low frequency wavelet coefficient of 2-D LDWT

Fig. 6. Example of 5/3 LDWT operations.

$b(0,0)=-[x(0,0)+x(0,2)]/2+x(0,1)$. The pixels, $x(0,2)$, $x(0,3)$, and $x(0,4)$ are used to calculate the next high-frequency wavelet coefficient $b(0,1)$. Herein $x(0,2)$ is used to calculate both of $b(0,0)$ and $b(0,1)$, and is called the overlapped pixel. The low-frequency wavelet coefficient is calculated using two consecutive high-frequency wavelet coefficients and the overlapped pixel. For example, $b(0,0)$ and $b(0,1)$ cope with $x(0,2)$ to find the low-frequency wavelet coefficient $c(0,1)$, where $c(0,1)=[b(0,0)+b(0,1)]/4+x(0,2)$. The calculated high-frequency wavelet coefficients, $b(i,j)$, and the low frequency wavelet coefficients, $c(i,j)$, are then used in the second stage 1-D LDWT to calculate the four-subbands coefficients, HH, HL, LH and LL. The general form of the mask coefficients is derived first, and the complexity is further reduced by employing the symmetric feature of the mask.

3.2 Simplified 2-D SMDWT using symmetric features

1. High-High (HH) band mask coefficients reduction for 2-D SMDWT

According to the 2-D 5/3 LDWT, the HH band coefficients of the SMDWT can be derived as follows:

$$HH(i,j)=x(2i+1,2j+1)+(1/4)\sum^{1}_{u=0}\sum^{1}_{v=0}x(2i+2u,2j+2v)+(-1/2)\sum^{2}_{u=-1}x(2i+|u|,2j+|1-u|). \quad (13)$$

The mask as shown in Fig. 7(a) can be obtained by Eq. 13, where the variables $\alpha=-1/2$, $\beta=1/4$, and $\gamma=1$. Figure 7(b) shows the DSP architecture and Fig. 7(c) shows the hardware architecture.

The transpose memory requirement is a very important issue in multimedia IC design. Therefore, to make the SMDWT architecture suitable for VLSI implementation, the design processing element must be as simple and modular as possible. However, the product of cost and computation time is always the most important consideration from a standardization provides economies of scale for VLSI solution point of view. Therefore, speed is sometimes sacrificed to obtain less cost hardware, while still satisfying the performance requirement. In other words, the SMDWT architecture can be decomposed so as to adjust the cost and computation time product. Its hardware cost and computation time tradeoffs must be carefully considered to find the optimal design for VLSI implementation. A simple SMDWT method for cost and computation time savings is introduced below.

Figure 7(c) shows the concept of the proposed HH-band architecture for SMDWT. The proposed HH-band architecture consists of a shifter (α, β, and γ) and one adder tree with propagation registers, as shown in Fig. 7(c). The architecture design can be divided as follows:

- Input arrangement unit: Three pixels in a column are inputted into a processing element for address generator circuits in each cycle. Simultaneously, the input arrangement to assign input original signals used in multiplexer (MUX) fetch 3 pixels in each cycle to switch for group 1, group 2 and group 3 to operations, respectively.
- Coefficient shifter unit: The coefficient shifter values are $\alpha=-1/2$, $\beta=1/4$, and $\gamma=1$. Shifters replace multipliers to achieve a high-efficiency architecture by (reducing computational time, critical path, area cost and power consumption (Tan & Arslan, 2003)).
- Adder tree unit: An adder tree architecture is adopted to avoid the long signal path length, signal skewing, and hazards caused by signal dependency. Each adder tree level can be viewed as a parallel pipeline stage. This architecture is suitable for the realization in hardware design.

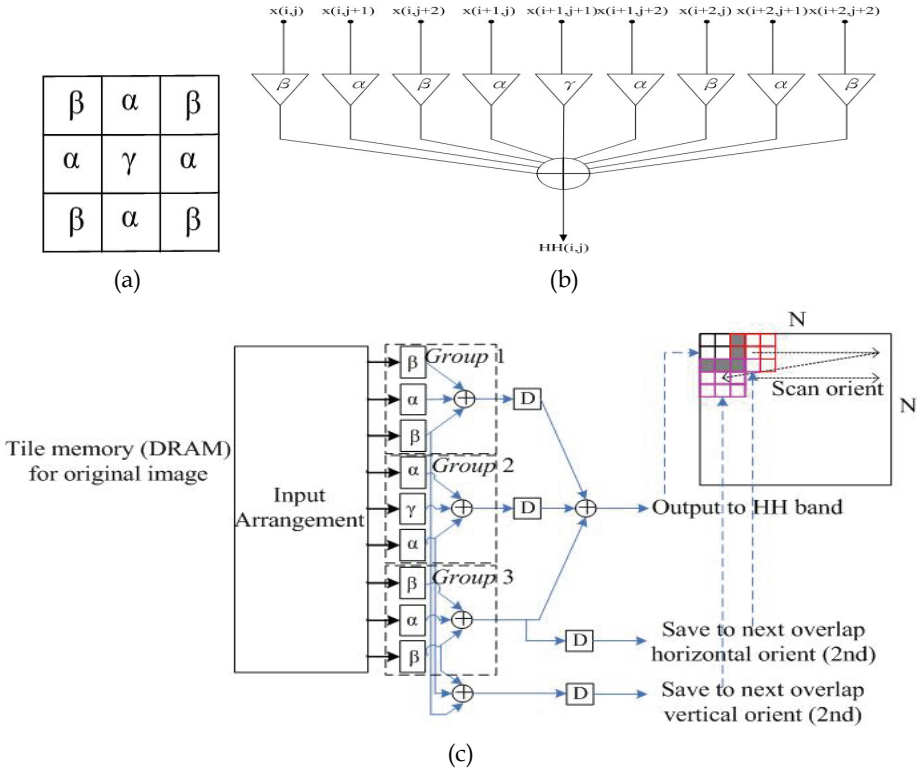

Fig. 7. HH band mask coefficients and the corresponding DSP architecture. (a) Coefficients. (b) DSP architecture. (c) Hardware architecture design.

- Propagation register unit: Current pixels are stored to assign subband coefficients computation needs in each group, and next horizontal or vertical scan oriented computation are stored in propagation registers for data reuse. This approach can reduce the next access time and computations. The pipeline design is the best method to improve the system throughput.

Based on this structure, the coefficient overlap part can be reused as show in Fig. 7(c).
The complexity of the mask-based method is further reduced by employing the symmetric feature of the mask. First, the initial horizontal scan is expressed by:

$$HH(0,0)=\beta\times x(0,0)+\alpha\times x(0,1)+\underline{\beta\times x(0,2)}+\alpha\times x(1,0)+\gamma\times x(1,1)$$
$$+\underline{\alpha\times x(1,2)}+\beta\times x(2,0)+\alpha\times x(2,1)+\underline{\beta\times x(2,2)} \quad (14)$$

The next coefficient can be calculated by:

$$HH(0,1)=\underline{\beta\times x(0,2)}+\alpha\times x(0,3)+\beta\times x(0,4)+\underline{\alpha\times x(1,2)}+\gamma\times x(1,3)+\alpha\times x(1,4)+\underline{\beta\times x(2,2)}+\alpha\times x(2,3)+\beta\times x(2,4)$$
$$=\alpha\times x(0,3)+\beta\times x(0,4)+\gamma\times x(1,3)+\alpha\times x(1,4)+\alpha\times x(2,3)+\beta\times x(2,4)+XM_H$$
$$=\beta\times(x(0,4)+x(2,4))+\alpha\times(x(0,3)+x(1,4)+x(2,3))+\gamma\times x(1,3)+XM_H, \quad (15)$$

where the variable XM_H denotes the repeated part after the horizontal third coefficient, where X denotes group of pixels x, M denotes the mask, and H denotes horizontal orientation. The general form can be derived as:

$$XM_H=\beta\times x(i,2j+2)+\alpha\times x(i+1,2j+2)+\beta\times x(i+2,2j+2). \quad (16)$$

Since γ=1, the general form can be expressed as:

$$HH(i,j+1)=\beta\times(x(i,2j+4)+x(i+2,2j+4))+\alpha\times(x(i,2j+3)+x(i+1,2j+4)+x(i+2,2j+3))+x(i+1,2j+3)+XM_H, \quad (17)$$

where i=0~N-1, j=0~N-2.
The vertical scan can be done in the same way, where HH(0,0) is the same as that in Eq. 14. The next coefficient can be calculated by:

$$HH(1,0)=\underline{\beta\times x(2,0)}+\underline{\alpha\times x(2,1)}+\underline{\beta\times x(2,2)}+\alpha\times x(3,0)+\gamma\times x(3,1)+\alpha\times x(3,2)+\beta\times x(4,0)+\alpha\times x(4,1)+\beta\times x(4,2)$$

$$=\alpha\times x(3,0)+\beta\times x(4,0)+\gamma\times x(3,1)+\alpha\times x(4,1)+\alpha\times x(3,2)+\beta\times x(4,2)+XM_V, \quad (18)$$

where the variable XM_V denotes the repeated part after the vertical third coefficient, where V denotes vertical orientation. The general form can be derived as:

$$XM_V=\beta\times x(2i+2,j)+\alpha\times x(2i+2,j+1)+\beta\times x(2i+2,j+2). \quad (19)$$

Since γ=1, the general form can be expressed as:

$$HH(i+1,j)=\beta\times(x(2i+4,j)+x(2i+4,j+2))+\alpha\times(x(2i+3,j)+x(2i+4,j+1)+x(2i+3,j+2))+x(2i+3,j+1)+XM_V. \quad (20)$$

where i=0~N-1, j=0~N-2.
Finally, the diagonal oriented scan can be derived as:

$$HH(1,1)=\underline{\beta\times x(2,2)}+\underline{\alpha\times x(2,3)}+\underline{\beta\times x(2,4)}+\alpha\times x(3,2)+\gamma\times x(3,3)+\alpha\times x(3,4)+\beta\times x(4,2)+\alpha\times x(4,3)+\beta\times x(4,4)$$

$$=\gamma\times x(3,3)+\alpha\times x(3,4)+\alpha\times x(4,3)+\beta\times x(4,4)+XM_D$$

$$=\beta\times x(4,4)+\alpha\times(x(3,4)+x(4,3))+\gamma\times x(3,3)+XM_D, \quad (21)$$

where the variable XM_D denotes the repeated part after the vertical fifth coefficient, where D denotes diagonal orientation. The general form can be expressed as:

$$XM_D=\beta\times x(2i+2,2j+2)+\alpha\times x(2i+2,2j+3)+\beta\times x(2i+2,2j+4)+\alpha\times x(2i+3,2j+2)+\beta\times x(2i+4,2j+2). \quad (22)$$

Since γ=1, the general form can be expressed as:

$$HH(i+1,j+1)=\beta\times x(2i+4,2j+4)+\alpha\times(x(2i+3,2j+4)+\beta\times x(2i+4,2j+3))+x(2i+3,2j+3)+XM_D. \quad (23)$$

where i=0~N-1, j=0~N-2.
The repeat part is only needed to be calculated once throughout the whole image. Hence it greatly reduces the complexity of the SMDWT.

2. High-Low (HL) and Low-High (LH) band mask coefficients reduction for 2-D SMDWT

According to the 2-D 5/3 lifting-based DWT, the HL-band coefficients of the mask-based DWT can be expressed as follows:

$$HL(i,j)=(3/4)x(2i+1,2j)+(1/16)\sum^{1}_{u=0}\sum^{1}_{v=0}x(2i+4u,2j-2+2v)+(-1/8)\sum^{1}_{u=0}x(2i+4u,2j)$$

$$+(-1/8)\sum^{1}_{u=0}\sum^{1}_{v=0}x(2i+2u,2j-1+2v)+$$

$$(1/4)\sum^{1}_{u=0}x(2i+1,2j-1+2u)+(-3/8)\sum^{1}_{u=0}x(2i+2u,2j). \quad (24)$$

The mask as shown in Fig. 8(a) can be obtained via Eq. 24, where α=-1/8, β=1/16, γ=1/4, δ=-3/8, and ε=3/4. The DSP and hardware architecture are also depicted in Figs. 8(b) and (c). The complexity of the SMDWT is further reduced by employing the symmetric feature of the mask.

The initial horizontal scan is expressed by:

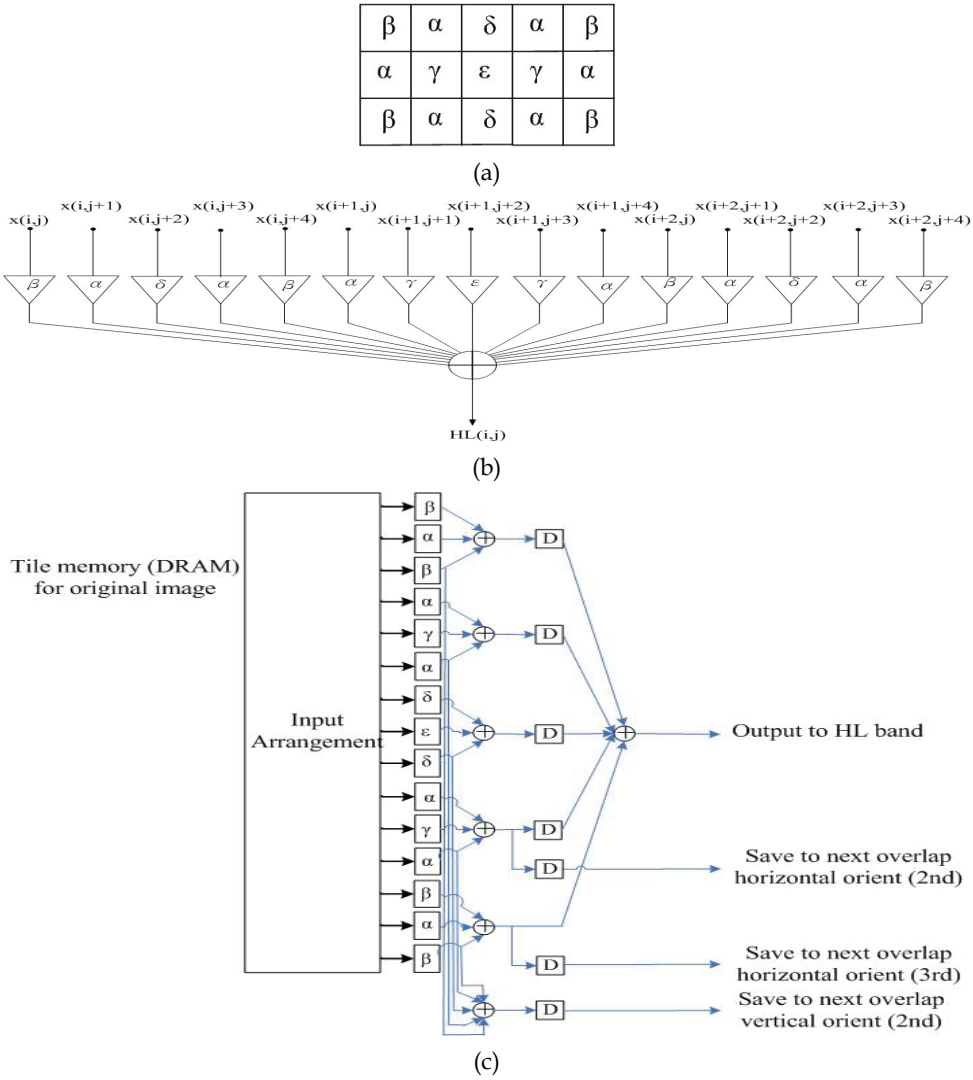

Fig. 8. HL band mask coefficients and the corresponding DSP architecture. (a) Coefficients. (b) DSP architecture. (c) Hardware architecture design.

$$HL(0,0)=\beta\times x(0,0)+\alpha\times x(0,1)+\delta\times x(0,2)+\underline{\alpha\times x(0,3)}+\underline{\beta\times x(0,4)}+\alpha\times x(1,0)+\gamma\times x(1,1)+\varepsilon\times x(1,2)+$$
$$+\gamma\times x(1,3)+\alpha\times x(1,4)+\beta\times x(2,0)+\alpha x(2,1)+\delta\times x(2,2)+\alpha\times x(2,3)+\beta\times x(2,4)$$
$$=\beta\times x(0,0)+\alpha\times x(0,1)+\delta\times x(0,2)+\underline{\beta\times x(0,4)}+\alpha\times x(1,0)+\gamma\times x(1,1)+\varepsilon\times x(1,2)+$$
$$+\underline{\alpha\times x(1,4)}+\beta\times x(2,0)+\alpha\times x(2,1)+\delta\times x(2,2)+\underline{\beta\times (2,4)}+XM_{H+1}, \quad (25)$$

where the variable XM_{H+1} denotes the repeated part after the first horizontal coefficient. The next coefficient can be calculated as:

$$HL(0,1)=\beta\times x(0,2)+\underline{\alpha\times x(0,3)}+\delta\times x(0,4)+\underline{\alpha\times x(0,5)}+\beta\times x(0,6)+\alpha\times x(1,2)+\underline{\gamma\times x(1,3)}+\varepsilon\times x(1,4)+$$
$$+\underline{\gamma\times x(1,5)}+\alpha\times x(1,6)+\beta\times x(2,2)+\underline{\alpha x(2,3)}+\delta\times x(2,4)+\underline{\alpha\times x(2,5)}+\beta\times x(2,6)$$
$$=\beta\times x(0,2)+\delta\times x(0,4)+\underline{\alpha\times x(0,5)}+\beta\times x(0,6)+\alpha\times x(1,2)+\varepsilon\times x(1,4)+\underline{\gamma\times x(1,5)+}$$
$$+\alpha\times x(1,6)+\beta\times x(2,2)+\delta\times x(2,4)+\underline{\alpha\times x(2,5)}+\beta\times (2,6)+XM_{H+1}, \quad (26)$$

The general form of the first horizontal step can be derived as:

$$HL(i,1)=\beta\times x(i,j+2)+\delta\times x(i,j+4)+\alpha\times x(i,j+5)+\beta\times x(i,j+6)+\alpha\times x(i+1,j+2)+\varepsilon\times x(i+1,j+4)+$$
$$+\gamma\times x(i+1,j+5)+\alpha\times x(i+1,j+6)+\beta\times x(i+2,j+2)+\delta\times x(i+2,j+4)+\alpha\times x(i+2,j+5)+\beta\times x(i+2,j+XM_{H+1}, \quad (27)$$

where i=0~N-1, and

$$XM_{H+1}=\alpha\times x(i,3)+\gamma\times x(i+1,3)+\alpha\times x(i+2,3). \quad (28)$$

The next coefficient can be calculated as:

$$HL(0,2)=\underline{\beta\times x(0,4)}+\underline{\alpha\times x(0,5)}+\delta\times x(0,6)+\alpha\times x(0,7)+\beta\times x(0,8)+\underline{\alpha\times x(1,4)}+\underline{\gamma\times x(1,5)+}$$
$$+\varepsilon\times x(1,6)+\gamma\times x(1,7)+\alpha\times x(1,8)+\underline{\beta\times x(2,4)}+\underline{\alpha x(2,5)}+\delta\times x(2,6)+\alpha\times x(2,7)$$
$$+\beta\times x(2,8)=\delta\times x(0,6)+\alpha\times x(0,7)+\beta\times x(0,8)+\varepsilon\times x(1,6)+\gamma\times x(1,7)+\alpha\times x(1,8)+$$
$$+\delta\times x(2,6)+\alpha\times x(2,7)+\beta\times x(2,8)+XM_{H+n}, \quad (29)$$

where the variable XM_{H+n} denotes the repeated part after the second horizontal coefficient. From Eq. 29, the general form can be expressed as:

$$HL(i,j+2)=\delta\times x(i,2j+6)+\alpha\times x(i,2j+7)+\beta\times x(i,2j+8)+\varepsilon\times x(i+1,2j+6)+\gamma\times x(i+1,2j+7)+\alpha\times x(i+1,2j+8)+$$
$$+\delta\times x(i+2,2j+6)+\alpha\times x(i+2,2j+7)+\beta\times x(i+2,2j+8)+XM_{H+n}, \quad (30)$$

where i=0~N-1, j=0~N-2, and

$$XM_{H+n}=\beta\times x(i,2j+4)+\alpha\times x(i,2j+5)+\alpha\times x(i+1,2j+4)+\gamma\times x(i+1,2j+5)+\beta\times x(i+2,2j+4)+\alpha\times x(i+2,2j+5). \quad (31)$$

The vertical scan can be done in the same way, where HL(0,0) is the same as that in Eq. 25. The next coefficient can be calculated as:

$$HL(1,0)=\beta\times x(2,0)+\alpha\times x(2,1)+\delta\times x(2,2)+\alpha\times x(2,3)+\beta\times x(2,4)+\alpha\times x(3,0)+\gamma\times x(3,1)+$$

$$+\varepsilon\times x(3,2)+\gamma\times x(3,3)+\alpha\times x(3,4)+\beta\times x(4,0)+\alpha\times(4,1)+\delta\times x(4,2)+\alpha\times x(4,3)+\beta\times x(4,4)$$

$$=\alpha\times x(3,0)+\gamma\times x(3,1)+\varepsilon\times x(3,2)+\gamma\times x(3,3)+\alpha\times x(3,4)+\beta\times x(4,0)+\alpha\times x(4,1)+$$

$$+\delta\times x(4,2)+\alpha\times x(4,3)+\beta\times x(4,4)+XM_V, \quad (32)$$

where the variable XM_V denotes the repeated part after the vertical fifth coefficient. The general form can be expressed as:

$$HL(i+1,j)=\alpha\times x(2i+3,j)+\gamma\times x(2i+3,j+1)+\varepsilon\times x(2j+3,j+2)+\gamma\times x(2j+3,j+3)+\alpha\times x(2j+3,j+4)+$$

$$+\beta\times x(2j+4,j)+\alpha\times x(2j+4,j+1)+\delta\times x(2j+4,j+2)$$

$$+\alpha\times x(2j+4,j+3)+\beta\times x(2j+4,j+4)+XM_V, \quad (33)$$

where i=0~N-1, j=0~N-1, and

$$XM_V=\beta\times x(2i+2,j)+\alpha\times x(2i+2,j+1)+\delta\times x(2i+2,j+2)+\alpha\times x(2i+2,j+3)+\beta\times x(2i+2,j+4). \quad (34)$$

Finally, the diagonal oriented scan can be expressed as:

$$HL(1,1)=\beta\times x(2,2)+\alpha\times x(2,3)+\delta\times x(2,4)+\alpha\times x(2,5)+\beta\times x(2,6)+\alpha\times x(3,2)+\gamma\times x(3,3)+\varepsilon\times x(3,4)+$$

$$+\gamma\times x(3,5)+\alpha\times x(3,6)+\beta\times x(4,2)+\underline{\alpha x(4,3)}+\delta\times x(4,4)+\alpha\times x(4,5)+\beta\times x(4,6)$$

$$=\alpha\times x(3,2)+\varepsilon\times x(3,4)+\gamma\times x(3,5)+\alpha\times x(3,6)+\beta\times x(4,2)+\delta\times x(4,4)+\alpha\times x(4,5)+\beta\times x(4,6)+XM_{D+1}, \quad (35)$$

where the variable XM_{D+1} denotes the repeated part as shown in the gray part of Fig. 9 after the first diagonal scan. Next, the HL(2,2) is calculated as:

$$HL(2,2)=\beta\times x(4,4)+\alpha\times x(4,5)+\delta\times x(4,6)+\alpha\times x(4,7)+\beta\times x(4,8)+\alpha\times x(5,4)+\gamma\times x(5,5)+$$

$$+\varepsilon\times x(5,6)+\gamma\times x(5,7)+\alpha\times x(5,8)+\underline{\beta\times x(6,4)}+\underline{\alpha\times(6,5)}+\delta\times x(6,6)+\alpha\times x(6,7)+\beta\times x(6,8)$$

$$=\varepsilon\times x(5,6)+\gamma\times x(5,7)+\alpha\times x(5,8)+\delta\times x(6,6)+\alpha\times x(6,7)+\beta\times x(6,8)+XM_{D+n}, \quad (36)$$

x(2,2)	x(2,3)	x(2,4)	x(2,5)	x(2,6)
x(3,2)	x(3,3)	x(3,4)	x(3,5)	x(3,6)
x(4,2)	x(4,3)	x(4,4)	x(4,5)	x(4,6)

Fig. 9. Repeat part (in gray) of the diagonal scanned position HL(1,1).

where the variable XM_{D+n} denotes the repeated part as shown in the gray part of Fig. 10 after the first diagonal scan. The general form of XM_{D+n} can be expressed as:

$$XM_{D+n}=\beta\times x(2i+4,2i+4)+\alpha\times x(2i+4,2i+5)+\delta\times x(2i+4,2i+6)+\alpha\times x(2i+4,2i+7)+\beta\times$$

$$\times x(2i+4,2i+8)+\alpha\times x(2i+5,2i+4)+\gamma\times x(2i+5,2i+5)+\varepsilon\times x(2i+5,2i+6)+$$

$$+\gamma\times x(2i+5,2i+7)+\alpha\times x(2i+5,2i+8)+\beta\times x(2i+6,2i+4)+\alpha\times x(2i+6,2i+5)+$$

$$+\delta\times x(2i+6,2i+6)+\alpha\times x(2i+6,2i+7)+\beta\times x(2i+6,2i+8), \quad (37)$$

x(4,4)	x(4,5)	x(4,6)	x(4,7)	x(4,8)
x(5,4)	x(5,5)	x(5,6)	x(5,7)	x(5,8)
x(6,4)	x(6,5)	x(6,6)	x(6,7)	x(6,8)

Fig. 10. Repeat part (in gray) of the diagonal scanned position HL(2,2).

The general form of the rest part can be expressed as:

$$HL(i+1,j+1)=\beta\times x(2i+6,2j+8)+\alpha\times(x(2i+5,2j+8)+x(2i+6,2j+7))+\gamma\times x(2i+5,2j+7)+$$
$$+\delta\times x(2i+6,2j+6)+\varepsilon\times x(2i+5,2j+6)+XM_{D+n}, \quad (38)$$

where i=1~N-1, j=1~N-1.

The HL-band can be derived in the same way. According to the 2-D 5/3 LDWT, the LH-band coefficients of the SMDWT can be derived as follows:

$$LH(i,j)=(3/4)x(2i,2j+1)+(1/16)\sum^{1}_{u=0}\sum^{1}_{v=0}x(2i-2+2u,2j+4v)+$$
$$+(-1/8)\sum^{1}_{u=0}x(2i,2j+4u)+(-1/8)\sum^{1}_{u=0}\sum^{1}_{v=0}x(2i-1+2u,2j+2v)+$$
$$(1/4)\sum^{1}_{u=0}x(2i-1+2u,2j+1)+(-3/8)\sum^{1}_{u=0}x(2i,2j+2u). \quad (39)$$

The mask as shown in Fig. 11(a) can be obtained via Eq. 39, where α=-1/8, β=1/16, γ=1/4, δ=-3/8, and ε=3/4. The DSP and hardware architecture are depicted in Figs. 11(b) and (c). The complexity of the SMDWT is further reduced by employing the symmetric feature of the mask. First, the initial horizontal scan is calculated by the method that is similar to that of HL SMDWT, where the variable XM_H denotes the repeated part after the horizontal fifth coefficient. The general form can be expressed as:

$$LH(i,j+1)=\alpha\times x(i,2j+3)+\beta\times x(i,2j+4)+\gamma\times x(i+1,2j+3)+\alpha\times x(i+1,2j+4)+\varepsilon\times x(i+2,2j+3)+$$
$$+\delta\times x(i+2,2j+4)+\gamma\times x(i+3,2j+3)+$$
$$\alpha\times x(i+3,2j+4)+\alpha\times x(i+4,2j+3)+\beta\times x(i+4,2j+4)+XM_H, \quad (40)$$

where i=0~N-1, j=0~N-1, and

$$XM_H=\beta\times x(i,2j+2)+\alpha\times x(i+1,2j+2)+\delta\times x(2i+2,j+2)+\alpha\times x(i+3,2j+2)+\beta\times x(i+4,2j+2). \quad (41)$$

Next, the initial vertical scan is calculated by the method similar to that of HL mask-based DWT, where the variable XM_{V+1} denotes the repeated part after the vertical first coefficient. The general form of the first vertical step can be expressed as:

$$LH(1,j)=\beta\times x(i+2,j)+\alpha\times x(i+2,j+1)+\beta\times x(i+2,j+2)+\delta\times x(i+4,j)+\varepsilon\times x(i+4,j+1)+\delta\times x(i+4,j+2)+$$
$$+\alpha\times x(i+5,j)+\gamma\times x(i+5,j+1)+\alpha\times x(i+5,j+2)+$$
$$+\beta\times x(i+6,j)+\alpha\times x(i+6,j+1)+\beta\times x(i+6,j+2)+XM_{V+1}, \quad (42)$$

where i=0, j=0~N-1, and

$$XM_{V+1}=\alpha\times x(2i+3,0)+\gamma\times x(2i+3,1)+\alpha\times x(2i+3,2). \quad (43)$$

Next, the second vertical scan is calculated with the method similar to that of HL SMDWT.

$$LH(i+2,j)=\delta\times x(2i+6,j)+\varepsilon\times x(2i+6,j+1)+\delta\times x(2i+6,j+2)+\alpha\times x(2i+7,j)+\gamma\times x(2i+7,j+1)+$$
$$+\alpha\times x(2i+7,j+2)+\beta\times x(2i+8,j)+\alpha\times x(2i+8,j+1)+\beta\times x(2i+8,j+2)+XM_{V+n}, \quad (44)$$

where i=0~N-1, j=0~N-2, and

$$XM_{V+n}=\beta\times x(2i+4,j)+\alpha\times x(2i+4,j+1)+\beta\times x(2i+4,j+2)+\alpha\times x(2i+5,j)+\gamma\times x(2i+5,j+1)+\alpha\times x(2i+5,j+2). \quad (45)$$

Finally, the diagonal oriented scan can be derived as:

$$LH(1,1)=\alpha\times x(3,4)+\varepsilon\times x(4,3)+\delta\times x(4,4)+\alpha\times x(5,2)+\gamma\times x(5,3)+\beta\times x(6,2)+\alpha\times x(6,3)+\beta\times x(6,4)+XM_{D+1}, \quad (46)$$

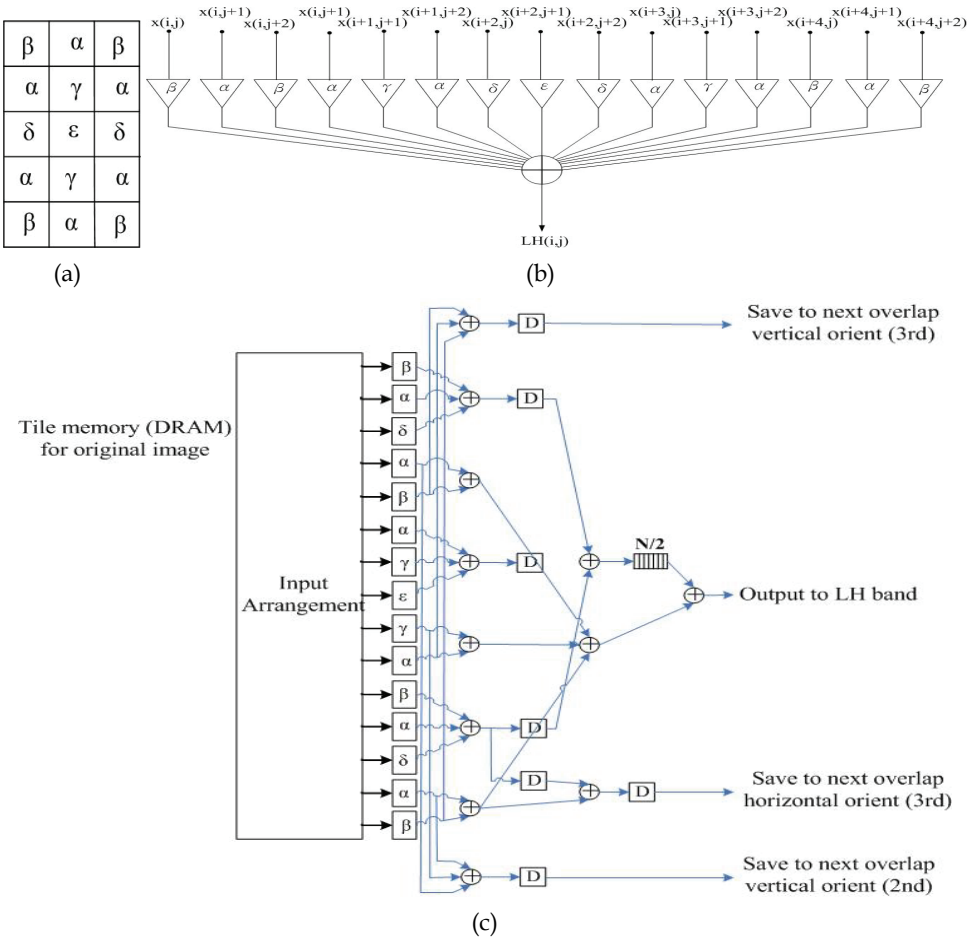

Fig. 11. LH band mask coefficients and the corresponding DSP architecture. (a) Coefficients. (b) DSP architecture. (c) Hardware architecture design.

where the variable XM_{D+1} denotes the repeated part as shown in the gray part of Fig. 12 after the first diagonal scan.
Next the LH(2,2) is calculated as:

$$LH(2,2)=\alpha\times x(5,4)+\varepsilon\times x(6,5)+\delta\times x(6,6)+\gamma\times x(7,5)+\alpha\times x(7,6)+\beta\times x(8,4)+\alpha\times x(8,5)+XM_{D+n}, \quad (47)$$

where the variable XM_{D+n} denotes the repeated part as shown in the gray part of Fig. 13 after the first diagonal scan. The general form of XM_{D+n} can be expressed as:

$$XM_{D+n}=\beta\times x(2i+4,2i+4)+\alpha\times x(2i+4,2i+5)+\beta\times x(2i+4,2i+6)+\alpha\times x(2i+5,2i+4)+\gamma\times x(2i+5,2i+5)+$$
$$+\alpha\times x(2i+5,2i+6)+\delta\times x(2i+6,2i+4)+\alpha\times x(2i+7,2i+4)+\beta\times x(2i+8,2i+4). \quad (48)$$

x(2,2)	x(2,3)	x(2,4)
x(3,2)	x(3,3)	x(3,4)
x(4,2)	x(4,3)	x(4,4)
x(5,2)	x(5,3)	x(5,4)
x(6,2)	x(6,3)	x(6,4)

Fig. 12. Repeat part (in gray) of the diagonal scanned position LH(1,1).

x(4,4)	x(4,5)	x(4,6)
x(5,4)	x(5,5)	x(5,6)
x(6,4)	x(6,5)	x(6,6)
x(7,4)	x(7,5)	x(7,6)
x(8,4)	x(8,5)	x(8,6)

Fig. 13. Repeat part (in gray) of the diagonal scanned position LH(2,2).

The general form of the rest part can be expressed as:

$$LH(i+1,j+1)=\beta\times x(2i+8,2j+6)+\alpha\times(x(2i+7,2j+6)+x(2i+8,2j+5))+\gamma\times x(2i+7,2j+5)+$$
$$+\delta\times x(2i+6,2j+6)+\varepsilon\times x(2i+5,2j+6)+XM_{D+n}. \quad (49)$$

where i=1~N-1, j=1~N-1.

3. Low-Low (LL) band mask coefficients reduction for 2-D SMDWT

According to the 2-D 5/3 LDWT, the LL-band coefficients of the SMDWT can be expressed as follows:

$$LL(i,j)=(9/16)x(2i,2j)+(1/64)\sum^{1}_{u=0}\sum^{1}_{v=0}x(2i\text{-}2+4u,2j\text{-}2+4v)+$$
$$+(1/16)\sum^{1}_{u=0}\sum^{1}_{v=0}x(2i\text{-}1+2u,2j\text{-}1+2v)+(-1/32)\sum^{1}_{u=0}\sum^{1}_{v=0}x(2i\text{-}1+2u,2j\text{-}2+4v)+$$

$$+(-1/32)\sum^{1}_{u=0}\sum^{1}_{v=0}x(2i\text{-}2+4u,2j\text{-}1+2v)+(3/16)\sum^{1}_{u=0}[x(2i\text{-}1+2u,2j)+P(2i,2j\text{-}1+2u)]+$$

$$+(-3/32)\sum^{1}_{u=0}[x(2i\text{-}2+4u,2j)+x(2i,2j\text{-}2+4u)]. \quad (50)$$

The mask as shown in Fig. 14(a) can be obtained via Eq. 50, where α=-1/32, β=1/64, γ=1/16, δ=-3/32, ε=3/16 and ζ=9/16. The DSP and hardware architecture are depicted in Figs. 14(b) and (c). The complexity of the SMDWT is further reduced by employing the symmetric feature of the mask. First, the initial horizontal scan LL(0,0). The next coefficient can be calculated as LL(0,1). where the variable XM_{H+1} denotes the repeated part after the first horizontal coefficient. The general form of the first horizontal step can be expressed as:

$$LL(i,1)=\beta\times x(i,j+2)+\delta\times x(i,j+4)+\alpha\times x(i,j+5)+\beta\times x(i,j+6)+\alpha\times x(i+1,j+2)+\varepsilon\times x(i+1,j+4)+$$

$$+\gamma\times x(i+1,j+5)+\alpha\times x(i+1,j+6)+\delta\times x(i+2,j+2)+\zeta\times x(i+2,j+4)+\varepsilon\times x(i+2,j+5)+\delta\times x(i+2,j+6)+$$

$$+\alpha\times x(i+3,j+2)+\varepsilon\times x(i+3,j+4)+\gamma\times x(i+3,j+5)+\alpha\times x(i+3,j+6)+\beta\times x(i+4,j+2)+$$

$$+\delta\times x(i+4,j+4)+\alpha\times x(i+4,j+5)+\beta\times x(i+4,j+6)+XM_{H+1}, \quad (51)$$

where i=0~N-1, and

$$XM_{H+1}=\alpha\times x(i,3)+\gamma\times x(i+1,3)+\varepsilon\times x(i+2,3)+\gamma\times x(i+3,3)+\alpha\times x(i+4,3). \quad (52)$$

The next coefficient can be calculated as LL(0,2). where the variable XM_{H+n} denotes the repeated part after the second horizontal coefficient. From LL(0,2), the general form can be expressed as:

$$LL(i,j+2)=\delta\times x(i,2j+6)+\alpha\times x(i,2j+7)+\beta\times x(i,2j+8)+\varepsilon\times x(i+1,2j+6)+\gamma\times x(i+1,2j+7)+$$

$$+\alpha\times x(i+1,2j+8)+\zeta\times x(i+2,2j+6)+\varepsilon\times x(i+2,2j+7)+\delta\times x(i+2,2j+8)+$$

$$+\varepsilon\times x(i+3,2j+6)+\gamma\times x(i+3,2j+7)+\alpha\times x(i+3,2j+8)+\delta\times x(i+4,2j+6)+$$

$$+\alpha\times x(i+4,2j+7)+\beta\times x(i+4,2j+8)+XM_{H+n}, \quad (53)$$

where i=0~N-1, j=0~N-2, and

$$XM_{H+n}=\beta\times x(i,2j+4)+\alpha\times x(i,2j+5)+\alpha\times x(i+1,2j+4)+\gamma\times x(i+1,2j+5)+\delta\times x(i+2,2j+4)+$$

$$+\varepsilon\times x(i+2,2j+5)+\alpha\times x(i+3,2j+4)+\gamma\times x(i+3,2j+5)+\beta\times x(i+4,2j+4)+\alpha\times x(i+4,2j+5). \quad (54)$$

β	α	δ	α	β
α	γ	ε	γ	α
δ	α	ζ	α	δ
α	γ	ε	γ	α
β	α	δ	α	β

(a)

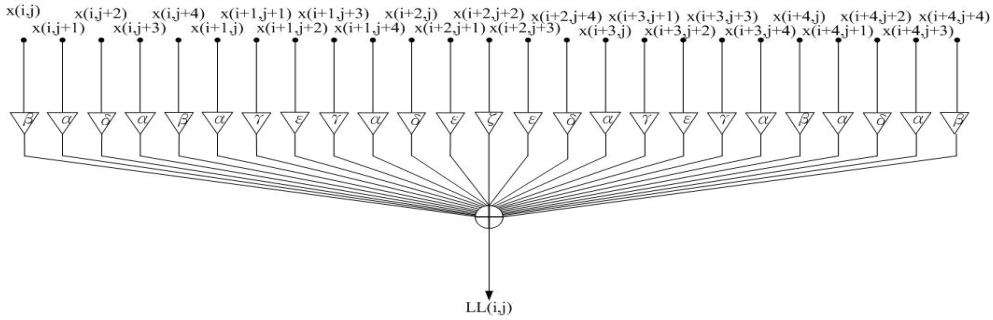

(b)

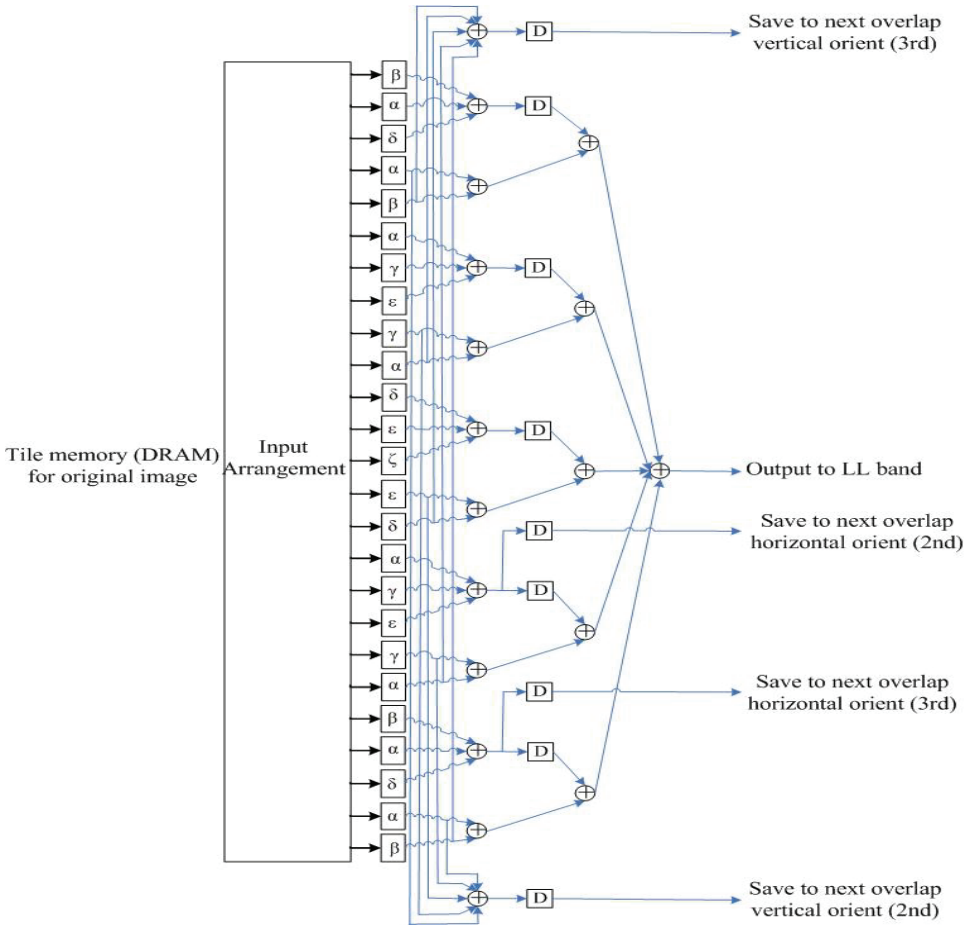

(c)

Fig. 14. LL band mask coefficients and the corresponding DSP architecture. (a) Coefficients. (b) DSP architecture. (c) Hardware architecture design.

The vertical scan can be done in the same way, where LL(0,0) is the same as that horizontal in LL(0,0). The next coefficient can be calculated as LL(1,0). Next, the initial vertical scan is calculated by the method similar to that of LH SMDWT, where the variable XM_{V+1} denotes the repeated part after the vertical first coefficient. The general form of the first vertical step can be expressed as:

$$LL(1,j)=\beta\times x(2i,j)+\alpha\times x(2i,j+1)+\delta\times x(2i,j+2)+\alpha\times x(2i,j+3)+\beta\times x(2i,j+4)+\delta\times x(2i+4,j)+$$
$$+\varepsilon\times x(2i+4,j+1)+\zeta\times x(2i+4,j+2)+\varepsilon\times x(2i+4,j+3)+\delta\times x(2i+4,j+4)+\alpha\times x(2i+5,j)+$$
$$+\gamma\times x(2i+5,j+1)+\varepsilon\times x(2i+5,j+2)+\gamma\times x(2i+5,j+3)+\alpha\times x(2i+5,j+4)+$$
$$+\beta\times x(2i+6,j)+\alpha\times(2i+6,j+1)+\delta\times x(2i+6,j+2)+\alpha\times x(2i+6,j+3)+\beta\times x(2i+6,j+4)+XM_{V+1}, \quad (55)$$

where i=0, j=0~N-1, and

$$XM_{V+1}=\alpha\times x(3,j)+\gamma\times x(3,j+1)+\varepsilon\times x(3,j+2)+\gamma\times x(3,j+3)+\alpha\times x(3,j+4). \quad (56)$$

Next, the second vertical scan is calculated by the method similar to that of LH SMDWT.

$$LL(i+2,j)=\delta\times x(2i+6,j)+\varepsilon\times x(2i+6,j+1)+\zeta\times x(2i+6,j+2)+\varepsilon\times x(2i+6,j+3)+\delta\times x(2i+6,j+4)+$$
$$+\varepsilon\times x(2i+7,j+2)+\gamma\times x(2i+7,j+1)+\varepsilon\times x(i,2j+7)+\gamma\times x(2i+7,j+3)+\alpha\times x(2i+7,j+4)+\beta\times x(i,2j+8)+$$
$$+\alpha\times x(2i+8,j+1)+\delta\times x(2i+8,j+2)+\alpha\times x(2i+8,j+3)+\beta\times x(2i+8,j+4)+XM_{V+n}, \quad (57)$$

where i=0~N-1, j=0~N-2, and

$$XM_{V+n}=\beta\times x(2i+4,j)+\alpha\times x(2i+4,j+1)+\delta\times x(2i+4,j+2)+\alpha\times x(2i+4,j+3)+\beta\times x(2i+4,j+4)+$$
$$+\beta\times x(2i+5,j)+\gamma\times x(2i+5,j+1)+\varepsilon\times x(2i+5,j+2)+\gamma\times x(2i+5,j+3)+\alpha\times x(2i+5,j+4). \quad (58)$$

Finally, the diagonal oriented scan can be derived as:

$$LL(1,1)=\beta\times x(2,2)+\alpha\times x(2,5)+\beta\times x(2,6)+\zeta\times x(4,4)+\varepsilon\times x(4,5)+\alpha\times x(5,2)+\varepsilon\times x(5,4)+$$
$$+\gamma\times x(5,5)+\alpha\times x(5,6)+\beta\times x(6,2)+\delta\times x(6,4)+\alpha\times x(6,5)+\beta\times x(6,6)+XM_{D+1}, \quad (59)$$

where the variable XM_{D+1} denotes the repeated part as shown in the gray part of Fig. 15 after the first diagonal scan.
Next the HL(2,2) is calculated as:

$$LL(2,2)=\varepsilon\times x(6,5)+\zeta\times x(6,6)+\varepsilon\times x(6,7)+\gamma\times x(7,5)+\varepsilon\times x(7,6)+\gamma\times x(7,7)+\alpha\times x(7,8)+$$
$$+\alpha\times x(8,5)+\delta\times x(8,6)+\alpha\times x(8,7)+\beta\times x(8,8)+XM_{D+n}, \quad (60)$$

where the variable XM_{D+2} denotes the repeated part as shown in the gray part of Fig. 16 after the first diagonal scan. The variable XM_{D+1} denotes the repeated part as shown in the gray part of Fig. 17 after the first diagonal scan. The general form of XM_{D+n} can be expressed as:

x(2,2)	x(2,3)	x(2,4)	x(2,5)	x(2,6)
x(3,2)	x(3,3)	x(3,4)	x(3,5)	x(3,6)
x(4,2)	x(4,3)	x(4,4)	x(4,5)	x(4,6)
x(5,2)	x(5,3)	x(5,4)	x(5,5)	x(5,6)
x(6,2)	x(6,3)	x(6,4)	x(6,5)	x(6,6)

Fig. 15. Repeat part (in gray) of the diagonal scanned position LL(1,1).

x(4,4)	x(4,5)	x(4,6)	x(4,7)	x(4,8)
x(5,4)	x(5,5)	x(5,6)	x(5,7)	x(5,8)
x(6,4)	x(6,5)	x(6,6)	x(6,7)	x(6,8)
x(7,4)	x(7,5)	x(7,6)	x(7,7)	x(7,8)
x(8,4)	x(8,5)	x(8,6)	x(8,7)	x(8,8)

Fig. 16. Repeat part (in gray) of the diagonal scanned position LL(2,2).

x(6,6)	x(6,7)	x(6,8)	x(6,9)	x(6,10)
x(7,6)	x(7,7)	x(7,8)	x(7,9)	x(7,10)
x(8,6)	x(8,7)	x(8,8)	x(8,9)	x(8,10)
x(9,6)	x(9,7)	x(9,8)	x(9,9)	x(9,10)
x(10,6)	x(10,7)	x(10,8)	x(10,9)	x(10,10)

Fig. 17. Repeat part (in gray) of the diagonal scanned position LL(3,3).

$$XM_{D+n}=\beta\times x(2i+6,2i+6)+\alpha\times x(2i+6,2i+7)+\delta\times x(2i+6,2i+8)+\alpha\times x(2i+6,2i+9)+$$
$$+\beta\times x(2i+6,2i+10)+\alpha\times x(2i+7,2i+6)+\gamma\times x(2i+7,2i+7)+\varepsilon\times x(2i+7,2i+8)+$$
$$+\gamma\times x(2i+7,2i+9)+\alpha\times x(2i+7,2i+10)+\delta\times x(2i+8,2i+6)+\varepsilon\times x(2i+8,2i+7)+$$
$$+\delta\times x(2i+8,2i+10)+\alpha\times x(2i+9,2i+6)+\gamma\times x(2i+9,2i+7)+\beta\times x(2i+10,2i+6)+\alpha\times x(2i+10,2i+7). \quad (66)$$

The general form of the rest part can be expressed as:

$$LL(i+1,j+1)=\zeta\times x(2i+8,2i+8)+\varepsilon\times x(2i+8,2i+9)+\varepsilon\times x(2i+9,2i+8)+\gamma\times x(2i+9,2i+9)+$$
$$+\alpha\times x(2i+9,2i+10)+\delta\times x(2i+10,2i+8)+\alpha\times x(2i+10,2i+9)+\beta\times x(2i+10,2i+10)+XM_{D+n}, \quad (67)$$

where i=1~N-1, j=1~N-1.

3.3 Summary of the complexity reduction

The four-matrix frameworks, HH, HL, LH, and LL lead to four different architectures. Each of these is described by the structural behavior of different components that makes up the digital signal processing (DSP) as shown in Table 1. The discussion above shows that the

complexity of the proposed SMDWT can be significantly reduced by exploiting the symmetric feature of the masks. Tables 2-5 show the overall complexity reductions from the original SMDWT to the simplified SMDWT.

HH	9	2
HL	15	2
LH	15	2
LL	25	2

Table 1. The Subband Mask for DSP.

XM_H of HH(i,j+1)	β×x(i,2j+2)+α×x(i+1,2j+2)+β×x(i+2,2j+2).
Complexity reduction	Original SMDWT: adder is 8, and multiplier is 9. (number of operations) Simplified SMDWT: adder is 5, and multiplier is 0. (The shifter is used to replace multiplier)
XM_V of HH(i+1,j)	β×x(2i+2,j)+α×x(2i+2,j+1)+β×x(2i+2,j+2).
Complexity reduction	Original SMDWT: adder is 8, and multiplier is 9. Simplified SMDWT: adder is 6, and multiplier is 0.

Table 2. HH-Band Wavelet Coefficient (Mask of Size 3×3).

XM_{H+1} of HL(i,1)	α×x(i,3)+γ×x(i+1,3)+α×x(i+2,3).
Complexity reduction	Original SMDWT: adder is 14, and multiplier is 15. Simplified SMDWT: adder is 12, and multiplier is 0.
XM_{H+n} of HL(i,j+2)	β×x(i,2j+4)+α×x(i,2j+5)+α×x(i+1,2j+4)+γ×x(i+1,2j+5)+β×x(i+2,2j+4)+α×x(i+2,2j+5).
Complexity reduction	Original SMDWT: adder is 14, and multiplier is 15. Simplified SMDWT: adder is 9, and multiplier is 0.
XM_V of HL(i+1,j)	β×x(2i+2,j)+α×x(2i+2,j+1)+δ×x(2i+2,j+2)+α×x(2i+2,j+3)+β×x(2i+2,j+4).
Complexity reduction	Original SMDWT: adder is 14, and multiplier is 15. Simplified SMDWT: adder is 10, and multiplier is 0.

Table 3. HL-Band Wavelet Coefficient (Mask of Size 5×3).

XM_H of LH(i,j+1)	β×x(i,2j+2)+α×x(i+1,2j+2)+δ×x(2i+2,j+2)+α×x(i+3,2j+2)+β×x(i+4,2j+2).
Complexity reduction	Original SMDWT: adder is 14, and multiplier is 15. Simplified SMDWT: adder is 10, and multiplier is 0.
XM_{V+1} of LH(1,j)	α×x(2i+3,0)+γ×x(2i+3,1)+α×x(2i+3,2).
Complexity reduction	Original SMDWT: adder is 14, and multiplier is 15. Simplified SMDWT: adder is 12, and multiplier is 0.
XM_{V+n} of LH(i+2,j)	β×x(2i+4,j)+α×x(2i+4,j+1)+β×x(2i+4,j+2)+α×x(2i+5,j)+γ×x(2i+5,j+1)+α×x(2i+5,j+2).
Complexity reduction	Original SMDWT: adder is 14, and multiplier is 15. Simplified SMDWT: adder is 9, and multiplier is 0.

Table 4. LH-Band Wavelet Coefficient (Mask of Size 3×5).

XMH+1 of LL(i,1)	α×x(i,3)+γ×x(i+1,3)+ε×x(i+2,3)+γ×x(i+3,3)+α×x(i+4,3).
Complexity reduction	Original SMDWT: adder is 24, and multiplier is 25. Simplified SMDWT: adder is 20, and multiplier is 0.
XMH+n of LL(i,j+2)	β×x(i,2j+4)+α×x(i,2j+5)+α×x(i+1,2j+4)+γ×x(i+1,2j+5)+δ×x(i+2,2j+4)+ε×x(i+2,2j+5)+α×x(i+3,2j+4)+γ×x(i+3,2j+5)+β×x(i+4,2j+4)+α×x(i+4,2j+5).
Complexity reduction	Original SMDWT: adder is 24, and multiplier is 25. Simplified SMDWT: adder is 15, and multiplier is 0.
XMV+1 of LL(1,j)	α×x(3,j)+γ×x(3,j+1)+ε×x(3,j+2)+γ×x(3,j+3)+α×x(3,j+4).
Complexity reduction	Original SMDWT: adder is 24, and multiplier is 25. Simplified SMDWT: adder is 20, and multiplier is 0.
XMV+n of LL(i+2,j)	β×x(2i+4,j)+α×x(2i+4,j+1)+δ×x(2i+4,j+2)+α×x(2i+4,j+3)+β×x(2i+4,j+4)+β×x(2i+5,j)+γ×x(2i+5,j+1)+ε×x(2i+5,j+2)+γ×x(2i+5,j+3)+α×x(2i+5,j+4).
Complexity reduction	Original SMDWT: adder is 24, and multiplier is 25. Simplified SMDWT: adder is 15, and multiplier is 0.

Table 5. LL-Band Wavelet Coefficient (Mask of Size 5×5).

4. Experimental results and performance comparisons

The proposed 2-D SMDWT algorithm is generally used to performing the 2-D DWT for still images. Figure 18 shows the schematic diagram of the 2-D SMDWT. The wavelet transform provides a multi-scale representation of image/video in the spatial-frequency domain. Besides the energy compaction and decorrelation properties that facilitate compression, a major advantage of the DWT is its scalability. The proposed algorithm is based on the four-subband matrices (HH, HL, LH, and LL) which are processed to achieve the same performance as the 5/3 LDWT algorithm. The SMDWT is implemented in the JPEG2000 reference software VM 9.0 and is compared with the original JPEG2000. The test image the used in this experiment was Lena of size 512×512. Experimental results show that the proposed algorithm not only significantly improves lifting-based latency, but also has the same visual quality as the normal 2-D 5/3 LDWT as shown in Fig. 19.

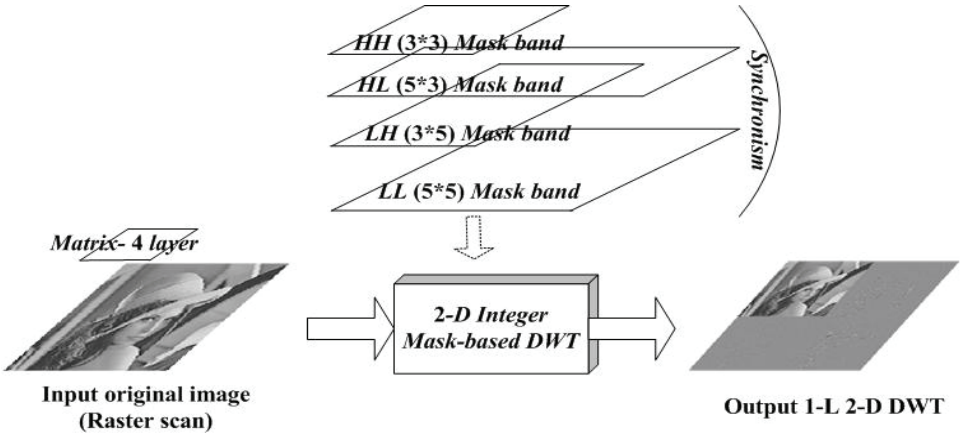

Fig. 18. Schematic diagram of the 2-D SMDWT.

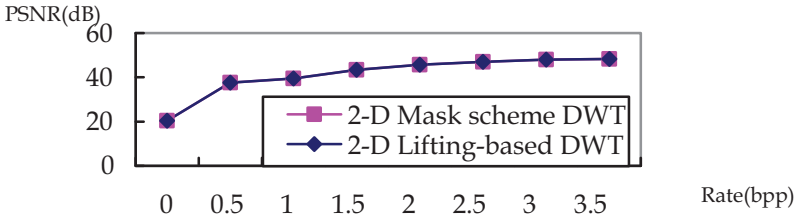

Fig. 19. PSNR (dB) versus Rate (bpp) comparison between 2-D LDWT and the proposed 2-D SMDWT.

The architecture of the 2-D SMDWT has many advantages compared to the 2-D LDWT. For example, the critical path of the 2-D LDWT is potentially longer than that of SMDWT. Moreover, the 2-D LDWT is frame-based with the implementation bottleneck being the huge amount of the transpose memory size. This work uses the symmetric feature of the masks in SMDWT to improve the design. Experimental results, as shown in Table 7 show that the proposed algorithm is superior to most of the previous works. The proposed algorithm has efficient solutions for reducing the critical path (which is defined as the longest, time-weighted sequence of events from the start of the program to its termination with examples shown in Figs. 7(c), 8(c), 11(c), 14(c)), latency (the time between the arrival of a new signal and its first signal output becoming available in the system), and hardware cost, as shown in Figs. 7, 8, 11, 14, and 20, and Table 6. The SMDWT approach requires a transpose memory of size (N/2)+26 ((N/2) is on-chip memory of size and 26 is number of register). The proposed 2-D DWT adopts parallel and pipeline schemes are employed to reduce the transpose memory and increase the operating speed. The shifters and adders replace multipliers in the computation to increase the hardware utilization and reduce the hardware cost. A $N \times N$ 2-D lifting-based DWT is RTL (Register Transistor Level) designed and simulated with VerilogHDL in this paper.

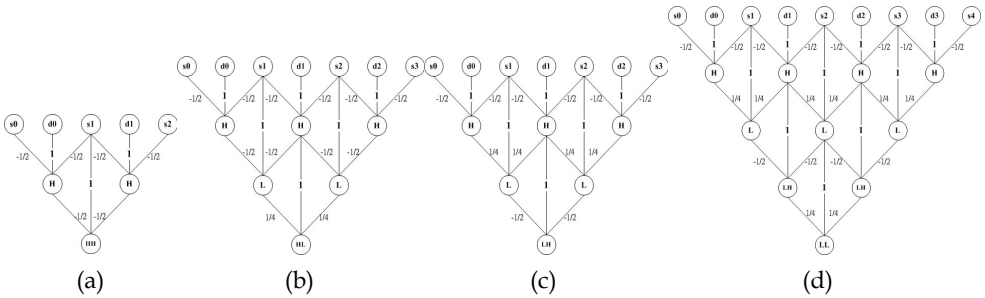

Fig. 20. 2-D LDWT critical path. (a) HH band. (b) HL band. (c) LH band. (d) LL band.

Subbands	LDWT critical path	SMDWT critical path
HH	$2T_M+2T_A$	$1T_M+2T_A$ Fig.7(c)
HL	$3T_M+3T_A$	$1T_M+2T_A$ Fig.8(c)
LH	$3T_M+3T_A$	$1T_M+3T_A$ Fig.11(c)
LL	$4T_M+4T_A$	$1T_M+3T_A$ Fig.14(c)

*T_M: Multiplier operation time; T_A: Adder operation time

Table 6. Subband Lifting-Based V.S. Mask-Based for Integer 2-D DWT.

Methods	2-D DWT	Wave stage	[1]Transpose memory	[2]Latency	[3]Computing time	Complexity
Chiang et al., 2005	LDWT	Integer	[4]N	7	$(3/4)N^2+7$	Simple
Chiang & Hsia, 2005	LDWT	Integer	$N^2/4+5N$	3	N^2	Medium
Diou et al., 2001	LDWT	Integer	3.5N	N/A	N/A	Simple
Chen & Wu, 2002	LDWT	Integer	2.5N	N/A	N^2	Complexity
Andra et al., 2002	LDWT	Integer	3.5N	2N+5	$(N^2/2)+N+5$	Simple
Tan & Arslan, 2003	LDWT	Integer	3N	N/A	$(N^2/2)+N+5$	Medium
Lee et al., 2003	LDWT	Integer	N	5	$(N^2/2)+5$	Medium
ISO/IEC, 2000	LDWT	Integer	N^2	N/A	N/A	Simple
Varshney et al., 2007	LDWT	Integer	3N	13	N/A	Medium
Chen, 2002	LDWT	Integer	3N	N/A	$(N^2/2)+N+5$	Medium
Proposed	*SMDWT*	Integer	*(N/2)+26*	2	*$N^2/4+3$*	*Simple*

[1] Transpose memory is used to store frequency coefficients in the 1-L 2-D DWT.
[2] In a system, latency is often used to mean any delay or waiting time that increases real or perceived response time beyond the response time desired. For example, specific contributors to 2-D DWT latency include from original image input to first subband output in signal.
[3] In a system, computing time represents the time used to compute an image of size $N \times N$.
[4] Suppose image is of size $N \times N$.

Table 7. Performance Comparisons.

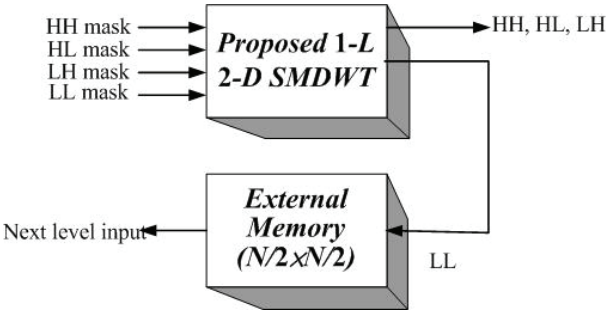

Fig. 21. The multilevel 2-D DWT architecture.

The multi-level DWT computation can be implemented similarly by the proposed 2-D SMDWT. For the multi-level computation, this architecture needs $(N^2/4)$ off-chip memory. As illustrated in Fig. 21, the off-chip memory temporarily stores the LL subband coefficients for the next iteration computations. The second level computation requires $N/2$ counters and $N/2$ FIFOs for the control unit. The third level computation requires $N/4$ counters and $N/4$ FIFOs for the control unit. Generally, the jth level computation needs $N/2^{j-1}$ counters and $N/2^{j-1}$ FIFOs. Therefore, the proposed architecture is suitable for multilevel DWT

computations. The SMDWT also has the advantages of regular signal coding, short critical path, reduced latency time, and independent subband coding processing. Moreover, SMDWT can easily reduce the transpose memory access time and overlap original signal access so that power consumption of 2-D LDWT can also be easily improved by SMDWT.

5. Conclusions

This work proposes a novel 2-D SMDWT fast algorithm, which is superior to the 5/3 LDWT. The algorithm solves the latency problem in the previous schemes caused by multiple-layer transpose decomposition operation. Moreover, it provides real-time requirement and can be further applied to the 3-D wavelet video coding [30].

The proposed 2-D SMDWT algorithm has the advantages of a fast computational speed, less complexity, reduced latency. Low-transpose memory and regular data flow, and is suitable for VLSI implementation. Possible future works are described below:

1. The Dual-Mode 2-D SMDWT on JPEG2000: The dual-mode 2-D SMDWT can be developed to support 5/3 (lossless) lifting or 9/7 (lossy) lifting using similar hardware architecture, since the 5/3 and 9/7 are very similar and both have less complexity.
2. High Performance JPEG2000 Codec: Since part of the JPEG2000 encoder is symmetric to the decoder the complexity of both the encoder and the decoder can be reduced.
3. An independent four-subband mask can be used in other visual coding fields (eg. visual processing, visual compression and visual recognition).

6. References

Andra, K.; Chakrabarti, C. & Acharya, T. (2000), A VLSI architecture for lifting-based wavelet transform, *IEEE Workshop on Signal Processing Systems*, (October 2000), pp. 70-79.

Andra, K.; Chakrabarti, C. & Acharya, T. (2002), A VLSI architecture for lifting-based forward and inverse wavelet transform, *IEEE Transactions on Signal Processing*, vol. 50, no.4, (April 2002), pp. 966-977.

Chen, S.-C. & Wu, C.-C. (2002). An architecture of 2-D 3-level lifting-based discrete wavelet transform, *Proceeding of the VLSI Design/ CAD Symposium*, (August 2002), pp. 351-354.

Chen, P.-Y. (2002). VLSI implementation of discrete wavelet transform using the 5/3 filter, *IEICE Transactions on Information and Systems*, vol. E85-D, no.12, (December 2002), pp. 1893-1897.

Chen, P. & J. W. Woods. (2004). Bidirectional MC-EZBC with lifting implementation, *IEEE Transactions on Circuits and Systems for Video Technology*, vol. 14, no. 10, (October 2004), pp. 1183-1194.

Chiang, J.-S.; Hsia, C.-H. & Chen, H.-J. (2005). 2-D discrete wavelet transform with efficient parallel scheme, *International Conference on Imaging Science, Systems, and Technology: Computer Graphics*, (June 2005), pp. 193-197.

Chiang, J.-S.; Hsia, C.-H.; Chen, H.-J. & Lo, T.-J. (2005). VLSI architecture of low memory and high speed 2-D lifting-based discrete wavelet transform for JPEG2000 applications, *IEEE International Symposium on Circuits and Systems*, (May 2005), pp. 4554-4557.

Chiang, J.-S. & Hsia, C.-H. (2005). An efficient VLSI architecture for 2-D DWT using lifting scheme, *IEEE International Conference on Systems and Signals*, (April 2005), pp. 528-531.

Daubechies, I. & Sweldens, W. (1998). Factoring wavelet transforms into lifting steps, *The Journal of Fourier Analysis and Applications*, vol. 4, no.3, (1998), pp. 247-269.

Diou, C.; Torres, L. & Robert, M. (2001). An embedded core for the 2-D wavelet transform, *IEEE on Emerging Technologies and Factory Automation Proceedings*, vol. 2, (2001), pp. 179-186.

Feig, E.; Peterson, H. & Ratnakar, V. (1995). Image compression using spatial prediction, *IEEE International Conference on Acoustics, Speech, and Signal Processing*, vol. 4, (May 1995), pp. 2339-2342.

Habibi, A. & Hershel, R. S. (1974). A unified representation of differential pulse code modulation (DPCM) and transform coding systems, *IEEE Transaction on Communications*, vol. 22, no. 5, (May 1974), pp. 692-696.

Huang, C.-T.; Tseng, P.-C. & Chen, L.-G. (2005). Analysis and VLSI architecture for 1-D and 2-D discrete wavelet transform, *IEEE Transactions on Signal Processing,* vol. 53, no. 4., (April 2005), pp. 1575-1586.

ISO/IEC JTC1/SC29 WG1. (2000). *JPEG 2000 Part 1 Final Committee Draft Version 1.0*, Information Technology.

ISO/IEC JTC1/SC29/WG1 Wgln 1684. (2000). *JPEG 2000 Verification Model 9.0*.

ISO/IEC JTC1/SC29 WG11. (2001). *Coding of Moving Pictures and Audio,* Information Technology.

ISO/IEC ISO/IEC 15444-3. (2002). *Motion JPEG2000,* Information Technology.

Kondo, H. & Oishi, Y. (2000). Digital image compression using directional sub-block DCT, *International Conference on Communications Technology*, vol. 1, (August 2000), pp.21-25.

Lan, X.; Zheng, N. & Liu, Y. (2005). Low-power and high-speed VLSI architecture for lifting-based forward and inverse wavelet transform, *IEEE Transactions on Consumer Electronics*, vol. 51, no.2, (May 2005), pp. 379-385.

Lee, W.-T.; Chen, H.-Y.; Hsiao, P.-Y. & Tsai, C.-C. (2003). An efficient lifting based architecture for 2-D DWT used in JPEG2000, *Proceeding of the VLSI Design/ CAD Symposium*, (August 2003), pp. 577-580.

Lian, C.-J.; Chen, K.-F.; Chen, H.-H. & Chen, L.-G. (2001). Lifting based discrete wavelet transform architecture for JPEG2000, *IEEE International Symposium on Circuits and Systems*, vol. 2, (May 2001), pp. 445-448.

Liao, H.; Mandal, M. Kr. & Cockburn, B. F. (2004). Efficient architecture for 1-D and 2-D lifting-based wavelet transforms, *IEEE Transactions on Signal Processing*, vol. 52, no. 5, (May 2004), pp. 1315-1326.

Mallat, S. G. (1989). A theory for multi-resolution signal decomposition: The wavelet representation, *IEEE Transaction on Pattern Analysis and Machine Intelligence*, vol. 11, no. 7, (July 1989), pp. 674-693.

Ohm, J.-R. (2005). Advances in scalable video coding, *Proceedings of the IEEE,* Invited Paper, vol. 93, no.1, (January 2005), pp. 42-56.

Srinivasan, K. S. S. (2002). VLSI implementation of 2-D DWT/IDWT cores using 9/7-tap filter banks based on the non-expansive symmetric extension scheme, *IEEE International Conference on VLSI Design*, (January 2002), pp. 435-440.

Sweldens, W. (1996). The lifting scheme: A custom-design construction of biorthogonal wavelets, *Applied and Computation Harmonic Analysis*, vol. 3, no. 0015, (1996), pp.186-200.

Tan, K.C.B. & Arslan, T. (2003). Shift-accumulator ALU centric JPEG 2000 5/3 lifting based discrete wavelet transform architecture, *IEEE International Symposium on Circuits and Systems,* vol. 5, (May 2003), pp. V161-V164.

Varshney, H.; Hasan, M. & Jain, S. (2007). Energy efficient novel architecture for the lifting-based discrete wavelet transform, *IET Image Process*, vol. 1, no. 3, (September 2007), pp.305-310.

Weeks, M. & Bayoumi, M. A. (2002). Three-dimensional discrete wavelet transform architectures, *IEEE Transactions on Signal Processing*, vol. 50, no.8, (August 2002), pp. 2050-2063.

Wu, B.-F. & Lin, C.-F. (2005). A high-performance and memory-efficient pipeline architecture for the 5/3 and 9/7 discrete wavelet transform of JPEG2000 codec, *IEEE Transactions on Circuits and Systems for Video Technology*, vol. 15, no.12, (December 2005), pp. 1615-1628.

Part 3

Biomedical Applications

8

ECG Signal Compression Using Discrete Wavelet Transform

Prof. Mohammed Abo-Zahhad
Vice-Dean for Graduate Studies, Faculty of Engineering, University of Assiut, Egypt

1. Introduction

Transmission techniques of biomedical signals through communication channels are currently an important issue in many applications related to clinical practice. These techniques can allow experts to make a remote assessment of the information carried by the signals, in a very cost-effective way. However, in many situations this process leads to a large volume of information. The necessity of efficient data compression methods for biomedical signals is currently widely recognized. This chapter introduces the compression of ElectroCardioGram (ECG or EKG) signals using Discrete Wavelet Transform (DWT). It is well known that modern clinical systems require the storage, processing and transmission of large quantities of ECG signals. ECG signals are collected both over long periods of time and at high resolution. This creates substantial volumes of data for storage and transmission. Data compression seeks to reduce the number of bits of information required to store or transmit digitized ECG signals without significant loss of signal quality. Although storage space is currently relatively cheap, electronic ECG archives could easily become extremely large and expensive. Moreover, sending ECG recordings through mobile networks would benefit from low bandwidth demands. ECG signal compression attracted considerable attention over the last decade. Several examples of ECG compression algorithms have been described in the literature with compression ratios ranging approximately from 2:1 up to 50:1 (Jalaleddine et al., 1990; Addison, 2005). The main goal here is to provide an up-to-date introduction to this fascinating field; through presenting some of the latest algorithmic innovations and to stimulate readers to investigate the subject in greater depth using the extensive set of references provided (Addison, 2005; Padma et al., 2009). Section 2 introduces the production of the ECG signal and its main time- and frequency-domain parameters. Different ECG signal compression techniques including direct, transformed and optimization methods are presented in section 3. Section 4 discusses the fundamentals of DWTs and their filter bank realizations. Subjective and objective performance measures of compression algorithms are explained in section 5. In section 6, DWT based ECG signal compression algorithms are presented. This includes optimization-based, SPIHT, 2-D, hybrid, and linear prediction based algorithms. Thresholding, and coding of DWT coefficients considering energy packing efficiency and binary significant map are discussed in sections 7 and 8 respectively.

2. ElectroCardioGraphy

ECG signal is a recording of the electrical activity of the heart over time produced by an electrocardiograph and is a well-established diagnostic tool for cardiac diseases. ECG signal is monitored by placing sensors at defined positions on chest and limb extremities of the subject. Each heart beat is caused by a section of the heart generating an electrical signal which then conducts through specialized pathway to all parts of the heart. These electrical signals also get transmitted through the chest to the skin where they can be recorded. The following four steps in the generation of ECG signal can be monitored:

1. The S-A node (natural pacemaker) creates an electrical signal.
2. The electrical signal follows natural electrical pathways through both atria. The movement of electricity causes the atria to contract, which helps push blood into the ventricles.
3. The electrical signal reaches the A-V node (electrical bridge). There, the signal pauses to give the ventricles time to fill with blood.
4. The electrical signal spreads through the His-Purkinje system. The movement of electricity causes the ventricles to contract and push blood out to lungs and body.

ECG signal is obtained from a machine known as an Electrocardiograph, which captures the signal through an array of electrode sensors placed at standard locations on the skin of the human body. Modern electrocardiographs record ECG signals by digitizing and then storing the signal in magnetic or optical discs. An automated diagnostic system is required to speed up the diagnostic process and assist the cardiologists in examining patients using non-invasive techniques. Electrical impulses in the heart originate in the sinoatrial node and travel through the heart muscle where they impart electrical initiation of systole or contraction of the heart. The electrical waves can be measured at selectively placed electrodes (electrical contacts) on the skin. Electrodes on different sides of the heart measure the activity of different parts of the heart muscle. An ECG displays the voltage between pairs of these electrodes, and the muscle activity that they measure, from different directions, also understood as vectors. The ECG signal is composed from five waves labeled using five capital letters from the alphabet: P, Q, R, S, and T. The width of a wave on the horizontal axis represents a measure of time. The height and depth of a wave represent a measure of voltage. An upward deflection of a wave is called positive deflection and a downward deflection is called negative deflection. A typical representation of the ECG waves is presented in Figure (1) (Moody, (1992).

The electrocardiogram essentially reads the electrical impulses that stimulate the heart to contract. It is probably the most useful tool to determine whether the heart has been injured or how it is functioning. The ECG signal is made up of a number of segments or waves of different durations, amplitudes, and forms: ‘slow’, low-frequency P and T waves and short and high-frequency Q, R, and S waves, forming the QRS complex. P wave, QRS wave, and T wave, they are diagnostic critical waves. The P wave represents the atrial depolarization where the blood is squeezed from the atria to the ventricles. The QRS segment is when the ventricles depolarize and squeeze the blood from the right ventricle to the aorta. The T wave represents the period of time when the ventricles repolarize (get ready for the next heart beat). Most of the ECG signal energy is concentrated in the QRS complex, but there are diagnostically important changes in the low amplitude PQ and ST intervals, the P and T waves.

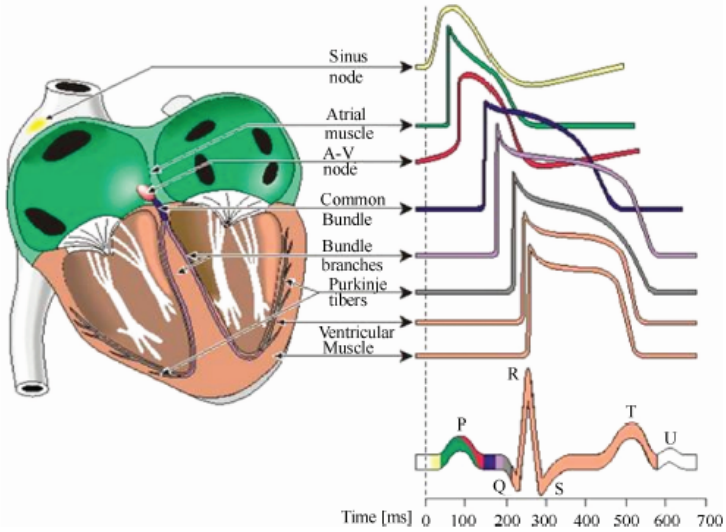

Fig. 1. A typical representation of the ECG waves.

Figure (2) illustrates the ECG signal in time and frequency domains. Compressing the ECG signal while preserving the original shape of the reconstructed signal and especially the amplitudes of Q, R and S peaks, without introducing distortions in the low amplitude ST segment, P and T waves are the main objectives of this chapter. In fact, most ECG compression algorithms produce ripple effects around QRS complexes and could also reduce the sharp waves' amplitudes.

3. ECG signal compression

Data reduction of ECG signal is achieved by discarding digitized samples that are not important for subsequent pattern analysis and rhythm interpretation. The data reduction algorithms are empirically designed to achieve good reduction without causing significant distortion error. ECG compression techniques can be categorized into: direct time-domain techniques; transformed frequency-domain techniques and parameters optimization techniques.

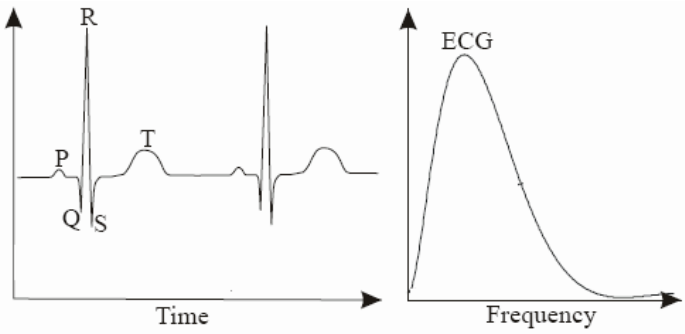

Fig. 2. ECG signal in time and frequency domains.

1. **Direct Signal Compression Techniques:** Direct methods involve the compression performed directly on the ECG signal. These are also known as time domain techniques dedicated to compression of ECG signal through the extraction of a subset of significant samples from the original sample set. Which signal samples are significant, depends on the underlying criterion for the sample selection process. To get a high performance time-domain compression algorithm, much effort should be put in designing intelligent sample selection criteria. The original signal is reconstructed by an inverse process, most often by drawing straight lines between the extracted samples. This category includes the FAN (Dipersio & Barr, 1985), CORTES (Abenstein & Tompkins, 1982), AZTEC (Cox et al., 1968), Turning Point (Mueller W., 1978) and TRIM (Moody et al., 1989) algorithms. The more recent cardinality constrained shortest path technique (Haugland et al., 1997) also fits into this category. Many of the time domain techniques for ECG signal compression are based on the idea of extracting a subset of significant signal samples to represent the original signal. The key to a successful algorithm is the development of a good rule for determining the most significant samples. Decoding is based on interpolating this subset of samples. The traditional ECG time domain compression algorithms all have in common that they are based on heuristics in the sample selection process. This generally makes them fast, but they all suffer from sub-optimality.
2. **Transformed ECG Compression Methods:** Transform domain methods, as their name implies, operate by first transforming the ECG signal into another domain. These methods mainly utilize the spectral and energy distributions of the signal by means of some transform, and properly encoding the transformed output. Signal reconstruction is achieved by an inverse transformation process. This category includes traditional transform coding techniques applied to ECG signals such as the Karhunen–Loève transform (Olmos et al., 1996), Fourier transform (Reddy & Murthy, 1986), Cosine transform (Ahmed et al., 1975), subband-techniques (Husøy & Gjerde, (1996), vector quantization (VQ) (Mammen & Ramamurthi, 1990), and more recently the wavelet transform (WT) (Chen et al., 1993; (Miaou et al.., 2002). Wavelet technique is the obvious choice for ECG signal compression because of its localized and non-stationary property and the well-proven ability of wavelets to see through signals at different resolutions. Wavelets are mathematical functions that cut up data into different scale-shift components. The wavelet decomposition splits the analyzing signal into average and detail coefficients, using finite impulse response digital filters. The main task in wavelet analysis (decomposition and reconstruction) is to find a good analyzing function (mother wavelet) to perform an optimal decomposition. Wavelet-based ECG compression methods have been proved to perform well. The ability of DWT to separate out pertinent signal components has led to a number of wavelet-based techniques which supersede those based on traditional Fourier methods. The discrete wavelet transform has interesting mathematics and fits in with standard signal filtering and encoding methodologies. It produces few coefficients, and the user does not have to worry about losing energy during the transform process or its inverse. While the DWT is faster and maps quickly to the sub-band coding of signals, the Continuous Wavelet Transform (CWT) allows the user to analyze the signal at various scales and translations according to the problem.
3. **Optimization Methods For ECG Compression:** More recently, many interesting optimization based ECG compression methods, the third category, have been developed. The goal of most of these methods is to minimize the reconstruction error

given a bound on the number of samples to be extracted or the quality of the reconstructed signal to be achieved. In (Haugland et al., 1997), the goal is to minimize the reconstruction error given a bound on the number of samples to be extracted. The ECG signal is compressed by extracting the signal samples that, after interpolation, will best represent the original signal given an upper bound on their number. After the samples are extracted they are Huffman encoded. This leads to the best possible representation in terms of the number of extracted signal samples, but not necessarily in terms of bits used to encode such samples. In (Nygaard et al., 1999), the bit rate has been taken into consideration in the optimization process.

The vast majority of the above mentioned methods do not permit perfect reconstruction of the original signals. In fact; there is no automatic way to assure that the distortion in the reconstructed signal will not affect clinically important features of the ECG. To preserve the clinical diagnostic features of the reconstructed ECG signals both the wavelet filters' parameters and the threshold levels in all subbands should be selected carefully. Thus, the aim is to present ECG compression technique that achieves maximum data volume reduction while preserving the significant signal morphology features upon reconstruction. This has been achieved through the minimization of both the bit rate and the distortion of the reconstructed ECG signal through parameterization of the wavelet filters and the selection of optimum threshold levels of the wavelet coefficients in different subbands.

4. Discrete wavelet transform

In technical literature, a number of time–frequency methods are currently available for the high resolution signal decomposition. This includes the short time Fourier transform (STFT), Wigner–Ville transform (WVT), Choi–Williams distribution (CWD) and the WT. Of these, the wavelet transform has emerged as the most favored tool by researchers as it does not contain the cross terms inherent in the WVT and CWD methods while possessing frequency-dependent windowing which allows for arbitrarily high resolution of the high frequency signal components. The DWT is the appropriate tool for the analysis of ECG signals as it removes the main shortcomings of the STFT; namely it uses a single analysis window which is of fixed length in both time and frequency domains. This is a major drawback of the STFT, since what are really needed are a window of short length (in time domain) for the high frequency content of a signal and a window of longer length for the low frequency content of the signal. The WT improves upon the STFT by varying the window length depending on the frequency range of analysis. This effect is obtained by scaling (contractions and dilations) as well as shifting the basis wavelet. The continuous wavelet transform (CWT) transforms a continuous signal into highly redundant signal of two continuous variables — translation and scale. The resulting transformed signal is easy to interpret and valuable for time-frequency analysis. The continuous wavelet transform of continuous function, $f(x)$ relative to real-valued wavelet, $\psi(x)$ is described by:

$$W_{\psi}(s,\tau) = \int_{-\infty}^{\infty} f(x)\psi_{s,\tau}(x)\,dx \tag{1}$$

where,

$$\psi_{s,\tau}(x) = \frac{1}{\sqrt{s}}\psi\left(\frac{x-\tau}{s}\right) \tag{2}$$

s and τ are called scale and translation parameters, respectively. $W_\psi(s,\tau)$ denotes the wavelet transform coefficients and ψ is the fundamental mother wavelet. If $W_\psi(s,\tau)$ is given, $f(x)$ can be obtained using the inverse continuous wavelet transform (ICWT) that is described by:

$$f(x)=\frac{1}{C_\psi}\int_0^\infty\int_{-\infty}^{\infty} W_\psi(s,\tau)\frac{\psi_{s,\tau}(x)}{s^2}d\tau\, ds \tag{3}$$

where, $\Psi(u)$ is the Fourier transform of $\psi(x)$ and

$$C_\psi=\int_{-\infty}^{\infty}\frac{|\Psi(u)|^2}{|u|}du \tag{4}$$

The discrete wavelet transform can be written on the same form as Equation (1), which emphasizes the close relationship between CWT and DWT. The most obvious difference is that the DWT uses scale and position values based on powers of two. The values of s and τ are: $s=2^j, \tau=k*2^j$ and $(j,k)\in Z^2$ as shown in Equation (5).

$$\psi_{j,k}(x)=\frac{1}{\sqrt{s_o^j}}\psi\left(\frac{x-k\tau_o s_o^j}{s_o^j}\right) \tag{5}$$

The key issues in DWT and inverse DWT are signal decomposition and reconstruction, respectively. The basic idea behind decomposition and reconstruction is low-pass and high-pass filtering with the use of down sampling and up sampling respectively. The result of wavelet decomposition is hierarchically organized decompositions. One can choose the level of decomposition j based on a desired cutoff frequency. Figure (3-a) shows an implementation of a three-level forward DWT based on a two-channel recursive filter bank, where $h_0(n)$ and $h_1(n)$ are low-pass and high-pass analysis filters, respectively, and the block $\downarrow 2$ represents the down sampling operator by a factor of 2. The input signal $x(n)$ is recursively decomposed into a total of four subband signals: a coarse signal $C_3(n)$, and three detail signals, $D_3(n)$, $D_2(n)$, and $D_1(n)$, of three resolutions. Figure (3-b) shows an implementation of a three-level inverse DWT based on a two-channel recursive filter bank, where $\tilde{h}_0(n)$ and $\tilde{h}_1(n)$ are low-pass and high-pass synthesis filters, respectively, and the block $\uparrow 2$ represents the up sampling operator by a factor of 2. The four subband signals $C_3(n)$, $D_3(n)$, $D_2(n)$ and $D_1(n)$, are recursively combined to reconstruct the output signal $\tilde{x}(n)$. The four finite impulse response filters satisfy the following relationships:

$$h_1(n)=(-1)^n h_0(n) \tag{6}$$

$$\tilde{h}_0(n)=h_0(1-n) \tag{7}$$

$$\tilde{h}_1(n)=(-1)^n h_0(1-n) \tag{8}$$

so that the output of the inverse DWT is identical to the input of the forward DWT.

5. Compression algorithms performance measures

5.1 Subjective judgment

The most obvious way to determine the preservation of diagnostic information is to subject the reconstructed data for evaluation by a cardiologist. This approach might be accurate in some cases but suffers from many disadvantages. One drawback is that it is a subjective measure of the quality of reconstructed data and depends on the cardiologist being consulted, thus different results may be presented. Another shortcoming of the approach is that it is highly inefficient. Moreover, the subjective judgment solution is expensive and can generally be applied only for research purposes (Zigel et al., 2000).

5.2 Objective judgment

Compression algorithms all aim at removing redundancy within data, thereby discarding irrelevant information. In the case of ECG compression, data that does not contain diagnostic information can be removed without any loss to the physician. To be able to compare different compression algorithms, it is imperative that an error criterion is defined such that it will measure the ability of the reconstructed signal to preserve the relevant diagnostic information. The criteria for testing the performance of the compression algorithms consist of three components: compression measure, reconstruction error and computational complexity. The compression measure and the reconstruction error depend usually on each other and determine the rate-distortion function of the algorithm. The computational complexity component is related to practical implementation consideration and is desired to be as low as possible.

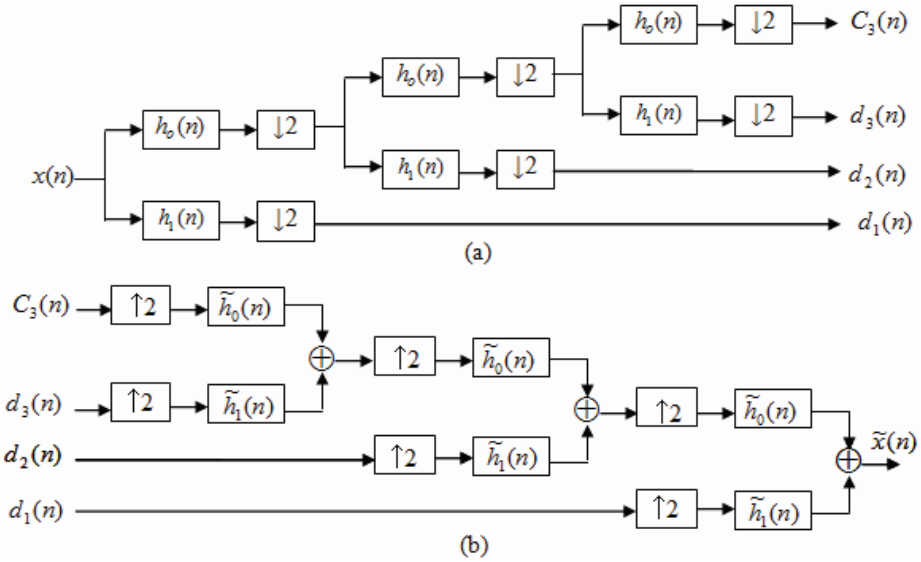

Fig. 3. A three-level two-channel iterative filter bank (a) forward DWT (b) inverse DWT

The compression ratio (*CR*) is defined as the ratio of the number of bits representing the original signal to the number required for representing the compressed signal. So, it can be calculated from:

$$CR = \frac{N\, b_C}{(N_S + M)(b_S + 1)} \tag{9}$$

Where, b_C is the number of bits representing each original ECG sample. One of the most difficult problems in ECG compression applications and reconstruction is defining the error criterion. Several techniques exist for evaluating the quality of compression algorithms. In some literature, the root mean square error (*RMS*) is used as an error estimate. The *RMS* is defined as

$$RMS = \sqrt{\frac{\sum_{n=1}^{N} (x(n) - \hat{x}(n))^2}{N}} \tag{10}$$

where $x(n)$ is the original signal, $\hat{x}(n)$ is the reconstructed signal and N is the length of the window over which the *RMS* is calculated(Zou & Tewfik, 1993). This is a purely mathematical error estimate without any diagnostic considerations.

The distortion resulting from the ECG processing is frequently measured by the percent root-mean-square difference (*PRD*) (Ahmed et al., 2000). However, in previous trials focus has been on how much compression a specific algorithm can achieve without loosing too much diagnostic information. In most ECG compression algorithms, the *PRD* measure is employed. Other error measures such as the *PRD* with various normalized root mean square error and signal to noise ratio (*SNR*) are used as well (Javaid et al., 2008). However, the clinical acceptability of the reconstructed signal is desired to be as low as possible. To enable comparison between signals with different amplitudes, a modification of the RMS error estimate has been devised. The *PRD* is defined as:

$$PRD = \sqrt{\frac{\sum_{n=1}^{N} (x(n) - \hat{x}(n))^2}{\sum_{n=1}^{N} x^2(n)}} \tag{11}$$

This error estimate is the one most commonly used in all scientific literature concerned with ECG compression techniques. The main drawbacks are the inability to cope with baseline fluctuations and the inability to discriminate between the diagnostic portions of an ECG curve. However, its simplicity and relative accuracy make it a popular error estimate among researchers (Benzid et al., 2003; Blanco-Velasco et al., 2004).

As the PRD is heavily dependent on the mean value, it is more appropriate to use the modified criteria:

$$PRD_1 = \sqrt{\frac{\sum_{n=1}^{N} (x(n) - \hat{x}(n))^2}{\sum_{n=1}^{N} (x(n) - \bar{x})^2}} \tag{12}$$

where $\bar{x}$ is the mean value of the signal. Furthermore, it is established in (Zigel et al., 2000), that if the PRD_1 value is between 0 and 9%, the quality of the reconstructed signal is either

'very good' or 'good', whereas if the value is greater than 9% its quality group cannot be determined. As we are strictly interested in very good and good reconstructions, it is taken that the PRD value, as measured with (11), must be less than 9%.

In (Zigel et al., 2000), a new error measure for ECG compression techniques, called the weighted diagnostic distortion measure (*WDD*), was presented. It can be described as a combination of mathematical and diagnostic subjective measures. The estimate is based on comparing the PQRST complex features of the original and reconstructed ECG signals. The *WDD* measures the relative preservation of the diagnostic information in the reconstructed signal. The features investigated include the location, duration, amplitudes and shapes of the waves and complexes that exist in every heartbeat. Although, the *WDD* is believed to be a diagnostically accurate error estimate, it has been designed for surface ECG recordings. More recently (Al-Fahoum, 2006), quality assessment of ECG compression techniques using a wavelet-based diagnostic measure has been developed. This approach is based on decomposing the segment of interest into frequency bands where a weighted score is given to the band depending on its dynamic range and its diagnostic significance.

6. DWT based ECG signal compression algorithms

As described above, the process of decomposing a signal x into approximation and detail parts can be realized as a filter bank followed by down-sampling (by a factor of 2) as shown in Figure (4). The impulse responses $h[n]$ (low-pass filter) and $g[n]$ (high-pass filter) are derived from the scaling function and the mother wavelet. This gives a new interpretation of the wavelet decomposition as splitting the signal x into frequency bands. In hierarchical decomposition, the output from the low-pass filter h constitutes the input to a new pair of filters. This results in a multilevel decomposition. The maximum number of such decomposition levels depends on the signal length. For a signal of size N, the maximum decomposition level is $\log_2(N)$.

The process of decomposing the signal x can be reversed, that is given the approximation and detail information it is possible to reconstruct x. This process can be realized as up-sampling (by a factor of 2) followed by filtering the resulting signals and adding the result of the filters. The impulse responses h' and g' can be derived from h and g. If more than two bands are used in the decomposition we need to cascade the structure.

In (Chen et al., 1993), the wavelet transform as a method for compressing both ECG and heart rate variability data sets has been developed. In (Thakor et al., 1993), two methods of data reduction on a dyadic scale for normal and abnormal cardiac rhythms, detailing the errors associated with increasing data reduction ratios have been compared. Using discrete orthonormal wavelet transforms and Daubechies D_{10} wavelets, Chen et al., compressed ECG data sets resulting in high compression ratios while retaining clinically acceptable signal quality (Chen & Itoh, 1998). In (Miaou & Lin, 2000), D_{10} wavelets have been used, with the incorporating of adaptive quantization strategy which allows a predetermined desired signal quality to be achieved. Another quality driven compression methodology based on Daubechies wavelets and later on biorthogonal wavelets has been proposed (Miaou & Lin, 2002). The latter algorithm adopts the set partitioning of hierarchical tree (SPIHT) coding strategy. In (Bradie, 1996), the use of a wavelet-packet-based algorithm for the compression of the ECG signal has been suggested. By first normalizing beat periods using multi rate processing and normalizing beat amplitudes the ECG signal is converted into a near cyclostationary sequence (Ramakrishnan & Saha, 1997). Then Ramakrishnan and Saha

employed a uniform choice of significant Daubechies D_4 wavelet transform coefficients within each beat thus reducing the data storage required. Their method encodes the QRS complexes with an error equal to that obtained in the other regions of the cardiac cycle. More recent DWT data compression schemes for the ECG include the method using non-orthogonal wavelet transforms (Ahmed et al., 2000), and SPIHT algorithm (Lu et al., 2000).

6.1 Optimization-based compression algorithm

As it has been mentioned before, many of the resulting wavelet coefficients are either zero or close to zero. These coefficients are divided into two classes according to their energy content; namely: high energy coefficients and low energy coefficients. By coding only the larger coefficients, many bits are already discarded. The high energy coefficients should be compressed very accurately because they contain more information. So, they are threshold with low threshold levels. However, the low energy coefficients that represent the details are threshold with high threshold levels. The success of this scheme is based on the fact that only a fraction of nonzero value wavelet coefficients may be encoded using a small number of bits.

In (Zou & Tewfik, 1993), the problem of finding a wavelet that best matches the wave shape of the ECG signal has been addressed. The main idea behind this approach is to find the minimum distortion representation of a signal, subject to a given bit budget or to find the minimum bit rate representation of a signal, subject to a target PRD. If, for a given wavelet, the error associated with the compressed signal is minimal, then its wavelet coefficients are considered to best represent the original signal. Therefore, the selected wavelet would more effectively match the signal under analysis when compared to standard wavelets (Daubechies, 1998). The DWT of the discrete type signal x[n] of length N is computed in a recursive cascade structure consisting of decimators $\downarrow 2$ and complementing low-pass (h) and high-pass (g) filters which are uniquely associated with a wavelet. The signal is iteratively decomposed through a filter bank to obtain its discrete wavelet transform. This gives a new interpretation of the wavelet decomposition as splitting the signal into frequency bands. Figure (4) depicts a diagram of the filter bank structure. In hierarchical decomposition, the output from the low-pass filter constitutes the input to a new pair of filters. The filters coefficients corresponding to scaling and wavelet functions are related by

$$g[n] = (-1)^n h[L - n], \quad n = 0, 1, \ldots, L-1 \tag{13}$$

where L is the filter length. To adapt the mother wavelet to the signals for the purpose of compression, it is necessary to define a family of wavelets that depend on a set of parameters and a quality criterion for wavelet selection (i.e. wavelet parameter optimization). These concepts have been adopted to derive a new approach for ECG signal compression based on dyadic discrete orthogonal wavelet bases, with selection of the mother wavelet leading to minimum reconstruction error. An orthogonal wavelet transform decomposes a signal into dilated and translated versions of the wavelet function $\psi(t)$. The wavelet function $\psi(t)$ is based on a scaling function $\varphi(t)$ and both can be represented by dilated and translated versions of this scaling function.

$$\varphi(t) = \sum_{n=0}^{L-1} h(n)\varphi(2t-n) \quad \textit{and} \quad \psi(t) = \sum_{n=0}^{L-1} g(n)\varphi(2t-n) \tag{14}$$

With these coefficients *h(n)* and *g(n)*, the transfer functions of the filter bank that are used to implement the discrete orthogonal wavelet transform, can be formulated.

$$H(z) = \sum_{b=0}^{L-1} h(n) z^{-n} \quad and \quad G(z) = \sum_{b=0}^{L-1} g(n) z^{-n} \tag{15}$$

For a finite impulse response (FIR) filter of length *L*, there are $L/2+1$ sufficient conditions to ensure the existence and orthogonality of the scaling function and wavelets (Donoho & Johnstone, 1998). Thus $L/2-1$ degrees of freedom (free parameters) remain to design the filter *h*.

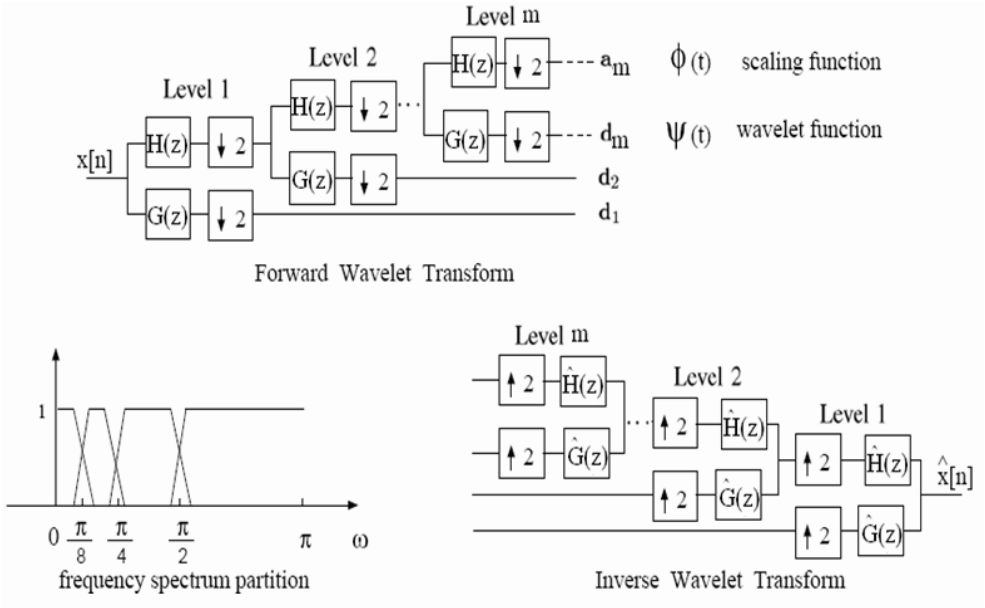

Fig. 4. The DWT implementation using a filter bank structure.

The lattice parameterization described in (Vaidyanathan, 1993) offers the opportunity to design *h* via unconstrained optimization: the *L* coefficients of *h* can be expressed in term of $L/2-1$ new free parameters. These parameters can be used to choose the wavelets which results in a good coding performance. The Daubechies wavelet family was constructed by using all the free parameters to maximize the number of vanishing moments. Coiflet wavelets were designed by imposing vanishing moments on both the scaling and wavelet functions. In (Zou & Tewfik, 1993) wavelet parameterizations have been used to systematically generate *L*-tap orthogonal wavelets using the $L/2-1$ free parameters for *L* = 4, 6 and 8. The order of a wavelet filter is important in achieving good coding performance. A higher order filter can be designed to have good frequency localization which in turn increases the energy compaction. Consequently, by restriction to the orthogonal case, *h* defines ψ. For this purpose consider, the orthogonal 2x2 rotational angles, realized by the lattice section shown in Figure (5), and defined by the matrix:

$$R(\beta_i) = \begin{bmatrix} \cos\beta_i & -\sin\beta_i \\ \sin\beta_i & \cos\beta_i \end{bmatrix} \tag{16}$$

The polyphase matrix $H_p(z)$ can be defined in terms of the rotational angles as

$$H_p(z) = \begin{bmatrix} H_e(z^2) & H_o(z^2) \\ G_e(z^2) & G_o(z^2) \end{bmatrix} = \prod_{i=o}^{L/2-1} \left(\begin{bmatrix} \cos\beta_i & -\sin\beta_i \\ \sin\beta_i & \cos\beta_i \end{bmatrix} \begin{bmatrix} 1 & 0 \\ 0 & z^{-1} \end{bmatrix} \right) \tag{17}$$

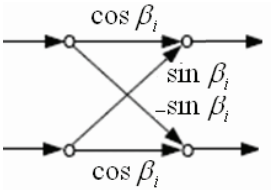

Fig. 5. Lattice Implementation

where, $H_e(z)$, $H_o(z)$, $G_e(z)$ and $G_o(z)$ are defined, respectively, from the decomposition of $H(z)$ and $G(z)$ as

$$H(z) = H_e(z^2) + z^{-1} H_o(z^2) \tag{18a}$$

and

$$G(z) = G_e(z^2) + z^{-1} G_o(z^2) \tag{18b}$$

To obtain the expressions for the coefficients of *H(z)* in terms of the rotational angles, it is necessary to multiply out the above matrix product. In order to parameterize all orthogonal wavelet transforms leading to a simple implementation, the following facts should be considered.

1. Orthogonality is structurally imposed by using lattice filters consisting of orthogonal rotations.
2. The sufficient condition for constructing a wavelet transform, namely one vanishing moment of the wavelet, is guaranteed, by assuring the sum of all rotation angles of the filters to be exactly -45^o .

A suitable architecture for the implementation of the orthogonal wavelet transforms are lattice filters. However, the wavelet function should be of zero mean, which is equivalent to the wavelet having at least one vanishing moment and the transfer functions *H(z)* and *G(z)* have at least one zero at z =-1 and z=1 respectively. These conditions are fulfilled if the sum of all rotation angles is 45^o (Xie & Morris, 1994), i.e.,

$$\sum_{i=1}^{L/2} \beta_i = 45^o \tag{19}$$

Therefore, a lattice filter whose sum of all rotation angles is 45^o performs an orthogonal WT independent of the angles of each rotation. For a lattice filter of length *L*, *L*/2 orthogonal

rotations are required. Denote the rotation angles by β_i , $i = 1, 2, \ldots, L/2$, and considering the constraint given in (19), the number of design angles θ s is *L/2-1.* The following is the relation between the rotation angles and the design angles.

$$\left.\begin{aligned} \beta_1 &= 45^o - \theta_1 , \\ \beta_i &= (-1)^i (\theta_{i-1} + \theta_i) \ \ for \ \ i = 2, 3, \ldots, L/2 - 1, \\ \beta_{L/2} &= (-1)^{L/2} \ \theta_{L/2-1} \end{aligned}\right\} \tag{20}$$

At the end of the decomposition process, a set of vectors representing the wavelet coefficients is obtained

$$C = \left\{ d_1 \ , \ d_2 \ , \ d_3 \ , \ \ldots \ , \ d_j \ , \ \ldots \ , \ d_m \ , \ a_m \right\} \tag{21}$$

where, *m* is the number of decomposition levels of the DWT. This set of approximation and detail vectors represents the DWT coefficients of the original signal. Vectors d_j contain the detail coefficients of the signal in each scale *j*. As *j* varies from 1 to *m*, a finer or coarser detail coefficients vector is obtained. On the other hand, the vector a_m contains the approximation wavelet coefficients of the signal at scale *m*. It should be noted that this recursive procedure can be iterated $(m \le \log_2 N)$ times at most. Depending on the choice of *m*, a different set of coefficients can be obtained. The inverse transform can be performed using a similar recursive approach. Thus, the process of decomposing the signal *x* can be reversed, that is given the approximation and detail information it is possible to reconstruct *x*. This process can be realized as up-sampling (by a factor of 2) followed by filtering the resulting signals and adding the result of the filters. The impulse responses *h*′ and *g*′ can be derived from *h* and *g*. However, to generate an orthogonal wavelet, *h* must satisfy some constraints. The basic condition is $\sum_{n=1}^{L} h(n) = \sqrt{2}$, to ensure the existence of ϕ . Moreover, for orthogonality, *h* must be of norm one and must satisfy the quadratic condition

$$\sum_{n=1}^{L} h(n) \sum_{n=1}^{L} h(n - 2k) = 0, \ \ for \ \ k = 1, \ldots, L/2 - 1 \tag{22}$$

The lattice parameterization described in (Vaidyanathan, 1993) offers the opportunity to design *h* using unconstrained optimization by expressing the $L/2 - 1$ free parameters in terms of the design parameter vector θ . For instance, if *L* = *6*, two-component design vector, $\theta = [\theta_1 \ , \theta_2]$ is needed, and *h* is given by (Vaidyanathan, 1993):

$$i = 0 \ , 1 \qquad h(i) = \left[\left(1 + (-1)^i \cos\theta_1 + \sin\theta_1\right)\left(1 - (-1)^i \cos\theta_2 - \sin\theta_2\right) + (-1)^i \, 2 \sin\theta_2 \cos\theta_1 \right] / 4\sqrt{2}$$

$$i = 2 \ , 3 \qquad h(i) = \left[1 + \cos(\theta_1 - \theta_2) + (-1)^i \sin(\theta_1 - \theta_2) \right] / 2\sqrt{2}$$

$$i = 4 \ , 5 \qquad h(i) = 1/\sqrt{2} - h(i-4) - h(i-2) \tag{23}$$

For other values of *L*, expressions of *h* are given in (Maitrot et al., 2005). With this wavelet parameterization there are infinite available wavelets which depend on the design parameter vector θ to represent the ECG signal at hand. Different values of θ may lead to different quality in the reconstructed signal. In order to choose the optimal θ values, and thus the optimal wavelet, a blind criterion of performance is needed. Figure (6) illustrates the block diagram of the proposed compression algorithm. In order to establish an efficient solution scheme, the following precise problem formulation is developed. For this purpose, consider the one-dimensional vector *x(i), i=1, 2, 3, …., N* represents the frame of the ECG signal to be compressed; where *N* is the number of its samples. The initial threshold values are computed separately for each subband by finding the mean (μ) and standard deviation (σ) of the magnitude of the non-zero wavelet coefficients in the corresponding subband. If the σ is greater than μ then the threshold value in that subband is set to (2*μ), otherwise, it is set to (μ-σ). Also, define the targeted performance measures PRD_{target} and CR_{target} and start with an initial wavelet design parameter vector $\theta = [\theta_{10}, \theta_{20}, \ldots, \theta_{L-10}]$ to construct the wavelet filters *H(z)* and *G(z)*. Figure (7) illustrates the compression algorithm for satisfying predefined *PRD* (PRD_1) with minimum bit rate representation of the signal. The same algorithm with little modifications is used for satisfying predefined bit rate with minimum signal distortion measured by PRD (PRD_1); case 2. In this case, the shaded two blocks are replaced by: CR calculation and predefined CR is reached?, respectively.

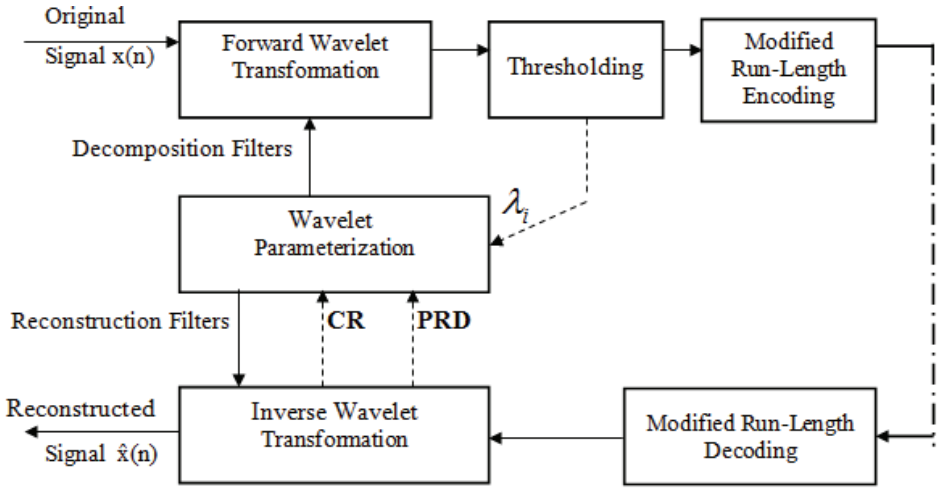

Fig. 6. Block diagram for the proposed compression algorithm.

6.2 Compression of ECG signals using SPIHT algorithm

SPIHT is an embedded coding technique; where all encodings of the same signal at lower bit rates are embedded at the beginning of the bit stream for the target bit rate. Effectively, bits are ordered in importance. This type of coding is especially useful for progressive transmission and transmission over a noisy channel. Using an embedded code, an encoder can terminate the encoding process at any point, thereby allowing a target rate or distortion parameter to be met exactly. Typically, some target parameters, such as bit count, is monitored in the encoding

process and when the target is met, the encoding simply stops. Similarly, given a bit stream, the decoder can cease decoding at any point and can produce reconstruction corresponding to all lower-rate encodings. EZW, introduced in (Shapiro, 1993) is a very effective and computationally simple embedded coding algorithm based on discrete wavelet transform, for image compression. SPIHT algorithm introduced for image compression in (Said & Pearlman, 1996) is a refinement to EZW and uses its principles of operation.

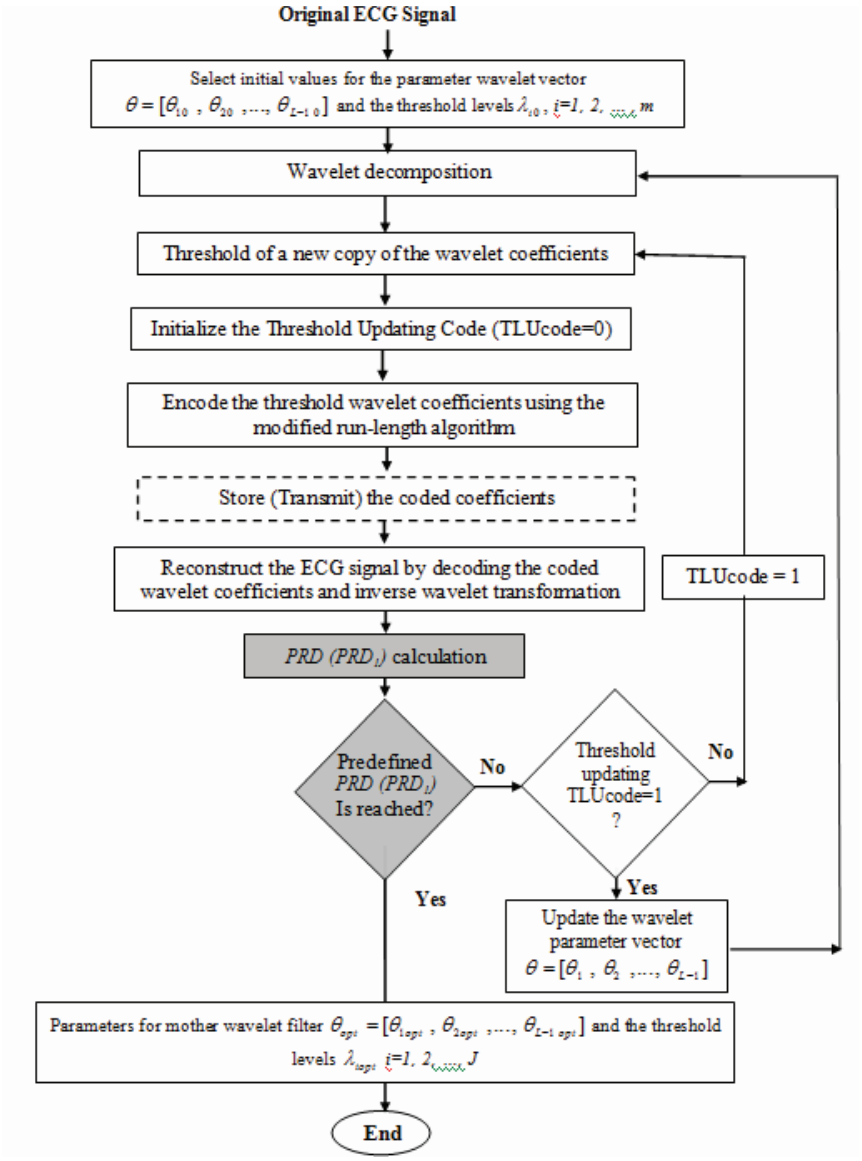

Fig. 7. Compression Algorithm for Satisfying Predefined *PRD* with Minimum Bit Rate.

These principles are partial ordering of transform coefficients by magnitude with a set partitioning sorting algorithm, ordered bit plane transmission and exploitation of self-similarity across different scales of an image wavelet transform. The partial ordering is done by comparing the transform coefficients magnitudes with a set of octavely decreasing thresholds. In this algorithm, a transmission priority is assigned to each coefficient to be transmitted. Using these rules, the encoder always transmits the most significant bit to the decoder. In (Lu et al., 2000), SPIHT algorithm is modified for 1-D signals and used for ECG compression. For faster computations SPIHT algorithm can be described as follows:

1. ECG signal is divided to contiguous non-overlapping frames each of N samples and each frame is encoded separately.
2. DWT is applied to the ECG frames up to L decomposition levels.
3. Each wavelet coefficient is represented by a fixed-point binary format, so it can be treated as an integer.
4. SPIHT algorithm is applied to these integers (produced from wavelet coefficients) for encoding them.
5. The termination of encoding algorithm is specified by a threshold value determined in advance; changing this threshold, gives different compression ratios.
6. The output of the algorithm is a bit stream (0 and 1). This bit stream is used for reconstructing signal after compression. From it and by going through inverse of SPIHT algorithm, we compute a vector of N wavelet coefficients and using inverse wavelet transform, we make the reconstructed N sample frame of ECG signal.

In (Pooyan et al., 2005), the above algorithm is tested with N=1024 samples, L=6 levels and the DWT used is biorthogonal 9/7 (with symmetric filters h(n) with length 9 and g(n) with length 7). The filters' coefficients are given in Table (1).

n	0	±1	±2	±3	±4
h(n)	0,852699	0,377403	-0.11062	-0.023849	0.037829
g(n)	0.788485	0.418092	-0.04069	-0.064539	

Table 1. Coefficients of the Biorthogonal 9/7 Tap Filters.

6.3 2-D ECG compression methods based on DWT

By observing the ECG waveforms, a fact can be concluded that the heartbeat signals generally show considerable similarity between adjacent heartbeats, along with short-term correlation between adjacent samples. However, most existing ECG compression techniques did not utilize such correlation between adjacent heartbeats. A compression scheme using two-dimensional DWT transform is an option to employ the correlation between adjacent heartbeats and can thus further improve the compression efficiency. In (Reza et al., 2001; Ali et al., 2003) a 2-D wavelet packet ECG compression approach and a 2-D wavelet based ECG compression method using the JPEG2000 image compression standard have been presented respectively. These 2-D ECG compression methods consist of: 1) QRS detection, 2) preprocessing (cut and align beats, period normalization, amplitude normalization, mean removal), 3) transformation, and 4) coefficient encoding. Period normalization helps utilizing the interbeat correlation but incurs some quantization errors. Mean removal helps maximizing the interbeat correlation since dc value of each beat is different due to baseline change. Recently (Tai et al., 2005), a 2-D approach for ECG compression that utilizes the

redundancy between adjacent heartbeats has been presented. The QRS complex in each heartbeat is detected for slicing and aligning a 1-D ECG signal to a 2-D data array, and then 2-D wavelet transform is applied to the constructed 2-D data array. Consequently, a modified SPIHT algorithm is applied to the resulting wavelet coefficients for further compression. The way that the 2-D ECG algorithm presented in (Tai et al., 2005) differs from other 2-D algorithms, (Reza et al., 2001; Ali et al., 2003), is that it not only utilizes the interbeat correlation but also employs the correlation among coefficients in relative subbands. More recently (Wang & Meng, 2008), a new 2-D wavelet-based ECG data compression algorithm has been presented. In this algorithm a 1-D ECG data is first segmented and aligned to a 2-D data array, thus the two kinds of correlation of heartbeat signals can be fully utilized. And then 2-D wavelet transform is applied to the constructed 2-D ECG data array. The resulting wavelet coefficients are quantized using a modified vector quantization (VQ). This modified VQ algorithm constructs a new tree vector which well utilizing the characteristics of the wavelet coefficients. Experimental results show that this method is suitable for various morphologies of ECG data, and that it achieves higher compression ratio with the characteristic features well preserved.

6.4 Hybrid ECG signal compression methods

Hybrids ECG signal compression methods are constructed from more than time and/or frequency domain techniques (Ahmed et al., 2007). These include Modified Discrete Cosine Transform (MDCT) and DWT; linear prediction coding and DWT. By studying the ECG waveforms, it can be concluded that the ECG signals generally show two types of correlation, namely correlation between adjacent samples within each ECG cycles (intrabeat correlation) and correlation between adjacent heartbeats (interbeat correlation) (Xingyuan & Juan, 2009). However, most existing ECG compression techniques did not utilize such correlation between adjacent heartbeats. Hybrid compression methods of ECG signals are discussed in this section, which fully utilizes the interbeat correlation and thus can further improve the compression efficiency.

6.4.1 ECG signal compression based on combined MDCT and DWT

In (Ahmed et al., 2008), a hybrid two-stage electrocardiogram (ECG) signals compression method based on the MDCT and DWT has been proposed. The ECG signal is partitioned into blocks and the MDCT is applied to each block to decorrelate the spectral information. Then, the DWT is applied to the resulting MDCT coefficients. The resulting wavelet coefficients are then threshold and compressed using energy packing and binary-significant map coding technique for storage space saving. MDCT is a linear orthogonal lapped transform, based on the idea of time domain aliasing cancellation (TDAC). It is designed to be performed on consecutive blocks of a larger dataset, where subsequent blocks are overlapped so that the last half of one block coincides with the first half of the next block. This overlapping, in addition to the energy-compaction qualities of the DCT, makes the MDCT especially attractive for signal compression applications. Thus, it helps to avoid artifacts stemming from the block boundaries (Britanak & Rao, 2002; Nikolajevic & Fettweis, 2003). MDCT is critically sampled, which means that though it is 50% overlapped, a sequence data after MDCT has the same number of coefficients as samples before the transform (after overlap-and-add). This means that, a single block of IMDCT data does not correspond to the original block on which the MDCT was performed. When subsequent

blocks of inverse transformed data are added, the errors introduced by the transform cancel out TDAC. The MDCT is defined as (Nikolajevic & Fettweis, 2003):

$$X_C(k) = \sum_{n=0}^{N-1} x(n) \cos\left[\left(n + \frac{M+1}{2}\right)\left(k + \frac{1}{2}\right)\frac{\pi}{M}\right], \quad k = 0, 1, \ldots M-1 \tag{24}$$

where, *x(n), n=0, 1, 2, …*, N-1 is the sequence to be transformed, N=2M is the window length and M is the number of transform coefficients. The computation burden can be reduced if the transform coefficients given by equation (24) are rewritten in the following recursive form

$$X_C(k) = x(0)\cos\left[(M+1)\frac{\theta_k}{2}\right] + V_1 \cos\left[(M+3)\frac{\theta_k}{2}\right] - V_2 \cos\left[(M+1)\frac{\theta_k}{2}\right] \tag{25}$$

Where,

$$V_m = x(m) + 2\cos\theta_k V_{m+1} - V_{m+2}, \; m = N-1, N-2, \ldots, 1, 0 \tag{26}$$

and

$$\theta_k = \left(k + \frac{1}{2}\right)\frac{\pi}{M} \tag{27}$$

The MDCT computation algorithm of a data sequence *x(n)* can be summarized in the following:

1. Partition the data sequence in N_b consecutive blocks, each one with *N=64* samples.
2. Recursively generate the V_m from the input sequence *x(n)* according to (26) and (27).
3. Calculate the MDCT coefficients for each block by evaluating the k-th MDCT coefficient using (25) at the N-th step.

In the decompression stage, the inverse MDCT, that is termed IMDCT, is adopted. Because there are different numbers of inputs and outputs, at first glance it might seem that the MDCT should not be invertible. However, perfect invertability is achieved by adding the overlapped IMDCTs of subsequent overlapping blocks, causing the errors to cancel and the original data to be retrieved. The IMDCT transforms the *M* real coefficients, $X_C(0), X_C(1), \ldots, X_C(M-1)$, into *N=2M* real numbers, *x(0), x(1), ….. , x(N-1)*, according to the formula:

$$x(n) = \sum_{k=0}^{M-1} X_C(k)\cos\left[\left(n + \frac{M+1}{2}\right)\left(k + \frac{1}{2}\right)\frac{\pi}{M}\right], \quad n = 0, 1, \ldots N-1 \tag{28}$$

Again, the computation burden of *x(n)* can be reduced considerably if equation (28) is rewritten in the following recursive form

$$x(n) = X_C(0)\cos\left[\frac{\theta_n}{2}\right] + V_1 \cos\left[\frac{3\theta_n}{2}\right] - V_2 \cos\left[\frac{\theta_n}{2}\right] \tag{29}$$

Where, $V_m = X_C(m) + 2\cos\theta_n V_{m+1} - V_{m+2}$ and $\theta_n = \left(n + \frac{M+1}{2}\right)\frac{\pi}{M}$ (30)

6.4.2 ECG signal compression based on the linear prediction of DWT coefficients

In (Abo-Zahhad et al., 2000; Ahmed & Abo-Zahhad, 2001), a new hybrid algorithm for ECG compression based on the compression of the linearly predicted residuals of the wavelet coefficients is presented. The main goal of the algorithm is to reduce the bit rate while keeping the reconstructed signal distortion at a clinically acceptable level. In this algorithm, the input signal is divided into blocks and each block goes through a discrete wavelet transform; then the resulting wavelet coefficients are linearly predicted. In this way, a set of uncorrelated transform domain signals is obtained. These signals are compressed using various coding methods, including modified run-length and Huffman coding techniques. The error corresponding to the difference between the wavelet coefficients and the predicted coefficients is minimized in order to get the best predictor.

7. Thresholding and coding of DWT coefficients

Thresholding DWT coefficients are very similar to the method that our ears take to de-noise a music signal. We concentrate on the high peaks and try to ignore the low crackling of the white noise. Because DWT coefficients are based on amplitude and location of the signal, we can separate much of the noise from the signal relatively easily. The technique of thresholding takes the DWT coefficients, and throws out (makes them zero) coefficients below a certain threshold, leaving the peaks of the signal. Then each coefficient after thresholded is quantized. A non-uniform quantization method is commonly used to increase the compression and decrease the distortion in the reconstructed signal. The quantized coefficients are then encoded. The wavelet domain representation itself does not introduce any compression. Compression is obtained by encoding the thresholded wavelet coefficients using optimal thresholding levels. Given that most of the energy in the signal is in the lower subbands, it is reasonable to assume that after thresholding a substantial number of higher band wavelet coefficients will be set to zeros. Since these zeros tend to occur in clusters, as a direct consequence of the way in which the data are organized in vectors, run-length coding of these zeros makes sense. The basic idea of this technique is to encode a sequence of equal symbols with a certain codeword depending on the length of that sequence. Thus, two types of codewords may be used: the counter-words and the value-words. For example, the string "aaabbbbd" is encoded as: (a, 3), (b, 4), and (d, 1). In case of ECG compression, the run-length coding is done by representing the thresholded wavelet coefficients vectors in the forum of (Run, Level), where Run is the number of zeros before each nonzero coefficients, and Level is the amplitude of the coefficient following a number of zeros given by Run. The event that the last coefficient are all zeros is represented by the special code (0 , 0). For example, the set of wavelet coefficients given by Wbefore = {0 1 0 0 0 4 5 0 0 0 0 0 0 0 0 0 } is run-length coded as Wafter = { (1 , 1) (3 , 4) (0 , 5) (0 , 0) }. As it has been mentioned in section 3, the compression is based on representing the thereshold wavelet coefficients with a small number of bits. This has been carried out by discarding the WT-coefficients, which are less than a given threshold. These coefficients are considered insignificant with their values set to zero. The remaining N_S coefficients are the significant coefficients. The number of the discarded coefficients is $N_I=N-N_S$. Most of these coefficients are concentrated at the end of the coefficients' vector. In technical literature, many algorithms are suggested to deal with signals that have repeated samples' values such as run-length coding and Huffman coding. The need of at least one bit for the mostly repeated sample is the main limitation of the Huffman coding. The disadvantage of the run-

length algorithm is the need of two words for the representation of each group of repeated samples: one for the repeated value and the other for the number of repetitions. In this section a more efficient coding algorithm, a modified run-length algorithm, is presented for dealing with this situation. The algorithm is based on representing each significant coefficient by b_S+1 bits. The insignificant coefficients (of value zero) are manipulated in a different manner. First, the repeated groups of zeros are counted and the resulting count is represented by b_S+1 bits. Then the train of coefficients representing the ECG signal is transformed to another train of numbers. Some of these numbers represent the significant coefficients and the rest are the numbers representing the repeated group of zeros (K_1, K_2, …., K_M). Here, M denotes the number of these groups. The problem here is how to differentiate between the coefficients and the numbers representing the group of zeros. For example, the number 18 may be found twice in the new train of numbers, where the first 18 may be a significant coefficient and the second one may indicate 18 repeated zeros. To overcome this problem, the first bit in the representation of each number is used as a control bit. In case of the significant coefficient this bit is set to one and in case of repeated zeros it is reset to zero.

- representation of significant residual coefficient

1	b_S – bits

- representation of a group of repeated zeros

0	b_S – bits

8. Quantization and coding of DWT coefficients

A quantizer simply reduces the number of bits needed to store the transformed coefficients by reducing the precision of those values. A quantization scheme maps a large number of input values into a smaller set of output values. This implies that some information is lost during the quantization process. The original wavelet coefficients $c(n)$ cannot be recovered exactly after quantization. An encoder further compresses the quantized values losslessly to give better overall compression. The most commonly used encoders are the Huffman encoder and the arithmetic encoder, although for applications requiring fast execution, simple run-length encoding (RLE) has proven very effective (Ahmed & Abo-Zahhad, 2001). In the following, wavelet coefficients quantization and coding algorithms are described.

8.1 Energy packing efficiency strategy

In this section, the quantization strategy adopted is based on the energy packing efficiency (EPE). It guarantees the balance between the compression achievement and information loss. Here, quantization process is performed by selecting an appropriate threshold level λ to control the compression ratio. Due to the careful representation of the ECG signal performed by DWT, it is reasonable to assume that only a few coefficients contain information about the real signal while others appear as less important details. The goal is to extract these significant coefficients and to ignore others smaller than specified threshold level λ. The optimal value of λ is determined such that the reconstructed signal is as close to the original one as possible. Usually the selection of optimal threshold level is not an easy task, because some of the coefficients that represent the actual signal details may be also killed, and as a result, signal distortion is the side effect. In (Abo-Zahhad & Rajoub, 2001, 2002) Energy Packing Efficiency (EPE) strategy has been utilized for decreasing the

distortion of the reconstructed signal. This has been performed by thresholding the wavelet coefficients of the approximation and details subbands with different threshold levels.
As it can be deduced from the above discussion, the approximation band is the smallest band in size and it includes high amplitude approximation coefficients. The wavelet coefficients other than these included in the approximation band, detail coefficients, have small magnitudes. Most of the energy is captured by these coefficients of the lowest resolution band. This can be seen from the decomposition of 4096-sample ECG signal up to the fifth level. The total energy of the signal is 94393.5. About 99.73% of this energy is concentrated in the 136 approximation coefficients and only 0.27% of the energy is concentrated in the remaining 3960 detail coefficients. Here, threshold levels are defined according to the energy packing efficiencies of the signal for all subbands. EPE for a set of coefficients in the ith subband is defined as the ratio of the energy captured by the subband coefficients and the energy captured by the whole number of coefficients.

$$EPE_i = \frac{\sum_{n=1}^{L_i} (c(n))^2}{\sum_{n=1}^{L} (c(n))^2} x100 \tag{31}$$

Where L_i and L are the number of coefficients in the ith subband and the whole number of coefficients respectively. A large threshold could attain high data reduction but poor signal fidelity and a small threshold would produce low data reduction but high signal fidelity. To explore the effect of threshold level (λ) selection and the coefficients representation on the compression ratio and PRD, the following thresholding rule is set:

Keep all the wavelet coefficients in the approximation subband without thresholding and calculate the threshold value for each details subband separately by preserving the higher amplitude wavelet coefficients in the ith details subband that contribute to α_i % of the energy in that subband.

One important feature of this rule is that the integer part of the wavelet coefficients in each subband is represented by different number of bits.

8.2 Binary significant map coding algorithm

The coding algorithm adopted here is based on grouping the significant coefficients in one vector and the locations of the insignificant coefficients in another vector. The significant coefficients are arranged from high scale coefficients to low scale coefficients. Each significant coefficient is decomposed into integer part and fractional part, where M-bits are assigned to represent the integer part (signed representation) and N-bits represent the fractional part; i.e. each coefficient is represented by N+M bits. A binary significant map is used as flags to indicate if the coefficient is significant or not. This binary stream is compressed further as will be shown in the following:

1. Threshold the wavelet coefficients, $c(n)$, to produce the threshold coefficients $\overline{c}(n)$. The threshold level (λ) is determined by using the above-mentioned rule such that the distortion in the reconstructed signal $\overline{x}_i$ is acceptable. The distortion is measured using PRD and/or visual inspection. The optimal non-orthogonal wavelet transform developed in (Ahmed et al., 2000) may be used to minimize the PRD in least mean square sense. Here, the threshold λ is determined such that the PRD is less or equal to a prescribed acceptable value defined by a cardiologist.

2. Search the vector $\bar{c}(n)$ to isolate the significant coefficient in another vector $\hat{C}_S(m)$.
3. Use finite word length representation to represent the integer and fractional parts of the coefficients, $\hat{C}_S(m)$. The number of bits used to represent these coefficients is determined as follows:
   3.1 Search the vector $\hat{C}_S(m)$ to find the maximum coefficient (in absolute value) and determine the number of bits that represents this coefficient. This can be done by finding $k = \text{Int}\left\langle \max|\hat{C}_S(m)| \right\rangle$ where $\text{Int}\langle . \rangle$ denotes the integer part. Then convert k to a binary number and count the number of bits, M.
   3.2 Similarly, find the number of bits, N, that represent the minimum value of the fractional part of each significant coefficient in such a way to keep the distortion within acceptable limits.
4. Generate a binary stream, b(n), of 1's and 0's that encodes the zero-locations in $\bar{c}(n)$. This is done by coding each significant coefficient in $\bar{c}(n)$ by a binary 1. The length of the binary stream equals n_1, where n_1 designates the index value of the last significant coefficients in $\bar{c}(n)$. Hence, there is no need to encode the zeros for $n > n_1$. The value of n_1 need not be stored because it can be determined as the length of the vector b(n) in the decoding process.
5. Compress the binary stream using run length encoding of 0's and 1's as follows:
   5.1 Set i = 1, Run-type= b(i), and set the run length Z to 1;
   If b(i) ≠ b(i+1) increment i by Z. Else, while b(i+1) = b(i), increment i by 1 and Z by 1 end; end.
   5.2 From Table (2), find the inequality that Z satisfies. Then output the symbol that specifies the run type followed by the number Z. i.e., code = [code χ Z] , where χ designates concatenation operator.
   5.3 If index < n_1 set Z=1 and go to step (5.1).
6. Represent the obtained run length code in binary format. There are 16 different symbols that can be generated from step 5. These are the digits 0-9 and the letters A-F. Hence, 4 bits can be used to represent each symbol.

Symbol	Run Type	Range
A	0	$100 \le Z \le 999$
B	0	$10 \le Z \le 99$
C	0	$2 \le Z \le 9$

Symbol	Run Type	Range
D	1	$100 \le Z \le 999$
E	1	$10 \le Z \le 99$
F	1	$2 \le Z \le 9$

Table 2. Run Length Encoding of 0's and 1.

9. Conclusion

In literature, numerous ECG compression methods have been developed. They may be defined either as reversible methods (offering low compression ratios but guaranteeing an exact or near-lossless signal reconstruction), irreversible methods (designed for higher compression ratios at the cost of a quality loss that must be controlled and characterized), or scalable methods (fully adapted to data transmission purposes and enabling lossy reconstruction). Choosing one method mainly depends on the use of the ECG signal. In the case of the needs of a first diagnosis, a reversible compression would be most suitable.

However, if compressed data has to be stored on low-capacity data supports, an irreversible compression would be necessary. Finally, scalable techniques clearly suit data transmission. All compression solutions presented in this chapter adopt DWT as a reversible compression tool. As a consequence, the following question remains: why should they all be compressed using the same algorithm? Unsurprisingly, this discussion still remains open.

10. References

Jalaleddine S. M. S., Hutchens C. G., Strattan R. D., & Coberly W. A. (1990). ECG data compression techniques-A unified approach, IEEE Trans Biomed. Eng., vol. 37, 329–343.

Addison P. S. (2005). Wavelet transforms and the ECG: a review. Institute Of Physics Publishing Physiological Measurement, vol. 26, R155–R199.

Padma T., Latha M. M., and Ahmed A. (2009). ECG compression and labview implementation, J. Biomedical Science and Engineering, vol. 3, 177-183.

Moody G. (1992). MIT-BIH Arrhythmia Database, Overview. Massachusetts Institute of Technology, Cambridge, 1992.

Dipersio D. A. and Barr R. C. (1985). Evaluation of the fan method of adaptive sampling on human electrocardiograms, Med. Biol. Eng. Comput., 401–410.

Abenstein J. and Tompkins W., (1982). New data-reduction algorithm for real-time ECG analysis. IEEE Trans. Biomed. Eng., vol. BME-29, 43–48, Jan. 1982.

Cox J., Noelle F., Fozzard H., and Oliver G. (1968). AZTEC: A preprocessing program for real-time ECG rhythm analysis. IEEE Trans. Biomed. Eng., BME-15, 128–129, Apr. 1968.

Mueller W., (1978). Arrhythmia detection program for an ambulatory ECG monitor. Biomed. Sci. Instrument, vol. 14, 81–85, 1978.

Moody G. B., Mark R. G., and Goldberger A. L., (1989). Evaluation of the TRIM ECG data compressor. Proc. Of Comput. Cardiol., 1989, 167–170.

Haugland D., Heber J., and Husøy J., (1997). Optimization algorithms for ECG data compression. Med. Biol. Eng. Comput, vol. 35, 420–424, July 1997.

Olmos S., Millán M., García J., and Laguna P., (1996). ECG data compression with the Karhunen-Loève transform. Proc. Comput. Cardiol. , Indianapolis, 253–256, Sept. 1996.

Reddy B. R. S., and Murthy I. S. N., (1986). ECG data compression using Fourier descriptions. IEEE Trans. Biomed. Eng., vol. 33, 428–434, Apr. 1986.

Ahmed N., Milne P. J., and Harris S. G., (1975). Electrocardiographic data compression via orthogonal transforms. IEEE Trans. Biomed. Eng., vol. BME-22, 484–487, Nov. 1975.

Husøy J. H. and Gjerde T., (1996). Computationally efficient subband coding of ECG signals," Med. Eng. Phys., vol. 18, 132–142, Mar. 1996.

Mammen C. P. and Ramamurthi B., (1990). Vector quantization for compression of multichannel ECG. IEEE Trans. Biomed. Eng., vol. 37, 821–825, Sept. 1990.

Chen J., Itoh S., and Hashimoto T., (1993). ECG data compression by using wavelet transform. IEICE Trans. Inform. Syst., vol. E76-D, 1454–1461, Dec. 1993.

Miaou S. G., Yen H. L. and Lin C.L., (2002). Wavelet-based ECG compression using dynamic vector quantization with tree codevectors in single codebook. IEEE Trans. Biomed. Eng., vol. 49, 671–680, 2002.

Nygaard R., Melnikov G., and Katsaggelos A. K., (1999). Rate distortion optimal ECG signal compression. in Proc. Int. Conf. Image Processing, 348–351, Oct. 1999, Kobe, Japan.

Zigel Y., Cohen A., and Katz A., (2000). The Weighted Diagnostic Distortion (WDD) Measure for ECG Signal Compression. IEEE Trans. Biomed. Eng., 47, 1422-1430, 2000.

Zou H. and Tewfik A. H., (1993). Parameterization of compactly supported orthonormal wavelets. IEEE Trans. on Signal Processing, vol. 41, no. 3, 1428-1431, March 1993.

Ahmed S. M., Al-Shrouf A. and Abo-Zahhad M., (2000). ECG data compression using optimal non-orthogonal wavelet transform. Med. Eng. Phys. 22, 39–46, 2000.

Javaid R., Besar R., Abas F. S., (2008). Performance Evaluation of Percent Root Mean Square Difference for ECG Signals Compression. Signal Processing: An International Journal (SPIJ): 1–9, April 2008.

Benzid R., Marir F., Boussaad A., Benyoucef M., and Arar D., (2003). Fixed percentage of wavelet coefficients to be zeroed for ECG compression. Electronics Letters, vol. 39, 830–831, 2003.

Blanco-Velasco M., Cruz-Rolda´n F., Godino-Llorente J. I., and Barner K. E., (2004). ECG compression with retrieved quality guaranteed. Electronics Letters, vol. 40, no. 23, 900–901, 2004.

Al-Fahoum A. S., (2006). Quality assessment of ECG compression techniques using a wavelet-based diagnostic measure. IEEE Trans. in Biomedicine, vol. 10, 182-191, 2006.

Thakor N. V., Sun Y. C., Rix H. and Caminal P., (1993). Multiwave: a wavelet-based ECG data compression algorithm. IEICE Trans. Inf. Syst. E76D 1462–9, 1993.

Chen J. and Itoh S., (1998). A wavelet transform-base ECG compression method guaranteeing desired signal quality. IEEE Trans. Biomed. Eng. 45, 1414–1419, 1998.

Miaou S. G. and Lin H. L., (2000). Quality driven gold washing adaptive vector quantization and its application to ECG data compression. IEEE Trans. Biomed. Eng., 47 209–218, 2000.

Miaou S. G. and Lin C. L. (2002). A quality-on-demand algorithm for wavelet-based compression of electrocardiogram signals. IEEE Trans. Biomed. Eng. 49, 233–239, 2002.

Bradie B., (1996). Wavelet packet-based compression of single lead ECG. IEEE Trans. Biomed. Eng. 43, 493–501, 1996.

Ramakrishnan A. G. and Saha S., (1997). ECG coding by wavelet-based linear prediction. IEEE Trans. Biomed. Eng., vol. 44, 1253–1261, 1997.

Lu Z., Kim D. Y. and Pearlman W. A., (2000). Wavelet compression of ECG signals by the set partitioning in hierarchical trees algorithm. IEEE Trans. Biomed. Eng., 47, 849–855, 2000.

Daubechies I., (1998). Orthonormal bases of compactly supported wavelets. Communication on Pure and Applied Mathematics, vol. 41, no. 7, 909-996, Nov. 1998.

Donoho D. L., and Johnstone I. M., (1998). Minimax estimation via wavelet shrinkage. Ann. Statist., vol. 26, 879–921, 1998.

Vaidyanathan P. P., (1993). Multirate digital filters, filter banks, polyphase networks and applications: A tutorial review. Proceedings of the IEEE, vol. 41, 3463-3479, Dec. 1993.

Xie H. and Morris J. M., (1994). Design of orthonormal wavelets with better time-frequency resolution. Proc. Of SPIE, Wavelet Applications, 878-997, Orlando, Florida, 1994.

Maitrot A., Lucas M. F., Doncarli C., and Farina D., (2005). Signal-dependent wavelet for electromyogram classification. Med. Biol. Eng. Computers., vol. 43, 487–92, 2005.

Shapiro J. M., (1993). Embedded Image Coding Using Zero trees of Wavelet Coefficients. IEEE Trans. Signal Processing, vol. 41, no. 12, 3445-3462, Dec. 1993.

Said A., and Pearlman W. A., (1996). A New, Fast and Efficient Image Codec Based on Set Partitioning in Hierarchical Trees. IEEE Trans. Circuits & Systems, vol. 6, 243-250, 1996.

Lu Z., Kim D. Y., Pearlman W. A., (2000). Wavelet Compression of ECG Signals by the Set Partitioning in Hierarchical Trees Algorithm. IEEE Trans. Biomed. Eng., vol. 47, no. 7, 849-856, July 2000.

Pooyan M., Taheri A., Moazami-Goudarzi M., and Saboori I., (2005). Wavelet Compression of ECG Signals Using SPIHT Algorithm. World Academy of Science, Engineering and Technology, vol. 2, 212-215, 2005.

Reza A., Moghaddam A., and Nayebi K., (2001). A two dimensional wavelet packet approach for ECG compression. Proc. Int. Symp. Signal Processing Applications, 226–229, Aug. 2001.

Ali B., Marcellin M.W., and Altbach M. I., (2003). Compression of electrocardiogram signals using JPEG2000. IEEE Trans. Consumer Electronics, vol. 49, no. 4, Nov. 2003.

Tai S. C., Sun C. C., and Yan W. C., (2005). A 2-D ECG compression method based on wavelet transform and modified SPIHT. IEEE Trans. Biomed. Eng., 52, 999–1008, 2005.

Wang X., and Meng J., (2008). A 2-D ECG compression algorithm based on wavelet transform and vector quantization. Digital Signal Processing vol. 18, 179–188, 2008.

Ahmed S. M., Al-Zoubi Q., and Abo-Zahhad M., (2007). A hybrid ECG compression algorithm based on singular value decomposition and discrete wavelet transform. J. Med. Eng. Technology, vol. 31, 54-61, 2007.

Xingyuan W. and Juan M., (2009). Wavelet-based hybrid ECG compression technique", Analog Integrated Circuits Signal Processing, vol. 59, 301–308, 2009.

Ahmed S. M., Al-Ajlouni A. F., Abo-Zahhad M., and Harb B., (2008). ECG signal compression using combined modified discrete-cosine and discrete-wavelet transforms. 2008.

Britanak V. and Rao K. R., (2002). A new fast algorithm for the unified forward and inverse MDCT/MDST computation. Signal Processing 82, 433-459, 2002.

Nikolajevic V. and Fettweis G., (2003). A new Recursive Algorithm for the Unified Forward and Inverse MIDCT/MIDST. Journal of VLSI Signal Processing, vol. 9, 203-208, 2003.

Abo-Zahhad M., Ahmed S. M., and Al-Shrouf A., (2000). Electrocardiogram data compression algorithm based on the linear prediction of the wavelet coefficients. Proc. of 7th IEEE Int. Conf., Electronics, Circuits and Systems, Lebanon, 599–603, Dec. 2000.

Ahmed S. M., and Abo-Zahhad M., (2001). A new hybrid algorithm for ECG signal compression based on the wavelet transformation. Medical Engineering and Physics, vol. 24, no. 3, 50-66, 2001.

Abo-Zahhad M., and Rajoub B. A., (2001). ECG compression algorithm based on coding and energy compaction of the wavelet coefficients. The 8th IEEE International Conf. On Electronics, Circuits and Systems, Malta, 441-444, Sept. 2001.

Abo-Zahhad M., and Rajoub B. A., (2002). An effective coding technique for the compression of one-dimensional signals using wavelets. Med. Eng. and Phy., vol. 24, 185-199, 2002.

9

Shift Invariant Biorthogonal Discrete Wavelet Transform for EEG Signal Analysis

Juuso T. Olkkonen and Hannu Olkkonen
VTT Technical Research Centre of Finland, 02044 VTT,
Department of Applied Physics,
University of Kuopio, 70211 Kuopio,
Finland

1. Introduction

Since the discovery of the compactly supported conjugate quadrature filter (CQF) based discrete wavelet transform (DWT) (Smith & Barnwell, 1986; Daubechies, 1988), a variety of data and image processing tools have been developed. It is well known that real-valued CQFs have nonlinear phase, which may cause image blurring or spatial dislocations in multi-resolution analysis. In many applications the CQFs have been replaced by the biorthogonal discrete wavelet transform (BDWT), where the low-pass scaling and high-pass wavelet filters are symmetric and linear phase. In VLSI hardware the BDWT is usually realized via the ladder network-type filter (Sweldens, 1988). Efficient lifting wavelet transform algorithms implemented by integer arithmetic using only register shifts and summations have been developed for VLSI applications (Olkkonen et al. 2005).

In multi-scale analysis the drawback of the BDWT is the sensitivity of the transform coefficients to a small fractional shift $\tau \in [0,1]$ in the signal, which disturbs the statistical comparison across different scales. There exist many approaches to construct the shift invariant wavelet filter bank. Kingsbury (2001) proposed the use of two parallel filter banks having even and odd number of coefficients. Selesnick (2002) has described the nearly shift invariant CQF bank, where the two parallel filters are a half sample time shifted versions of each other. Gopinath (2003) generalized the idea by introducing the M parallel CQFs, which have a fractional phase shift with each other. Both Selesnick and Gopinath have constructed the parallel CQF bank with the aid of the all-pass Thiran filters, which suffers from nonlinear phase distortion effects (Fernandes, 2003).

In this book chapter we introduce a linear phase and shift invariant BDWT bank consisting of M fractionally delayed wavelets. The idea is based on the B-spline interpolation and decimation procedure, which is used to construct the fractional delay (FD) filters (Olkkonen & Olkkonen, 2007). The FD B-spline filter produces delays $\tau = N/M$ ($N, M \in \mathbb{N}$, $N = 0,\ldots,M-1$). We consider the implementation of the shift invariant FD wavelets, especially for the VLSI environment. The usefulness of the method was tested in wavelet analysis of the EEG signal waveforms.

2. Theoretical considerations

2.1 Two-channel BDWT filter bank

The two-channel BDWT analysis filters are of the general form (Olkkonen et al. 2005)

$$\begin{aligned} H_0(z) &= (1+z^{-1})^K P(z) \\ H_1(z) &= (1-z^{-1})^K Q(z) \end{aligned} \tag{1}$$

where $H_0(z)$ is the Nth order low-pass scaling filter polynomial having the Kth order zero at $\omega = \pi$. $P(z)$ is polynomial in z^{-1}. $H_1(z)$ is the corresponding Mth order high-pass wavelet filter having Kth order zero at $\omega = 0$. $Q(z)$ is polynomial in z^{-1}. For a two-channel perfect reconstruction filter bank, the well known perfect reconstruction (PR) condition is

$$\begin{aligned} H_0(z)G_0(z) + H_1(z)G_1(z) &= 2\, z^{-k} \\ H_0(-z)G_0(z) + H_1(-z)G_1(z) &= 0 \end{aligned} \tag{2}$$

where $G_0(z)$ and $G_1(z)$ are the low-pass and high-pass reconstruction filters defined as

$$\begin{aligned} G_0(z) &= H_1(-z) \\ G_1(z) &= -H_0(-z) \end{aligned} \tag{3}$$

A typical set of the scaling and wavelet filter coefficients is given in (Olkkonen et al. 2005). In this work we apply the following essential result concerning on the PR condition (2).

Lemma 1: If $H_0(z)$ and $H_1(z)$ are the scaling and wavelet filters, the following modified analysis and synthesis filters obey the PR condition

$$\begin{aligned} \overline{H_0(z)} &= P(z)H_0(z) \\ \overline{H_1(z)} &= P^{-1}(-z)H_1(z) \\ \overline{G_0(z)} &= P^{-1}(z)G_0(z) \\ \overline{G_1(z)} &= P(-z)G_1(z) \end{aligned} \tag{4}$$

where P(z) is any polynomial in z^{-1} and $P^{-1}(z)$ its inverse. Proof: The result can be proved by direct insertion of (4) into (2).

2.2 Fractional delay B-spline filter

The ideal FD operator has the z-transform

$$D(\tau, z) = z^{-\tau} \tag{5}$$

where $\tau \in [0,1]$. In (Olkkonen & Olkkonen, 2007) we have described the FD filter design procedure based on the B-spline interpolation and decimation procedure for the construction of the fractional delays $\tau = N/M$ ($N, M \in \mathbb{N}, N = 0,1,...,M-1$). The FD filter has the following representation

$$D(N,M,z) = \beta_p^{-1}(z)\left[z^{-N}\beta_p(z)F(z) \right]_{\downarrow M} \tag{6}$$

where $\beta_p(z)$ is the discrete B-spline filter (Appendix I). Decimation by M is denoted by $\downarrow M$, and the polynomial $F(z)$ is of the form

$$F(z) = \frac{1}{M^{p-1}}\left(\frac{1-z^{-M}}{1-z^{-1}}\right)^p = \frac{1}{M^{p-1}}\left(\sum_{k=o}^{M-1} z^{-k}\right)^p \tag{7}$$

For convenience we use the following polyphase decomposition

$$\beta_p(z)F(z) = \sum_{k=0}^{M-1} P_k(z^M)z^{-k} \tag{8}$$

By inserting (8) into (6) we have

$$D(N,M,z) = \beta_p^{-1}(z)P_N(z) \tag{9}$$

Table I gives the polyphase components $P_N(z)$ for $M=4$ and $N=0,1,...,M$. It appears generally that $P_0(z)=\beta_p(z)$ and $P_M(z)=z^{-1}\beta_p(z)$. Hence, $D(0,M,z)=1$ and $D(M,M,z)=z^{-1}$. The implementation of the inverse discrete B-spline filter $\beta_p^{-1}(z)$ in (9) is described in Appendix I. Fig. 1 shows the magnitude and phase spectra of the FD B-spline filter (9) for $M=4$ and $N=1,2$ and 3.

2.3 FD BDWT bank

As a direct application of *Lemma 1*, the fractionally delayed BDWT consists of the analysis and synthesis filters ($N=0,1,2,...,M-1$)

$$\begin{aligned} H_0(N,M,z) &= D(N,M,z)H_0(z) \\ H_1(N,M,z) &= D^{-1}(N,M,-z)H_1(z) \\ G_0(N,M,z) &= D^{-1}(N,M,z)G_0(z) \\ G_1(N,M,z) &= D(N,M,-z)G_1(z) \end{aligned} \tag{10}$$

The FD B-spline filter (9) suits readily for the implementation of the FD BDWT bank (10). For example, if we construct the four parallel filter banks, we select $M=4$ and $N=0,1,2$ and 3. For M=4 the wavelet filter $H_1(0,4,z)$ equals the original $H_1(z)$, which is FIR. However, the filters $H_1(1,4,z)$, $H_1(2,4,z)$ and $H_1(3,4,z)$ are IIR-type. In the following we present a novel modification of the FD BDWT filter bank (10), where all FD wavelet filters are FIR-type.

N	$P_N(z)$
0	[1 4 1 0]/6
1	[27 235 121 1]/384
2	[1 23 23 1]/48
3	[1 121 235 27]/384
4	[0 1 4 1]/6

Table I. Polyphase components $P_N(z)$ for $M=4$ and $N=0,1,...,M$ ($p=4$).

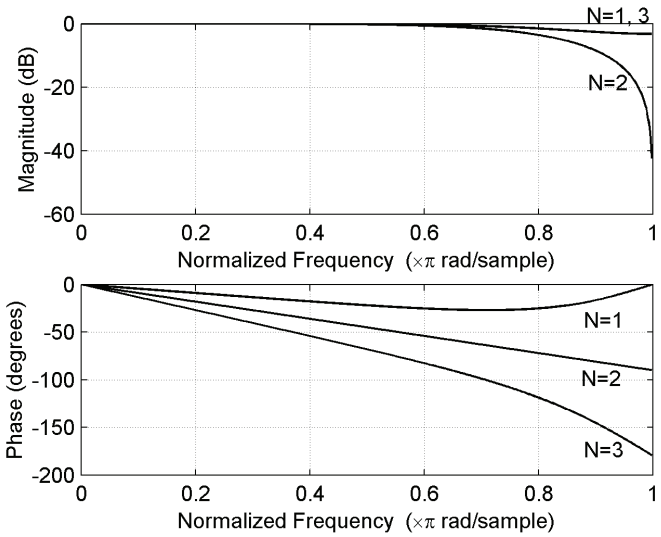

Fig. 1. The FD B-spline ($p = 4$) filter for $M = 4$ and $N = 1,2$ and 3 .

2.4 FIR FD wavelet filters

In VLSI and microprocessor environment the FIR filters are preferable due to the straightforward implementation by direct convolution. In tree structured multi-scale analysis the nondelayed scaling coefficients are fed to the following scale and only the wavelet coefficients are fractionally delayed. Next we describe a modification of the FD BDWT bank (10), where all the FD wavelet filters are FIR. The idea is based on the fact that only the relative time shift of the wavelet coefficients is essential for shift invariance. Hence, due to *Lemma 1* we may replace the original scaling and wavelet filters by

$$\begin{aligned} H_0(0,M,z) &= \beta_p^{-1}(z)H_0(z) \\ H_1(0,M,z) &= \beta_p(-z)H_1(z) \end{aligned} \tag{11}$$

which obey the PR condition. Since the discrete B-spline filter $\beta_p(z)$ contains no zeroes at $z = -1$, the regulatory degree (the number of zeros at $z = -1$) of the scaling filter is not affected. The corresponding fractionally delayed wavelet filters are

$$H_1(N,M,z) = P_N(-z)H_1(z) \quad N = 1,2,...,M-1 \tag{12}$$

Now, for $N = 0,1,...,M-1$ all the wavelet filters are FIR-type and they are the fractionally delayed versions of each other. The polyphase components $P_N(-z)$ in (12) have high-pass filter characteristics. Hence, the frequency response of the modified wavelet filters is only slightly altered. Fig. 2 shows the impulse responses of the BDWT wavelet filter (Olkkonen et al. 2005) and the corresponding fractionally delayed wavelet filters for M = 4 and N = 0, 1,2 and 2. The energy (absolute value) of the impulse response is a smooth function, which warrants the shift invariance. The corresponding impulse responses of the fractionally

delayed Daubechies 7/9 wavelet filters (Unser & Blu, 2003) are given in Fig. 3 and the fractionally delayed Legall 3/5 wavelet filters (Unser & Blu, 2003) in Fig. 4.

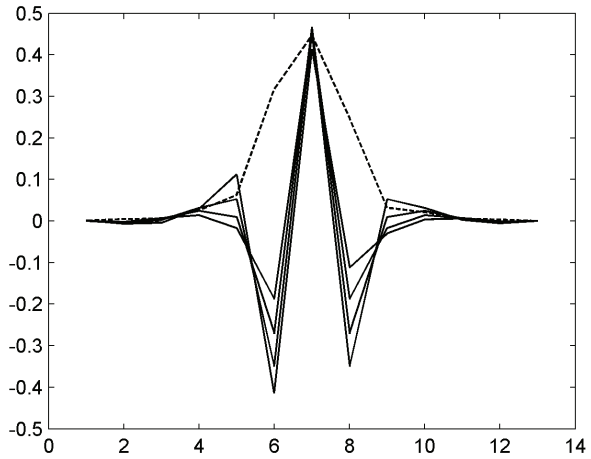

Fig. 2. The FD impulse responses of the BDWT wavelet filter (M=4 and N=0,1,2 and 3). $h_1[n]$ = [1 -1 -8 -8 62 -62 8 8 1 -1]/128. The dashed line denotes the energy (absolute value) of the wavelet filter coefficients.

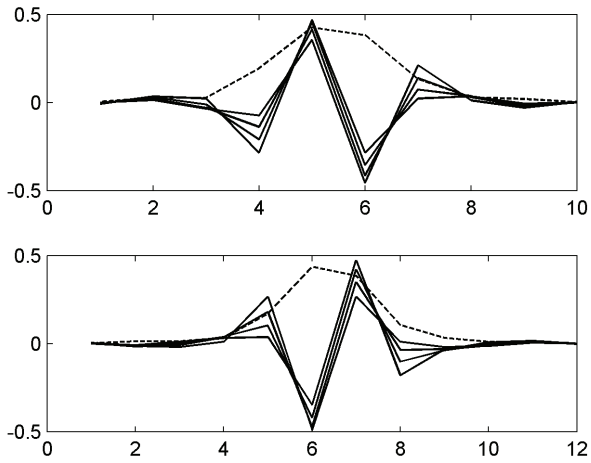

Fig. 3. The FD impulse responses of the Daubechies 7/9 BDWT wavelet filters (M=4 and N=0,1,2 and 3). The energy of the wavelet filter coefficients is denoted by the dashed line.

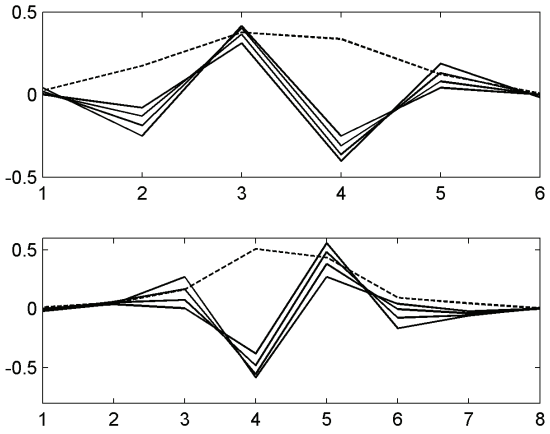

Fig. 4. The FD impulse responses of the Legall 3/5 BDWT wavelet filters (M=4 and N=0,1,2 and 3).The dashed line denotes the energy of the wavelet filter coefficients.

3. Experimental

The usefulness of the FD B-spline method was tested for the EEG signal waveforms. For comparison the EEG signals were analysed using the well established Hilbert transform assisted complex wavelet transform (Olkkonen et al. 2006). The EEG recording method is described in detail in our previous work (Olkkonen et al. 2006). The EEG signals were treated using the BDWT bank given in (Olkkonen et al. 2005). The FD wavelet coefficients were calculated via (12) using M=4 and N=0,1,2 and 3. Fig. 5A shows the nondelayed wavelet coefficients. Fig. 5B shows the energy (absolute value) of the wavelet coefficients and Fig. 5C the energy of the wavelet coefficients computed via the Hilbert transform method (Olkkonen et al. 2006).

4. Discussion

This book chapter presents an original idea for construction of the shift invariant BDWT bank. Based on the FD B-spline filter (9) we obtain the FD BDWT filter bank (12), which yields the wavelet sequences by the FIR filters. The integer valued polyphase components (Table I) enable efficient implementation in VLSI and microprocessor circuits. The present paper serves as a framework, since the FD B-spline filter implementation can be adapted in any of the existing BDWT bank, such as the lifting DWT (Olkkonen et al. 2005), Daubechies 7/9 and Legall 3/5 wavelet filters (Unser &Blu, 2003).

The present idea is highly impacted on the work of Selesnick (2002). He observed that if the impulse responses of the two scaling filters are related as $h_0[n]$ and $h_0[n-0.5]$, then the corresponding wavelets form a Hilbert transform pair. We may treat the two parallel wavelets as a complex sequence

$$w_c[n] = w[n] + j\,w[n-0.5] \tag{13}$$

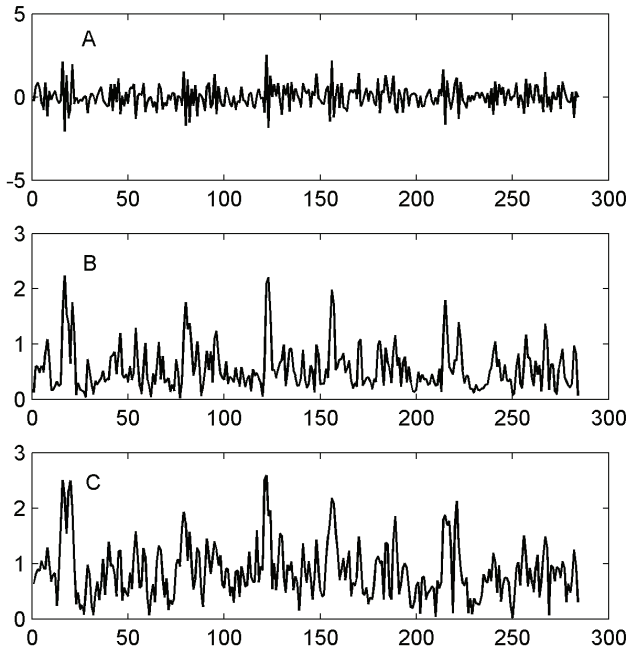

Fig. 5. The FD BDWT analysis of the neuroelectric signal waveform recorded from the frontal cortex at a 300 Hz sampling rate. The nondelayed wavelet coefficients (A). The energy of the FD wavelet coefficients (M=4, N = 0,1,2 and 3) (B). The Hilbert transform assisted energy (envelope) of the wavelet coefficients (C).

The energy (absolute value) of the complex wavelet corresponds to the envelope, which is a smooth function. Hence, the energy of the complex wavelet sequence is nearly shift invariant to fractional delays of the signal.

Gopinath (2003) has studied the effect of the M parallel CQF wavelets on the shift invariance. According to the theoretical treatment the shift invariance improves most from the change M=1 to 2. For M=3,4,…. the shift invariance elevates, but only gradually. Hence, M = 4 is usually optimal for computation cost and data redundancy. If we consider the case M=4 the corresponding hyper complex (hc) wavelet sequence is

$$w_{hc}[n] = w[n] + i\,w[n-0.25] + j\,w[n-0.5] + k\,w[n-0.75] \tag{14}$$

where i, j and k are the unit vectors in the hc space. It is evident that the energy of the hc wavelet coefficients is more shift invariant to the fractional delay in the signal compared with the dual tree complex wavelets (13). According to our experience the values M > 4 do not produce any additional advantage to the treatment of the EEG data.

The FD BDWT bank offers an effective tool for EEG data compression and denoising applications. Instead of considering the wavelet coefficients we may threshold the energy of the hc wavelet coefficients as

$$if \quad |w_{hc}[n]| < \varepsilon \quad then\ w[n] = 0 \tag{15}$$

where ε is a small number. Due to the smooth behaviour of the energy function, ε can be made relatively high compared with the conventional wavelet denoising methods. In tree structured BDWT applications only the nondelayed scaling sequence is fed to the next scale. Usually the scaling sequence is not thresholded, but only the wavelet coefficients. The FD BDWT bank does not increase the memory requirement (redundancy) compared with the original nondelayed BDWT bank, since the reconstruction of the data can be performed by knowing only the nondelayed scaling and wavelet sequences. The FD BDWT bank can be considered as a subsampling device, which improves the quality of the critically sampled wavelet sequence. As an example we consider the multi-scale analysis of the neuroelectric signal (Fig. 5). The energy of the signal in different scales can be estimated with the aid of the Hilbert transform (Olkkonen et al. 2006). Applying the result of this work the energy of the wavelet sequence $w_{hc}[n]$ (14) approaches closely to the energy (envelope) of the signal. However, the delayed wavelet sequence is produced only by the polyphase filter $P_N(z)$ (N=1,2,…,M-1)(12), while the Hilbert transform requires the FFT based signal processing (Olkkonen et al. 2006). In the EEG signal recorded from the frontal cortex, the spindle waves have concentrated energy, which is clearly revealed both by the FD BDWT and the Hilbert transform analysis (Fig. 5). The energy content of the EEG signal yielded by the two different methods is remarkably similar.

The essential difference compared with the half-sample shifted CQF filter bank (Selesnick, 2002) is the linear phase of the BDWT bank and the FD B-spline filters adapted in this work. The shifted CQF filter bank is constructed with the aid of the all-pass Thiran filters and the scaling and wavelet coefficients suffer from nonlinear phase distortion effects (Fernandes, 2003). The linear phase warrants that the wavelet sequences in different scales are accurately time related. The FD wavelet coefficients enable the high resolution computation of the cross and autocorrelation and other statistical functions.

Appendix I

The discrete B-spline filter

B-splines $\beta_p(t)$ are defined as p -times convolution of a rectangular pulse

$$\beta_p(t) = \underbrace{p(t) * p(t) * \ldots p(t)}_{p \text{ times}} \qquad p(t) = \begin{cases} 1 \text{ for } 0 \le t \le 1 \\ 0 \text{ elsewhere} \end{cases} \tag{16}$$

The Laplace transform of the B-spline comes from

$$L\{p(t)\} = \frac{1}{s}(1 - e^{-s}) \;\Rightarrow\; \beta_p(s) = \frac{1}{s^p}\left(1 - e^{-s}\right)^p = \sum_{k=0}^{p} (-1)^k \binom{p}{k} \frac{e^{-ks}}{s^p} \tag{17}$$

and the inverse Laplace transform gives the time domain solution

$$\beta_p(t) = \frac{1}{(p-1)!} \sum_{k=0}^{p} \binom{p}{k} (-1)^k (t-k)_+^{p-1} \tag{18}$$

The discrete B-spline $\beta_p[n]$ equals to the continuous B-spline at integer values of time. Hence, the Laplace transform (17) and the z-transform of the discrete B-spline have inverse transforms which coincide at integer values in the time domain. Using the relation

$$L^{-1}\left(\frac{1}{s^p}\right)=\frac{t_+^{p-1}}{(p-1)!} \tag{19}$$

we obtain the z-transform of the discrete B-spline

$$\beta_p(z)=Z\left\{\beta_p[n]\right\}=Z\left\{L^{-1}\left(\frac{1}{s^p}(1-e^{-s})^p\right)\right\}=N_p(z)(1-z^{-1})^p \tag{20}$$

where

$$N_p(z)=Z\left\{L^{-1}\left(\frac{1}{s^p}\right)\right\}=\sum_{n=0}^{\infty}\frac{n^{p-1}}{(p-1)!}z^{-n} \tag{21}$$

We have $N_1(z)=1/(1-z^{-1})$. By differentiating in respect to z we obtain a recursion

$$N_{p+1}(z)=\frac{-z}{p}\frac{dN_p(z)}{dz} \tag{22}$$

As an example we may obtain the discrete B-spline for p=4 as $\beta_4(z)=(1+4z^{-1}+z^{-2})/6$. The inverse discrete B-spline filter can be written as a cascade realization

$$\beta_p^{-1}(z)=c\prod_{i=1}^{n}\frac{1}{1-b_iz^{-1}}\prod_{j=1}^{m}\frac{1}{1-b_jz^{-1}}=c\prod_{i=1}^{n}S_i(z)\ \prod_{j=1}^{m}R_j(z) \tag{23}$$

where c is a constant and the roots $b_i\le 1$ and $b_j>1$. The $S_i(z)$ filters in (23) can be directly implemented. The $R_j(z)$ filters in (23) can be implemented by the following recursive filtering procedure. First we replace z by z^{-1}

$$R_i(z)=\frac{1}{1-b_jz^{-1}}=\frac{Y(z)}{U(z)}\quad\Rightarrow\quad R_i(z^{-1})=\frac{-b_j^{-1}z^{-1}}{1-b_j^{-1}z^{-1}}=\frac{Y(z^{-1})}{U(z^{-1})} \tag{24}$$

where $U(z)$ and $Y(z)$ denote z-transforms of the input $u[n]$ and output $y[n]$ signals ($n=0,1,2,...,N$). The $U(z^{-1})$ and $Y(z^{-1})$ are the z-transforms of the time reversed input $u[N-n]$ and output $y[N-n]$. The $R_j(z^{-1})$ filter is stable having a root b_j^{-1} inside the unit circle. The following Matlab program **rfilter.m** demonstrates the computation procedure:

```
function y=rfilter(u,b)
u=u(end:-1:1);
y=filter([0 -1/b],[1 -1/b],u);
y=y(end:-1:1);
```

5. References

Daubechies, I. (1988). Orthonormal bases of compactly supported wavelets. *Commmun. Pure Appl. Math.,* Vol. 41, 909-996.

Fernandes,F., Selesnick , I.W., van Spaendonck, R. & Burrus, C. (2003). Complex wavelet transforms with allpass filters, *Signal Processing*, Vol. 83, 1689-706.

Gopinath, R.A. (2003).The phaselet transform - An integral redundancy nearly shift invariant wavelet transform, *IEEE Trans. Signal Process.* Vol. 51, No. 7, 1792-1805.

Kingsbury, N.G. (2001). Complex wavelets for shift invariant analysis and filtering of signals. *J. Appl. Comput. Harmonic Analysis.* Vol. 10, 234-253.

Olkkonen, H., Pesola, P. & Olkkonen, J.T. (2005). Efficient lifting wavelet transform for microprocessor and VLSI applications. *IEEE Signal Process. Lett.* Vol. 12, No. 2, 120-122.

Olkkonen, H., Pesola, P., Olkkonen, J.T. & Zhou, H. (2006). Hilbert transform assisted complex wavelet transform for neuroelectric signal analysis. *J. Neuroscience Meth.* Vol. 151, 106-113.

Olkkonen, J.T. & and Olkkonen, H. (2007). Fractional Delay Filter Based on the B-Spline Transform, *IEEE Signal Processing Letters*, **V**ol. 14, No. 2, 97-100.

Selesnick, I.W. (2002). The design of approximate Hilbert transform pairs of wavelet bases. *IEEE Trans. Signal Process.* Vol. 50, No. 5, 1144-1152.

Smith, M.J.T. & Barnwell, T.P. (1986). Exaxt reconstruction for tree-structured subband coders. *IEEE Trans. Acoust. Speech Signal Process.* Vol. 34, 434-441.

Sweldens, W. (1988). The lifting scheme: A construction of second generation wavelets. *SIAM J. Math. Anal.* Vol. 29, 511-546.

Unser, M. & Blu,T. (2003), Mathematical properties of the JPEG2000 wavelet filters, *IEEE Trans. Image Process.*, Vol. 12, No. 9, 1080-1090.

10

Shift-Invariant DWT for Medical Image Classification

April Khademi, Sridhar Krishnan, Anastasios Venetsanopoulos
Department of Electrical and Computer Engineering, University of Toronto and Ryerson University
Canada

1. Introduction

The discrete wavelet transform (DWT) is gaining momentum as a feature extraction and/or classification tool, because of its ability to localize structures with good resolution in a computationally effective manner. The result is a unique and discriminatory representation, where important and interesting structures (edges, details) are quantified efficiently by few coefficients. These coefficients may be used as features themselves, or features may be computed from the wavelet domain that describe the anomalies in the data.

As a result of the potential that the DWT possesses for feature extraction and classification applications, the current work focuses on its utility in a computer-aided diagnosis (CAD) framework. CAD systems are computer-based methods that offer diagnosis support to physicians. The images are automatically analyzed and the presence of pathology is identified using quantitative measures (features) of disease.

With traditional radiology screening techniques, visually analyzing medical images is labourious, time consuming, expensive (in terms of the radiologist's time) and each individual scan is prone to interpretation error (the error rate among radiologists is reported to hover around 30% Lee (2007)). Additionally, visual analysis of radiographic images is subjective; one rater may choose a particular lesion as a candidate, while another radiologist may find this lesion insignificant. Consequently, some lesions are being missed or misinterpreted. To reduce the error rates, a secondary opinion may be obtained with a CAD system (automatically reanalyze the images after the physician). Such methods are advantageous not only because they are cost effective, but also because they are designed to *objectively* quantify pathology in a *robust*, *reliable* and *reproducible* manner.

There has been a lot of research in CAD-system design for specific modalities or applications with excellent results, i.e. see Sato et al. (2006) for CT, or Guliato et al. (2007) for mammography. Although these techniques may render good results for the particular modality it was built for, the technique is not transferable and has little-to-no utility in other CAD problems (cannot be applied to other images or databases). Since CAD systems are being employed widely, a framework that encompasses a variety of imaging modalities - not just a single one - would be of value.

To this end, this work concerns the development of a *generalized* computer-aided diagnosis system that is based on the DWT. It is considered generalized, since the same framework can

be applied to different images with no modifications. There are three image databases that are used to test the generalized CAD system: small bowel, mammogram and retinal images. Although these images are very different from one another, a common attribute is noticed: pathology is rough and heterogeneous, and healthy (normal) tissue is uniform. These images are described in Section 2.
To quantify these differences between textures in normal and abnormal images, a texture analysis scheme based on human texture perception is proposed. To describe the elemetary units of texture (which are needed for overall texture perception), important features such as scale, frequency and orientation are used for texture discrimination. The DWT is a perfect mechanism to highlight these space-localized features, since it offers a high resolution, scale-invariant representation of nonstationary phenomena (such as texture). Multiresolutional analysis, the wavelet transform, DWT with its properties and implementations are discussed in Section 4.
Although the DWT has many beneficial qualities, the DWT is shift-variant. Therefore, any texture metrics extracted from the wavelet coefficients will also be shift-variant, reducing the classification performance of our system. To combat this, a shift-invariant DWT (SIDWT) is utilized to ensure that only translation invariant features are extracted (see Section 5). To robustly quantify these texture elements (as described by the wavelet coefficients), a multiscale texture analysis scheme is employed on the shift-invariant coefficients. At various levels of decomposition, wavelet-domain graylevel cooccurrence matrices were implemented in a variety of directions over all subbands to capture the orientation of such texture elements. Texture features were extracted from each of the wavelet subbands to quantify the randomness of the coefficients and they are classified using a linear classifier. The multiscale texture analysis scheme and the classification technique are described in Section 6 and Section 7. Section 8 and Section 9 presents the results of the proposed generalized CAD framework for all images and the concluding remarks, respectively. This work is a consolidation of several research efforts Khademi (2006) Khademi & Krishnan (2007) Khademi & Krishnan (2008).

2. Biomedical imagery

Three imaging modalities are utilized to test the classification system: mammography, retinal and small bowel images. Each one of these image types are used to diagnose diseases from a specific anatomical region. Although these images are quite different from one another, the current work develops a generalized framework for CAD that may be applied directly to each of the images. The only apriori assumption is a very general one: the texture between normal tissue and pathology is different.
The first modality, mammography, is an imaging technology which acquires an x-ray image of the breast Ferreira & Borges (2001). They are currently the most effective method for early detection of breast cancers Cheng et al. (2006) Wei et al. (1995). A challenging problem in human-based analysis of mammography is the discrimination between malignant and benign masses. Incorrectly identifying the lesion type results in negative to positive biopsies ratios as high as 11:1 in some clinics Rangayyan et al. (1997). Normal tissue masks the lesions and breast parenchyma is much more prominent than the lesion itself Ferreira & Borges (2001).
To test the CAD system with mammography images, a database is used where images contain either a benign or malignant lesion(s). Examples of benign and malignant masses (along with the contrast enhanced versionS) are shown in Figure 1. Normal regions are also shown for comparison.

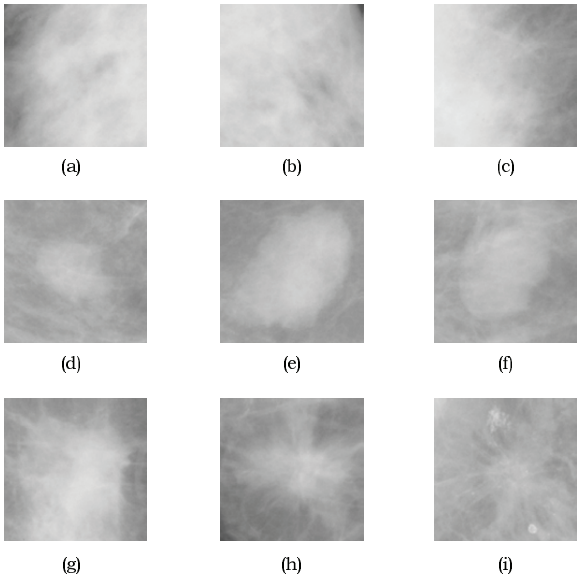

(a) Regular

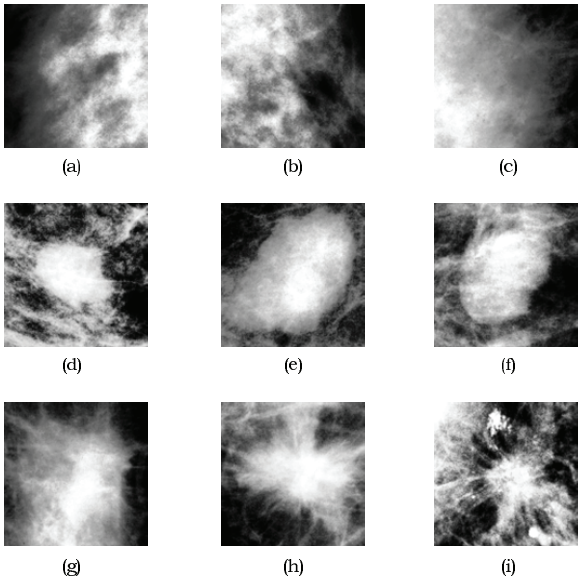

(b) Enhanced

Fig. 1. Mammographic regions (128 × 128). (a)-(c) Normal regions, (d)-(f) circumscribed benign masses, (g)-(i) spiculated malignant masses. The contrast enhanced versions of these regions are also included to highlight the textural differences between lesions.

The benign masses have a rounded appearance with a defined boundary, while the inside of the mass is relatively uniform and radiolucent. This has also been noted by other others, see Ferreira & Borges (2001) Rangayyan et al. (1997) Mudigonda et al. (2000). In contrast, the malignant masses possess ill-defined boundaries, are of higher density (radiopaque) and have an overall nonuniform appearance in comparison to the benign lesions. Furthermore, spicules from malignant masses cause disturbances in the homogeneity of tissues in the surrounding breast parenchyma Rangayyan (2005). Since benign and malignant masses carry different textural qualities, these textural differences will be exploited in the CAD system.
The second type of images are known as small bowel images. They are acquired by Given Imaging Ltd.'s capsule endoscopy known as the PillCam^{TM} SB video capsule. The PillCam^{TM} is a tiny capsule (10mm $\times$ 27mm Kim et al. (2005)), which is ingested from the mouth. As natural peristalsis moves the capsule through the gastrointestinal tract it captures video and wirelessly transmits it to a data recorder the patient is wearing around his or her waist Given Imaging Ltd. (2006a). This video provides visualization of the 21 foot long small bowel, which was originally seen as a "black box" to doctors Given Imaging Ltd. (2006b).
Video is recorded for approximately eight hours and then the capsule is excreted naturally

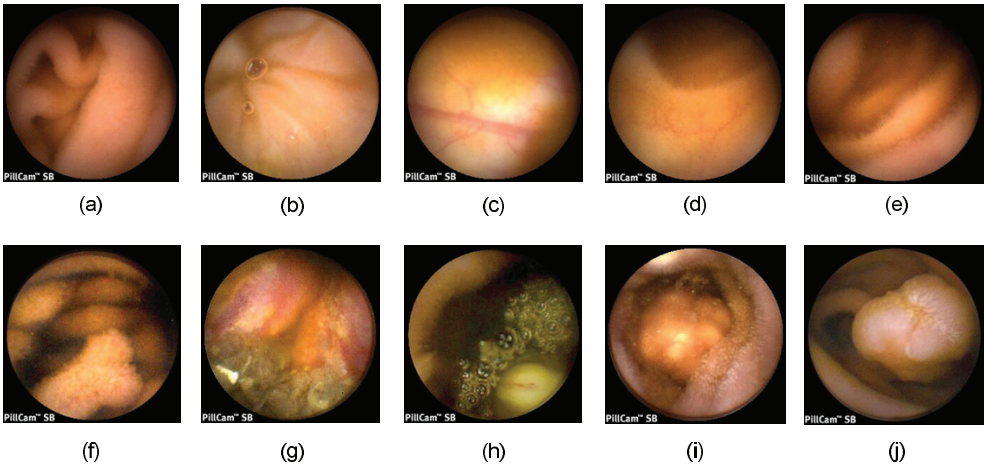

Fig. 2. Small bowel images captured by the PillCam^{TM} SB, which exhibit textural characteristics. (a) Healthy small bowel, (b) normal neocecal valve, (c) normal colonic mucosa, (d) normal small bowel, (e) normal jejunum, (f) small bowel polyp, (g) small bowel lymphoma, (h) GIST tumor, (i) polypoid mass, (j) small bowel polyp.

with a bowel movement Given Imaging Ltd. (2006a). Clinical results for the PillCam^{TM} show that it is a superior diagnostic method for diseases of the small intestine Given Imaging Ltd. (2006c). The downfall of this technology comes from the large amount of data which is collected while the PillCam^{TM} - the doctor has to watch and diagnose eight hours of footage! This is quite a labourious task, which could cause the physicians to miss important clues due to fatigue, boredom or due to the repetitive nature of the task. To combat missed pathologies, the proposed CAD system could be used to double check the image data.
To test out the generalized CAD system, a small bowel image database is utilized that contains both normal (healthy regions) and several abnormal images. As shown Figure 2(a)-(e), the

normal small bowel images contain smooth, homogeneous texture elements with very little disruption in uniformity except for folds and crevices.
Many types of pathologies are found in the small bowel image database ("abnormal" image class), such as “Abnormal”: polyp, Kaposi’s sarcoma, carcinoma, etc. These diseases may occur in various sizes, shapes, orientations and locations within the gastrointestinal tract. Abnormalities have some common textural characteristics: the diseased region contains many different textured areas simultaneously and these diseased areas are composed of heterogeneous texture components. This may be seen in Figure 2(f)-(j).
The data for each patient is a series of 2D colour images. As the current chapter is focused on grayscale processing, the colour images are converted to grayscale first. Additionally, each image has been lossy JPEG compressed, so feature extraction is completed in the compressed domain. Feature extraction in the compressed domain has become an important topic recently Chiu et al. (2004) Xiong & Huang (2002) Chang (1995) Armstrong & Jiang (2001) Voulgaris & Jiang (2001), since the prevalence of images stored in lossy formats far supersedes the number of images stored in their raw format.
The last set of images are known as retinal images. Ophthalmologists use digital fundus cameras to acquire and collect retinal images of the human eye Sinthanayothin et al. (2003), which includes the optic nerve, fovea, surrounding vessels and the retinal layer Goldbaum (2002). Although screening with retinal imaging reduces the risk of serious eye impairment (i.e. blindness caused by diabetic retinopathy by 50% Sinthanayothin et al. (2003)), it also creates a large number of images which the doctors need to interpret Brandon & Hoover (2003). This is expensive, time consuming and may be prone to human error. The current automated system can be used to help the doctors with this diagnostic task by offering a secondary opinion of the images.
The current database contains several normal (healthy) retinal images as well as several images that contain a variety of pathologies. Examples of normal and abnormal retinal images are shown in Figure 3. Healthy eyes are easily characterized by their overall homogeneous appearance, as easily seen in Figure 3(a)-(c).
Eyes which contain disease do not possess uniform texture qualities. Three cases of abnormal retinal images are shown in Figure 3(d)-(f). Diabetic retinopathy, which is characterized by exudates or lesions (random whitish/yellow patches locations Wang et al. (2000)) are shown in Figure 3(a).
Another clinical sign of diabetic retinopathy are microaneurysms and haemorrhages and macular degeneration, which can cause blindness if it goes untreated. Macular degeneration may be characterized by drusens, which appear as yellowish, cloudy blobs, which exhibit no specific size or shape Brandon & Hoover (2003). This is shown in Figure 3(e). These pathologies disrupt the homogeneity of normal tissues. Other diseases include central retinal vein and/or artery occlusion shown in Figure 3(f) (an oriented texture pattern which radiates from the optic nerve).

2.1 Texture for pathology discrimination

As shown in the previous subsection, pathological regions in the images have a heterogeneous appearance and normal regions are uniform. Moreover, texture elements occur at a variety of orientations, scales and locations. Thus the CAD system must be robust to all these variances, but still remain modality- or database-independent (i.e. not tuned specifically for a modality). Computing devices are becoming an integral part of our daily lives and in many times, these

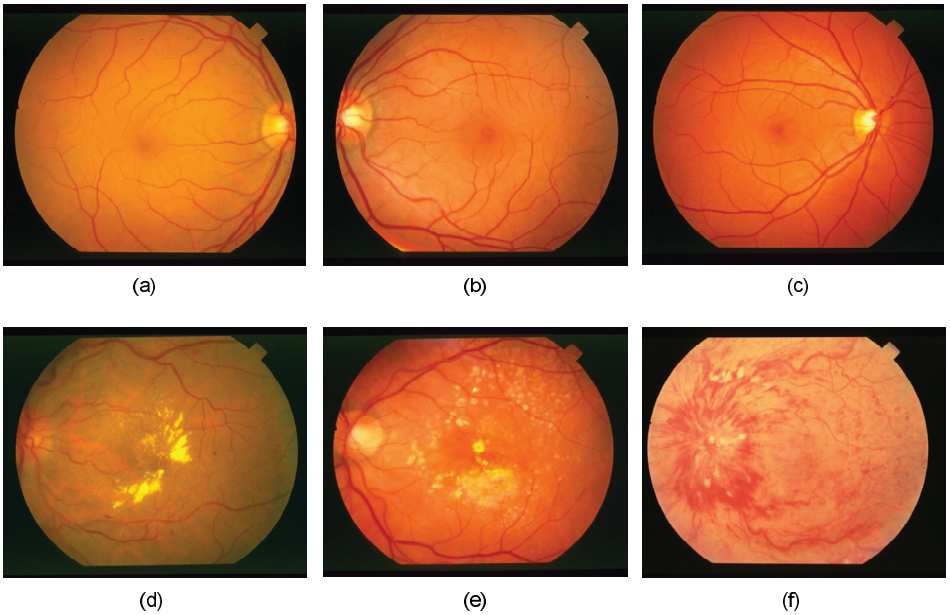

Fig. 3. Retinal images which exhibit textural characteristics. (a)-(c) Normal, homogeneous retinal images, (d) background diabetic retinopathy (dense, homogeneous yellow clusters), (e) macular degeneration (large, radiolucent drusens with heterogeneous texture properties), (f) central retinal vein occlusion (oriented, radiating texture).

algorithms are designed to mimic human behaviour. In fact, this is the major motivation of many CAD systems; to understand and analyze medical image content in the same fashion as humans do. Since texture has been shown to be an important feature for discrimination in medical images, understanding how humans perceive texture provides important clues into how a computer vision system should be designed to discriminate pathology.

As shown, these images possess textural characteristics that differentiate between pathological and healthy (normal) tissues. A common denominator is that the pathological (cancerous) lesions seem to have heterogeneous, oriented texture characteristics, while the normal images are relatively homogeneous. These differences are easily spotted by the human observer and thus we want our system to also differentiate between these two texture types (homogeneity and heterogeneity) for classification purposes.

To build a system that understands textural properties that is in line with human texture perception, a human texture analysis model must first be examined. When a surface is viewed, the human visual system can discriminate between textured regions quite easily. To describe how the human visual system can differentiate between textures, Julesz defined textons, which are elementary units of texture Julesz (1981). Textured regions can be decomposed using these textons, which include elongated blobs, lines, terminators and more. It was found that the frequency content, scale, orientation and periodicity of these textons can provide important clues on how humans differentiate between two or more textured areas Julesz (1981). Therefore, to create a system which mimics human understanding of texture for pathology discrimination, it is necessary that the analysis system can detect the properties of

the fundamental units of texture (texture markers). In accordance to Julesz's model, textural events will be detected based on their scale, frequency and orientation.

3. Feature invariance

To describe the textural characteristics of medical images, a feature extraction scheme will be used. The extracted features are fed into a classifier, which arrives at a decision related to the diagnosis of the patient. Let $\mathcal{X} \subset \mathbf{R}^n$ represent the signal space which contains all biomedical images with the dimensions of $n = N \times N$. Since the images $\mathcal{X}$ can be expected to have a very high dimensionality, using all these samples to arrive at a classification result would be prohibitive Coifman & Saito (1995). Furthermore, the original image space $\mathcal{X}$ is also redundant, which means that all the image samples are not necessary for classification. Therefore, to gain a more useful representation, a *feature extraction operator* f may map the subspace $\mathcal{X}$ into a feature space $\mathcal{F}$

$$f : \mathcal{X} \rightarrow \mathcal{F}, \tag{1}$$

where $\mathcal{F} \subset \mathbf{R}^k$, $k \leq n$ and a particular sample in the feature space may be written as a feature vector: $F = \{F_1, F_2, F_2, \cdots, F_k\}$. If $k < n$, the feature space mapping would also result in a dimensionality reduction.

Although it is important to choose features which provide the maximum discrimination between textures, it is also important that these features are robust. A feature is robust if it provides consistent results across the entire application domain Umbaugh et al. (1997). To ensure robustness, the numerical descriptors should be rotation, scale and translation (RST) invariant. In other words, if the image is rotated, scaled or translated, the extracted features should be insensitive to these changes, or it should be a rotated, scaled or translated version of the original features, but not modified Mallat (1998). This would be useful for classifying unknown image samples since these test images will not have structures that have the same orientation and size as the images in the training set Leung & Peterson (1992). By ensuring invariant features, it is possible to account for the natural variations and structures within the retinal, mammographic and small bowel images.

As will be shown in the next section, such features are extracted from the wavelet domain. If a feature is extracted from a transform domain, it is also important to investigate the invariance properties of the transform since any invariance in this domain also translates to an invariance in the features. For instance, the 1-D Fourier spectrum is a well-known translation-invariant transform since any translation in the time domain representation of the signal, does not change the magnitude spectrum in the Fourier domain

$$f(t - \tau_o) \Leftrightarrow F(\omega) \cdot e^{-j\omega\tau_o}, \tag{2}$$

for all real values of τ_o. Similarly, scaling in time results in a easily definable reaction in the frequency domain

$$f(\alpha t) \Leftrightarrow \frac{1}{|\alpha|} \cdot F\left(\frac{\omega}{\alpha}\right), \tag{3}$$

where α is an integer value.

Although the types of feature extraction algorithms that will be used have not yet been discussed, prior to designing any feature extractor, it is important to understand the necessity of robust features. The following sections will detail the analysis tool used to localize the

texture events, as well as the feature extraction framework that is used to extract robust features (in the RST-invariant sense).

4. Multiresolutional analysis

All signals and images may be categorized into one of two categories: 1) deterministic or 2) non-deterministic (random). Deterministic signals allow for advanced prediction of signal quantities, since the signal may be described by a mathematical function. In contrast, instantaneous values of non-deterministic signals are unpredictable due to their random nature and must be represented using a probabilistic model Ross (2003). This stochastic model describes the inherent behaviour of the signal or image in question.

Random signals (both 1D and 2D) may be further classified into two groups: 1) stationary or 2) nonstationary. A stationary signal (1D) is a signal which has a constant probability distribution for all time instants. As a consequence, first order statistics such as the mean and second order statistics such as variance must also remain constant. In contrast, a nonstationary signal has a time-varying probability distribution which causes quantities computed from the probability density function (PDF) to also be time-varying. For instance, the mean, variance and autocorrelation function of a nonstationary signal would change with time. Since the Fourier transform of the autocorrelation function is equal to the power spectral density (PSD) of a signal (which is related to the spectral content), the PSD of a nonstationary signal is also time-varying. Consequently, a nonstationary signal has time-varying spectral content.

The medical images (as with most natural images) are nonstationary since they have spatially-varying frequency components. Texture is comprised of a variety of frequency content (and may be found in any location in the image), and therefore texture is also a type of nonstationary phenomena. Since textured regions provide important clues that discriminate between pathologies and/or healthy tissue, nonstationary analysis would add extra utility in the sense that it would quantify or localize these textural elements. As discussed, the theory of human texture perception is defined in terms of several features for texture discrimination: the scale, frequency, orientation of textons. Therefore, analyzing the scale, frequency and orientation properties of textural elements by nonstationary image analysis is in accordance to the human texture perception model.

The type of nonstationary image analysis tool that will be utilized is part of the multiresolutional analysis family, and is known as the Discrete Wavelet Transform (DWT). As will be discussed, wavelet transforms are optimal for texture localization since the wavelet basis have excellent joint space-frequency resolution Mallat (1998).

The section will begin by presenting the signal decomposition theory needed to understand the fundamentals of the DWT. Following the introduction, the wavelet transform (with descriptions of the wavelet and scaling basis functions) are given, with emphasis given to signal space definitions. The DWT is then defined using the filter-bank method which was implemented by the lifting-approach for the 5/3 Le Gull wavelet.

4.1 Signal decomposition techniques

Signal decomposition techniques can be used to transform the images into a representation that highlights features of interest. As such decomposition techniques are used to define the wavelet transform and its variants, some brief background is given here.

A decomposition technique linearly expands a signal or image using a set of mathematical functions. For a 1D signal, using a set of real-valued expansion coefficients a_k, and a series

of 1-D mathematical functions $\psi_k(t)$ known as an expansion set ($\psi_k(t) = \psi(t-k)$ for all integer values of k), a signal $f(t)$ may be expressed as a weighted linear combination of these functions

$$f(t) = \sum_k a_k \cdot \psi_k(t), \quad k \in \mathbf{Z}. \tag{4}$$

If the members of the expansion set $\psi_k(t)$ are orthogonal to one another:

$$\langle \psi_k(t), \psi_l(t) \rangle = 0, \quad k \neq l, \tag{5}$$

then it is possible to find the expansion coefficients a_k

$$a_k = \langle f(t), \psi_k(t) \rangle, \tag{6}$$

where the inner product $\langle \cdot \rangle$ of two signals $x(t)$ and $y(t)$ is defined by

$$\langle x(t), y(t) \rangle = \int_t x^*(t) \cdot y(t) dt. \tag{7}$$

The definition of an expansion set depends on various properties. For instance, if there is a signal $f(t)$ which belongs to a subspace S ($f(t) \in S$), then $\psi_k(t)$ will *only* be called an expansion set for S if $f(t)$ can be expressed with linear combinations of $\psi_k(t)$. The expansion set forms a *basis* if the representation it provides is unique Burrus et al. (1998). Similarly, a basis set may be defined first and then the space S *spans* all functions $f(t)$ which can be expressed by $f(t) = \sum_k a_k \cdot \psi_k(t)$.

For images, the basis functions may be dependant on both the horizontal and vertical spatial variables (x, y). This leads to 2D basis functions $\psi_{m,n}(x, y)$, where $\psi_{m,n}(x, y) = \psi(x-n, y-m)$, for all $(m, n) \in \mathbf{Z}$. Therefore, a 2D function (image) $f(x, y)$, that belongs to the space of the basis functions, may be rewritten as a linear expansion

$$f(x, y) = \sum_m \sum_n a_{m,n} \cdot \psi_{m,n}(x, y), \tag{8}$$

where $a_{m,n}$ are the 2-D expansion coefficients found by

$$a_{m,n} = \langle \psi_{m,n}(x, y), f(x, y) \rangle. \tag{9}$$

Using decomposition techniques, a new representation is generated. In feature extraction problems, we want this representation (i.e. coefficients a_k or $a_{n,m}$) to highlight the features we are interested in. This requires us to choose basis functions that are tuned to the properties of our image (i.e. nonstationary structures). While choosing which basis set to use, one of the main considerations is the functions' space-frequency resolution.

Consider the basis function $\psi_k(t)$ which has an energy distribution that is concentrated near the time instant k and is spread out over the interval Δt Mallat (1998). This basis function $\psi_k(t)$ can identify time-localized features (at k) with a resolution of $\frac{1}{\Delta t}$. Similarly, in the frequency domain, the Fourier representation $\Psi_\xi(\omega)$ is concentrated in energy near the frequency ξ and spread over the interval of $\Delta\omega$, which captures frequency-localized features (at ξ) with a resolution of $\frac{1}{\Delta\omega}$.

Ideally, basis functions with infinitely small time and frequency would provide the best representation since time-frequency structures would be represented with infinite resolution.

However, this is not possible, because there is a direct trade off between time and frequency resolution of basis functions as governed by the Heisenburg uncertainty principal Burrus et al. (1998) Mallat (1998). The Heisenburg uncertainty principal states that resolution of the time-frequency functions are lower bounded by

$$\Delta\omega \cdot \Delta t \geq 1/2. \tag{10}$$

Therefore, to capture nonstationary events with good space-frequency localization, we need basis functions that aim to operate near the theoretical lower bound. Many basis functions offer solutions, but are not optimal for all applications. For example, the Short-Time Fourier Transform (STFT) bases are not optimal because (1) they offer a fixed resolution for the entire decomposition process (thus missing features that are comprised with different scales and frequencies), (2) do not offer an easy method to access and manage the coefficients and (3) creates a drastic increase in memory consumption and computational resources. The following section will describe how the wavelet transform poses solutions to all these problems.

4.2 Wavelet transforms

The wavelet transform offers solutions to all the problems associated with other basis functions (such as the STFT) Mallat (1989) Wang & Karayiannis (1998) Vetterli & Herley (1992) Mallat (1998). It offers a multiresolutional representation (decomposes the image using various scale-frequency resolutions), which is achieved by dyadically changing the size of the window. Space-frequency events are localized with good results since the changing window function is tuned to events which have high frequency components in a small analysis window (scale) or low frequency events with a large scale Burrus et al. (1998). Therefore, texture events could be efficiently represented using a set of multiresolutional basis functions. Additionally, the discrete wavelet transform utilizes critical subsampling along rows and columns and uses these subsampled subbands as the input to the next decomposition level. For a 2-D image, this reduces the number of input samples by a factor of four for each level of decomposition. This representation may be stored back on to the original image for minimum memory usage and it also permits for an organized, computationally efficient manner to access these subbands and extract meaningful features.

The wavelet transform utilizes both wavelet basis $\psi_{j,k}(t)$ and scaling basis $\phi_k(t)$ functions. The wavelet functions are used to localize the high frequency content, whereas the scaling function examines the low frequencies. The scale of the analysis window changes with each decomposition level, thus achieving a multiresolutional representation. Starting with the initial scale $j = 0$, the wavelet transform of any function $f(t)$ which belongs to $L^2(\mathbf{R})$ is found by

$$f(t) = \sum_{k=-\infty}^{k=\infty} c(k) \cdot \phi_k(t) + \sum_{j=0}^{j=\infty} \sum_{k=-\infty}^{k=\infty} d(j,k) \cdot \psi_{j,k}(t), \tag{11}$$

where $c(k)$ are the scaling or averaging coefficients (low frequency material) defined by

$$c(k) = c_0(k) = \langle f(t), \phi_k(t) \rangle = \int f(t)\phi_k(t)\, dt, \tag{12}$$

and $d_j(k)$ are the detail wavelet coefficients (high frequency content) defined by

$$d_j(k) = d(j,k) = \langle f(t), \psi_{j,k}(t) \rangle = \int f(t)\psi_{j,k}(t)\, dt. \tag{13}$$

In order to achieve a wavelet transform, the functions $\psi_{j,k}(t)$ and $\phi_k(t)$ have to meet specific criteria. These criteria, the properties of the scaling/wavelet functions and the corresponding signal spaces are described next.

4.2.1 Scaling function subspaces

Consider a set of basis functions $\{\phi_k(t)\}$ which may be created by translating the prototype scaling function $\phi(t)$ Burrus et al. (1998)

$$\phi_k(t) = \phi(t-k), \quad k \in \mathbf{Z}, \tag{14}$$

where $\phi_k(t)$ spans the space $\mathcal{V}_o$

$$\mathcal{V}_o = \overline{\text{Span}_\text{k}\{\phi_k(t)\}}. \tag{15}$$

If a set of basis functions span a signal space $\mathcal{V}_o$, then any function $f(t)$ which also belongs to that space can be completely represented using those basis functions as in: $f(t) = \sum_k a_k \cdot \phi_k(t)$ (for any $f(t) \in \mathcal{V}_o$).

For added flexibility, the time and frequency resolution of these scaling functions may be adjusted by including an additional scale parameter j in the characteristic basis function expression

$$\phi_{j,k}(t) = 2^{j/2} \cdot \phi(2^j t - k), \quad j,k \in \mathbf{Z}, \tag{16}$$

where the scalar multiple $2^{j/2}$ is included to ensure orthonormality Mallat (1989). Therefore, an entire series of basis functions can be created by simply dilating (changing the j value) or translating (changing the k value) the prototype scaling function $\phi(t)$. These basis functions span the subspace $\mathcal{V}_j$

$$\begin{aligned} \mathcal{V}_j &= \overline{\text{Span}_\text{k}\{\phi_k(2^j t)\}}, \\ &= \overline{\text{Span}_\text{k}\{\phi_{j,k}(t)\}}, \end{aligned} \tag{17}$$

and any signal $f(t)$ can be expressed using this expansion set, as long as it is also a set of $\mathcal{V}_j$

$$f(t) = \sum_k a_k \cdot \phi(2^j t - k), \quad f(t) \in \mathcal{V}_j. \tag{18}$$

The introduction of a scale parameter changes the time duration of the scaling functions. This allows different resolutions to isolate different anomalies in the signals or images. For instance, if $j > 0$, $\phi_{j,k}(t)$ is narrower and would provide a good representation of finer detail. For $j < 0$, the basis functions $\phi_{j,k}(t)$ are wider and would be ideal to represent coarse information Burrus et al. (1998).

4.2.2 Wavelet basis functions

Although the scaling functions give way to a multiresolution representation, it is also necessary to investigate the spaces which span the *differences* of the spaces spanned by the scaling functions. These regions correspond to the high frequency details of the data.

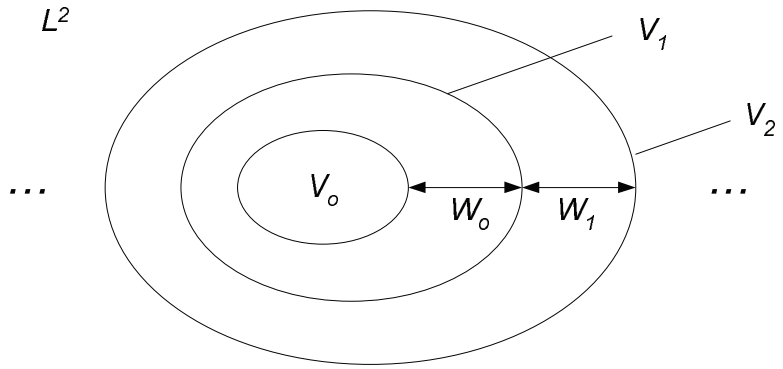

Fig. 4. Nested wavelet and scaling signal spaces.

The types of basis functions that can localize the details are known as wavelets $\psi(t)$ and their corresponding signal spaces are denoted as $\mathcal{W}$. Similar to scaling functions, a series of wavelet basis functions can be generated by dilating and translating the mother wavelet $\psi(t)$

$$\psi_{j,k}(t) = 2^{j/2}\psi(2^j t - k), \quad j,k \in \mathbf{Z}. \tag{19}$$

To find the mother wavelet $\psi(t)$, it is necessary to find the relationship between the mother wavelet $\psi(t)$ and the generating scaling function $\phi(t)$.
Starting with an initial resolution of $j = 0$, the nested subspaces may be written as

$$\mathcal{V}_o \subset \mathcal{V}_1 \subset \mathcal{V}_2 \subset \cdots \subset L^2. \tag{20}$$

The corresponding spaces spanned by the wavelet basis functions are shown in Figure 4, which illustrates how each $\mathcal{W}$ subspace spans the difference of two subspaces. As shown in Figure 4, the signal spaces $\mathcal{V}_1$ and $\mathcal{V}_2$ may be expressed as

$$\mathcal{V}_1 = \mathcal{V}_o \oplus \mathcal{W}_o, \tag{21}$$

and

$$\mathcal{V}_2 = \mathcal{V}_o \oplus \mathcal{W}_o \oplus \mathcal{W}_1, \tag{22}$$

where $\oplus$ is a direct sum. If $\mathcal{V}_j$ is the space spanned by the scaling functions $\phi_{j,k}(t)$ and $\mathcal{V}_{j+1}$ is the space spanned by the functions $\phi_{j+1,k}(t)$, then $\mathcal{W}_j$ is the disjoint difference or the orthogonal compliments of $\mathcal{V}_j$ and $\mathcal{V}_{j+1}$ spanned by the wavelet basis functions $\psi_{j,k}(t)$. This may be shown by

$$\mathcal{V}_{j+1} = \mathcal{V}_j \oplus \mathcal{W}_j, \quad \forall j \in \mathbf{Z}. \tag{23}$$

Using Equation 21, Equation 22 and Figure 4, a general expression for the L^2 subspace may be developed:

$$L^2 = \mathcal{V}_o \oplus \mathcal{W}_o \oplus \mathcal{W}_1 \oplus \mathcal{W}_2 \oplus \cdots, \tag{24}$$

and since these subspaces are orthogonal to one another

$$\mathcal{V}_o \perp \mathcal{W}_o \perp \mathcal{W}_1 \perp \mathcal{W}_2 \perp \mathcal{W}_3 \cdots, \tag{25}$$

the corresponding basis functions which span these spaces are also orthogonal

$$\langle \phi_{j,k}(t), \psi_{j,k}(t) \rangle = \int \phi_{j,k}(t) \cdot \psi_{j,k}(t) dt = 0. \tag{26}$$

Furthermore, wavelet spaces at a scale j are a subset of the scale spaces at the next scale $j+1$

$$\mathcal{W}_j \subset \mathcal{V}_{j+1}. \tag{27}$$

Consequently, wavelets reside in the space spanned by the next narrower scaling function and can be expressed as a weighted sum of shifted scaling functions, $\phi(2t)$

$$\psi(t) = \sum_n h_1(n) \cdot \sqrt{2} \cdot \phi(2t - n), \quad n \in \mathbf{Z}, \tag{28}$$

where $h_1(n)$ are the wavelets' coefficients. Equation 28 shows that the generating wavelet $\psi(t)$ can be produced from the prototype scaling function $\phi(t)$ by choosing the appropriate $h_1(n)$. In order to ensure orthogonality, the scaling and wavelet coefficients must be related by Burrus et al. (1998)

$$h_1(n) = (-1)^n h_o(1 - n). \tag{29}$$

Therefore, for analysis with orthogonal wavelets, the highpass filter $h_1(n)$, which is half-band, is calculated as the quadrature mirror filter of the lowpass $h_o(n)$. These filters may be used to efficiently implement the wavelet transform for discrete signals (the Discrete Wavelet Transform) and is discussed next.

4.3 Discrete wavelet transform

In order to perform the wavelet transform for discrete images, implementation of the DWT using filterbanks is popular choice since the complexities of the wavelet transform are explained in terms of filtering operations (which is intuitive). The material is first presented for one dimensional signals and then is expanded to 2D for images.

After performing a series of simplifications and change of variables Burrus et al. (1998) Mallat (1998) Vetterli & Herley (1992), Equation 28 may be rewritten as

$$c_j(k) = \sum_m h_o(m - 2k) c_{j+1}(m), \tag{30}$$

and

$$d_j(k) = \sum_m h_1(m - 2k) c_{j+1}(m). \tag{31}$$

This illustrates that $c_j(k)$ and $d_j(k)$ can be found by filtering $c_{j+1}(k)$ with h_o and h_1, respectively, followed by a decimation by a factor of 2. The two filters, $h_o(n)$ and $h_1(n)$ are half-band lowpass and highpass filters, respectively. Consequently, the lowpass filter $h_o(n)$ produces lowpassed or averaged coefficients $c_j(k)$ and the highpass filter $h_1(n)$ creates highpassed or detail coefficients $d_j(k)$.

To compute the DWT coefficients for two levels, examine the two stage analysis filterbank in Figure 5(a) alongside the signal spaces in Figure 5(b). Note that the initial scale here is $j+1$, and therefore c_{j+1} would represent the original input signal. After one level of decomposition, the lowpass coefficients c_j and the highpass details d_j are produced. For a multiresolutional representation, c_j are further decomposed with h_o and h_1, to produce the coefficients $c_{j-1}(k)$

and $d_{j-1}(k)$ (they describe the next scale of low and high frequency structures). The 2D extension for images is detailed next.

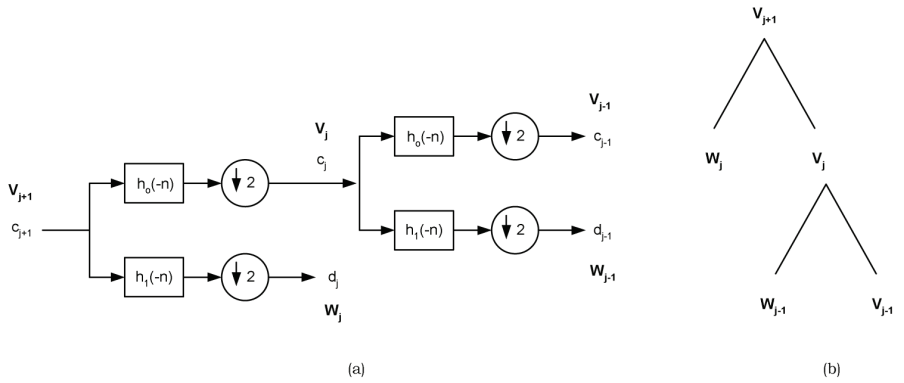

Fig. 5. (a) Computing the 1-D wavelet and scaling coefficients using filtering and decimation with a 2-stage analysis filterbank, (b) corresponding decomposition tree showing the division of signal spaces.

4.3.1 2-D extension for images

Instead of having a wavelet or filter which is a function of the two spatial dimensions of an image, the filter can be separable, which allows a particular 1D filter to be applied to the rows and columns of an image separately to gain the desired overall 2D response Lawson & Zhu (2004). A separable filter for two dimensions may be denoted by:

$$H(z_1, z_2) = H(z_1) \cdot H(z_2), \tag{32}$$

where z_1 and z_2 relate to the spatial dimensions of an image. Therefore, the filters defined for the 1D DWT may be applied separably to gain a 2D DWT representation for images. The 2-D DWT filterbank scheme for an $N \times N$ image $x(m,n)$ is shown in Figure 6. Initially, the filters $H_o(z)$ and $H_1(z)$ are applied to the rows of image $x(m,n)$, creating two images which respectively contain the low and high frequency content of the image in question. After this, both frequency bands are subsampled by a factor of 2, and are sent to the next set of filters for filtering along the columns. After these bands have been filtered, decimation by a factor of 2 is again performed, but this time along columns. At the output of one level of decomposition, as shown in Figure 6, there are four subband images of size $\frac{N}{2} \times \frac{N}{2}$ labeled LL, LH, HL and HH. Using the separability concept, at scale j, these subbands may be computed by

$$LL^j(x,y) = \sum_m \sum_n h_o(m-2x) h_o(n-2y) \cdot LL^{j+1}(m,n), \tag{33}$$

$$HL^j(x,y) = \sum_m \sum_n h_o(m-2x) h_1(n-2y) \cdot LL^{j+1}(m,n), \tag{34}$$

$$LH^j(x,y) = \sum_m \sum_n h_1(m-2x) h_o(n-2y) \cdot LL^{j+1}(m,n), \tag{35}$$

$$HH^j(x,y) = \sum_m \sum_n h_1(m-2x) h_1(n-2y) \cdot LL^{j+1}(m,n). \tag{36}$$

The first letter of the subimages indicates the operation that was performed on the columns (i.e. L is for lowpass filtering with $H_o(z)$ and H is for highpass filtering with $H_1(z)$) whereas the last letter indicates which operation was performed on the rows. If more levels

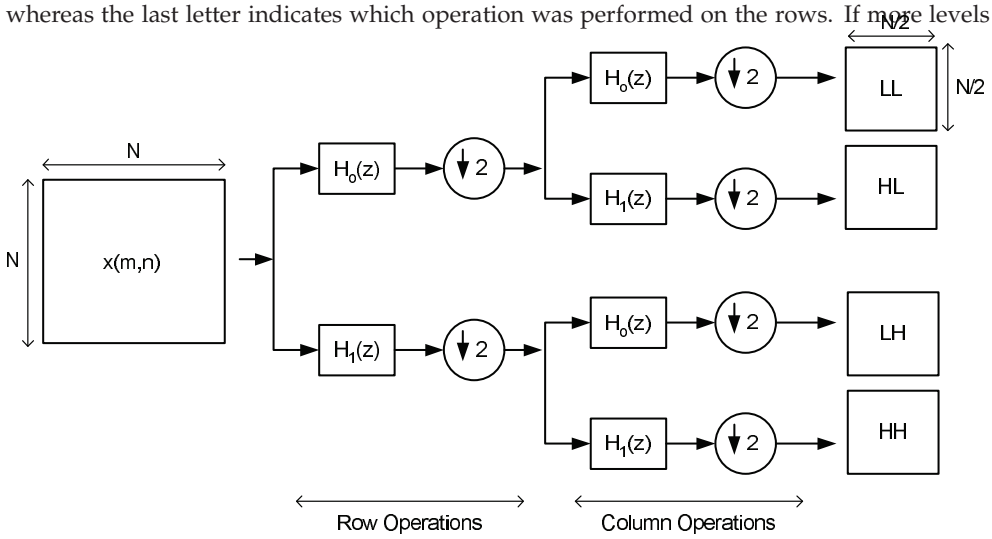

Fig. 6. Filterbank implementation of 2-D discrete wavelet transform (DWT).

of decomposition are required, the LL band may be recursively reapplied to the analysis filterbank of Figure 6. For two levels of decomposition, the placement of the coefficients back onto the image is shown in Figure 7.

To examine the localization properties of the 2D DWT, consider Figure 8. The edges and

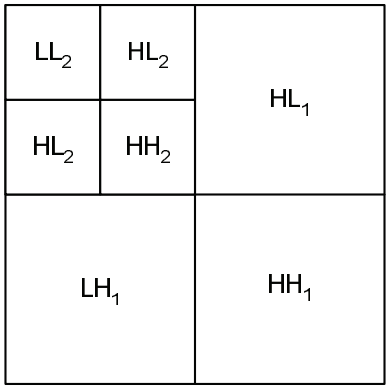

Fig. 7. Graphical depiction of wavelet coefficient placement for two levels of decomposition.

corners of the square (the original image) are composed of localized high frequency content, which is captured in the high frequency subbands in the wavelet domain, regardless of the orientation (horizontal, diagonal, vertical). As texture is comprised of such localized high frequency events, utilization of such a transform will be able to describe the textural events as required. The diffusion of textural features or events will occur across subbands, which

allows features to be captured not only *within* subbands, but also *across* subbands.
For an example of the localization properties of wavelets in a medical image, as well as the textural differences between normal and abnormal medical images, see Figure 9. The normal image's decomposition exhibits an overly homogeneous appearance of the wavelet coefficients in the HH, HL and LH bands (which reflects the uniform nature of the original image). The decomposition of the retinal image with diabetic retinopathy shows that each of the higher frequency subbands localizes the retinopathy, which appears as heterogeneous textured blobs (high-valued wavelet coefficients) in the center of the subband. This illustrates how the DWT can localize the textural differences in medical images also how multiscale texture may be used to discriminate between pathological cases . Similar results are obtained with the small bowel and mammographic lesions, however, are not shown here due to space constraints.

Another benefit of wavelet analysis is that the basis functions are scale-invariant.

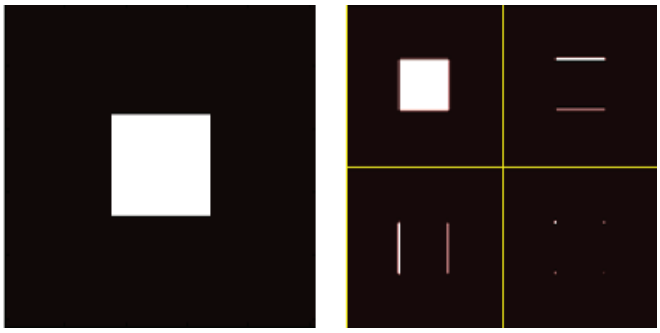

Fig. 8. Left: original image. Right: one level of DWT of left image.

Scale-invariant basis functions will give rise to a localized description of the texture elements, regardless of their size or scale, i.e. coarse texture can be made up of large textons, while fine texture is comprised of smaller elementary units. Therefore, the DWT can handle both of these scenarios.

Although the filterbank method is efficient, it requires a lot of filtering operations which is computationally expensive. For more efficient implementations of the filterbank-based DWT, the lifting-based approach is one such approach that is employed in the current framework and detailed next.

4.4 Lifting-based DWT

To compute the DWT in an efficient manner, the lifting based approach is used Fernández et al. (1996) Sweldens (1995) Sweldens (1996). To increase computation speed, lifting based approaches make optimal use of similarities which exist between the lowpass ($H_1(z)$) and highpass ($H_o(z)$) filters. All 1D implementations will be later extended to 2D implementations by 'lifting' both the columns and the rows separately.
The lifting based DWT is an efficient scheme since it aims to implement complicated functions with simple and invertible stages Zhang & Zeytinoglu (1999). Compared to the filterbank method, the lifting based DWT method offers a less computationally expensive solution to compute the DWT Zhang & Zeytinoglu (1999) Sweldens (1996).
The lifting based scheme relies on three operations to achieve the discrete wavelet transform:

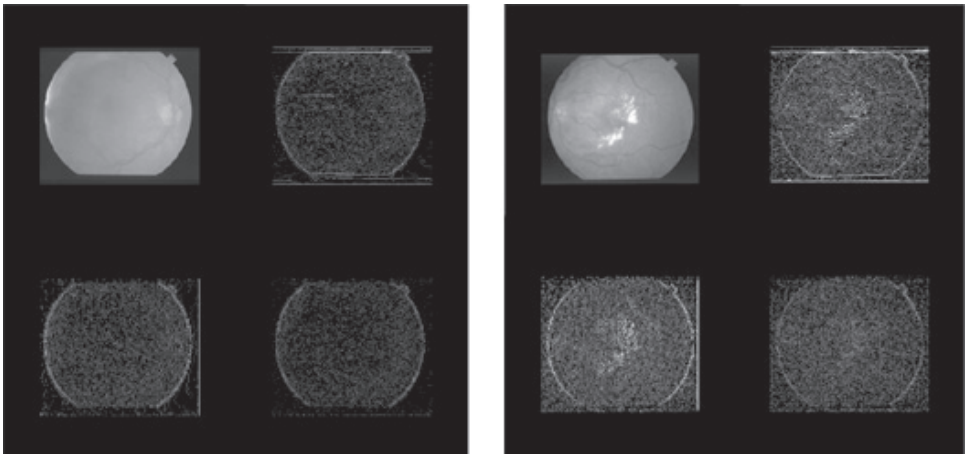

Fig. 9. One level of DWT decomposition of retinal images. Left: normal image decomposition. Right: decomposition of retinal image with diabetic retinopathy. Contrast enhancement was performed in the higher frequency bands (HH, LH, HL) for visualization purposes.

1) split, 2) predict and 3) update. These three operations which comprise the 1-D lifting scheme, are shown in Figure 10, where $\mathcal{S}$ is the splitting function, $\mathcal{P}$ is the predictor function and $\mathcal{U}$ is the update operation. As shown by Figure 10, the scaling and wavelet coefficients ($c_j(n)$ and $d_j(n)$) are still from the previous level's coefficients, $c_{j+1}(n)$. Lifting may be also applied separably to the rows and columns of an image to arrive at a 2D DWT.

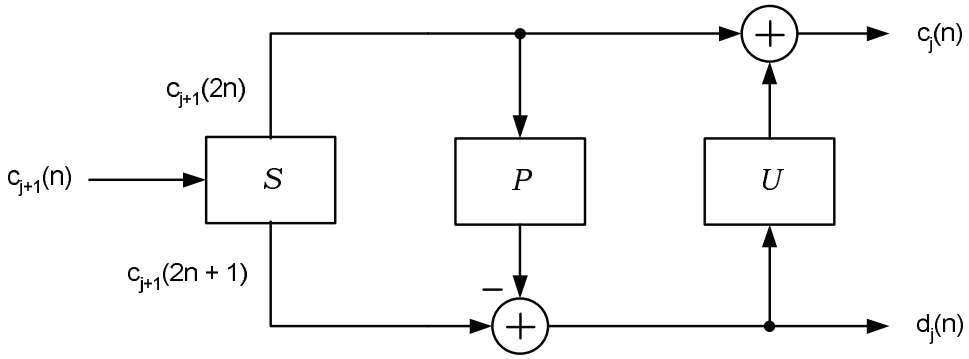

Fig. 10. Generalized 1-D lifting based implementation of the DWT.

4.4.1 Splitting

The splitting operation divides the 1-D input string into even and odd samples, as denoted by $c_{j+1}(2n)$ and $c_{j+1}(2n+1)$, respectively. Using digital signal processing, the even samples may be obtained by decimating the original signal by a factor of 2, and the odd samples may be obtained by subsampling a time shifted (single unit of time) version of the original signal by 2. This is often referred to as the Lazy Wavelet Transform Fernández et al. (1996).

4.4.2 Prediction

In order to compute the wavelet coefficients $d_j(n)$, a lifting scheme uses a predictor to interpolate the odd-indexed coefficients from the previous scale ($c_{j+1}(2n+1)$). The prediction is subtracted from the original odd-indexed signal to produce the wavelet coefficients $d_j(n)$. This may expressed as

$$d_j(n) = c_{j+1}(2n+1) - \mathcal{P}(c_{j+1}(2n+1)), \tag{37}$$

where $\mathcal{P}(\cdot)$ is the predictor function. As stated earlier, the wavelet coefficients correspond to the high frequency components which makes this operation equivalent to highpass filtering. A good predictor function would produce small valued wavelet coefficients (ideally zero), since the predicted version of the signal would be identical to the original. However, for nonstationary signals (such as biomedical images) that have properties which change over time, it is not possible to exactly predict the signal Zhang & Zeytinoglu (1999) and non-zero wavelet coefficients can be expected. There are many different predictor functions which may be used Maragos et al. (1984) Haijiang et al. (2004) Denecker et al. (1997), however, in order to implement the forward wavelet transform, the interpolation function is chosen such that it relates to the wavelet $\psi(t)$ Zhang & Zeytinoglu (1999).

4.4.3 Updating

In a lifting based DWT implementation, the scaling coefficients $c_j(n)$ are computed as the sum of the even-indexed samples ($c_{j+1}(2n)$) and an updated version of the wavelet coefficients $d_j(n)$ as shown below:

$$c_j(n) = c_{j+1}(2n) + \mathcal{U}(d_j(n)), \tag{38}$$

where $\mathcal{U}(\cdot)$ is the update function. This operation isolates the low frequency components within the original signal. For images, lifting based DWT must be extended to two dimensions. As shown earlier in the 2D DWT filterbank approach, 1D wavelet transforms were applied separably to the images in order to gain a 2D DWT representation. This also applies to lifting based schemes as well. By sequentially applying the lifting operation first to the rows and then to the columns of an image, the forward transformation is achieved. The forward operation is depicted in Figure 11.

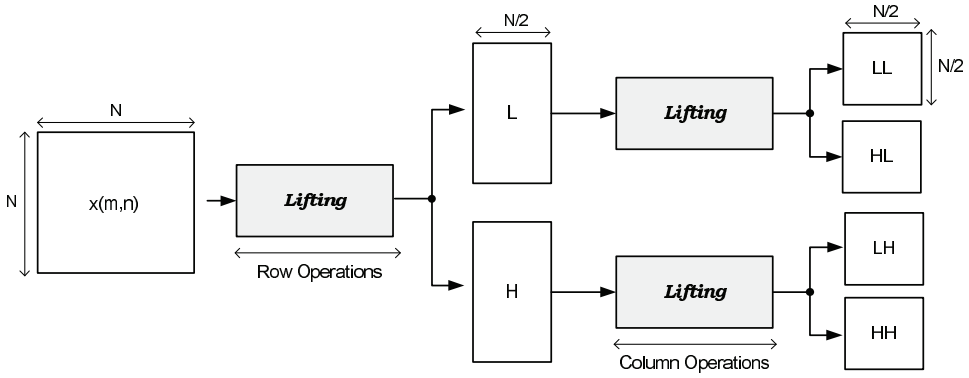

Fig. 11. Lifting-based implementation of the DWT for two dimensional signals.

4.5 5/3 Wavelet

The integer wavelet which will be used is part of the Odd-Length Analysis/Synthesis Filter (OLASF) family, where the number of filter taps in the FIR filter (for the filterbank implementation) are odd Adams & Ward (2003). Additionally, biomedical images are high resolution images, which results in large image sizes. Consequently, for these large-sized images, a wavelet with fewer taps is desired so that the overall computational load may be reduced. The 5/3 Le Gull wavelet will be used since the filter lengths are small (5 and 3 taps for the analysis low and highpass filters) and can warrant an efficient implementation Marcellin et al. (2000) Zhang & Fritts (2004) . The 5/3 filter coefficients are listed in Table **??**.

	Analysis Coefficients		**Synthesis Coefficients**	
i	$h_o(i)$	$h_1(i)$	$h_o(i)$	$h_1(i)$
0	$+\frac{6}{8}$	$+1$	$+1$	$+\frac{6}{8}$
±1	$+\frac{2}{8}$	$-\frac{1}{2}$	$-\frac{1}{2}$	$+\frac{2}{8}$
±2	$-\frac{1}{8}$			$+\frac{1}{8}$

Table 1. Analysis and synthesis filter coefficients for the 5/3 wavelet.

Using the 5/3 integer wavelet, the highpass details $d_j(n)$ can be computed using a lifting based approach:

$$d_j(n) = c_{j+1}(2n+1) - \left\lfloor \frac{c_{j+1}(2n) + c_{j+1}(2n+2)}{2} \right\rfloor, \tag{39}$$

where $\lfloor X \rfloor$ is the greatest integer less than or equal to X. The low frequency, average coefficients $c_j(n)$ may be found using an update function

$$c_j(n) = c_{j+1}(2n) + \left\lfloor \frac{d_j(n) + d_j(n-1) + 2}{4} \right\rfloor. \tag{40}$$

For reconstruction, the reverse DWT can be found by reversing the arithmetic operations of the forward transform. This is shown below:

$$c_{j+1}(2n) = c_j(n) + \left\lfloor \frac{d_j(n) + d_j(n-1) + 2}{4} \right\rfloor, \tag{41}$$

$$c_{j+1}(2n+1) = d_j(n) - \left\lfloor \frac{c_{j+1}(2n) + c_{j+1}(2n+2)}{2} \right\rfloor. \tag{42}$$

These equations may be applied separably to the images in order to gain a 2-D DWT representation.

5. Shift-invariant discrete wavelet transform

Although the DWT is scale-invariant, it is well known that the DWT is shift-variant Mallat (1998), i.e. the coefficients of a circularly shifted image are not translated versions of the

original image's coefficients. For instance, the DWT of an input biomedical image $f(x,y)$ can be shown as:

$$f(x,y) \longrightarrow \boxed{\text{DWT}} \longrightarrow \widehat{F}(k_1,k_2,j)$$

where $\widehat{F}(k_1,k_2,j)$ are the 2-D DWT coefficients at scale j. A shift of the image will result in a different set of coefficients

$$f(x+\Delta x, y+\Delta y) \longrightarrow \boxed{\text{DWT}} \longrightarrow \widehat{F}(k_1^{'},k_2^{'},j)$$

where $k_1^{'} \neq k_1 + a_1 \cdot \Delta x$ and $k_2^{'} \neq k_2 + a_2 \cdot \Delta y$ for (a_1,a_2), $(\Delta x, \Delta y) \in \mathbf{Z}$, indicating that the two sets of coefficients are not translated versions of one another.

Shift-variance causes significant challenges in a feature extraction problem. For example,

Fig. 12. Image (simulated benign lesion).

consider the image of Figure 12 (the center circle can be considered as a circumscribed benign lesion, or something to that effect). If this circle is translated by a small amount (which is equivalent to the lesion being located in different regions of an image), the extracted features would be different. To illustrate this, the image in Figure 12 is translated by shifts of $(\Delta x, \Delta y)$ = {(0,0), (0,1), (1,0), (1,1)} and for each translation, the DWT is performed. Then, the mean and variance of the wavelet coefficients are extracted from the LH band (moments are RST invariant, so any invariance would be a consequence of the transform). The extracted features are shown in Table 2. As shown by these results, images with pathology (texture) located in different regions of the images would result in different feature sets, thus leading to high misclassification results.

For shift-invariant features, it is necessary to utilize a shift-invariant discrete wavelet

Input shift $(\Delta x, \Delta y)$	**Mean** μ	**Variance** σ^2
(0,0)	-0.050537	97.017
(0,1)	-0.051025	100.42
(1,0)	0.057861	96.82
(1,1)	0.058350	98.383

Table 2. Mean μ and variance σ^2 of the DWT coefficients of the *LH* band for circular translates $(\Delta x, \Delta y)$ of Figure 12.

transform (SIDWT) on the input image $f(x,y)$

$$f(x,y) \longrightarrow \boxed{\text{SIDWT}} \longrightarrow \widetilde{F}(k_1,k_2,j)$$

to compute the wavelet coefficients $\widetilde{F}(k_1, k_2, j)$. The representation achieved by such a transform would be considered shift-invariant if a shift of the input image $(\Delta x, \Delta y) \in \mathbf{Z}$ results in output coefficients which are exactly the same as $\widetilde{F}(k_1, k_2, j)$, or a spatially shifted version of it. This may be shown by

$$f(x + \Delta x, y + \Delta y) \longrightarrow \boxed{\text{SIDWT}} \longrightarrow \widetilde{F}(k_1', k_2', j)$$

where $k_1' = k_1 + b_1 \cdot \Delta x$ and $k_2' = k_2 + b_2 \cdot \Delta y$ for some $(b_1, b_2) \in \mathbf{Z}$. If the coefficients are exactly the same: $b_1 = b_2 = 0$.

The shift-variant property of the DWT is widely known and several solutions have been proposed. Mallat et. al use an overcomplete, redundant dictionary, which corresponds to filtering without decimation Mallat (1998) Bradley (2003). From the filtered and fully sampled version of the image, local extrema are used for translation invariance since a shift in the input image results in a corresponding shift of the extrema Mallat (1998) Liang & Parks (1994). Since there is no decimation, each level of decomposition contains as many samples as the input image, thus making the algorithm computationally complex. It also requires significant memory bandwidth.

Simoncelli et. al propose an approximate shift-invariant DWT algorithm by relaxing the critical sampling requirements of the DWT Simoncelli et al. (1992). This algorithm is known as the power-shiftable DWT since the power in each subband remains constant. As explained in Bradley (2003), the shift-variant property is also related to aliasing caused by the DWT filters. The power shiftable transform tries to remedy this problem by reducing the aliasing of the mother wavelet in the frequency domain. The modifications to the mother wavelet result in a loss of orthogonality Liang & Parks (1998).

The Matching Pursuit (MP) algorithm can also achieve a shift-invariant representation, when the decomposition dictionary contains a large amount of redundant wavelet basis functions Mallat & Zhang (1993). However, the MP algorithm is extremely computationally complex and arriving at a transformed representation causes significant delays Cohen et al. (1997). Bradley combines features of the DWT pyramidal decomposition with the *à trous* algorithm Mallat (1998), which provides a trade off between sparsity of the representation and time-invariance Bradley (2003). Critical sampling is only carried out for a certain number of subbands and the rest are all fully sampled. This representation only achieves an approximate shift-invariant DWT Bradley (2003).

The algorithms discussed either try to minimize the aliasing error by relaxing critical subsampling and/or add redundancy into the wavelet basis set. However, these algorithms either suffer from lack of orthogonality (which is not always an issue for feature extraction), achieve an approximate shift-invariant representation, are computationally complex or require significant memory resources. To combat these downfalls, the SIDWT algorithm proposed by Beylkin, which computes the DWT for all circular shifts in a computationally efficient manner Beylkin (1992) is utilized. The proposed SIDWT utilizes orthogonal wavelets, thereby resulting in less redundancy in the representation Liang & Parks (1994), and a more efficient implementation. Belkyn's work has also been extended to 2-D signals by Liang et. al Liang & Parks (1994) Liang & Parks (1998) Liang & Parks (1996) and its performance in a biomedical image feature extraction application will be investigated.

5.1 2D SIDWT algorithm

For different shifts of the input image, it was shown that the DWT can produce one of four possible representations after one level of decomposition. These four DWT coefficient sets (cosets) are not translated versions of one another and each coset may be generated as the DWT response to one of four shifts of the input: $(0,0)$, $(0,1)$, $(1,0)$, $(1,1)$, where the first index corresponds to the row shift and the second index is the column shift. All other shifts of the input (at this decomposition level) will result in coefficients which are shifted versions of one of these four cosets. Therefore, to account for all possible representations, these four cosets may be computed for each level of decomposition. This requires the LL band from each level to be shifted by the four translates $\{(0,0), (0,1), (1,0), (1,1)\}$ and each of these new images to be separately decomposed to account for all representations.

To compute the coefficients at the j^{th} decomposition level, for the input shift of $(0,0)$, the subbands LL^j, LH^j, HL^j, HH^j may be found by filtering the previous levels coefficients LL^{j+1}, as shown below:

$$LL^j_{(0,0)}(x,y) = \sum_m \sum_n h_o(m-2x)h_o(n-2y) \cdot LL^{j+1}(m,n), \tag{43}$$

$$LH^j_{(0,0)}(x,y) = \sum_m \sum_n h_1(m-2x)h_o(n-2y) \cdot LL^{j+1}(m,n), \tag{44}$$

$$HL^j_{(0,0)}(x,y) = \sum_m \sum_n h_o(m-2x)h_1(n-2y) \cdot LL^{j+1}(m,n), \tag{45}$$

$$HH^j_{(0,0)}(x,y) = \sum_m \sum_n h_1(m-2x)h_1(n-2y) \cdot LL^{j+1}(m,n). \tag{46}$$

The subband expressions listed in Equation 43 through to Equations 46 contain the coefficients which would appear the same if LL^{j+1} is circularly shifted by $\{0,2,4,6,\cdots,s\}$ rows and $\{0,2,4,6,\cdots,s\}$ columns, where s is the number of row and column coefficients in each of the subbands for the level $j+1$.

The subband coefficients which are the response to a shift of (0,1) in the previous level's coefficients may be computed by

$$LL^j_{(0,1)}(x,y) = \sum_m \sum_n h_o(m-2x)h_o(n-2y) \cdot LL^{j+1}(m,n-1), \tag{47}$$

$$LH^j_{(0,1)}(x,y) = \sum_m \sum_n h_1(m-2x)h_o(n-2y) \cdot LL^{j+1}(m,n-1), \tag{48}$$

$$HL^j_{(0,1)}(x,y) = \sum_m \sum_n h_o(m-2x)h_1(n-2y) \cdot LL^{j+1}(m,n-1), \tag{49}$$

$$HH^j_{(0,1)}(x,y) = \sum_m \sum_n h_1(m-2x)h_1(n-2y) \cdot LL^{j+1}(m,n-1), \tag{50}$$

which contain all the coefficients for $\{0,2,4,6,\cdots,s\}$ row shifts and $\{1,3,5,7,\cdots,s-1\}$ column shifts of LL_{j+1}. Similarly, for a shift of (1,0) in the input, the DWT coefficients may be found by

$$LL^j_{(1,0)}(x,y) = \sum_m \sum_n h_o(m-2x)h_o(n-2y) \cdot LL^{j+1}(m-1,n), \tag{51}$$

$$LH^j_{(1,0)}(x,y) = \sum_m \sum_n h_1(m-2x)h_o(n-2y) \cdot LL^{j+1}(m-1,n), \tag{52}$$

$$HL^{j}_{(1,0)}(x,y) = \sum_m \sum_n h_o(m-2x)h_1(n-2y) \cdot LL^{j+1}(m-1,n), \tag{53}$$

$$HH^{j}_{(1,0)}(x,y) = \sum_m \sum_n h_1(m-2x)h_1(n-2y) \cdot LL^{j+1}(m-1,n), \tag{54}$$

which contain all the coefficients if the previous levels' coefficients LL_{j+1} are shifted by $\{1,3,5,7,\cdots,s-1\}$ rows and $\{0,2,4,6,\cdots,s\}$ columns. For an input shift of (1,1), the subbands may be computed by

$$LL^{j}_{(1,1)}(x,y) = \sum_m \sum_n h_o(m-2x)h_o(n-2y) \cdot LL^{j+1}(m-1,n-1), \tag{55}$$

$$LH^{j}_{(1,1)}(x,y) = \sum_m \sum_n h_1(m-2x)h_o(n-2y) \cdot LL^{j+1}(m-1,n-1), \tag{56}$$

$$HL^{j}_{(1,1)}(x,y) = \sum_m \sum_n h_o(m-2x)h_1(n-2y) \cdot LL^{j+1}(m-1,n-1), \tag{57}$$

$$HH^{j}_{(1,1)}(x,y) = \sum_m \sum_n h_1(m-2x)h_1(n-2y) \cdot LL^{j+1}(m-1,n-1). \tag{58}$$

Similarly, these subband coefficients account for all DWT representations, which correspond to $\{1,3,5,7,\cdots,s-1\}$ row shifts and $\{1,3,5,7,\cdots,s-1\}$ column shifts of the input subband LL_{j+1}.

Performing a full decomposition will result in a tree which contains the DWT coefficients for all N^2 circular translates of an $N \times N$ image. At each level of decomposition, the LL band is shifted four times, and for each shift $(0,0)$, $(0,1)$, $(1,0)$, $(1,1)$, four new sets of subbands are generated. The decomposition tree is shown in Figure 13 and each circular node corresponds to only three subband images: HH, LH and HL, since at each level the LL band is shifted and then further decomposed. The number of coefficients in each node (per decomposition level) remains constant at $3N^2$, and a complete decomposition tree will have $N^2(3log_2N+1)$ elements Liang & Parks (1994). To compute the DWT for all N^2 translates of the image costs $O(N^2log_2N)$, due to the periodicity of the rate change operators Liang & Parks (1998).

To achieve shift-invariance, a subset of the wavelet coeffieints in the Tree of Figur e13 must be chose in a consistent manner. To do this, metrics can be computed from the tree. This requires an organized way to address each of the coefficients. A proper addressing scheme will help to find the wavelet transform for a particular translate (m,n), where m is the row shift and n is the column translate of the input image.

For a path in the tree, which originates from the root, terminates at a leaf node and corresponds to the translate (m,n), an expression may be developed which considers all row shifts and all column shifts as binary vectors, where each vector entry can be either 0 or 1. Therefore, the binary expansions may be rewritten as

$$m = \sum_{i=1}^{log_2N} a_i 2^{i-1}, \tag{59}$$

$$n = \sum_{i=1}^{log_2N} b_i 2^{i-1}, \tag{60}$$

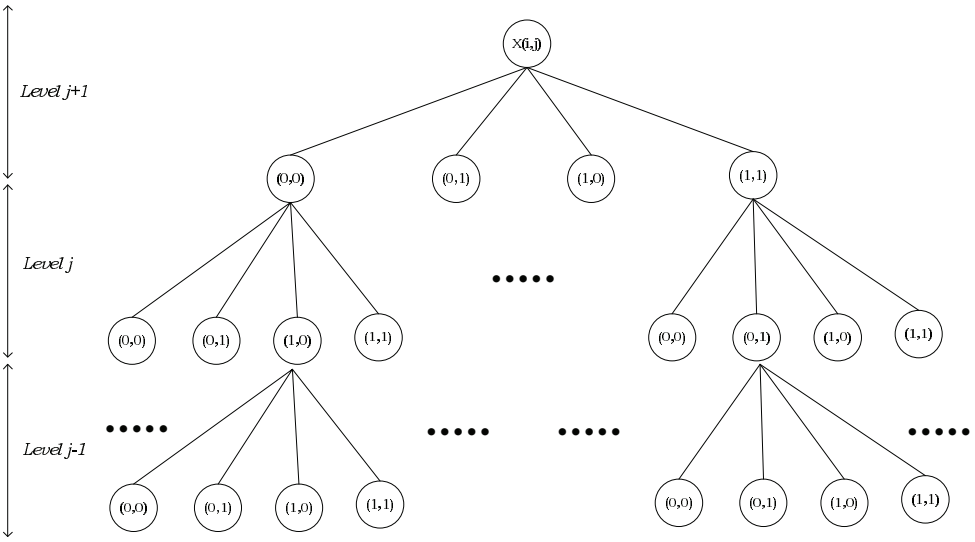

Fig. 13. Shift-invariant DWT decomposition tree for three decomposition levels.

where a_i and b_i correspond to the binary symbol which represents the row and column shift at decomposition level i, respectively. In order to find the three subimages (HL, HH and LH) which correspond to the translate (m, n) in the K^{th} decomposition level in the tree, it is necessary to find the S^{th} node which corresponds to this shift, as shown below

$$S = 2 \cdot \sum_{i=1}^{K} a_i 4^{K-i} + \sum_{i=1}^{K} b_i 4^{K-i}. \tag{61}$$

After the three subimages are located within the tree, to ensure that they correspond to the translate of the input by (m, n), these three images (HH, LH, HL) must be shifted by $(\text{xShift}, \text{yShift})$

$$\text{xShift} = \sum_{i=K+1}^{log_2 N} a_i 2^{i-K-1}, \tag{62}$$

$$\text{yShift} = \sum_{i=K+1}^{log_2 N} b_i 2^{i-K-1}. \tag{63}$$

This scheme allows us to address the wavelet coefficients that correspond to a particular shift of the input. The following section, which focuses on Coifmen and Wickenhauser's best basis selection technique Coifman & Wickerhauser (1992), is focused on a method to select a consistent set of wavelet coefficients which are independent of the input translation. Since the same coefficients are selected every time the algorithm is run, regardless of any initial offset, shift-invariance is achieved.

5.2 Best basis paradigm

Coifmen and Wickerhauser defined a method to choose a set of basis functions, based on the minimization of a cost function $\mathcal{J}$ Coifman & Wickerhauser (1992). The cost function $\mathcal{J}$ is often called an "information cost" and it evaluates and compares the efficiency of many basis sets Coifman & Saito (1995). Although there are many choices for cost functions, an additive information cost is preferred so that a fast-divide and conquer tree search algorithm may be used to find the best set of wavelet coefficients Liang & Parks (1994). A cost function $\mathcal{J}$ is additive if it maps a sequence $\{x_i\}$ to $\mathbf{R}$ while ensuring that the following properties are always true:

$$\mathcal{J}(0) = 0, \tag{64}$$

$$\mathcal{J}(\{x_i\}) = \sum_i \mathcal{J}(x_i). \tag{65}$$

To choose a consistent set of wavelet coefficients, an entropy cost function $\mathcal{J}$ is used for best basis determination. Entropy gives insight about the uniformity of the coefficients' representation (maximum energy compaction), which may be used for texture analysis. Furthermore, entropy is beneficial since it can achieve additivity Coifman & Saito (1995). Shown below is the expression of entropy which is minimized:

$$h_r(x) = \sum_i |x_i|^r log|x_i|^r, \tag{66}$$

where r is usually set to 1 or 2.

To choose the best basis representation, we begin at the bottom of the decomposition tree (see

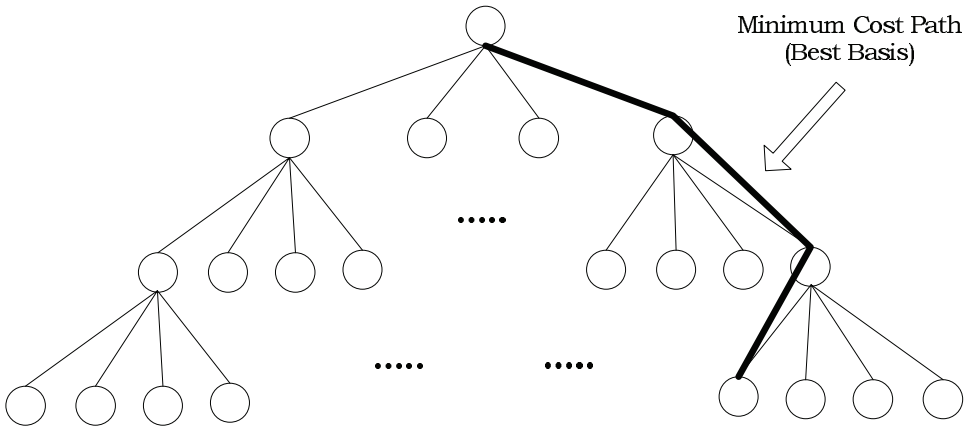

Fig. 14. Best basis selection corresponding to the minimum cost path.

Figures 13 and 14) and work upwards. For each parent node, there are four child nodes, each containing the high frequency subbands of a particular translate. The cost $\mathcal{A}$ of a particular translate $(p,q) \in \{(0,0),(0,1),(1,0)(1,1)\}$ at some node is computed by summing the cost of the individual high frequency subbands for that shift:

$$\mathcal{A}_{(p,q)} = \mathcal{J}(LH_{(p,q)}) + \mathcal{J}(HL_{(p,q)}) + \mathcal{J}(HH_{(p,q)}). \tag{67}$$

To minimize entropy, the node with the minimum cost for each parent would be selected at every decomposition level. The path which is connected from the root of the tree all the way down to the leaves, is selected as the the minimum cost path, as shown in Figure 14. This path corresponds to the DWT of a particular translate and is chosen as the consistent set of basis functions in order to achieve shift-invariance.

6. Multiscale texture analysis

Now that a transformation has been employed which can robustly localize the scale-frequency properties of the textured elements in the medical images, it is important to design an analysis scheme which can quantify such textured events. To do this, this work proposes the use of a multiscale texture analysis scheme. Extracting features from the wavelet domain will result in a *localized* texture description, since the DWT has excellent space-localization properties.
To extract texture-based features, normalized graylevel cooccurrence matrices (GCMs) are employed in the *wavelet domain*. GCMs count the the number of two-pixel combinations and are typically normalized so that the matrix may be treated as a probability density function (PDF). In the wavelet domain, each entry of the normalized GCM is represented as

$$p\left(l_1, l_2, d, \theta\right) = \frac{P(l_1, l_2)}{\sum_{l_1=0}^{L-1} \sum_{l_2=0}^{L-1} P(l_1, l_2)}, \tag{68}$$

where $P(l_1, l_2)$ is the number of occurrences of wavelet coefficients l_1 and l_2 at a distance d and angle θ. Additionally, $\sum_{l_1} \sum_{l_2} P(l_1, l_2)$ is the normalizing factor and L is the maximum number of graylevels in the image. Note that these matrices are symmetric: $p\left(l_1, l_2, d, \theta\right) = p\left(l_2, l_1, d, \theta\right)$.
In the wavelet domain, GCMs are computed for adjacent wavelet coefficients. Such a second order PDF examines the correlation or relationship of wavelet coefficients to one another. Since texture is captured by the multiresolutional analysis scheme (large valued coefficients for edgy regions in a variety of scales), wavelet-based GCMs describe the statistical nature of the texture in our image. As texture is localized in a variety of directions, the GCMs are computed for each scale j at several angles θ. They are computed at multiple angles and scales since orientation and scale is play an important role in texture discrimination.
In the wavelet domain, each subband isolates different frequency components - the HL band isolates horizontal edge components, the LH subband isolates horizontal edges, the HH band captures the diagonal high frequency components and LL band contains the lowpass filtered version of the original. Consequently, to capture these oriented texture components, the GCM is computed at 0° in the HL band, 90° in the LH subband, 45° and 135° in the HH band and 0°, 45°, 90° and 135° in the LL band to account for any directional elements which may still may be present in the low frequency subband. Moreover, $d = 1$ for fine texture analysis.
From these GCMs, homogeneity h and entropy e are computed for each decomposition level using Equation 69 and 70. Homogeneity (h) describes how uniform the texture is and entropy (e) is a measure of nonuniformity or the complexity of the texture.

$$h(\theta) = \sum_{l_1=0}^{L-1} \sum_{l_2=0}^{L-1} p^2\left(l_1, l_2, d, \theta\right) \tag{69}$$

$$e(\theta) = -\sum_{l_1=0}^{L-1}\sum_{l_2=0}^{L-1} p\,(l_1, l_2, d, \theta)\log_2(p\,(l_1, l_2, d, \theta)) \tag{70}$$

These features describe the relative uniformity of textured elements in the wavelet domain (which are localized with good results due to the space-frequency resolution of the bases). Recall that abnormal and normal cases were shown to have significant differences in terms of their texture uniformity (normal images contained smooth texture while abnormal images were heterogeneous). Therefore, such a scheme, which captures textural differences between images, should be able to arrive at high classification results for CAD (i.e. the classification of normal and abnormal retinal and small bowel images, and differentiation between malignant and benign lesions in the mammogram images).

For each decomposition level j, more than one directional feature is generated for the HH and LL subbands. The features in these subbands are averaged so that: features are not biased to a particular orientation of texture and the representation will offer some rotational invariance. The features generated in these subbands (HH and LL) are shown below (note that the quantity in parenthesis is the angle at which the GCM was computed):

$$\begin{aligned}
\widetilde{h}^{j}_{\mathrm{HH}} &= \frac{1}{2}\left(h^{j}_{\mathrm{HH}}(45^\circ) + h^{j}_{\mathrm{HH}}(135^\circ)\right),\\
\widetilde{e}^{j}_{\mathrm{HH}} &= \frac{1}{2}\left(e^{j}_{\mathrm{HH}}(45^\circ) + e^{j}_{\mathrm{HH}}(135^\circ)\right),\\
\widetilde{h}^{j}_{\mathrm{LL}} &= \frac{1}{4}\left(h^{j}_{\mathrm{LL}}(0^\circ) + h^{j}_{\mathrm{LL}}(45^\circ) + h^{j}_{\mathrm{LL}}(90^\circ) + h^{j}_{\mathrm{LL}}(135^\circ)\right),\\
\widetilde{e}^{j}_{\mathrm{LL}} &= \frac{1}{4}\left(e^{j}_{\mathrm{LL}}(0^\circ) + e^{j}_{\mathrm{LL}}(45^\circ) + e^{j}_{\mathrm{LL}}(90^\circ) + e^{j}_{\mathrm{LL}}(135^\circ)\right).
\end{aligned}$$

As a result, for each decomposition level j, two feature sets are generated:

$$F^{j}_{h} = \left[h^{j}_{\mathrm{HL}}(0^\circ),\, h^{j}_{\mathrm{LH}}(90^\circ),\, \widetilde{h}^{j}_{\mathrm{HH}},\, \widetilde{h}^{j}_{\mathrm{LL}}\right], \tag{71}$$

$$F^{j}_{e} = \left[e^{j}_{\mathrm{HL}}(0^\circ),\, e^{j}_{\mathrm{LH}}(90^\circ),\, \widetilde{e}^{j}_{\mathrm{HH}},\, \widetilde{e}^{j}_{\mathrm{LL}}\right], \tag{72}$$

where $\widetilde{h}^{j}_{\mathrm{HH}}$, $\widetilde{h}^{j}_{\mathrm{LL}}$, $\widetilde{e}^{j}_{\mathrm{HH}}$ and $\widetilde{e}^{j}_{\mathrm{LL}}$ are the averaged texture descriptions from the HH and LL band previously described and $h^{j}_{\mathrm{HL}}(0^\circ)$, $e^{j}_{\mathrm{HL}}(0^\circ)$, $h^{j}_{\mathrm{LH}}(90^\circ)$ and $e^{j}_{\mathrm{LH}}(90^\circ)$ are homogeneity and entropy texture measures extracted from the HL and LH bands. Since directional GCMs are used to compute the features in each subband, the final feature representation is not biased for a particular orientation of texture and may provide a semi-rotational invariant representation.

7. Classification

After the multiscale texture features have been extracted, a pattern recognition technique is needed classify the features. A large number of test samples are required to evaluate a classifier with low error (misclassification) rates since a small database will cause the parameters of the classifiers to be estimated with low accuracy. This requires the biomedical image database to be large, which may not always be the case since acquiring the images for specific diseases can take years. If the extracted features are strong (i.e. the features are mapped into nonoverlapping clusters in the feature space) the use of a simple (linear)

classification scheme will be sufficient in discriminating between classes. The desire is to test the robustness of the found feature set to the variations found in image databases. This can be easily determined by a linear classifier.
To satisfy the above criteria, linear discriminant analysis (LDA) will be the classification scheme used in conjunction with the *Leave One Out Method* (LOOM). In LOOM, one sample is removed from the whole set and the discriminant functions are derived from the remaining $N-1$ data samples and the left out sample is classified. This procedure is completed for all N samples. LOOM will allow the classifier parameters to be estimated with least bias Fukunaga & Hayes (1989).

8. Results

The objective of the proposed system is to automatically classify pathologies based on their textural characteristics. Such a system examines texture in accordance to the human texture perception model and is shown in Figure 15.

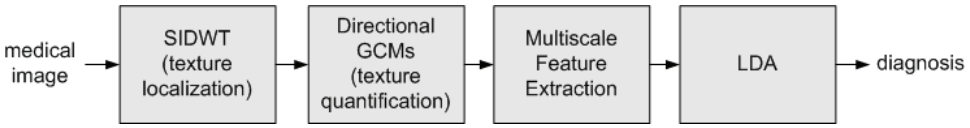

Fig. 15. System block diagram for the classification of medical images.

The classification performance of the proposed system is evaluated for three types of imagery:

1. **Small Bowel Images:** 41 normal and 34 abnormal (submucosal masses, lymphomas, jejunal carcinomas, multifocal carcinomas, polypoid masses, Kaposi's sarcomas, etc.),
2. **Retinal Images:** 38 normal, 48 abnormal (exudates, large drusens, fine drusens, choroidal neovascularization, central vein and artery occlusion, arteriosclerotic retinopathy, histoplasmosis, hemi-central retinal vein occlusion and more),
3. **Mammograms:** 35 benign and 19 malignant lesions.

The image specifications are shown in Table 3 and example images were shown earlier in Section 2. Only the luminance plane was utilized for the colour images (retinal and small bowel), in order to examine the performance of grayscale-based features. Furthermore, in the mammogram images, only a 128×128 region of interest is analyzed which contains the candidate lesion (to strictly analyze the textural properties of the lesions). Features were

Small Bowel	**Retinal**	**Mammogram**
Colour (24 bpp)	Colour (24 bpp)	Grayscale (8 bpp)
Lossy (.jpeg)	Lossy (.jpeg)	Raw (.pgm)
256×256	700×605	1024×1024

Table 3. Medical image specifications

extracted from the higher levels of decomposition (the last three levels were not included as further decomposition levels contain subbands of 8×8 or smaller, resulting in skewed probability distribution (GCM) estimates). Therefore, the extracted features are F_e^j and F_h^j for $j = \{1, 2, \cdots, J\}$, where J is the number of decomposition levels minus three.

In order to find the optimal sub-feature set, an exhaustive search was performed (i.e. all possible feature combinations were tested using the proposed classification scheme). For the small bowel images, the optimal classification performance was achieved by combining homogeneity features from the first and third decomposition levels with entropy from the first decomposition level (see Khademi & Krishnan (2006) for more details):

$$F_h^1 = \left[h_{\mathrm{HL}}^1(0^\circ),\, h_{\mathrm{LH}}^1(90^\circ),\, \widetilde{h}_{\mathrm{HH}}^1,\, \widetilde{h}_{\mathrm{LL}}^1\right], \tag{73}$$

$$F_h^3 = \left[h_{\mathrm{HL}}^3(0^\circ),\, h_{\mathrm{LH}}^3(90^\circ),\, \widetilde{h}_{\mathrm{HH}}^3,\, \widetilde{h}_{\mathrm{LL}}^3\right], \tag{74}$$

$$F_e^1 = \left[e_{\mathrm{HL}}^1(0^\circ),\, e_{\mathrm{LH}}^1(90^\circ),\, \widetilde{e}_{\mathrm{HH}}^1,\, \widetilde{e}_{\mathrm{LL}}^1,\right]. \tag{75}$$

The optimal feature set for the retinal images were found to be homogeneity features from the fourth decomposition level with entropy from the first, second and fourth decomposition levels (see Khademi & Krishnan (2007) for more details):

$$F_h^4 = \left[h_{\mathrm{HL}}^4(0^\circ),\, h_{\mathrm{LH}}^4(90^\circ),\, \widetilde{h}_{\mathrm{HH}}^4,\, \widetilde{h}_{\mathrm{LL}}^4\right], \tag{76}$$

$$F_e^1 = \left[e_{\mathrm{HL}}^1(0^\circ),\, e_{\mathrm{LH}}^1(90^\circ),\, \widetilde{e}_{\mathrm{HH}}^1,\, \widetilde{e}_{\mathrm{LL}}^1\right], \tag{77}$$

$$F_e^2 = \left[e_{\mathrm{HL}}^2(0^\circ),\, e_{\mathrm{LH}}^2(90^\circ),\, \widetilde{e}_{\mathrm{HH}}^2,\, \widetilde{e}_{\mathrm{LL}}^2\right], \tag{78}$$

$$F_e^4 = \left[e_{\mathrm{HL}}^4(0^\circ),\, e_{\mathrm{LH}}^4(90^\circ),\, \widetilde{e}_{\mathrm{HH}}^4,\, \widetilde{e}_{\mathrm{LL}}^4,\right]. \tag{79}$$

Lastly, the optimal feature set for the mammographic lesions were found by combining homogeneity features from the second decomposition level with entropy from the fourth decomposition level:

$$F_h^2 = \left[h_{\mathrm{HL}}^2(0^\circ),\, h_{\mathrm{LH}}^2(90^\circ),\, \widetilde{h}_{\mathrm{HH}}^2,\, \widetilde{h}_{\mathrm{LL}}^2\right], \tag{80}$$

$$F_e^4 = \left[e_{\mathrm{HL}}^4(0^\circ),\, e_{\mathrm{LH}}^4(90^\circ),\, \widetilde{e}_{\mathrm{HH}}^4,\, \widetilde{e}_{\mathrm{LL}}^4\cdot\right]. \tag{81}$$

Using the above features in conjunction with LOOM and LDA, the classification results for the small bowel, retinal and mammogram images are shown as a confusion matrix in Table 4, Table 5 and Table 6, respectively.

	Normal	**Abnormal**
Normal	35 (85%)	6 (15%)
Abnormal	5 (15%)	29 (85%)

Table 4. Results for small bowel image classification.

	Normal	**Abnormal**
Normal	30 (79%)	8 (21%)
Abnormal	7 (14.6%)	41 (85.4%)

Table 5. Results for retinal image classification.

	Benign	Malignant
Benign	28 (80%)	7 (20%)
Malignant	8 (42%)	11 (58%)

Table 6. Results for mammogram ROI classification.

9. Conclusions

A total of 75 abnormal and normal bowel images were correctly classified at an average rate of 85%, 86 retinal images had an average classification accuracy of 82.2% and the mammogram lesions (54) were classified correctly 69% on average. The classification results are quite high, considering that the system wasn't tuned for a specific modality. The system performed well, even though: (1) pathologies came in various orientations, (2) pathologies arose in a variety of locations in the image, (3) the masses and lesions were of various sizes and shapes and (4) there was no restriction on the type of pathology for the retinal and small bowel images. Accounting for all these scenarios in one algorithm was a major challenge while designing such a unified framework for computer-aided diagnosis.

Although the classification results are high, any misclassification can be accounted to cases where there is a lack of statistical differentiation between the texture uniformity of the pathologies. Additionally, normal tissue can sometimes assume the properties of abnormal regions; for example, consider a normal small bowel image which has more than the average amount of folds. This may be characterized as non-uniform texture and consequently would be misclassified. In a normal retinal image, if the patient has more than the average number of vessels in their eye, this may be detected as oriented or heterogeneous texture and could be misclassified. Moreover, when considering the mammogram lesions, the normal breast parenchyma is overlapping with the lesions and also assumes some textural properties itself. In order to improve the performance of the mammogram lesions, a segmentation step could be applied prior to feature extraction.

Another important consideration arises from the database sizes. As was stated in Section 7, the number of images used for classification can determine the accuracy of the estimated classifier parameters. Since only a modest number of images were used, misclassification could result due to the lack of proper estimation of the classifiers parameters (although the scheme tried to combat this with LOOM). This could be the case for the mammogram lesions especially, since the number of benign lesions outnumbered the malignant lesions by almost double - this could have caused difficulties in classification parameter accuracy. Additionally, finding the right trade off between number of features and database size is an ongoing research topic and has yet to be perfectly defined Fukunaga & Hayes (1989).

The overall success of the system is a result of the design of the algorithm, which aimed to account for all the pathological scenarios previously described. Firstly, the utilization of the DWT was important to gain a space-localized representation of the images' elementary texture units (textons), which is in accordance to human texture perception. Secondly, the choice of wavelet-based statistical texture measures (entropy and homogeneity) was critical in quantifying the localized texture properties of the images (which provided discrimination between normal and other pathological cases). Utilization of the SIDWT allowed for the extraction of consistent (i.e. shift-invariant) features. Furthermore, due to the scale-invariant basis functions of the DWT, pathologies of varying sizes were captured within one transformation (i.e. the features were scale-invariant).

By design, the system is relatively robust to pathologies which occurred in various

orientations. Features were collected at various angles (0°, 45°, 90°, 135°) in the respective subbands in order to describe the texture elements, regardless of their orientation. The feature set thus offered a semi-rotational invariant representation which could account for oriented textural properties (of pathology).

A last point for discussion is the fact that features were successfully extracted from the compressed domain in the retinal and small bowel images. Since many forms of multi-media are being stored in lossy formats, it is important that classification systems may also be successful when utilized in the compressed domain.

A generalized framework for computer-aided diagnosis was designed in accordance to the human texture perception model. The unified feature extraction and classification scheme utilized the DWT and textural features were extracted from the wavelet domain for a localized description of the relative homogeneity of the images. To ensure the DWT representation was suitable for the consistent extraction of features, a shift-invariant discrete wavelet transform (SIDWT) was computed. To combat the small database size, a small number of features and LDA classification were used in conjunction with the LOOM to gain a more accurate approximation of the classifier's parameters.

A total of 75 abnormal and normal bowel images were correctly classified at an average rate of 85%, 86 retinal images had an average classification accuracy of 82.2% and the mammogram lesions (54) were classified correctly 69% on average. The success of the system can be accounted to the semi-rotational invariant, scale-invariant and shift-invariant features, which permitted the extraction of discriminating features regardless of the location, shape, size or orientation of the pathologies.

10. References

Adams, M. D. & Ward, R. K. (2003). Symmetric-extension-compatible reversible integer-to-integer wavelet transforms, *IEEE Transactions on Signal Processing* 51(10): 2624–2636.

Armstrong, A. & Jiang, J. (2001). An efficient image indexing algorithm in JPEG compressed domain, International Conference on Image Processing, pp. 350–351.

Beylkin, G. (1992). On the representation of operators in bases of compactly supported wavelets, *SIAM Journal of Numerical Analysis* 29: 1716–1740.

Bradley, A. (2003). Shift-invariance in the discrete wavelet transform, Digital Image Computing: Techniques and Applications, pp. 29 – 38.

Brandon, L. & Hoover, A. (2003). Drusen detection in a retinal image using multi-level analysis, Vol. 1, MICCAI, pp. 618–625.

Burrus, C., Gopinath, R. & Guo, H. (1998). *Introduction to Wavelets and Wavelet Transforms - A Primer*, Prentice Hall International, Inc., Houston, Texas.

Chang, S. (1995). Compressed-domain techniques for image/video indexing and manipulation, Vol. 1, International Conference on Image Processing, pp. 314 – 317.

Cheng, H. D., Shi, X. J., Min, R., Hu, L. M., Cai, X. P. & Du, H. N. (2006). Approaches for automated detection and classification of masses in mammograms, *Pattern Recognition* 39(4): 646–668.

Chiu, C., Wong, H. & Ip, H. H. S. (2004). Compressed domain feature transformation using evolutionary strategies for image classification, Vol. 1, International Conference on Image Processing, pp. 429 – 432.

Cohen, I., Raz, S. & Malah, D. (1997). Orthonormal shift invariant wavelet packet decomposition and representation, *Elsevier: Signal Processing* 57: 251–270.

Coifman, R. R. & Saito, N. (1995). Local discriminant bases and their applications, *Journal of Mathematical Imaging and Vision* 5: 337–358.

Coifman, R. R. & Wickerhauser, M. V. (1992). Entropy-based algorithms for best basis selection, *IEEE Transactions on Information Theory* 38: 713 – 718.

Denecker, K., Assche, S. V., Phillips, W. & Lemahieu, I. (1997). State of the art concerning lossless medical image coding, PRORISC IEEE Benelux Workshop on Circuits, Systems and Signal Processing, pp. 129–136.

Fernández, G., Periaswamy, S. & Sweldens, W. (1996). LIFTPACK: A software package for wavelet transforms using lifting, Proceedings of the SPIE - Wavelet Applications in Signal and Image Processing IV, pp. 396–408.

Ferreira, C. B. R. & Borges, D. L. (2001). Automated mammogram classification using a multiresolution pattern recognition approach, Proceedings of XIV Brazilian Symposium on Computer Graphics and Image Processing, pp. 76 – 83.

Fukunaga, K. & Hayes, R. R. (1989). Effects of sample size in classifier design, *IEEE Transactions on Pattern Analysis and Machine Intelligence* 11(8): 873 – 885.

Given Imaging Ltd. (2006a). *Patient Brochure*, World Wide Web. http://www.givenimaging.com/Cultures /en-US /Given /English/Professionals/.

Given Imaging Ltd. (2006b). *Patient Information Guide*, World Wide Web. http://www.givenimaging.com/Cultures/en-US/Given/English/Patients/.

Given Imaging Ltd. (2006c). *PillCam™ SB Capsule Endoscopy - Product Information Guide*, World Wide Web. http://www.givenimaging.com/Cultures /en-US /Given/English /Products/CapsuleEndoscopy/.

Goldbaum, M. (2002). *STARE - STructured Analysis of the Retina*, World Wide Web. http://www.parl.clemson.edu/stare/.

Guliato, D., Rangayyan, R. M., de Carvalho, J. D. & Santiago, S. A. (2007). Polygonal modeling of contours of breast tumors with the preservation of spicules, *IEEE Trans. on Biomedical Engineering* .

Haijiang, T., Sei-Ichiro, K., Kazuyuki, T. & Masa-Aki, K. (2004). Lossless image compression via multi-scanning and adaptive linear prediction, Vol. 1, The 2004 IEEE Asia-Pacific Conference on Circuits and Systems, pp. 81–84.

Julesz, B. (1981). Textons, the elements of texture perception, and their interactions, *Nature* 290(5802): 91–97.

Khademi, A. (2006). *Multiresolutional analysis for classi□cation and compression of medical images*, Master's thesis. Ryerson University, Canada.

Khademi, A. & Krishnan, S. (2006). Multiresolution analysis and classification of small bowel medical images, Proceedings of IEEE Engineering in Medicine and Biology, pp. 4524 – 4527.

Khademi, A. & Krishnan, S. (2007). Shift-invariant discrete wavelet transform analysis for retinal image classification, *Journal of Medical and Biological Engineering and Computing* pp. 1–12. in press - online first.

Khademi, A. & Krishnan, S. (2008). Medical image texture analysis: A case study with small bowel, retinal and mammogram images, IEEE CCECE, pp. 1–6.

Kim, B., Park, S., Jee, C. & Yoon, S. (2005). An earthworm-like locomotive mechanism for capsule endoscopes, IEEE/RSJ International Conference on Intelligent Robots and Systems, pp. 2997 – 3002.

Lawson, S. & Zhu, J. (2004). Image compression using wavelets and JPEG2000: a tutorial, *Electronics & Communication Engineering Journal* 14(3): 112–121.

Lee, J. K. T. (2007). Interpretation accuracy and pertinence, *American College of Radiology* 4: 162–165.

Leung, M. M. & Peterson, A. M. (1992). Scale and rotation invariant texture classification, Vol. 1, Conference Record of The Twenty-Sixth Asilomar Conference on Signals, Systems and Computers, pp. 461 – 465.

Liang, J. & Parks, T. W. (1994). A two-dimensional translation invariant wavelet representation and its applications, Vol. 1, IEEE International Conference on Image Processing, pp. 66 – 70.

Liang, J. & Parks, T. W. (1996). Translation invariant wavelet transforms with symmetric extensions, *IEEE Digital Signal Processing Workshop* pp. 69–72.

Liang, J. & Parks, T. W. (1998). Image coding using translation invariant wavelet transforms with symmetric extensions, *IEEE Transactions on Image Processing* 7: 762 – 769.

Mallat, S. (1989). A theory for multiresolution signal decomposition: The wavelet representation, *IEEE Transactions on Pattern Analysis and Machine Intelligence* 11(7): 674–693.

Mallat, S. (1998). *Wavelet Tour of Signal Processing*, Academic Press, USA.

Mallat, S. G. & Zhang, Z. (1993). Matching pursuits with time-frequency dictionaries, *IEEE Transactions on Signal Processing* 41: 3397 – 3415.

Maragos, P., Mersereau, R. & Shafer, R. (1984). Two-dimensional linear prediction and its application to adaptive predictive coding of images, *IEEE Transactions on Acoustics, Speech, and Signal Processing* 32: 1213–1229.

Marcellin, M. W., Bilgin, A., Gormish, M. J. & Boliek, M. P. (2000). An overview of JPEG-2000, *Proceedings of the IEEE Data Compression Conference*, IEEE Computer Society, p. 523.

Mudigonda, N., Rangayyan, R. & Desautels, J. (2000). Gradient and texture analysis for the classification of mammographic masses, *IEEE Transactions on Medical Imaging* 19(10): 1032–1043.

Rangayyan, R. (2005). *Biomedical Image Analysis*, CRC Press LLC, United States of America.

Rangayyan, R. M., El-Faramawy, N. M., Desautels, J. E. L. & Alim, O. (1997). Measures of acutance and shape for classification of breast tumors, *IEEE Transactions on Medical Imaging* 16(6): 799 – 810.

Ross, S. (2003). *Introduction to Probability Models*, Academic Press, USA, California.

Sato, T., Abe, N., Tanaka, K., Kinoshita, Y. & He, S. (2006). Toward developing multiple organs and diseases diagnosing intellectual system referring to knowledge base and ct images, IEEE Symposium on Computer-Based Medical System, pp. 1–6.

Simoncelli, E. P., Freeman, W. T., Adelson, E. H. & Heeger, D. J. (1992). Shiftable multiscale transforms, *IEEE Transactions on Information Theory* 38: 587 – 607.

Sinthanayothin, C., Kongbunkiat, V., Phoojaruenchanachai, S. & Singalavanija, A. (2003). Automated screening system for diabetic retinopathy, Vol. 2, Proceedings of the 3rd International Symposium on Image and Signal Processing and Analysis, pp. 915 – 920.

Sweldens, W. (1995). The lifting scheme: A new philosophy in biorthogonal wavelet constructions, *in* A. F. Laine & M. Unser (eds), *Wavelet Applications in Signal and Image Processing III*, Proc. SPIE∼2569, pp. 68–79.

Sweldens, W. (1996). Wavelets and the lifting scheme: A 5 minute tour, *Z. Angew. Math. Mech.* 76 (Suppl. 2): 41–44.

Umbaugh, S. E., Wei, Y. S. & Zuke, M. (1997). Feature extraction in image analysis. a program for facilitating data reduction in medical image classification, *IEEE Engineering in Medicine and Biology Magazine* 16: 62–73.

Vetterli, M. & Herley, C. (1992). Wavelets and filter banks: theory and design, *IEEE Transactions on Signal Processing* 40(9): 2207 – 2232.

Voulgaris, G. & Jiang, J. (2001). Texture-based image retrieval in wavelets compressed domain, Vol. 2, International Conference on Image Processing, pp. 125 – 128.

Wang, H., Hsu, W., Goh, K. & Lee, M. (2000). An effective approach to detect lesions in color retinal images, Vol. 2, Proceedings of IEEE Conference on Computer Vision and Pattern Recognition, pp. 181–186.

Wang, T. C. & Karayiannis, N. B. (1998). Detection of microcalcifications in digital mammograms using wavelets, *IEEE Transactions on Medical Imaging* 17: 498 – 509.

Wei, D., Chan, H. P., Helvie, M. A., Sahiner, B., Petrick, N., Adler, D. D. & Goodsitt, M. M. (1995). Classification of mass and normal breast tissue on digital mammograms: multiresolution texture analysis, *Medical Physics* 22(9): 1501–1513.

Xiong, Z. & Huang, T. S. (2002). Wavelet-based texture features can be extracted efficiently from compressed-domain for JPEG2000 coded images, Vol. 1, International Conference on Image Processing, pp. 481–484.

Zhang, H. & Fritts, J. (2004). An overview of JPEG-2000, Proceedings of SPIE - Visual Communications and Image Processing, pp. 1333–1340.

Zhang, Y. & Zeytinoglu, M. (1999). Improved lifting scheme for block subband coding, IEEE Pacific Rim Conference on Communications, Computers and Signal Processing, pp. 487 – 490.

Part 4

Industrial Applications

11

Discrete Wavelet Transforms for Synchronization of Power Converters Connected to Electrical Grids

Alberto Pigazo and Víctor M. Moreno
University of Cantabria
Spain

1. Introduction

Electronic power converters connected to electrical grids allow industrial processes, traction applications and home appliances to be improved by controlling the energy flow depending on the operation conditions of both the electrical load and the grid. This is the case of variable frequency drives, which can be found in pump drives or ship propulsion systems (Bose, 2009) maintaining the electrical machine in the required operation state while ensuring a proper current consumption from the electrical grid. Recent researching and developing efforts on grid-connected power converters are due to the integration of renewable energy sources in electrical grids, which requires the implementation of new functionalities, such as grid support, while maintaining reduced current distortion levels and an optimal power extraction from the renewable energy source (Carrasco et al., 2006; Liserre et al., 2010).

In the most general case, a grid-connected power converter consists of power and control stages which ensures the appropriate energy management (Erickson & Maksimovic, 2001; Mohan et al., 2003). In the first one, electronic power devices, such as power diodes, thyristors, insulated gate bipolar transistors (IGBTs) or MOS-controlled thyristors (MCTs), and passive elements (inductances and capacitors) are found. The switching state of the power devices allows the voltage or/and current across the passive components to be controlled. Resistive behaviors must be minimized in order to avoid conduction power losses. The second stage, in case of controlled semiconductor devices, consists of a signal conditioning system and the required hardware for implementation of the converter controller (Bose, 2006).

Recent advances in field programmable gate arrays (FPGAs) and digital signal processors (DSPs) allow the complexity and functionalities of the controllers employed in power converters to be increased and improved (Bueno et al., 2009). In grid-connected power converters these functionalities include, in most cases, the synchronization with the electrical grid, the evaluation of the reference current amplitude at the grid-side and current control (Kazmierkowski et al., 2002). The amplitude and phase of the grid-side current depends on the reference current evaluation and the synchronization subsystems while the current controller ensures that the current waveform matches the reference one. The implementation of these subsystems depends on the application characteristics. Other functionalities, such as grid support (Ullah et al., 2009) or detection of the islanding condition (De Mango, Liserre & D'Aquila, 2006; De Mango, Liserre, D'Aquila & Pigazo, 2006), can be added if it is required.

These controller functionalities can be implemented by applying diverse approaches, such as digital signal processing techniques, i.e. Fourier Transforms (McGrath et al., 2005), Kalman

Filters (Moreno et al., 2007) or Discrete Wavelet Transforms (DWTs) (Pigazo et al., 2009). Frequency and time localization of wavelet analysis allow the performance of controllers in grid-connected power converters to be improved. This is the case of active power filters, where the compensation reference current can be evaluated by means of DWT (Driesen & Belmans, 2002), modulation techniques in controlled rectifiers (Saleh & Rahman, 2009) or the controller design process using averaging models of power converters (Gandelli et al., 2001).
This book chapter proposes to take advantage of DWTs' properties in order to improve the synchronization subsystem of controllers in grid-connected power converters. After a review of the state of art in wavelet analysis applied to power electronics, the main characteristics of controllers in grid-connected power converters are presented as well as the new approach for synchronization purposes. Results validating the proposal, considering diverse operation conditions, are shown.

2. Wavelet analysis applied to power converters

The wavelet analysis has been mainly applied to signal analysis and processing (i.e. identification and classification) in electrical power systems (voltage and current) during the last twenty years (Ribeiro, 1994; Robertson et al., 1994). The wavelet analysis was firstly applied to power system protection, power quality measurement, detection of power system transients, partial discharges, forecasting of electrical loads due to its its capability for fast and accurate identification of transients (Castro & Diaz, 2002). In recent years this signal processing technique has been also applied in order to control power electronic converters, such as dc-dc, inverters, rectifiers, active power filters and unified power quality conditioners (UPQCs). This chapter section shows some of these applications both to power systems and, more specifically, power converters.

2.1 Wavelet analysis in power systems

The power system protection can be improved by applying the wavelet analysis to activate the relays in case of power system transients. Time resolution capability of the wavelet analysis is employed in (Chaari et al., 1996) for detection of earth faults in case of a 20 kV resonant grounded network. High impedance faults identification and protection of transformers and generators by means of wavelets are also shown in (Solanki et al., 2001) and (Eren & Devaney, 2001) respectively. In this last case, the frequency resolution of wavelets allows the changes of the power signals' spectra to be measured in order to detect the degradation of the insulation and identify internal and external faults. Wavelets have been also employed for modeling of electrical machines in wind turbines and detection of turn-to-turn rotor faults (Dinkhauser & Fuchs, 2008).
The evaluation of the electrical power quality (PQ) can take advantage of wavelet analysis for detection and measurement of interferences, impulses, notches, glitches, interruptions, harmonics, flicker and other disturbances. In case of harmonic currents/voltages and voltage flicker the multiresolution analysis (MRA) using wavelet filter banks (Pham & Wong, 1999; Pham et al., 2000) and continuous wavelet transforms (Zhen et al., 2000) can be applied. The propagation of power system transients can be also analyzed by means of wavelets (Heydt & Galli, 1997; Wilkinson & Cox, 1996). The characteristics of partial discharges (short duration, high frequency and low amplitude) make it difficult to detect. Wavelet analysis allows partial discharges to be detected due to its time resolution, as it is shown in (Shim et al., 2000) in case of transformer windings and cables.

The efficient management of electrical power system requires a proper forecasting of electrical loads. The combination of wavelets and neural networks in (Huang & Yang, 2001; Yao et al., 2000) allows it by considering the current waveforms as a linear combination of different frequencies. The wavelet analysis can also be applied for measurement of the electrical active/reactive power and the root mean square (rms) value of line voltages and currents on a frequency band basis (Hamid & Kawasaki, 2001).

2.2 Wavelet analysis in controllers for power converters

Wavelets have been recently applied in power converters used in diverse applications. The covered functionalities include modeling of the power converter, its control and supervision tasks.

In order to obtain a more flexible model of a dc/dc power converter, wavelets are applied in (Ponci et al., 2009) for detection of the operation mode of the power converter, consisting on an extension of conventional analysis techniques based on state-space averaging. A model of a dc/ac converter based on wavelets is obtained in (Gandelli et al., 2002) in order to perform a detailed analysis and the optimization of the power converter.

Wavelet-based controllers have been also proposed in literature in order to improve the performance of the power converter. This is the case of (Hsu et al., 2008), where a wavelet-based neural network is employed in order to minimize the impact of input voltage and load resistance variations on a dc/dc converter. In (Saleh & Rahman, 2009) wavelets allow a new switching strategy to be developed in order to reduce the harmonic content of the output voltage in a ac/dc converter maintaining unity power factor. A three-phase induction generator (IG) system for stand-alone power systems is controlled by means of one ac/dc plus one dc/ac converter and applying a recurrent wavelet neural network (RWNN) controller with improved particle swarm optimization (IPSO) (Teng et al., 2009). The controllers in dc/ac converters can be optimized by applying wavelets, this is the case of (Mercorelli et al., 2004), where it is employed for optimization of the applied model predictive controller. The wavelet analysis is applied in (González et al., 2008) in order to evaluate the performance of the employed modulation technique, including the spectrum of the converter output voltage and its ripple. Controllers in multilevel converters can also take advantage of wavelets, as it is shown in (Iwaszkiewicz & Perz, 2007), in order to ensure a better and faster adaptation of their output voltage waveforms to sine waveforms and reduce the harmonic distortion of the output voltage at relatively low switching frequencies. High-level control functionalities, such as islanding detection or source impedance measurement, required in distributed generation systems connected to electrical grids can also obtain benefits from the wavelet analysis. The high frequency bands of voltage and current waveforms are evaluated in (Pigazo et al., 2009; 2007) in order to detect the islanding condition. The power system impedance can be measured in real-time by injecting a controlled disturbance into the electrical grid, the wavelet analysis allows an fast detection of faults (Sumner et al., 2006).The wavelets can be also applied for characterization of power converters' performance. In (Knezevic et al., 2000) the wavelet analysis is applied for measurement of transients caused by ac/dc converters.

3. Controllers in grid-connected power converters

The general structure of a single-phase grid-connected power converter, including both power and control stages, is shown in Fig. 1. The power stage of the dc/ac converter consists of an IGBT full-bridge with diodes, which synthesizes a low frequency ac voltage by changing the IGBTs' switching states, the gate circuit, which applies the required gate signals in order to

switch on and off the controlled power devices, an LCL-filter, employed as a second-order low pass filtering stage which allows the high frequency ripple of the full-bridge output voltage to be filtered out and a dc-side filtering stage, which can be implemented by means of one shunt capacitor (first order) or a series inductance plus a shunt capacitor (second order).

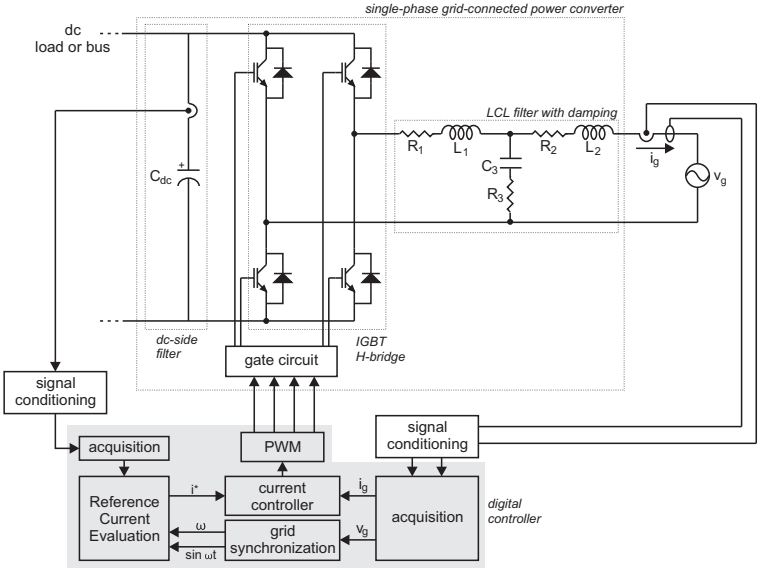

Fig. 1. Three-phases three-wires grid connected dc/ac converter.

Depending on the application characteristics, the converter controller functionalities are implemented using analog or digital circuitries and, in the second case, FPGAs, DPSs and microcontrollers (μCs) allow more flexible and complex controllers to be designed and implemented (Bueno et al., 2008; Koizumi et al., 2006; Kojabadi et al., 2006). In case of grid-connected power converters, both inverters and controlled rectifiers switching at relatively high frequencies (around 10 kHz), the main functionalities that must be implemented are grid synchronization, evaluation of the reference for current injection/consumption, grid side current control and pulse width modulation (PWM) (Kazmierkowski et al., 2002). The grid synchronization block must generate, at least, a reference signal $\sin \omega t$ which must track properly the fundamental component of the grid voltage v_g. Depending on the application, i.e. distributed generation systems, the grid frequency must be also measured in order to implement load sharing algorithms (Guerrero et al., 2004). The evaluation of the instantaneous values of the reference current i^* is required in order to determine the proper current which must flow from/to the electrical grid i_g. The implementation of this functionality depends on the application and, hence, on the implemented high level control functionalities such as reactive power requirements, harmonic control, tolerance to grid disturbances or the maintenance of the dc-bus voltage. The obtained values of i^* are applied to a current controller. This block must ensure that the grid side current i_g matches the reference ones i^*. Diverse approaches, such as hysteresis (Ho et al., 2009), deadbeat (Mohamed & El-Saadany, 2008), proportional-integral (PI) controllers (Dannehl et al., 2010), resonant controllers (Liserre et al., 2006), repetitive controllers (Weiss et al., 2004) or inner model controllers (Gabe et al., 2009), can be found in literature for this purpose.

Finally, the control action must be applied to the gate circuitry of the H-bridge, where square signal waveforms with variable width are required. In order to obtain these variable switching patterns, diverse approaches can be also found. A detailed description of these techniques is available in (Holmes & Lipo, 2003)

4. Synchronization subsystem in grid-connected power converters

Main approaches for synchronization of the power converter to the electrical grid are zero crossing detection (Vainio & Ovaska, 1995; Valiviita, 1999) and phase locked loops (PLLs) (El-Amawy & Mirbod, 1988; Freijedo et al., 2009). While the first one can be easily implemented by means of analog circuitry, power system disturbances such as partial discharges can result on synchronization problems and an erroneous reference current i^*. Due to this fact, the second approach and other based on digital signal processing techniques, i.e. DFT (McGrath et al., 2005) and Kalman filter (Moreno et al., 2007), are preferred. A common approach for implementation of PLLs includes a phase detection (PD) block, a low-pass filtering stage and a voltage controlled oscillator (VCO). By applying the PD block, the input signal v_g is shifted in the frequency domain to low frequency while other frequency components of the input signal are shifted to higher frequencies. The obtained signal is applied to a low-pass filtering stage for filtering out frequency components of the input signal which must not be tracked. Once filtered out, the obtained signal is proportional to the phase error of the input signal v_g and the signal which is generated by the VCO and applied to PD block. Due to the closed loop structure, and depending on the characteristics of the input signal, the PD block and the low-pass filtering stage, the VCO will adjust the relative phase and frequency of the generated signal in order to match the frequency component of v_g to be tracked.

Diverse approaches have been proposed in the literature in order to implement the functional blocks in the previous paragraph but one of the most applied ones in case of grid-connected power converters is based on the Park Transformation. Its general structure for the synchronization of a single-phase grid-connected power converter is shown in Fig. 2. The grid voltage is measured, digitized and applied to the software PLL by means of the input port V_g. This signal is employed to generate a virtual quadrature component, denoted as β, which allows the grid voltage, considered as α, to be represented as a phasor on a stationary complex reference frame (Clarke Transformation), obtaining $\alpha\beta$ components of this single-phase voltage signal. The obtained instantaneous values of this voltage phasor are transformed again by applying the Park Transformation, which carries out a frequency shift of the fundamental frequency tracked by the software PLL. This allows dq components of the voltage phasor, obtained in a rotating reference frame, to be generated. Once the software PLL is tracking the fundamental frequency properly (in phase), the q component of this transformation should be equal to zero and, hence, the instantaneous phase generated by the software PLL should be properly controlled. This is done by the *Controller* block. The impact of possible amplitude variations, i.e. due to voltage sags, can be prevented by means of a normalization block which generates dq components in the range [-1,1]. The *Controller* generates, as a result of its operation and once the software PLL is operating properly, a measure of the grid frequency. The instantaneous phase can be obtained by means of a discrete integrator and, then, a sinusoidal output signal with unity amplitude and in-phase with the grid voltage signal can be generated by applying *sin* and *cos* functions to the measured instantaneous phase. These trigonometric functions are required by the Park Transformation in order to generate the dq components.

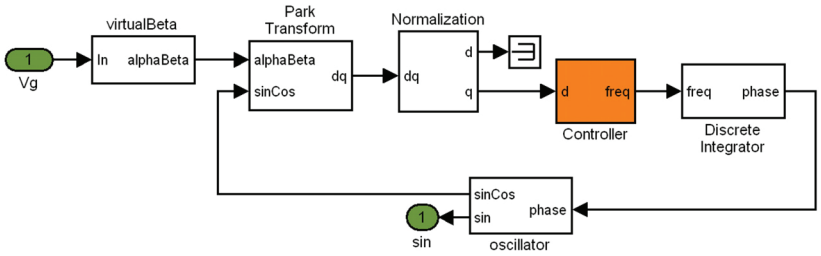

Fig. 2. Structure of software PLL for a single-phase grid-connected power converter.

4.1 Proposed synchronization subsystem

The *Controller* block of the software PLL is commonly implemented as a PI controller or, more generally, as a first order or second order low pass filter, however, recent researching works on DWTs for control applications suggest that the performance of PI controllers can be improved by using DWTs (Parvez & Gao, 2005). The proposed software PLL substitutes the PI controller by a DWT implemented using filter banks. The inner structure of the *Controller* in case of the proposed software PLL is shown in Fig. 3. As it can be seen, it consists of one *Buffer*, where 2^L samples of the input are buffered to be analyzed and L is the number of decomposition levels, the *Dyadic Analysis Filter Bank* from the Signal Processing Blockset in MatLab/Simulink, which generates an output vector containing the output at each sub-band. Then, the loop gains, contained in the *Constant Diagonal Matrix Block* and needed to adjust the response of the proposed software PLL, are applied. Finally, the *Controller* output signal is obtained by adding the current output of the previous stage at each sub-band.

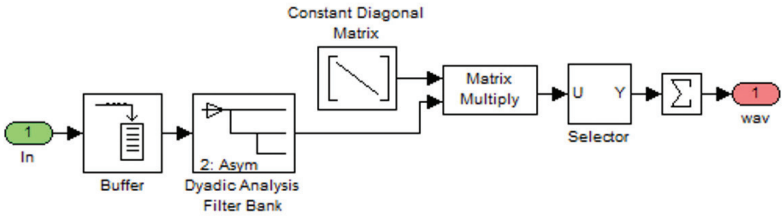

Fig. 3. Controller block in the wavelet PLL (WPLL).

5. Simulation results

In order to analyze the performance of the proposed synchronization block diverse simulation tests have been carried out. After the selection of the most suitable mother wavelet considering diverse decomposition levels and operation conditions, the proposed synchronization system is employed in order to control a dc machine by means of a grid connected controlled rectifier. The applied tests include step amplitude variations of the voltage grid from $23\sqrt{2}$ V to $230\sqrt{2}$ V and step frequency variations from 47.5 Hz to 52.5 Hz, in both cases including a 7% 5^{th} voltage harmonic. The employed sampling frequency is 6.4 kHz.

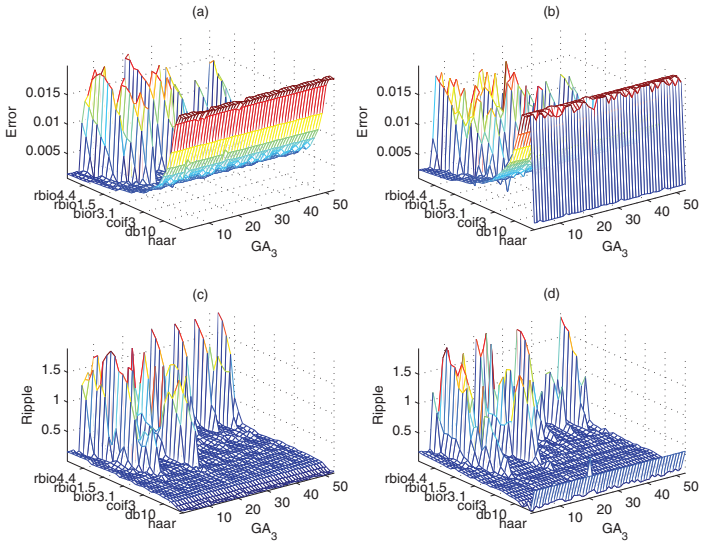

Fig. 4. L=3. a) Magnitude of the WPLL average error after the voltage amplitude step, b) magnitude of the WPLL average error after the fundamental grid frequency step, c) ripple of the WPLL error after the voltage amplitude step and d) ripple of the WPLL error after the voltage amplitude step.

5.1 Selection of the mother wavelet

The selection of the most suitable mother wavelet has been carried out considering decomposition levels (L) in the range $[3, 6]$. At each decomposition level, diverse values of the WPLL loop gains have been applied under the operation conditions described previously. The obtained results, the average error magnitude of the WPLL and the ripple of this error, have been measured 0.5 s after each transient in order to compare the performance of each mother wavelet. Figs. 4, 5, 6 and 7 show the obtained results for L in $[3, 6]$.

From Fig. 4, the best results at $L = 3$ are obtained by applying a *Daubechies 7* mother wavelet with a loop gain at the lowest frequency sub-band $GA_3 = 39$. In this case, the cumulative measured average error of the WPLL falls to $1.1 \cdot 10^{-3}$ V after the first transient, which reaches $5.2 \cdot 10^{-3}$ V after the frequency step. The error ripple measured after the grid voltage transients are 0.23 V and 0.16 V. The worst results are obtained in case of *Daubechies 4* at GA_3, reaching cumulative average errors of $2.0 \cdot 10^{-2}$ V after both grid voltage transients. In case of the measured error ripple, it decreases up to $5.4 \cdot 10^{-3}$ V and $4.6 \cdot 10^{-2}$ respectively but, as it will be shown in the following subsection, the phase of the input signal is not tracked accurately due to the average error.

In case of four decomposition levels ($L = 4$, in Fig. 5), the most suitable mother wavelet is *Haar* applying $GA_4 = 43$. The obtained cumulative average errors after each transient of the grid voltage are $1.1 \cdot 10^{-3}$ V and $2.0 \cdot 10^{-3}$ respectively. The measured ripples are 0.14 V and 0.16 V respectively. In comparison to the obtained results for $L = 3$, in this case ($L = 4$) the cumulative error after the grid frequency transient is reduced to 38%. The comparisson of the measured ripples using $L = 3$ and $L = 4$ shows that, after the first transient, $L = 4$ with *Haar* wavelets results on better results. The worst results in case of $L = 4$ are obtained

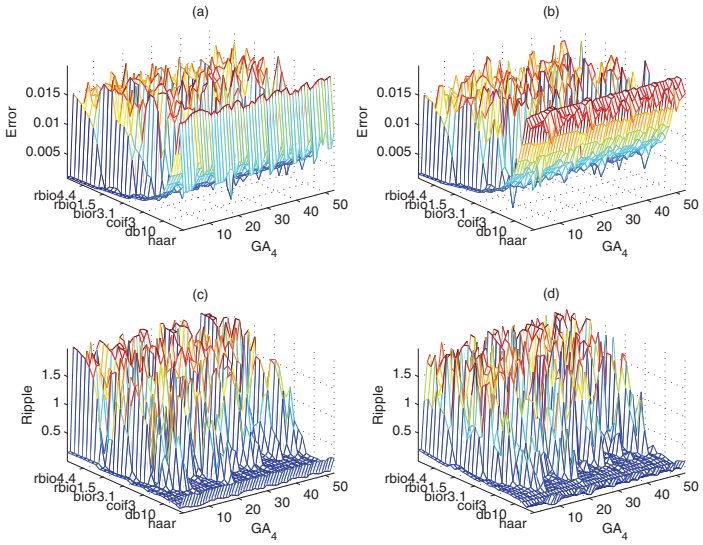

Fig. 5. L=4. a) Magnitude of the WPLL average error after the voltage amplitude step, b) magnitude of the WPLL average error after the fundamental grid frequency step, c) ripple of the WPLL error after the voltage amplitude step and d) ripple of the WPLL error after the voltage amplitude step.

by employing *Coif□et 5* as mother wavelet with $GA_4 = 21$. The obtained cumulative average errors are $2.0 \cdot 10^{-2}$ V and $8.6 \cdot 10^{-3}$ V while the measured ripples reach $1.1 \cdot 10^{-2}$ V and 1.5 V.

From Fig. 6, again *Haar* wavelets, in this case with $GA_5 = 29$, result on the best tracking of the applied grid voltage. The measured cumulative average errors were $8.1 \cdot 10^{-4}$ V and $2.6 \cdot 10^{-3}$ V after the amplitude and frequency steps respectively while, in case of the error ripple, the measured values were 0.14 V and 0.12 V. Comparing these results to the ones obtained in case of $L = 4$, the cumulative average error decreases after the amplitude step of the grid voltage due to the added fifth decomposition level. The worst results at $L = 5$ are obtained for *symlet 8*, where the cumulative average errors after the transients are $2 \cdot 10^{.2}$ V and $1.7 \cdot 10^{-2}$ V. The measured error ripples are $2.4 \cdot 10^{-2}$ and 0.16 V.

Again in case of $L = 6$ (Fig. 7), *Haar* wavelets with $GA_6 = 22$ allow the best tracking performance to be reached. The measured cumulative average errors in this case were $6.4 \cdot 10^{-4}$ V and $9.3 \cdot 10^{-4}$ V corresponding to amplitude and frequency transients respectively, which improves the obtained results in case of $L = 5$. The measured error ripples were 0.16 V and 0.22 V. The worst results were obtained in case of the mother wavelet *Biorthonormal 4.4*, with cumulative average errors equal to $2.0 \cdot 10^{-2}$ V and 1.6^{-2} V. The error ripple reached 0.02 V and 0.67 V for each grid voltage transient.

The evolution of the frequency measurement obtained by means of the WPLL in case of $L = 3$, *Daubechies 7*, $GA_3 = 39$ and $GD_3 = 30$ is shown in Fig. 8.a where the response time of the WPLL is 305 *ms*. Response times with *Haar* wavelet and four ($GA_4 = 43$, $GD_4 = 18.5$) and five ($GA_5 = 29$, $GD_5 = 4.5$ and $GD_4 = 3$) decomposition levels are shown in Fig. 8.b and 8.c. In these cases the measured response times are 64 *ms* and 150 *ms* corresponding to $L = 4$ and

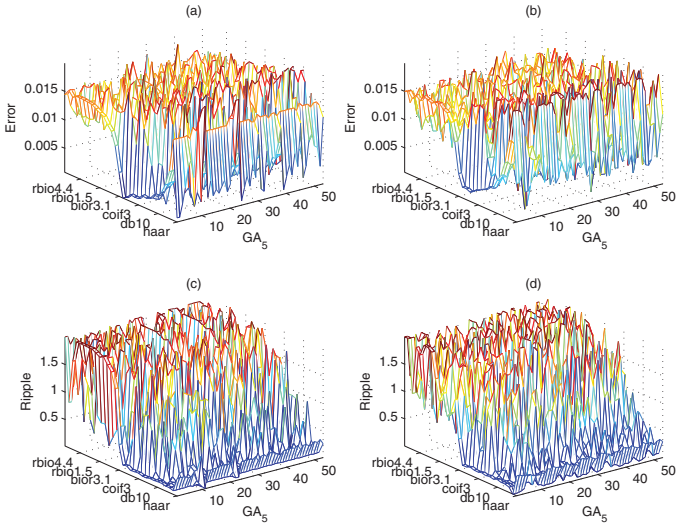

Fig. 6. L=5. a) Magnitude of the WPLL average error after the voltage amplitude step, b) magnitude of the WPLL average error after the fundamental grid frequency step, c) ripple of the WPLL error after the voltage amplitude step and d) ripple of the WPLL error after the voltage amplitude step.

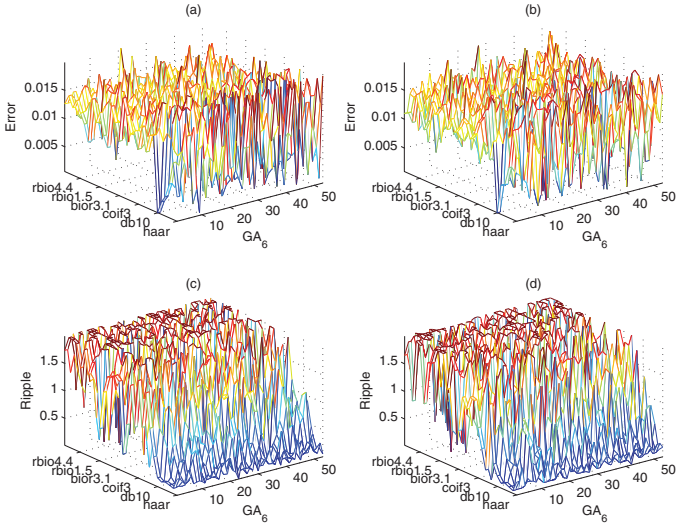

Fig. 7. L=6. a) Magnitude of the WPLL average error after the voltage amplitude step, b) magnitude of the WPLL average error after the fundamental grid frequency step, c) ripple of the WPLL error after the voltage amplitude step and d) ripple of the WPLL error after the voltage amplitude step.

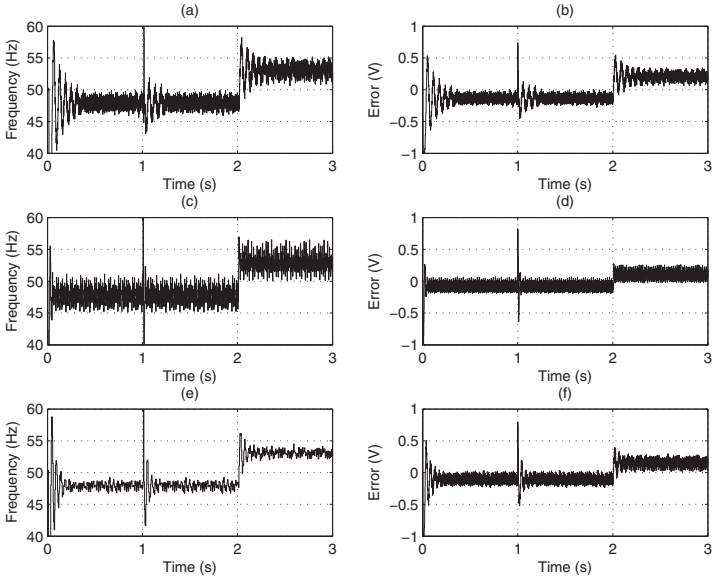

Fig. 8. Time response of the WPLL. a) Frequency measurement with $L = 3$, b) WPLL error with with $L = 3$, c) Frequency measurement with $L = 4$, d) WPLL error with with $L = 4$, e) Frequency measurement with $L = 5$ and f) WPLL error with with $L = 5$.

$L = 5$. In despite of a higher number of decomposition levels, the response time of *Daubechies 7* is the longest one due to the filter length. *Haar* wavelets result on simple filter banks with low response times. Moreover, from Fig. 8.e, the WPLL performance improves by selecting more decomposition levels which results on less frequency ripple.
The WPLL outputs, considering *Daubechies 7* ($L = 3$) and *Haar* ($L = 4$ and $L = 5$), for control purposes of the grid-connected power converter can be compared by means of Fig. 9, where

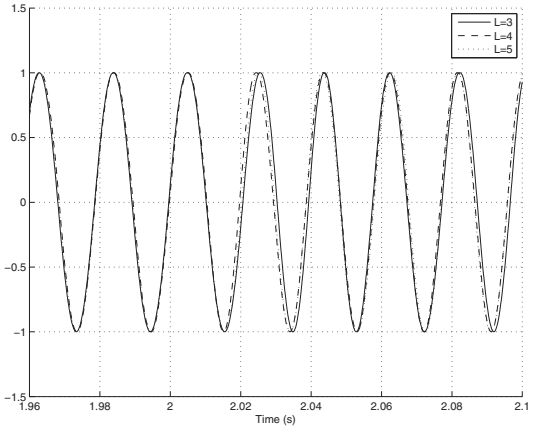

Fig. 9. Time response of the WPLL after the frequency step, at 2 s, from 47.5 Hz to 52.5 Hz.

the time response of the PLL after the frequency transient of the grid voltage (at $t = 2\ s$) is shown.

5.2 Control of a dc motor

The proposed synchronization subsystem has been tested in simulation as a part of the whole controller in case of a grid-connected power converter feeding a dc motor. The employed MatLab/Simulink simulation model, including the power stage, the converter controller and the measurement, is depicted in Fig. 10.

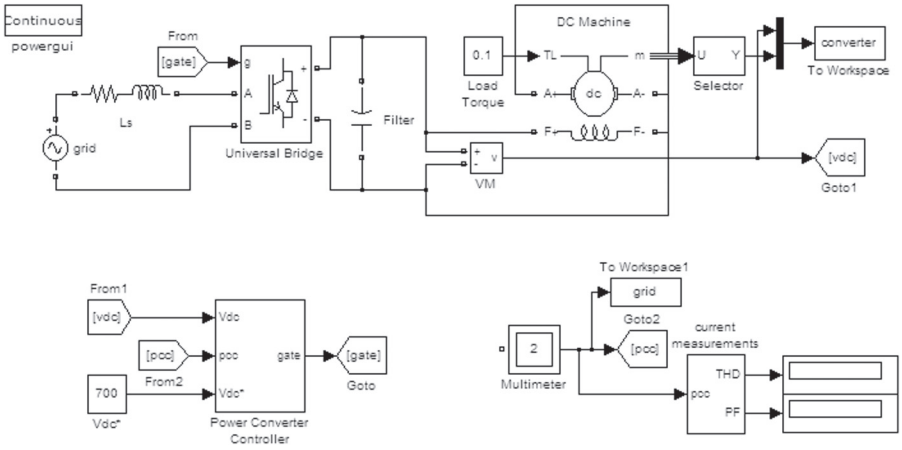

Fig. 10. MatLab/Simulink model of a dc motor controlled by means of a grid-connected power converter. Top: power stage, including the electrical grid, the power converter and the dc machine. Bottom: the controller of the power converter and measurement blocks.

The power stage includes a pure sinusoidal waveform with $230\sqrt{2}\ V$ amplitude and 50 Hz frequency as grid voltage. The grid impedance and the inverter side inductance have been modeled as a series RL with values 0.4 Ω and 2.5 mH. The IGBT+Diode H-bridge is modeled by means of the *Universal Bridge* block of the SimPowerSystems Blockset. The dc filtering stage consist of one 550 μF capacitor and it is connected to the dc motor windings, which are connected in series. The dc machine is modeled as a separately excited dc machine by means of the *DC Machine* block. The measured variables in this model are, at the dc motor side, the motor speed, the output voltage of the power converter (across the dc capacitor) and the output current (flowing through the dc motor), at the electrical grid side, the grid voltage and line current waveforms are also measured.

The inner structure of the employed controller is shown in Fig. 11. The power signals employed for control purposes (voltage across the dc capacitor, grid voltage and line current) are filtered out in order to avoid the aliasing due to the sampling process. The *PLL* block generates a sinusoidal signal, with unitary amplitude, which is employed to evaluate the reference current (applied to port *iGrid** in *current controller*). The proportional-integral (PI) block with $K_p = K_i = 0.4$, employed in case of the SPLL-based model, evaluates the amplitude of this reference current in order to maintain the dc bus voltage at the reference value, in this case 450 V. In order to compare the obatined results, the same reference voltage is employed in case of the WPLL-based model, where the *Haar* wavelet with five decomposition levels, that

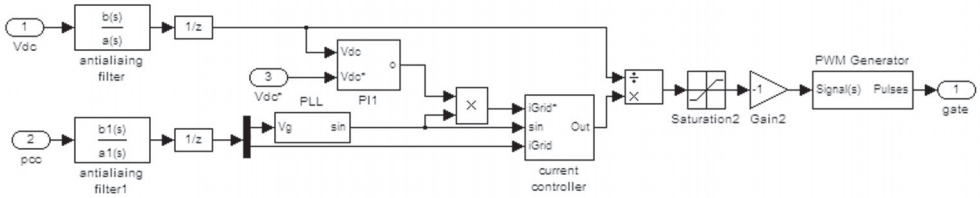

Fig. 11. Structure of the analyzed converter controller.

was analyzed in the previous sections, is applied. The current controller is implemented as a proportional-resonant controller and, in this case, three resonant blocks have been employed at frequencies $\omega_1 = 50\ Hz$, $\omega_3 = 150\ Hz$ and $\omega_3 = 250\ Hz$. The gains of the controller are $K_p = 7$ and $K_1 = K_3 = K_5 = 200$. After the control action, in order to obtain the switching pattern, the output of the current controller must be divided by the measured dc capacitor voltage. Then, the gate pulses of the H-bridge are generated by the block *PWM Generator*, which applies a triangular carrier signal whose frequency matches the sampling frequency, $f_s = 6.4\ kHz$.

The obtained results corresponding to the dc voltage, in case of both the conventional PLL and the WPLL, are shown in Fig. 12.a. As it can be seen, the WPLL subsystem results on an

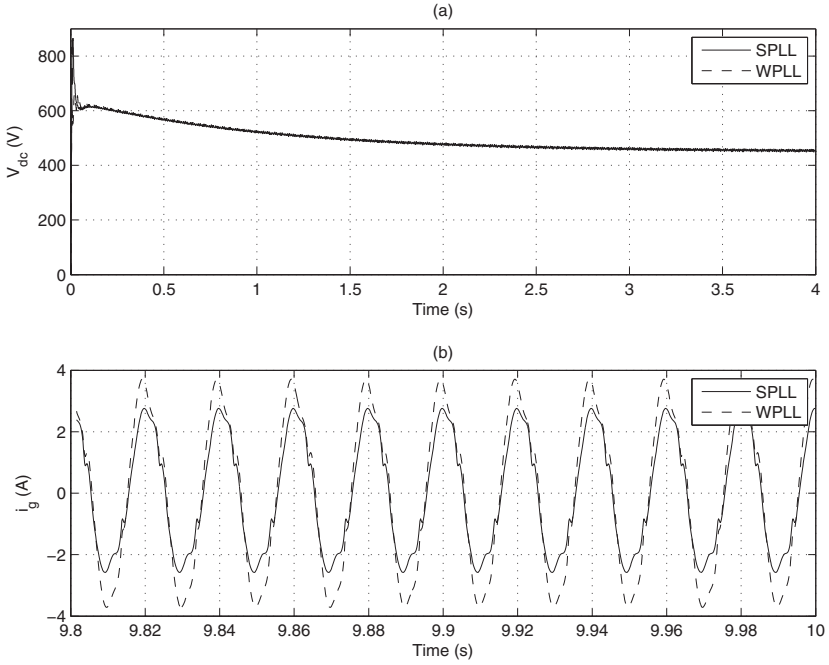

Fig. 12. Structure of the analyzed converter controller.

smoother dc voltage during the motor starting while the conventional SPLL subsystem, based on a PI controller, results on a 863 V transient, which could damage the power converter and the motor windings in case of no protection. The response times in both cases, after the

starting transient, are 3.72 s. This is due to the fact that reference current amplitude is obtained, in both cases, by applying the same PI controller. The current line waveforms, once the dc motor reaches the steady state in both models (with the conventional SPLL and the WPLL), are shown in Fig. 12.b. The measured current THDs are 0.67% and 0.55% corresponding to the conventional SPLL and the proposedl WPLL.

6. Conclusions

This book chapter presents an application of wavelets in grid-connected power converters. The proposed approach allows wavelet-based software phase locked loops (SPLLs) to be developed and implemented, replacing the proportional-integral controller in conventional SPLLs. The proposed approach results on a more flexible synchronization subsystem whose characteristics can be adjusted depending on the electrical grid disturbances. Simulation results, comparing the performance of the conventional SPLL and the wavelet-based proposed one, are given in case of a grid-connected power converter feeding a dc motor.

7. References

Bose, B. K. (2006). *Power electronics and motor drives : advances and trends*, Academic Press.

Bose, B. K. (2009). The past, present, and future of power electronics, *IEEE Industrial Electronics Magazine* 3(2): 7–11,14.

Bueno, E. J., Cobreces, S., Rodriguez, F. J., Hernandez, A. & Espinosa, F. (2008). Design of a back-to-back npc converter interface for wind turbines with squirrel-cage induction generator, *IEEE Transactions on Energy Conversion* 23(3): 932–945.

Bueno, E. J., Hernandez, A., Rodriguez, F. J., Giron, C., Mateos, R. & Cobreces, S. (2009). A dsp- and fpga-based industrial control with high-speed communication interfaces for grid converters applied to distributed power generation systems, *IEEE Transactions on Industrial Electronics* 56(3): 654–669.

Carrasco, J. M., Franquelo, L. G., Bialasiewicz, J. T., Galvan, E., Guisado, R. C. P., Prats, M. A. M., Leon, J. I. & Moreno-Alfonso, N. (2006). Power-electronic systems for the grid integration of renewable energy sources: A survey, *IEEE Transactions on Industrial Electronics* 53(4): 1002–1016.

Castro, R. M. & Diaz, H. N. (2002). An overview of wavelet transform application in power systems, 14^{th} *Power Systems Computation Conference*, pp. 6.1–6.9.

Chaari, O., Meunier, M. & Brouaye, F. (1996). Wavelets: a new tool for the resonant grounded power distribution systems relaying, *IEEE Transactions on Power Delivery* 11(3): 1301–1308.

Dannehl, J., Fuchs, F. W. & Thϕgersen, P. B. (2010). Pi state space current control of grid-connected pwm converters with lcl filters, *IEEE Transactions on Power Electronics* 25(9): 2320–2330.

De Mango, F., Liserre, M. & D'Aquila, A. (2006). Overview of anti-islanding algorithms for pv systems. part ii: Activemethods, *12th International Power Electronics and Motion Control Conference, EPE-PEMC 2006*, pp. 1884–1889.

De Mango, F., Liserre, M., D'Aquila, A. & Pigazo, A. (2006). Overview of anti-islanding algorithms for pv systems. part i: Passive methods, *12th International Power Electronics and Motion Control Conference, EPE-PEMC 2006*, pp. 1878–1883.

Dinkhauser, V. & Fuchs, F. W. (2008). Rotor turn-to-turn faults of doubly-fed induction generators in wind energy plants - modelling, simulation and detection, *13th International Power Electronics and Motion Control Conference*, pp. 1819–1826.

Driesen, J. & Belmans, R. (2002). Active power filter control algorithms using wavelet-based power definitions, *10th International Conference on Harmonics and Quality of Power*, Vol. 2, pp. 466–471.

El-Amawy, A. A. & Mirbod, A. (1988). An efficient software-controlled pll for low-frequency applications, *IEEE Transactions on Industrial Electronics* 35(2): 341 – 344.

Eren, L. & Devaney, M. J. (2001). Motor bearing damage via wavelet analysis of starting current transient, *Proc. of the* 18^{th} *IEEE Instrumentation and Measurement Technology Conference*, Vol. 3, pp. 1797–1800.

Erickson, R. W. & Maksimovic, D. (2001). *Fundamentals of power electronics*, Kluwer.

Freijedo, F. D., Doval-Gandoy, J., Lopez, O. & Acha, E. (2009). Tuning of phase-locked loops for power converters under distorted utility conditions, *IEEE Transactions on Industry Applications* 45(6): 2039–2047.

Gabe, I. J., Montagner, V. F. & Pinheiro, H. (2009). Design and implementation of a robust current controller for vsi connected to the grid through an lcl filter, *IEEE Transactions on Power Electronics* 24(6): 1444–1452.

Gandelli, A., Monti, A., Ponci, F. & Santi, E. (2001). Power converter control design based on haar analysis, *IEEE 32nd Annual Power Electronics Specialists Conference, PESC 2001.*, Vol. 3, pp. 1742–1746.

Gandelli, A., Monti, A., Santi, E. & Ponci, F. (2002). Extending haar domain analysis to dc/ac converters, *IEEE Annual Power Electronics Specialists Conference*, Vol. 4, pp. 1717–1721.

González, D., Bialasiewicz, J. T., Balcells, J. & Gago, J. (2008). Wavelet-based performance evaluation of power converters operating with modulated switching frequency, *IEEE Transactions on Industrial Electronics* 55(8): 3167–3176.

Guerrero, J. M., de Vicuna, L. G., Matas, J., Castilla, M. & Miret, J. (2004). A wireless controller to enhance dynamic performance of parallel inverters in distributed generation systems, *IEEE Transactions on Power Electronics* 19(5): 1205–1213.

Hamid, E. Y. & Kawasaki, Z. L. (2001). Wavelet packet transform for rms values and power measurements, *IEEE Power Engineering Review* 21(9): 49–51.

Heydt, G. & Galli, A. (1997). Transient power quality problems analyzed using wavelets, *IEEE Transactions on Power Delivery* 12(2): 908–915.

Ho, C. N.-M., Cheung, V. S. P. & Chung, H. S.-H. (2009). Constant-frequency hysteresis current control of grid-connected vsi without bandwidth control, *IEEE Transactions on Power Electronics* 24(11): 2484–2495.

Holmes, D. G. & Lipo, T. A. (2003). *Pulse Width Modulation for Power Converters: Principles and Practice*, Power, Energy & Industry Applications, 1 edn, Wiley-IEEE Press.

Hsu, C.-F., Lee, T.-T. & Wang, S.-L. (2008). Fpga-based adaptive wavelet neurcontroller design for dc-dc converter, *Proc. of the* 7^{th} *International Conference on Machine Learning and Cybernetics (ICMLC)*, Vol. 7, pp. 3833–3838.

Huang, C. & Yang, H. T. (2001). Evolving wavelet-based networs for short-term load forecasting, *IEE Proceedings - Generation, Transmission and Distribution* 148(3): 222–228.

Iwaszkiewicz, A. J. & Perz, B. J. (2007). A novel approach to control of multilevel converter using wavelets transform, *International Conference on Renewable Energies and Power Quality*.

Kazmierkowski, M. P., Krishnan, R. & Blaabjerg, F. (eds) (2002). *Control in power electronics : selected problems*, Academic Press.

Knezevic, J., Katic, V. & Graovac, D. (2000). Transient analysis of ac/dc converters input waveforms using wavelet, *Proceedings of the Mediterranean Electrotechnical Conference*, Vol. 3, pp. 1193–1196.

Koizumi, H., Mizuno, T., Kaito, T., Noda, Y., Goshima, N., Kawasaki, M., Nagasaka, K. & Kurokawa, K. (2006). A novel microcontroller for grid-connected photovoltaic systems, *IEEE Transactions on Industrial Electronics* 53(6): 1889–1897.

Kojabadi, H. M., Yu, B., Gadoura, I. A., Chang, L. & Ghribi, M. (2006). A novel dsp-based current-controlled pwm strategy for single phase grid connected inverters, *IEEE Transactions on Power Electronics* 21(4): 985–993.

Liserre, M., Sauter, T. & Hung, J. Y. (2010). Future energy systems: Integrating renewable energy sources into the smart power grid through industrial electronics, *IEEE Industrial Electronics Magazine* 4(1): 18–37.

Liserre, M., Teodorescu, R. & Blaabjerg, F. (2006). Multiple harmonics control for three-phase grid converter systems with the use of pi-res current controller in a rotating frame, *IEEE Transactions on Power Electronics* 21(3): 836–841.

McGrath, B. P., Holmes, D. G. & Galloway, J. J. H. (2005). Power converter line synchronization using a discrete fourier transform (dft) based on a variable sample rate, *IEEE Transactions on Power Electronics* 20(4): 877–884.

Mercorelli, P., Kubasiak, N. & Liu, S. (2004). Model predictive control of an electromagnetic actuator fed by multilevel pwm inverter, *IEEE International Symposium on Industrial Electronics*, Vol. 1, pp. 531–535.

Mohamed, Y. A.-R. & El-Saadany, E. F. (2008). Adaptive discrete-time grid-voltage sensorless interfacing scheme for grid-connected dg-inverters based on neural-network identification and deadbeat current regulation, *IEEE Transactions on Power Electronics* 23(1): 308–321.

Mohan, N., Undeland, T. M. & Robbins, W. P. (2003). *Power electronics : converters, applications and design*, John Wiley & Sons.

Moreno, V. M., Liserre, M., Pigazo, A. & Dell'Aquila, A. (2007). A comparative analysis of real-time algorithms for power signal decomposition in multiple synchronous reference frames, *IEEE Transactions on Power Electronics* 22(4): 1280–1289.

Parvez, S. & Gao, Z. (2005). A wavelet-based multiresolution pid controller, *IEEE Transactions on Industry Applications* 41(2): 537–543.

Pham, V. L. & Wong, K. P. (1999). Wavelet-transform-based algorithm for harmonic analysis of power system waveforms, *IEE Proceedings - Generation and Distribution* 146(3): 249–254.

Pham, V. L., Wong, K. P. & Arrillaga, J. (2000). Sub-harmonics state estimation in power system, *IEEE Power Engineering Society Winter Meeting*, Vol. 2, pp. 1168–1173.

Pigazo, A., Liserre, M., Mastromauro, R. A., Moreno, V. M. & Dell'Aquila, A. (2009). Wavelet-based islanding detection in grid-connected pv systems, *IEEE Transactions on Industrial Electronics* 56(11): 4445–4455.

Pigazo, A., Moreno, V. M., Liserre, M. & Dell'Aquila, A. (2007). Wavelet-based islanding detection algorithm for single-phase photovoltaic (pv) distributed generation systems, *IEEE International Symposium on Industrial Electronics*, pp. 2409–2413.

Ponci, F., Santi, E. & Monti, A. (2009). Discrete-time multi-resolution modeling of switching power converters using wavelets, *Simulation* 85(2): 69–88.

Ribeiro, P. F. (1994). Wavelet transform: an advanced tool for analysing non-stationary harmonic distortion in power system, *Proc. of the IEEE International Conference on Harmonics in Power Systems*.

Robertson, D., Camps, O. & Mayer, J. (1994). Wavelets and power system transients, *SPIE International Symposium on Optical Engineering in Aerospace Sensing*, pp. 474–487.

Saleh, S. A. & Rahman, M. A. (2009). Performance testing of a single-phase voltage-source wavelet modulated ac-dc converter, *Canadian Conference on Electrical and Computer Engineering, CCECE '09*, pp. 1049–1054.

Shim, I., Soragan, J. J., Siew, W. H., Sludden, K. & Gale, P. F. (2000). Robust partial discharge measurement in mv cable networks using discrete wavelet transforms, *IEEE Power Engineering Society Winter Meeting*, Vol. 1, pp. 718–723.

Solanki, M., Song, Y. H., Potts, S. & Perks, A. (2001). Transient protection of transmission lines using wavelet transform, *IEEE* 7^{th} *International Conference on Developments in Power System Protection*, pp. 299–302.

Sumner, M., Abusorrah, A., Thomas, D. & Zanchetta, P. (2006). Improved power quality control and intelligent protection for grid connected power electronic converters, using real time parameter estimation, *IEEE Industry Applications Society Annual Meeting*, Vol. 4, pp. 1709–1715.

Teng, L.-T., Lin, F.-J., Chiang, H.-C. & Lin, J.-W. (2009). Recurrent wavelet neural network controller with improved particle swarm optimisation for induction generator system, *IET Electric Power Applications* 3(2): 147–159.

Ullah, N., Bhattacharya, K. & Thiringer, T. (2009). Wind farms as reactive power ancillary service providersŮtechnical and economic issues, *IEEE Transactions on Energy Conversion* 24(3): 661–672.

Vainio, O. & Ovaska, S. (1995). Noise reduction in zero crossing detection by predictive digital filtering, *IEEE Transactions on Industrial Electronics* 42(1): 58–62.

Valiviita, S. (1999). Zero-crossing detection of distorted line voltages using 1-b measurements, *IEEE Transactions on Industrial Electronics* 46(5): 917–922.

Weiss, G., Zhong, Q.-C., Green, T. C. & Liang, J. (2004). h^{∞} repetitive control of dc-ac converters in microgrids, *IEEE Transactions on Power Electronics* 19(1): 319–230.

Wilkinson, W. A. & Cox, M. D. (1996). Discrete wavelet analysis of power system transient, *IEEE Transactions on Power Systems* 11(4): 2018–2044.

Yao, S. J., Song, Y. H., Zhan, L. Z. & Cheng, X. Y. (2000). Wavelet transform and neural networks for short-term electrical forecasting, *Energy Conversion and Management* 41(18): 1975–1988.

Zhen, R., Qungu, H., Lin, G. & Weniying, H. (2000). A new method for power system frequency tracking based on trapezoid wavelet transform, *International Conference on advances in Power System Control, Operation and Management*, Vol. 2, pp. 364–369.

12

Discrete Wavelet Transform Based Wireless Digital Communication Systems

Prof Ali A. A. MIEEE, MComSoc
Department of Electrical Engineering, Isra University,
Amman Jordan

1. Introduction

There has been paradigm shift in mobile communications systems every decade. Now, just coming into the new century, it might be a good time to start discussions on the fourth generation (4G) systems which may be in service around 2010. For systems beyond 3G, there may be a requirement for a new wireless access technology for the terrestrial components [1]. It's envisaged that these potential new radio interfaces will support up to approximately 100 Mbps for high mobility and up to 1 Gbps for the low mobility, such as nomadic, leads to the 4th generation system. The data rate figures are targets for research and investigation on the basic technologies necessary to implement the vision. The future system specification and the design will be based on the results of the research and investigations.

Due to the high rate requirements, additional spectrum will be needed for the new capabilities beyond International Mobile Telecommunications-2000 (IMT-2000). In conjunction with the future development of IMT-2000 and systems beyond IMT-2000 there will be an increasing relation ship between radio access and communication system, such as wireless Personal Area Networks (PAN_s), Local Area Networks (LAN_s), digital broadcast, and fixed wireless access.

In discussion about 2G systems in the 1980, two candidates for the radio access technique existed, Time Division Multiple Access (TDMA) and Code Division Multiple Access (CDMA) schemes. In discussion about 3G system, the Orthogonal Frequency Division Multiplexing (OFDM) appeared in the 1990_s and gained a lot of attention and is a potential candidate for 4G systems. OFDM is very efficient in spectrum usage and is very effective in a frequency selective channel. A variation of OFDM which allows multiple accesses is Multi-Carrier CDMA (MC-CDMA) which is essentially an OFDM technique where the individual data symbols are spread using spreading code in frequency domain. The inherent processing gain due to the spreading helps in interference suppression in addition to providing high data rates. OFDM is already the technique used in Digital Audio and Video Broadcasting (DAB, DVB) and $WLAN_s$, 802-11 family, and is believed to be the technique for future broadband wireless access [2]. The present third generation (3G) systems can provide a maximum data rate of 2 Mbps for indoor environment which is quite less than the needed for the currently evolving multimedia applications requiring very high bandwidth.

This had led the researchers worldwide to the evolution of the 4G systems that are expected to provide a data rate ranging from 20 Mbps to 100 Mbps on the air interface. The reader can easily understand the reason why the OFDM is suited for 4G systems, with some justifications that appeared as follows:

Multicarrier techniques can combat hostile frequency selective fading countered in mobile communications. The robustness against frequency selective fading is very attractive, especially for high-speed data transmission [3]
OFDM scheme has been well matured through research and development for high-rate wireless LAN_s and terrestrial digital video broadcasting.
By combining OFDM with CDMA, it has been synergistic effect, such as enhancement of robustness against frequency selective fading and high scalability in possible data transmission rate.
OFDM can provide higher data rates as is a very good choice for service providers to compete with wire-line carriers [3]. The CDMA scheme is robust to frequency selective fading and has been successfully introduced in commercial cellular mobile communications systems such as Interim Standard-95 (IS-95) and 3G systems. Combining multi-carrier OFDM transmissions with Code Division Multiple Accesses (CDMA) allows us to exploit the wideband channels inherent frequency diversity by spreading each symbol across multiple carriers.
Although OFDM is robust to frequency selective fading, it has severe disadvantages in sub-carrier synchronization and sensitivity to frequency offset estimation. The other one is related with the presence of a large number of sub-carriers which exhibit a non-constant nature in its envelope. The combining of OFDM and CDMA has one major advantage though; it can lower the symbol rate in each sub-carrier compared to OFDM so that longer symbol duration makes it easier to synchronize. The MC-CDMA not only mitigates the Inter-Symbol Interference (ISI) but also exploits the multipath. The MC-CDMA suffers only slightly in presence of interference as opposed to Direct Sequence-CDMA (DS-CDMA) whose performance decreases significantly in the presence of interference [4].
In the second section of this chapter, the theory of the Wavelet Transform (with a special concentration on the Discrete Wavelet Transform) will be presented in a very simple and comprehensive manner to make it understandable enough for the formulation of the next sections where the Wavelet based Wireless Digital Communication Systems will be discussed. Also performance comparisons of Fourier and Wavelet based communication systems on different channel models will be presented.

2. Wavelet transform

Any general signal can be decomposed into wavelets, i.e., the original function is synthesized by adding elementary building blocks, of constant shape but different size and amplitude. In this approach, one can design a set of basis functions by choosing a proper basic wavelet $\Psi(t)$ (mother wavelet) and use a delayed and scaled version of that. The most important properties of wavelets are the admissibility and the regularity conditions and these are the properties which gave wavelets their name. It can be shown [5] that square integrable functions $\Psi(t)$ satisfying the admissibility condition:

$$\int \frac{|\Psi(w)|^2}{|w|} dw < +\infty \tag{1}$$

can be used to first analyze and then reconstruct a signal without loss of information. In (1) $\Psi(w)$ stands for the Fourier transform of $\Psi(t)$. The admissibility condition implies that the Fourier transform of $\Psi(t)$ vanishes at the zero frequency, i.e.

$$\left|\Psi(w)\right|^2\Big|_{w=0} = 0 \tag{2}$$

A zero at the zero frequency also means that the average value of the wavelet in the time domain must be zero and therefore it must be oscillatory. In other words, $\Psi(w)$ must be a wave. The reconstruction or inverse transformation is satisfied whenever $\Psi(w)$ is of finite energy and band pass (oscillates in time like a short wave). These are the regularity conditions and they state that the wavelet function should have some smoothness and concentration in both time and frequency domains. For sufficiently regular $\Psi(w)$, the reconstruction condition is:

$$\int \Psi(t)\ dt = 0 \tag{3}$$

Summarizing, the admissibility condition gave us the wave, regularity and vanishing moments gave us the fast decay or the let, and together they give us the wavelet.

2.1 The discrete wavelet transform

Under the reconstruction condition (3), the continuously labeled basis functions (wavelets), $\Psi_{j,k}(t)$ behaves in the wavelet analysis and synthesis just like an orthonormal basis. By appropriately discretizing the time-scale parameters, τ, s, and choosing the right mother wavelet, $\Psi(t)$, it is possible to obtain a true orthonormal basis. The natural way is to discretizing the scaling variable s in a logarithmic manner $\left(s = s_0^{-j}\right)$ and to use Nyquist sampling rule, based on the spectrum of function x (t), to discretizing τ at any given scale $\left(\tau = k\ s_0^{-j}\ T\right)$. The resultant wavelet functions are then as follows:

$$\Psi_{j,k}(t) = s_0^{j/2}\ \Psi\left(s_0^j t - k\tau_0\right) \tag{4}$$

If s0 is close enough to one and if T is small enough, then the wavelet functions are over-complete and signal reconstruction takes place within non-restrictive conditions on $\Psi(t)$. On the other hand, if the sampling is sparse, e.g., the computation is done octave by octave (s0 = 0), a true orthonormal basis will be obtained only for very special choices of $\Psi(t)$. Based on the assumption that wavelet functions are orthonormal:

$$\int \Psi_{j,k}(t)\Psi_{m,n}(t)dt = \begin{cases} 1 & if\ j = m\ \ and\ \ k = n \\ 0 & otherwise \end{cases} \tag{5}$$

For discrete time cases, equation (4) is generally used with s0 = 2, the computation is done octave by octave. In this case, the basis for a wavelet expansion system is generated from simple scaling and translation. The generating wavelet or mother wavelet, represented by $\Psi(t)$, results in the following two-dimensional parameterization of $\Psi_{j,k}(t)$.

$$\Psi_{j,k}(t) = 2^{j/2}\Psi\left(2^j t - k\right) \tag{6}$$

The $2^{j/2}$ factor in equation (6) normalizes each wavelet to maintain a constant norm independent of scale j. In this case, the discretizing period in τ is normalized to one and is

assumed that it is the same as the sampling period of the discrete signal $\left(\tau = k\ 2^{j}\right)$. All useful wavelet systems satisfy the multiresolution conditions. In this case, the lower resolution coefficients can be calculated from the higher resolution coefficients by a tree-structured algorithm called filter-bank [6]. In wavelet transform literatures; this approach is referred to as discrete wavelet transform (DWT).

2.1.1 The scaling function

The multiresolution idea is better understood by using a function represented by $\Phi(t)$ and referred to as scaling function. A two-dimensional family of functions is generated, similar to (6), from the basic scaling function by [7]:

$$\Phi_{j,k}(t) = 2^{j/2}\ \Phi\left(2^{j}t - k\right) \tag{7}$$

Any continuous function, f(t), can be represented, at a given resolution or scale j0, by a sequence of coefficients given by the expansion:

$$f_{j_0}(t) = \sum_{k} f_{j_0}[k] \cdot \Phi_{j_0,k}(t) \tag{8}$$

In other words, the sequence $x_{j_0}[k]$ is the set of samples of the continuous function x(t) at resolution j0. Higher values of j correspond to higher resolution. Discrete signals are assumed samples of continuous signals at known scales or resolutions. In this case, it is not possible to obtain information about higher resolution components of that signal. The main required property is the nesting of the spanned spaces by the scaling functions. In other words, for any integer j, the functional space spanned by [8]:

$$\left\{\Phi_{j,k}(t)\ ;\ for\ \ k \in 1,2,\ldots\right\} \tag{9}$$

should be a subspace of the functional space spanned by:

$$\left\{\Phi_{j+1,k}(t)\ ;\ for\ \ k \in 1,2,\ldots\right\} \tag{10}$$

The nesting of the space spanned by $\Phi\left(2^{j}t - k\right)$ is achieved by requiring that $\Phi(t)$ be represented by the space spanned by $\Phi(2t)$. In this case, the lower resolution function, $\Phi(t)$, can be expressed by a weighted sum of shifted version of the same scaling function at the next higher resolution, $\Phi(2t)$, as follows:

$$\Phi(t) = \sum_{k} h(k)\ \sqrt{2}\ \Phi(2t - k) \tag{11}$$

The set of coefficients $h(k)$ being the scaling function coefficients and $\sqrt{2}$ maintains the norm of the scaling function with scale of two. $\Phi(t)$ being the scaling function which satisfies this equation which is sometimes called the refinement equation, the dilation equation, or the multiresolution analysis equation (MRA).

2.1.2 The wavelet functions

The important features of a signal can better be described or parameterized, not by using $\Phi_{j,k}(t)$ and increasing j to increase the size of the subspace spanned by the scaling functions, but by defining a slightly different set of functions $\Psi_{j,k}(t)$ that span the differences between the spaces spanned by the various scales of the scaling function.
Since it is assumed that these wavelets reside in the space spanned by the next narrower scaling function, they can be represented by a weighted sum of shifted version of the scaling function $\Phi(2t)$ as follows:

$$\Psi(t) = \sum_k g(k)\ \sqrt{2}\ \Phi(2t-k) \tag{12}$$

The set of coefficients $g(k)$'s is called the wavelet function coefficients (or the wavelet filter). It is shown that the wavelet coefficients are required by orthogonality to be related to the scaling function coefficients by [9, 10]:

$$g(k) = (-1)^n h(1-k) \tag{13}$$

One example for a finite even length-N $h(k)$

$$g(k) = (-1)^k h(N-1-k) \tag{14}$$

The function generated by equation (12) gives the prototype or mother wavelet $\Psi(t)$ for a class of expansion functions of the form shown in equation (6). For example the Haar scaling function is the simple unit-width, unit-height pulse function $\Phi(t)$ shown in Fig (1a) [7] and it is obvious that $\Phi(2t)$ can be used to construct $\Phi(t)$ by:

$$\Phi(t) = \Phi(2t) + \Phi(2t-1) \tag{15}$$

Which means (11) is satisfied for coefficients $h(0) = 1/\sqrt{2}$, $h(1) = 1/\sqrt{2}$.

The Haar wavelet function that is associated with the scaling function in Fig.(1a) is shown in Fig. (1b). For Haar wavelet, the coefficients in equation (14) are $g(0) = 1/\sqrt{2}$, $g(1) = -1/\sqrt{2}$.

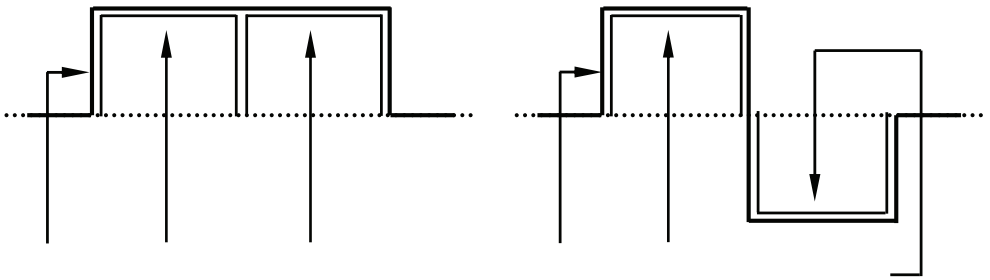

$\Phi(t) = \Phi(2t) + \Phi(2t-1)$ $\Psi(t) = \Phi(2t) - \Phi(2t-1)$

(a) (b)

Fig. 1. (a) Haar Scaling Function, (b) Haar wavelet function.

Any function $f(t)$ could be written as a series expansion in terms of the scaling function and wavelets by [11]:

$$f(t)=\sum_{k=-\infty}^{\infty} a_{j_0}(k)\Phi_{j_0,k}(t)+\sum_{j=j_0}^{\infty}\sum_{k=-\infty}^{\infty} b_j(k)\Psi_{j,k}(t) \tag{16}$$

In this expansion, the first summation gives a function that is a low resolution or coarse approximation of f(t) at scale j0 . For each increasing j in the second summation, a higher or finer resolution function is added, which adds increasing details. The choice of j0 sets taking the coarsest scale whose space is spanned by $\Phi_{j_0,k}(t)$. The rest of the function is spanned by the wavelets providing the high-resolution details of the function. The set of coefficients in the wavelet expansion represented by equation (14) is called the discrete wavelet transform (DWT) of the function f(t).
These wavelet coefficients, under certain conditions, can completely describe the original function, and in a way similar to Fourier series coefficients, can be used for analysis, description, approximation, and filtering. If the scaling function is well behaved, then at a high scale, samples of the signal are very close to the scaling coefficients. As mentioned before, for well-behaved scaling or wavelet functions, the samples of a discrete signal can approximate the highest achievable scaling coefficients.
It is shown that the scaling and wavelet coefficients at scale j are related to the scaling coefficients at scale (j + 1) by the following two relations.

$$a_j(k)=\sum_m h(m-2k)\; a_{j+1}(m) \tag{17}$$

$$b_j(k)=\sum_m g(m-2k)\; b_{j+1}(m) \tag{18}$$

2.2 Fast computation method of DWT

The implementation of equations (17) and (18) is illustrated in Fig. (2). In this figure, two levels of decomposition are depicted. h and g are low-pass and high-pass filters corresponding to the coefficients $h(n)$ and $g(n)$ respectively. The down-pointing arrows denote a decimation or down-sampling by two. This splitting, filtering and decimation can be repeated on the scaling coefficients to give the two-scale structure. The first stage of two banks divides the spectrum of $a_{j-1,k}$ into a low-pass and high-pass band, resulting in the scaling coefficients and wavelet coefficients at lower scale $a_{j,k}$ and $b_{j,k}$. The second stage then divides that low-pass band into another lower low-pass band and a high-pass filter.

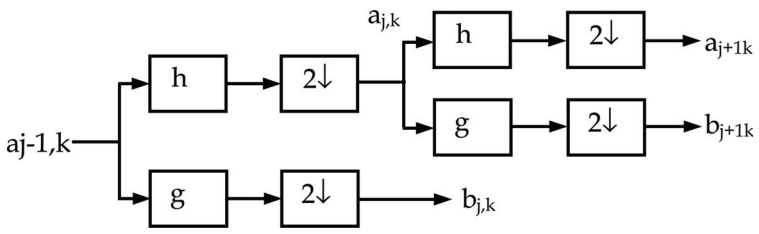

Fig. 2. The filter bank for calculating the wavelet coefficients.

3. OFDM and CDMA theory and concept

The purpose of this section is to describe the OFDM and CDMA systems. The majority of the information presented is intended as background information for the system simulation and evaluation presented in rest of the chapter. The basic theoretical aspects for mobile radio channels with a brief mathematical explanation of multi-path selective channels and their characteristic parameters are explored, due to their direct effect on the performance of the OFDM and CDMA modulation techniques. Then the FFT-based OFDM and different combinations of MC and CDMA are given together with their performances and simulation. Then it provides the basic theory of used transforms, wavelet, and its equations and a basic outlines for its computation algorithm using D4 wavelet. Also Multi-wavelets theory with its equations is introduced.

3.1 Orthogonal frequency division multiplexing (OFDM)

A simple multi-carrier communication system is the frequency division multiplexing (FDM) or multi-tone. The broad transmission bandwidth is divided into many narrow non-overlapping sub-channels, in which the data is transmitted in a parallel fashion. Ideally each sub-channel is narrow enough so that the sub-channel can be considered to be slow, flat fading to reduce the effect of ISI. The fundamental structure of a multi-carrier system is depicted in Fig. (3). The data stream is mapped to the desired waveform, filter banks are used to limit the signal bandwidth. After being modulated by separate center frequencies, these signals are multiplexed and transmitted. At the receiver the frequency multiplexed signal is down converted to different channels by multiplication with separate center frequencies, filtered by the filter banks to get the base band Multicarrier signal for further processing .

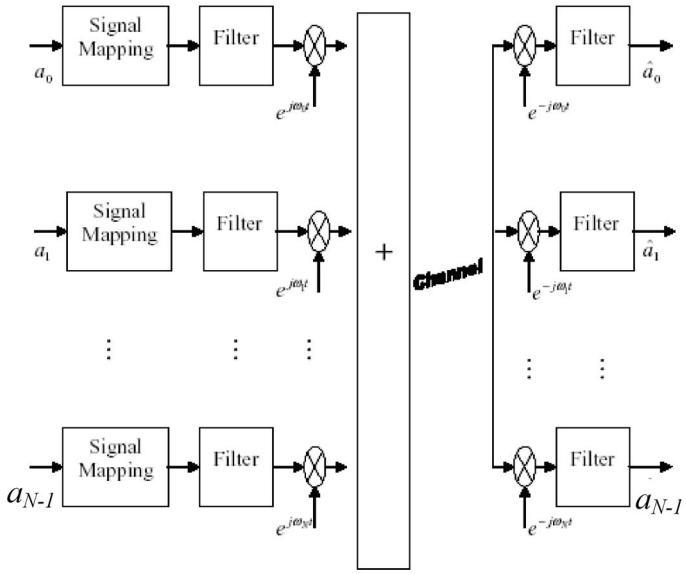

Fig. 3. Fundamental structure of a multi-carrier transceiver-carrier

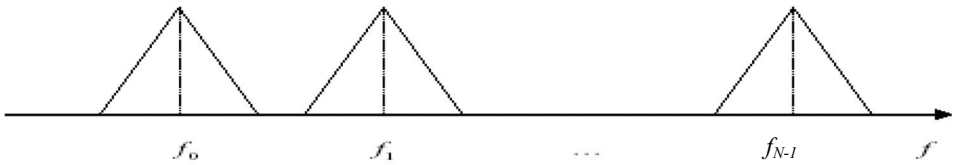

Fig. 4. FDM sub-bands spectrum distribution.

The spectrum allocation for sub-channels in a FDM system is shown in Fig (4), where f0, f1, _ _ _, fN-1 are the center frequencies of the sub-channels.

This modulation has the following disadvantages:

1. Since the sub-carriers are not overlapped with each other, the wide spacing between the sub-bands means lower spectrum efficiency.
2. The complexity will increase due to the N modulators and filters used at the transmitter and N demodulators and filters at the receiver which makes the system more complicated [13]

3.1.1 Implementation of OFDM signals

For Fig. (3), with input sequence {a[k]}, 0≤k≤N-1, the frequency spacing □Δf □ between the different sub-carriers and the symbol interval Tu, the transmitted data can be expressed as:

$$x_a(t) = \sum_{k=0}^{N-1} a[k]\ e^{j2\pi k\Delta ft}\ , \qquad 0 \le t \le Tu \tag{19}$$

If the signal is sampled at a rate Tu / N, then the above equation can be rewritten as:

$$x_a[n] = x_a(\frac{n}{N}T_u) = \sum_{k=0}^{N-1} a[k]e^{j2\pi k\Delta fT_u/N} \tag{20}$$

If the following equation:

$$\Delta f\ Tu = 1 \quad (\Delta f = \frac{1}{Tu}) \tag{21}$$

is satisfied, then the multi-carriers are orthogonal to each other and equation (20) can be rewritten as:

$$x_a[n] = \sum_{k=0}^{N-1} a[k]e^{j2\pi nk/N} \tag{22}$$

One of the major advantages of OFDM is that the modulation can be performed in the discrete domain using an Inverse Discrete Fourier Transform (IDFT) or more computationally efficient inverse Fast Fourier Transform (IFFT). The above equation is just the IDFT of the input signal stream {a[k]}, equation (22) can be rewritten as [14]:

$$X_e[n] = N.IDFT\{a[k]\} \tag{23}$$

At the receiver the DFT implementation to find the approximate signal â[k] can be written as:

$$\hat{a}[k] = DFT\{x_a[n]\} \tag{24}$$

$$= \sum_{n=0} x_a[n] e^{-j2\pi nk/N}$$

$$= \frac{1}{N} \sum_{n=0}^{N-1} \sum_{m=0}^{N-1} a[m] e^{j2\pi n(m-k)/N}$$

$$= \frac{1}{N} \sum_{m=0}^{N-1} a[m] \sum_{n=0}^{m=0} e^{j2\pi n(m-k)/N} \qquad = \frac{1}{N} \sum_{m=0}^{N-1} a[m] N\delta[m-k]$$

$$= a[k]$$

Here δ[m-k] is the delta function defined as :

$$\delta[n] \begin{cases} 1, & if\ n = 0 \\ 0, & otherwise \end{cases}$$

From the derivation above, it can be observed that there are two most important features of the OFDM technique, these are:

1. Each sub-carrier has a different center frequency. These frequencies are chosen so that the following integral over a symbol period is satisfied:

$$\int_0^{Tu} a_m e^{jw_m t} a_l e^{jw_l t} dt = 0, m \neq l \tag{25}$$

The sub-carrier signals in an OFDM system are mathematically orthogonal to each other. The sub-carrier pulse used for transmission is chosen to be rectangular. The rectangular pulse leads to a $\frac{\sin(x)}{x}$ type of spectrum. The spectrum of the three adjustment OFDM sub-carriers is illustrated in Fig. (5). The spectrum of the sub-carriers is overlapped to each other, thus the OFDM communication system has high spectrum efficiency. Maintenance of the orthogonality of the sub-carriers is very important in an OFDM system, which requires the transmitter and receiver to be in the perfect synchronization [12].

2. IDFT and DFT functions can be exploited to realize the OFDM modulation and demodulation instead of the filter banks in the transmitter and the receiver to lower the system implementation complexity and cost. This feature is attractive for practical use. The IFFT and FFT algorithms can be used to calculate the IDFT and DFT efficiently. IFFT and FFT are used to realize the OFDM modulation and demodulation to reduce the system implementation complexity and to improve the system running speed.

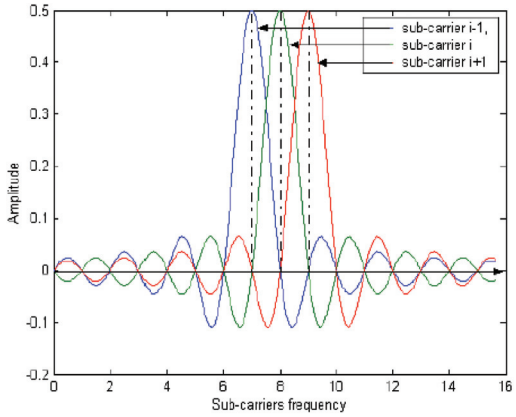

Fig. 5. Orthogonality principle of OFDM

It is necessary for a predetermined number of sub symbols to be available simultaneously at the inputs of the IFFT unit. For this reason the sequentially received data are temporarily stored, until the required number of sub symbols for parallel transmission have accumulated, and are then read out in parallel.

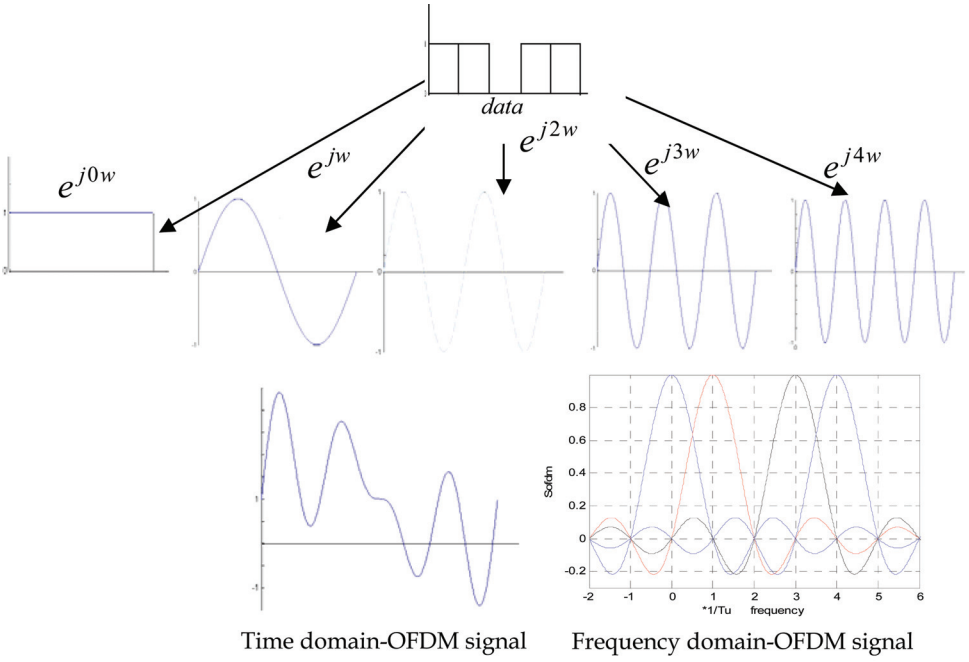

Fig. 6. Signal processing of OFDM

Fig.(6) above demonstrates by a simple example the principle of the signal processing within the subsequent IFFT unit. In this example an OFDM symbol is shaped from five consecutive

bits. The first diagram represents the serial data stream. After the parallel transformation each bit lies at one of the inputs of the IFFT unit for the duration Tu=5Tb and generates a sub signal. The frequencies of the individual sub signals result in integral multiples of f0 =1/Tu .They are therefore orthogonal to one another [15]

3.1.2 Guard Interval

One of the most important properties of OFDM transmissions is the robustness against multipath delay spread. This is achieved by having a long symbol period, which minimizes the inter-symbol interference. The level of robustness can in fact be increased even more by the addition of a guard period between transmitted symbols. The guard period allows time for multipath signals from the pervious symbol to die away before the information from the current symbol is gathered [16].

As long as the multipath delay echoes stay within the guard period duration, there is strictly no limitation regarding the signal level of the echoes: they may even exceed the signal level of the shorter path. The signal energy from all paths just adds at the input to the receiver, and since the FFT is energy conservative, the whole available power feeds the decoder. If the delay spread is longer then guard intervals then they begin to cause inter symbol interference. However, provided the echoes are sufficiently small they do not cause significant problems. This is true most of the time as multipath echoes delayed longer than the guard period will have been reflected off very distant objects. There are several types of guard interval such that cyclic prefix (CP), zero padded, and other variation of guard interval are possible.

3.1.3 Cyclic prefix

The most effective guard period to use is a cyclic extension of the symbol, see Fig (7). If a mirror in time, of the end of the symbol waveform is put at the start of the symbol as the guard period, this effectively extends the length of the symbol, while maintaining the orthogonality of the waveform. Using this cyclic extended symbol the samples required for performing the FFT can be taken anywhere over the length of the symbol. This provides multipath immunity as well as symbol time synchronization tolerance.

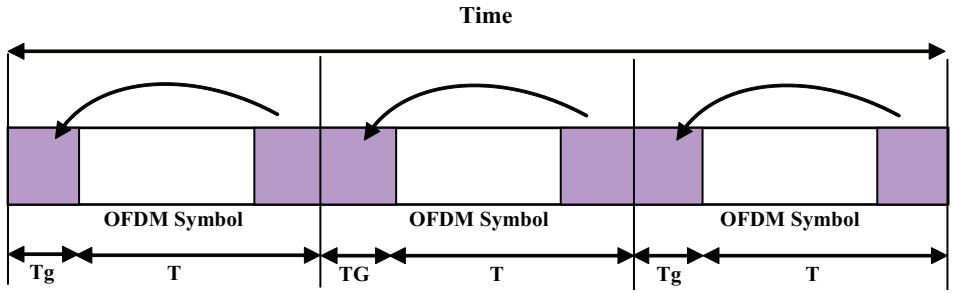

Fig. 7. Cyclic extension of OFDM transmitted symbol tation of OFDM

3.1.4 Zero padding

Another type of guard interval is a zero-padding .Instead of inducing the cyclic prefix, each IFFT processed block is zero padded, by many zeros depending on channel's order to

eliminate ISI. If the number of zeros padded is equal to cyclic prefix length, then ZP-OFDM and CP-OFDM transmission has the same spectral efficiency.
Other types of guard intervals are possible. One possible type is to have half the guard period a cyclic prefix of the symbol, as in cyclic prefix type, and the other half a zero padded, as above [16].

3.2 Synchronization of OFDM systems

Synchronization is a big hurdle in OFDM. Synchronization usually consists of three parts as follows:

3.2.1 Frame detection

Frame detection is used to determine the symbol boundary so that correct samples for a symbol frame can be taken. The sampling starting point TX at the receiving end must satisfy the condition $\tau_{\max} \langle T_x \langle T_g$,where τ_{max} is maximum delay spread. Since the previous symbol will only have effect over samples within [0,τmax],there is no ISI [18].
There are many algorithms that can be applied to estimate the start of an OFDM symbol based on pilots or on the cyclic prefix. A good synchronization method must be fast, have a reliable indication of the synchronized state and introduce a minimum of redundancy in the transmitted stream.
Most existing timing algorithms use correlations between repeated OFDM signal portions to create a timing plateau. Such algorithms are not able to give precise timing position especially when the SNR is low. To improve the robustness of the algorithms, in [29] they used a differentially coded time-domain PN sequence for frame detection. Because of its delta like self-correlation property, the PN sequence allows to find the precise timing position. The PN sequence is transmitted as part of the OFDM packet preamble. At the receiver, the received signal samples are correlated with the known sequence. When the transmitted PN sequence is aligned with receiver PN sequence, a correlation peak is observed from which the OFDM symbol boundary can be inferred.

3.2.2 Carrier synchronization error

Carrier frequency offset estimation plays an important role in OFDM communication systems because of their high sensitivity to carrier frequency offsets [19]. Due to the carrier frequency difference of the transmitter and receiver, each signal sample at time t contains an unknown phase factor $e^{j2\pi\Delta f_c t}$, where Δf is the unknown carrier frequency offset. This unknown phase factor must be estimated and compensated for each sample before FFT at the receiver, since otherwise the orthogonality between sub-carriers is lost.
The impact of a frequency error can be seen as an error in the frequency instants, where the received signal is sampled during demodulation by the FFT Fig (8) depicts this two-fold effect. The amplitude of the desired sub-carrier is reduced ('+') and inter-carrier-interference ICI arises from the adjacent sub-carriers ('0') [20].

3.2.3 Sampling error correction

Because the sampling clock difference between the transmitter and receiver, each signal sample is off from its correct sampling time by a small amount which is linearly increasing with the index of the sample. For example, for 100ppm crystal offset, it will be off by 1

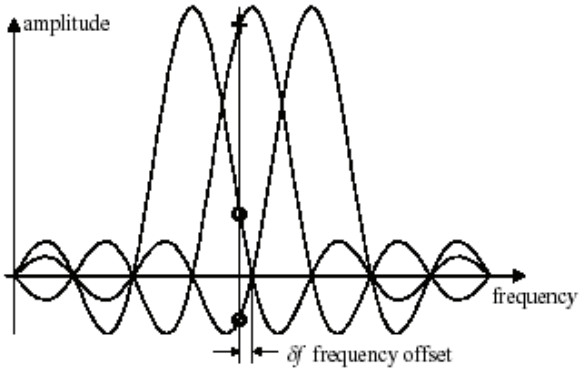

Fig. 8. Inter-carrier-interference (ICI) arises in case of a carrier synchronization error.

sample after 10000 samples. If a symbol contains 100 samples, then within each symbol the maximum offset will be 1% of a sample. Although this may cause the orthogonality degrading between the sub-carriers, it can usually be ignored. If sampling error must be corrected, then interpolation filter must be used to construct the signal at correct sampling time [18].

4. Mobile radio channels

In mobile radio channels, the transmitted signal suffers from different effects, which are characterized as follows [21],[22],[23]:

Multi-path propagation occurs as a consequence of reflection, scattering, and diffraction of the transmitted electromagnetic wave at natural and man-made objects. Thus, at the receiver antenna, a multitude of waves arrives from many different directions with different delays, attenuations, and phases as shown in Fig.(9), which shows that the terminal station (TS) may receive the direct signal from the base station (BS) as well as several signals generated due to reflections and scattering. The superposition of these waves results in amplitude and phase variations of the composite received signal.

Changes in the phases and amplitudes of the arriving waves occur, which lead to time-variant multi-path propagation. Even small movements on the order of the wavelength may result in a totally different wave superposition The varying signal strength due to time-variant multi-path propagation is referred to as fast fading. Shadowing is caused by obstruction of the transmitted waves by e.g., hills, buildings, wall, and trees, which results in more or less strong attenuation of the signal strength. Compared to fast fading, longer distances have to be covered to significantly change the shadowing constellation. The varying signal strength due to shadowing is called slow fading and can be described by a log-normal distribution

Path loss indicates how the mean signal power decays with distance between transmitter, and receiver. In free space, the mean signal power decreases with the square of the distance between (BS) and (TS). In a mobile radio channel, where often no line of site (LOS) path exists, signal power decreases with a power higher than two and is typically in the order of three to five. Variations of the received power due to shadowing and path loss can be efficiently counteracted by power control.

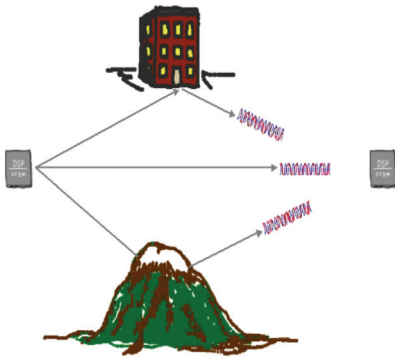

Fig. 9. Composite received signal due to reflections in mobile radio channel

4.1 Channel modeling

The mobile radio channel can be characterized by the time-variant channel impulse response h(τ,t) [24]. The channel impulse response represents the response of the channel at time t due to an impulse applied at time t-τ. The mobile radio channel is assumed to be a wide-sense stationary random process, i.e., the channel has a fading statistic that remains constant over short periods of time or small spatial distances. In environments with multi-path propagation, the channel impulse response is composed of a large number of scattered impulses received over Np different paths,

$$h(\tau,t)=\sum_{p=0}^{N_p-1} a_p e^{j(2\pi f_{d,p}t+\varphi_p)}\delta(\tau-\tau_p) \tag{27}$$

where,

$$\delta(\tau-\tau_p)=\begin{cases}1, & if\ \tau=\tau_p\\ 0, & otherwise\end{cases} \tag{28}$$

and a_p, $f_{d,p}$, φ_p, and τ_p are the amplitude, the Doppler frequency, the phase, and the propagation delay, respectively, associated with the path p, p=0,1,2,……,Np-1. A channel impulse response with corresponding channel transfer function is illustrated in Fig.(10), while, Fig.(11), is a block diagram representation of a fading channel with two paths, i.e., with two rays.

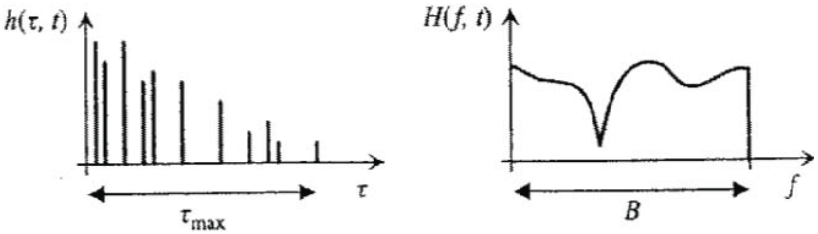

Fig. 10. Time-variant channel impulse response and channel transfer function with frequency-selective fading

The assigned channel transfer function is

$$H(f,t) = \sum_{p=0}^{N_p-1} a_p e^{j(2\pi(f_{d,p}t + f\tau_p)+\varphi_p)} \tag{29}$$

The delays are measured relative to the first detectable path at the receiver. The Doppler frequency is given by [22]:

$$f_{d,p} = \frac{v f_c \cos(\theta_p)}{c} \tag{30}$$

It is obvious that $f_{d,p}$ depends on the velocity v of the terminal station, the speed of light c, the carrier frequency f_c, and the angle of incidence θp of a wave assigned to a path p.

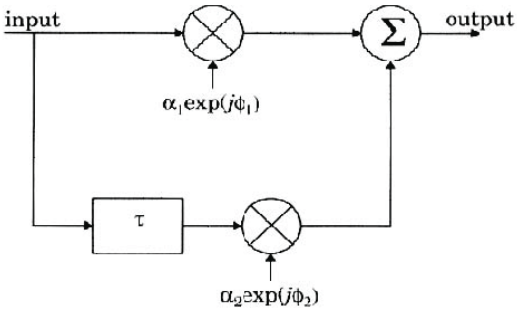

Fig. 11. 2-Ray fading channel

Fig. (12) illustrates the Doppler effect. The delay power density spectrum ρ(τ) that characterizes the frequency selectivity of the mobile radio channel gives the average power of the channel output as a function of the delay, τ. The mean delay $\bar{\tau}$, the root mean square (RMS) delay spread τRMS and the maximum

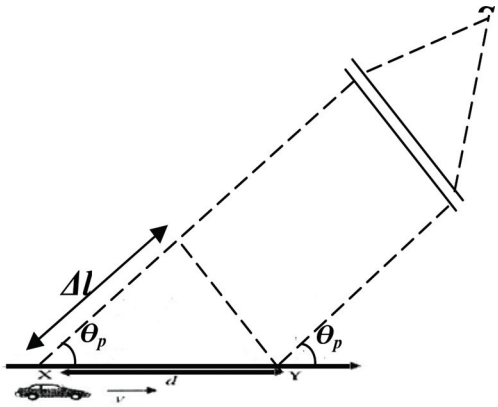

Fig. 12. Illustration of Doppler Effect

Delay τmax are characteristic parameters of the delay power density spectrum. The mean delay is:

$$\overline{\tau} = \frac{\sum_{P=0}^{N_p-1} \tau_P \left|a_P\right|^2}{\sum_{P=0}^{N_p-1} \left|a_P\right|^2} \tag{31}$$

where, the term $\left|a_P\right|^2$, in equation (31) represents the power of path p. The RMS delay spread is defined as:

$$\tau_P = \sqrt{\frac{\sum_{P=0}^{N_p-1} {\tau_P}^2 \left|a_P\right|^2}{\sum_{P=0}^{N_p-1} \left|a_P\right|^2} - (\overline{\tau})^2} \tag{32}$$

Similarly, the Doppler power density spectrum S(fd) can be defined as that characterizing the time variance of the mobile radio channel and gives the average power of the channel output as a function of the Doppler frequency fD. The frequency dispersive properties of multi-path channels are most commonly quantified by the maximum occurring Doppler frequency fD max and the Doppler spread fDspread. The Doppler spread is the bandwidth of the Doppler power density spectrum and can take on values up to two times $\left|\text{fDmax}\right|$ [25] , i.e.,

$$\text{fDspread} \le 2 \left|\text{fDmax}\right| \tag{33}$$

4.2 Channel fade statistics

The statistics of the fading process characterize the channel and are of importance for channel model parameter specifications. A simple and often used approach is obtained from the assumption that there is a large number of scatterers in the channel that contribute to the signal at the receiver side. The application of the central limit theorem leads to a complex-valued Gaussian process for the channel impulse response. In the absence of LOS or a dominant component, the process is zero-mean. The magnitude of the corresponding channel transfer function:

$$\text{a=a(f,t)=}\left|\text{H(f,t)}\right| \tag{34}$$

is the random variable, with Rayleigh's distribution given by:

$$p(a) = \frac{2a}{\Omega} e^{-\frac{a^2}{\Omega}} \tag{35}$$

where the average power is:

$$\Omega = \left\{a^2\right\} \tag{36}$$

The phase is uniformly distributed in the interval [0, 2π]. In the case that the multi-path channel contains a LOS or dominant component in addition to the randomly moving scatters. The channel impulse response can no longer be modeled as zero-mean. Under the assumption of a complex-valued Gaussian process for the channel impulse response, the magnitude of the channel transfer function has a Rice distribution given by:

$$P(a) = \frac{2a}{\Omega} e^{-(a^2/\Omega + K_{Rice})} I_0\left(2a\sqrt{\frac{K_{Rice}}{\Omega}}\right) \tag{37}$$

The Rice factor KRice is determined by the ratio of the power of the dominant path to the power of the scattered paths. Io is the zero-order modified Bessel function. The phase is uniformly distributed in the interval [0, 2π].

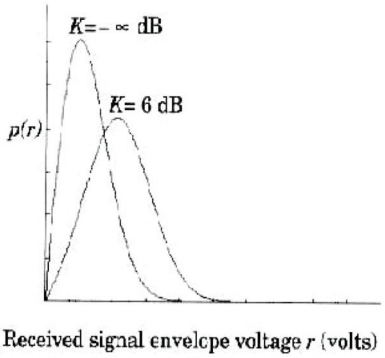

Fig. 13. Probability density function of Ricean Distribution, k=-∞ for (Rayleigh)

4.3 Inter-symbol interference (ISI) and inter-channel interference (ICI)

The delay spread can cause inter-symbol-interference (ISI), when adjacent data symbols overlap and interfere with each other due to different delays on different propagation paths. The number of interfering symbols in a single-carrier modulated system is given by

$$N_{ISI,\sin gle-carrier} = \left\lceil \frac{\tau_{\max}}{T_d} \right\rceil \tag{38}$$

For high data rate applications with very short symbol duration Td < τmax, the effect of ISI and, with that, the receiver complexity can increase significantly. The effect of ISI can be counteracted by different measures such as time or frequency domain equalization.

In spread spectrum systems, rake receivers with several arms are used to reduce the effect of ISI by exploiting the multi-path diversity such that individual arms are adapted to different propagation paths.

If the duration of the transmitted symbol is significantly larger than the maximum delay Td>>τmax, the channel produces a negligible amount of ISI. This effect is exploited with multi-carrier transmission where the duration of the transmitted symbol increases with the number of sub-carrier Nc and, hence, the amount of ISI decreases. The number of the interfering symbols in a multi-carrier modulated system is given by:

$$N_{ISI,multicarrier} = \left\lceil \frac{\tau_{\max}}{N_c T_d} \right\rceil \tag{39}$$

Residual ISI can be eliminated by the use of a guard interval. The maximum Doppler spread in mobile radio applications using single-carrier modulation is typically much less than the distance between adjacent channels, such that the effect of interference on adjacent channels due to Doppler spread is not a problem for a single-carrier modulated systems. For multi-carrier modulated systems, the sub-channel spacing Fs can become quite small, such that Doppler effects can cause significant ICI. As long as all sub-carriers are affected by a common Doppler shift fd, this Doppler shift can be compensated for in the receiver and ICI can be avoided. However, if Doppler spread on the order of several percent of the sub-carrier spacing occurs. ICI may degrade the system performance significantly. To avoid performance degradations due to ICI more complex receivers with ICI equalization should be used. The sub-carrier spacing Fs should be chosen as:

$$F_S >> f_{D\max} \tag{40}$$

such that the effect due to Doppler spread can be neglected.
Nevertheless, if a multi-carrier system design is chosen such that the Doppler spread is on the order of the sub-carrier spacing or higher, a rake receiver in the frequency domain can be used. With the frequency domain rake receiver each branch of the rake resolves a different Doppler frequency.

5. Code division multiple access scheme

In the context of broadband wireless communications using CDMA without the assistance of frequency/ time hopping, the main multiple access options include Multi-tone CDMA (MT-CDMA) using time domain DS spreading [26], Multicarrier CDMA (MC-CDMA) using frequency domain spreading, as well as Multicarrier DS-CDMA (MC DS-CDMA) using time domain DS spreading of the individual sub-carrier signals [27].
The behavior of the above three CDMA schemes will be investigated when communicating over broadband wireless channels. It will be shown that regardless of the communication environments encountered, both Multi-tone DS-CDMA and MC-CDMA exhibit more severe problems than MC DS-CDMA. Broad-band MC DS-CDMA augmented by transmit diversity is capable of mitigating the problems imposed by broadband wireless channels. It is shown that by appropriately selecting the system parameters, transmit diversity assisted broadband MC DS-CDMA is capable of supporting wireless communications in diverse propagation environments. Furthermore, the capacity improvement achievable by broadband MC DS-CDMA systems is also investigated. Let an overview first embark on a rudimentary of the above three CDMA schemes.

5.1 MC CDMA system

Multicarrier CDMA schemes can be broadly categorized into two groups. The first type spreads the original data stream using a spreading code and then modulates different carriers with each chip. This is usually referred to as MC-CDMA. The second type spreads the serial to parallel converted streams using a spreading code and then modulates different carriers with each data stream [21]. Denoting the bit duration as Tb and the chip duration as

Tc, then the sub-carrier spacing in one system is 1/Tc and the other is 1/Tb. The former is called the Multicarrier DS-CDMA (MC-DS-CDMA) and the latter is called the Multi-tone CDMA (MT-CDMA). The performance of these two schemes has been studied for an uplink channel in [29]. Hara has shown that MC-CDMA outperforms MC-DS-CDMA and MT-CDMA in terms of downlink BER performance. MC-CDMA is thus an attractive technique for the downlink [30]. A simple block diagram of a MC-CDMA system is as shown below in Figure (14) below.

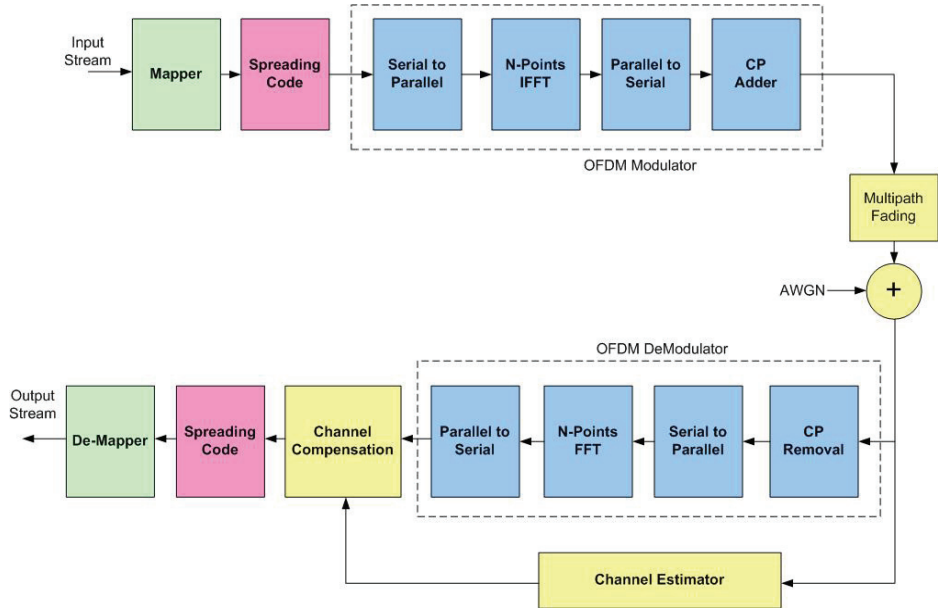

Fig. 14. Block Diagram of a FFT-MC-CDMA system

The input data stream is spread using the spreading sequence which could be a Walsh-Hadamard code or a PN sequence. The resultant chips after spreading the symbols are modulated into different sub-carriers using the IFFT operator. The end few symbols are appended at the beginning of the frame to act as the cyclic prefix. The cyclic prefix maintains Orthogonality between the sub-carriers in a multipath channel. The receiver first removes the cyclic prefix and then performs an FFT operation of the received symbols and brings them back to the frequency domain. Then dispreading and decoding of the chips in frequency domain are performed.

5.2 MC-DS CDMA system

The block diagram of MC-DS CDMA transmitter is shown in Fig(15(a)) The incoming data stream is first converted to a parallel stream and then spread in time using spreading codes. This ensures that the resulting spectrum has orthogonal sub-carriers. The spreading code is represented as C(t) and the processing gain is N. The receiver block is shown in Fig (15(b)). The dispreading is done in time after the FFT followed by a low pass filter and demodulation. The figures are adapted from [31].

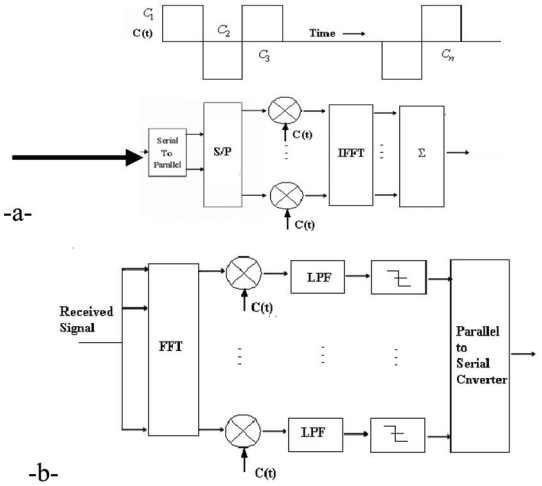

Fig. 15. (a) MC-DS CDMA Transmitter (b) MC-DS CDMA Receiver

5.3 Multi-tone CDMA (MT-CDMA) system

Multi-Tone CDMA transmitter spreads the serial parallel converted data streams using a spreading code in time domain so that the spreading operation can satisfy the Orthogonality condition. The MT-CDMA uses spreading codes in multiples of the number of sub-carriers as compared to MC-DS CDMA.

The transmitter block is shown in Fig (16(a)). The receiver employs Rake combining to effectively utilize the diversity due to multipath. The figures are adapted from [31, 32].

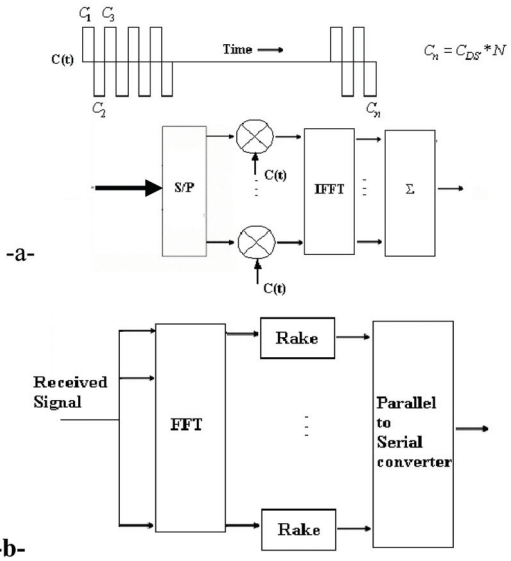

Fig. 16. (a) MT-CDMA Transmitter, (b) MT-CDMA Receiver

5.4 DWT based MC CDMA system

Figure (17) below shows the block diagram of the DWT-MC-CDMA system. The only difference is that DWT is used instead of the FFT in the OFDM modulator and demodulator. Since wavelet based OFDM will not add a cyclic prefix to OFDM symbol, its data rates can surpass those of the FFT implementation.

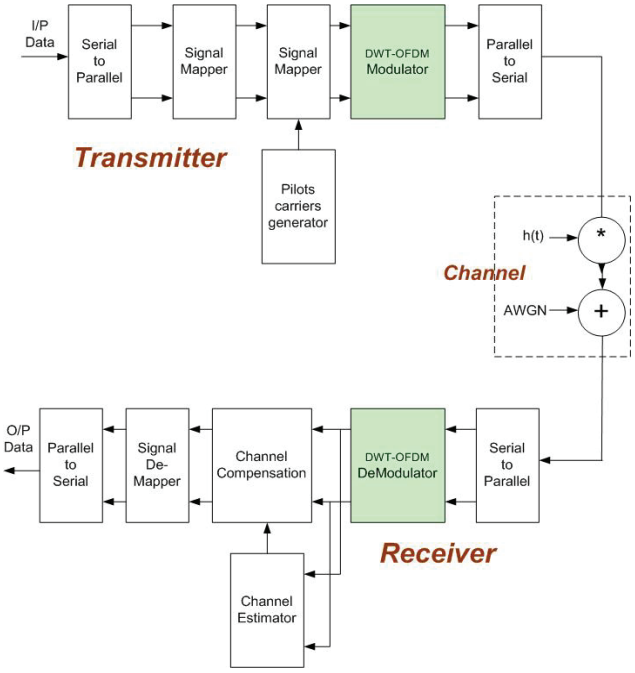

Fig. 17. Block Diagram of DWT-MC-CDMA System

5.5 DWT based STBC-MC-DS-CDMA system

The block diagram of the MC-DS-CDMA is depicted in Figure (18).This Figure illustrates a typical STBC-MC-DS-CDMA system used for Multicarrier modulation using one transmitter and one receiver.

6. Simulation results

In this section the simulation of the FFT based OFDM STBC DWTCS-OFDM system in MATLAB version 7 are achieved. And the BER performance of the OFDM system considered in different channel models, the AWGN channel, the flat fading channel. Table (1) shows the parameters of the system that are used in the simulations; the bandwidth used was 10MHz.

6.1 Performance of DWT-MC-CDMA in AWGN and flat fading channel models

Simulation results of the DWT-OFDM system is shown in figure (19). It is shown clearly that the DWT-MC-CDMA is much better than the system FFT-MC-CDMA. This is a reflection to the fact that the orthogonal bases of the wavelet is much significant than the orthogonal bases used in FFT-MC-CDMA.

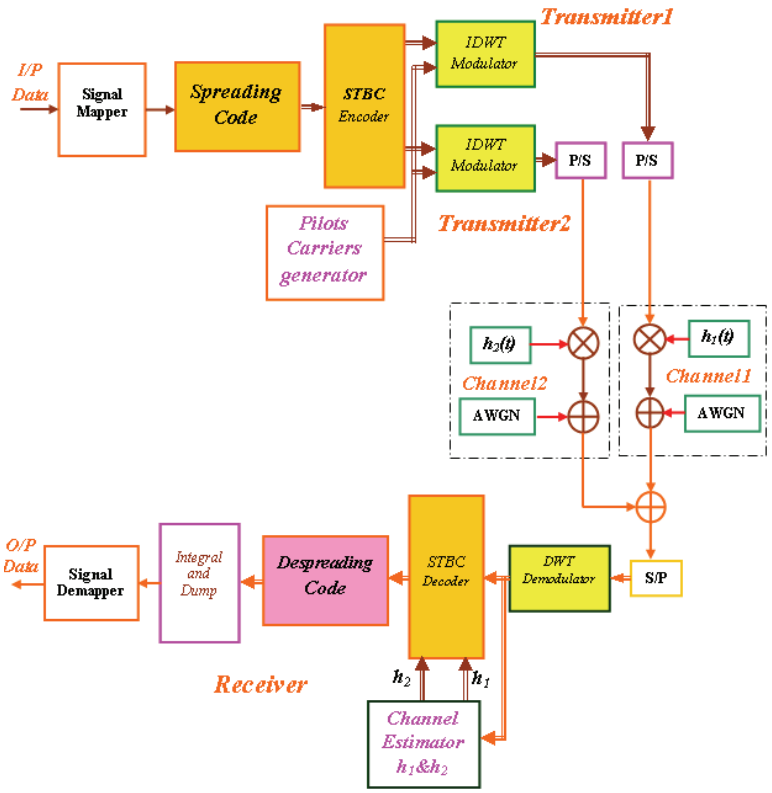

Fig. 18. Block Diagram of the DWT based STBC-MC-DS-CDMA System

Modulation Types	QPSK
Number of sub-carriers	64
Number of DMWT points	64
Channel model	AWGN
	Flat fading+ AWGN
	Frequency selective fading +AWGN

Table 1. Simulation Parameters

Figure (20) below shows simulation result of the DWT-MC-CDMA system in the flat fading channel that assumed all the frequency components of the transmitted signal are changed correlated in phase and magnitude. Maximum Doppler Shift taken was 5Hz.
It is shown that wavelet based MC-CDMA is still better than that based on FFT transform. The wavelet based MC-CDMA system has BER=10^{-3} at SNR=25dB, while in case of FFT based MC-CDMA system, the BER=10^{-3} achieved at approximately SNR=40dB, which means a gain of about 15dB has been achieved.

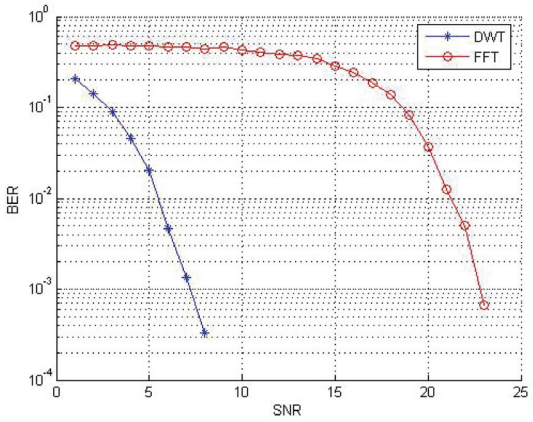

Fig. 19. BER performance of DMWT-OFDM in AWGN channel model

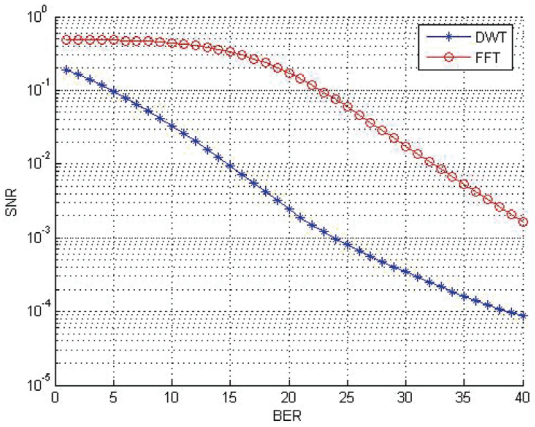

Fig. 20. BER performance of DWT-MC-CDMA in Flat Fading Channel at Max. Doppler Shift=5

6.2 Performance of STBC-MC-DS-CDMA systems in AWGN and flat fading channel models

Simulation result of the STBC-MC-DS-CDMA Systems in AWGN channel is shown in Figure (21). It is clearly shown that the STBC-MC-DS-CDMA Based on DWT is much better than STBC-MC-DS-CDMA systems Based on FFT.

In flat Fading Channel simulation a Doppler frequency of 10Hz is used. From Figure (22) it can be seen that for BER=10-4 the SNR required for DWT based STBC-MC-DS-CDMA was about 13dB and for FFT based STBC-MC-DS-CDMA has 25dB, therefore a gain of 12dB for the DWT against FFT is achieved.

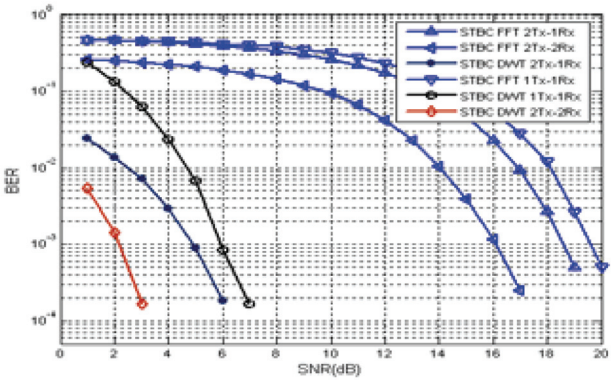

Fig. 21. Performance of STBC-MC-CDMA System in AWGN Channel.

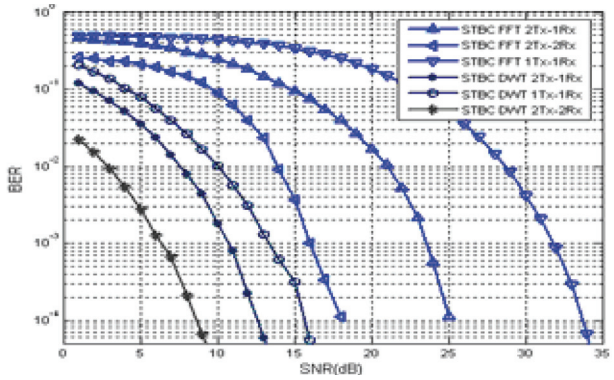

Fig. 22. Performance of S TBC-DS-CDMA in Flat Fading Channel Max. Doppler Shift= 10Hz.

7. Conclusions

The improved performance of MC-DS-CDMA system using STBC schemes and DWT is investigated. The performance comparisons of BER performance for the conventional MC-DS-CDMA based on FFT, STBC MC-DS-CDMA and DWT based STBC MC-DS-CDMA in the different channel models together with their comparison for best achievable BER have been presented. Simulation results were provided to demonstrate that significant gains can be achieved by introducing such combination technique with very little decoding complexity. Therefore, the DWT based STBC MC-DS-CDMA is a feasible way to reach the next generation of wireless communication for large data rates and applications

8. References

[1] Shinsuke Hara, and Ramjrr Prasad. "Multicarrier Techniques for 4G Mobile Communications," Artech House, Boston. London, (2003).

[2] Sttot J. H. "Explaining Some of the Magic COFDM," Proceedings of 20th International Television Symposium, (1997).
[3] Chuang J., and Sollenberger N. "Beyond 3G Wideband Wireless Data Access Based on OFDM and Dynamic Packet Assignment," IEEE Communication Magazine, vol. 38, no.7, pp. 78-87, July (2000)
[4] Kaiser S. "On the Performance of Different Detection Techniques for OFDM-CDMA in Fading Channels," IEEE ICC'95. pp. 2059-2063, June (1995).
[5] C. Valens, "A Really Friendly Guide to Wavelets", 1999.
[6] A. Graps, "An Introduction to Wavelets", IEEE Computational Science and Eng., Vol. 2, No. 2, 1995.
[7] Goswami J. C., Chan A. K., "Fundamentals of Wavelets Theory, Algorithms and Applications", John Wiley & Sons Ltd. 1999.
[8] Mallat S., "A Theory for Multiresolution Signal Decomposition: the Wavelet Representation, " IEEE Pattern Anal. And Machine Intel, vol. 11, no. 7, pp. 674-693. 1989.
[9] V. Strela, G. Strang et al, "The Application of Multiwavelet Filter Banks to Image Processing" IEEE Transaction on Image Processing, 1993.
[10] V. Strela, "Multiwavelets: Theory and Application", Ph.D Thesis, MIT, June 1996.
[11] H. Steendam and M. Moeneclaey "The Effect of Carrier Frequency Offsets on Downlink and Uplink MC-DS-CDMA", IEEE JOURNAL on Select. Areas in Comm., vol. 19, no. 12, Dec. 2001.
[12] S. Hara and R. Prasad "Multi-Carrier Techniques for 4G Mobile Communications", 1st Edition, Artech House, Boston, 2003
[13] Hanzo L. et al, "OFDM and MC-CDMA for Broadband Multi-User Communications, WLANs and Broadcasting," John Wiley & Sons, (2003): CS-Books@wiley.co.uk
[14] J. G. Proakis, "Digital Communications", Prentice-Hall, 4th edition, 2004.
[15] Minn H., Bhargava V.K., "An Investigation into Time Domain Approach for OFDM Channel Estimation" IEEE Transaction on Broadcasting, Vol. 46, Dec 2000.
[16] Y. Zigang, and et al, "Blind Bayesian Multiuser Receiver for Space-time Coded MC-CDMA System over Frequency-Selective Fading Channel", IEEE Trans. Veh. Techn, vol. VT-40, pp. 781-785, May 2001.
[17] M. Alard and R. Lassalle, "Principles of Modulation and Channel Coding for Digital Broadcasting for Mobile Receiver," Tech. Rep., no. 224, pp.47-69, Aug. 1987.
[18] P. Frederik and L. Geert "Space–Time Block Coding for Single-Carrier Block Transmission DS-CDMA Downlink" IEEE Journal On Selected Areas In Communications, Vol. 21, No. 3, pp. 350-361, APRIL 2003
[19] Hui Liu and Hujun Yin, "Receiver Design in Multi-carrier Direct-Sequence CDMA Communications", IEEE Trans. On Comm., vol. 49, no. 8, Aug. 2001.
[20] H. Steendam and M. Moeneclaey "The Effect of Carrier Frequency Offsets on Downlink and Uplink MC-DS-CDMA", IEEE JOURNAL on Select. Areas in Comm., vol. 19, no. 12, Dec. 2001.
[21] J. D. Gibson, "The Communication Handbook" 2nd Edition, Southern Methodist University Dallas, Texas, 2002.

[22] L. Hanzo, C.H. Wong, M.S. Yee, "Adaptive Wireless Transceivers Turbo-Coded, Turbo-Equalized and Space-Time Coded TDMA, CDMA and OFDM Systems," John Wiley & Sons Ltd, 2002.

[23] O.M Mustaf "Performance Evaluation of a Proposed MC-DS-CDMA for Broadband Wireless Access", PhD Thesis, University of Baghdad, 2006

[24] I. Barhumi et al, "Optimal Training Design for MIMO OFDM Systems in Mobile Wireless Channels", IEEE Trans. On Signal Processing, Vol.51, no. 6, June. 2003.

[25] Z. Cao et al "Efficient Structure-based Carrier Frequency Offset Estimation for Interleaved OFDMA Uplink", under publication of IEEE.

[26] F. Molisch "Wideband Wireless Digital Communications", 2nd Edition, Prentice Hall, New York, 2002.

[27] N.Yuan, "An Equalization Technique for High Rate OFDM Systems" M.Sc. Thesis University of Saskatchewan .Saskatoon, Dec.2003.

[28] Zhi Zliang and Li Guoqing, "A Novel Decoding Algorithm of STBC for CDMA Receiver in Multipath Fading Environments," IEEE Trans. on Comm., vol. 49, pp. 1956-1959, April 2001

[29] I. Barhumi et al, "Time-Varying FIR Equalization for Doubly-Selective Channels", IEEE Trans. On Wireless Comm., Vol. 4, no. 1, Jan. 2005.

[30] K. Ming and T. Chee "Hybrid OFDM-CDMA: A Comparison of MC/DS-CDMA, MC-CDMA and OFCDM" Dept of Electrical & Electronic, Adelaide University, SA 5005, Australia. 2002.

[31] J. Tang, and Xi Zhang, "Transmit Selection Diversity With Maximal-Ratio Combining for Multicarrier DS-CDMA Wireless Networks Over Nakagami-m Fading Channels", IEEE Journal On Selected Areas In Communications, VOL. 24, NO. 1, pp. 5710–5713, January 2006.

[32] Y. Jing "Space-Time Code Design and Its Applications in Wireless Networks" Ph.D. thesis in California Institute of Technology Pasadena, California, September 7, 2004